Controlled synthesis and characterization of ru-fullerene nanostructures and their catalyticapllications

Faqiang Leng

THÈSE

En vue de l'obtention du

DOCTORAT DE L'UNIVERSITÉ DE TOULOUSE

Délivré par :

Institut National Polytechnique de Toulouse (INP Toulouse)

Discipline ou spécialité :

Chimie Organométallique et de Coordination

Présentée et soutenue par :

M. FAQIANG LENG

le jeudi 6 octobre 2016

Titre :

CONTROLLED SYNTHESIS AND CHARACTERIZATION OF RU-FULLERENE NANOSTRUCTURES AND THEIR CATALYTIC APPLICATIONS

Ecole doctorale :

Sciences de la Matière (SDM)

Unité de recherche :

Laboratoire de Chimie de Coordination (L.C.C.)

Directeur(s) de Thèse :

M. PHILIPPE SERP

MME MARIA ROSA AXET MARTI

Rapporteurs :

M. JEAN-CYRILLE HIERSO, UNIVERSITE DE BOURGOGNE

Mme SOPHIE HERMANS, UNIVERSITE CATHOLIQUE DE LOUVAIN

Membre(s) du jury :

M. BRUNO CHAUDRET, INSA TOULOUSE, Président

Mme CARMEN CLAVER, UNIVERSITAT ROVIRA I VIRGILI TARRAGONA, Membre

Acknowledgement

First of all, I would like to express my sincere appreciation to my two supervisors: Professor Philippe SERP and Dr. M. Rosa AXET for their constant guidance and encouragement, and without this my thesis would not have been possible. For their selfless and unwavering support, I am truly grateful.

To my committee, Professor Bruno Chaudret, Professor Jean-Cyillle Hierso, Professor Sophie hermans, and Professor Carmen Claver, I am extremely grateful for your assistance and suggestions throughout my PhD defense.

To my collaborators, Dr. Iann Gerber in Laboratoire de Physique et Chimie des Nano-objets INSA Toulouse, I would like to thank you for his valuable DFT calculation results, which are very helpful for my PhD thesis.

To Professor Nazario Martin, I am very appreciated that he can receive as internship student work in his group, and I would like to thank you for his kindly guidance and help on the functionalized of fullerene in Complutense University of Madrid. The author would like to thank the entire team in Madrid for their warmly hospitality.

This thesis could not have been accomplished without the assistance of many people, whose contribution I grateful acknowledge. Especially thanks to Vincent Colliere for the TEM measurement. I am very much thankful for Pierre Lecante, who gave me a valuable WAXS analysis, and also thank you for S. Moldovan and M. Girleanu, who performed the electron tomography analysis in the thesis. Many thanks to Professor Wolfgang Bacsa for the Raman analysis, Jeff Miller for the EAXF analysis, Professor Hervé Martinez for the XPS analysis, and Dr. Philippe Poulin for SAXS measurement.

I also would like to thank my colleges and all present or former members of the Catalysis Fine Chemical groups, who I enjoyed to work with during stay in Toulouse. Laurent Ropiquet, Idaline Chanteperdrix and Nora Imlyhen are acknowledged for

their kindly help for my experiment work in the Lab. Dr. Jerome Volkman are thanked for kindly discussion and suggestions, and also thanks to Professor Martine Urrutigoity for her moral support. I also thank Maryse Gouygou, Professor Philippe Kalck, Odile Dechy-Cabaret, Jérôme Durand, Carole Le Berre for their kindly help during this research work. I am especially thankful to Stéphane Louisia, Justine Harmel, Nicolas Gimeno, Dr. Bruno Machado, Dr. Hania Ahouari, Liping Zhang, Dr. Jian Ye, Professor Rui Zhao, Cuiling Xu for their practical help, valuable friendship and encouragement during the past three years.

Many thanks to the whole LCC and ENSIACET staff, and I would like to thank all the people who cooperated in this way or another way to complete this research work.

I also thanks to my beloved friends Dr. Weikai Zong, Dr. Renjie Wang, Dr. Diandian Ke, Dr.Congzhang Gao, Xuefei Zhao, Zhouye Chen, Yu Chen for their friendship, support and motivation in the past three years.

Finally, I would like to thank my wife Mengmeng for standing beside me throughout my three years PhD life, she has been my motivation for continuing to improve my knowledge and move my research forward. A warm thank to my family for their trustful and supporting.

Faqiang LENG

Résumé

Le travail décrit dans cette thèse vise à produire des nanostructures bien ordonnées présentant une forte activité catalytique sur la base d'ensembles de nanoparticules de ruthénium et de fullerènes/fullerènes fonctionnalisés. Le **Chapitre 1** présente une analyse bibliographique sur l'utilisation des fullerènes en catalyse hétérogène, en mettant en avant leurs propriétés particulières telles que la stabilité thermique, une grande capacité d'adsorption d'hydrogène et la capacité d'obtenir diverses coordinations. Le **Chapitre 2** décrit la synthèse et la caractérisation de nanostructures $Ru@C_{60}$ obtenues par la réaction de décomposition par au dihydrogène du complexe [Ru(COD)(COT)] en présence de C_{60}. L'effet du solvant et des rapports de Ru/C_{60} utilisés durant la réaction ont été étudiés. Plusieurs caractérisations d'objets sphériques $Ru@C_{60}$ et des calculs DFT nous permettent de proposer une voie pour leur formation. Le **Chapitre 3** présente la préparation de nouveaux nano-assemblages obtenus à partir de [Ru(COD)(COT)] et de fullerènes fonctionnalisés en utilisant la même méthode décrite dans le chapitre 2. Tout d'abord la synthèse de fullerènes fonctionnalisés $C_{66}(COOH)_{12}$ est détaillée, puis la synthèse et la caractérisation des nanostructures $Ru@C_{66}(COOH)_{12}$ ont été étudiés. Le **Chapitre 4** décrit l'utilisation de ces nanomatériaux en catalyse. Nous avons préparé trois Ru@fullerene: $Ru@C_{60}$ dans du dichlorométhane, T-$Ru@C_{60}$ dans le toluène et $Ru@C_{66}(COOH)_{12}$. Ensuite, l'activité catalytique et la sélectivité des catalyseurs préparés $Ru@C_{60}$, T-$Ru@C_{60}$ et $Ru@C_{66}(COOH)_{12}$ ont été étudiées pour l'hydrogénation du nitrobenzène et du cinnamaldéhyde. Des calculs DFT ont permis de rationaliser les résultats obtenus pour l'hydrogénation sélective de nitrobenzène sur $Ru@C_{60}$.

Mots clés: ruthénium; nanoparticules; C_{60}; $C_{66}(COOH)_{12}$; catalyse; hydrogénation; nitrobenzène, cinnamaldéhyde

Abstract

The work described in this thesis aims to produce well-ordered nanostructures presenting high catalytic activity, on the bases of the assembly of ruthenium nanoparticles and fullerene/functionalized fullerene. **Chapter 1** provides a review on the use of fullerene and fullerene-based materials in heterogeneous catalysis, emphasizing their specific properties such as thermal stability, high capacity for hydrogen adsorption and the ability of various coordination modes. **Chapter 2** describes the synthesis and characterization of $Ru@C_{60}$ nanostructures produced by the decomposition reaction of [Ru(COD)(COT)] in the presence of C_{60}. The effect of the solvent and ratios of Ru/C_{60} on the course of the reaction have been investigated. Several characterizations of spherical $Ru@C_{60}$ objects and DFT calculations allow us to propose a pathway for their formation. **Chapter 3** presents new nano-assembly preparation based on [Ru(COD)(COT)] and functionalized fullerene using the same method as they are described in chapter 2. First, the synthesis of functionalized fullerene $C_{66}(COOH)_{12}$ is detailed, and then the synthesis and characterization of $Ru@C_{66}(COOH)_{12}$ is studied. **Chapter 4** describes the use of these nanomaterials in catalysis. We have prepared three Ru@fullerene catalysts, which are $Ru@C_{60}$ in dichloromethane, T-$Ru@C_{60}$ in toluene, and $Ru@C_{66}(COOH)_{12}$. Then, the catalytic activity and selectivity of the prepared catalyst $Ru@C_{60}$, T-$Ru@C_{60}$ and $Ru@C_{66}(COOH)_{12}$ are studied for the hydrogenation of nitrobenzene and cinnamaldehyde. DFT calculations allow to rationalize the results obtained for the selective hydrogenation of nitrobenzene over $Ru@C_{60}$.

Keywords: Ruthenium; nanoparticles; C_{60}; $C_{66}(COOH)_{12}$; catalysis; hydrogenation; nitrobenzene; cinnamaldehyde

Table of contents

Acknowledgement I

Résumé III

Abstract IV

Table of contents V

General introduction and objectives IX

References XI

List of abbreviations XII

Chapter 1 Introduction 1

1.1 Introduction 2

1.1.1 C_{60} structure 4

1.1.2 C_{60} synthesis 6

1.2 Coordination chemistry of fullerene C_{60} 7

1.2.1 η^2 coordination 8

1.2.2 η^5 coordination 18

1.2.3 η^1 coordination 21

1.2.4 η^3 and η^4 coordinations 24

1.2.5 η^6 coordination 25

1.3 Metal-C_{60} polymers 25

1.3.1 Synthesis of transition metal-fullerene polymers 26

1.3.2 Characterization of metal-fullerene polymers 32

1.4 Metal nanoparticles/fullerene C_{60} 37

1.4.1 Metallic nanocluster/C_{60} 37

1.4.2 Metallic nanoparticles/C_{60} 38

1.4.3 Metallic nanoparticles/functionalized C_{60} 41

1.4.4 Metallic nanoparticles/C_{60} crystals 43

1.5 Catalysis with metal/C_{60} 45

1.5.1 Catalysis with metal/C_{60} polymers 45

1.5.2 Catalysis with metal nanoparticles/C_{60} 47

1.6 Conclusions 50

1.7 References 53

Chapter 2 Synthesis and characterization of Ru@C_{60} nanostructures 65

2.1 Introduction 67

2.2 Results and discussion 69

2.2.1 Solvent effect 71

2.2.2 Ru/C_{60} ratio effect 81

2.2.3 Characterization of the Ru@C_{60} nanostructures 87

2.3 Conclusions 119

2.4 Experimental section 120

2.5 References 127

Chapter 3 Synthesis and characterization of ruthenium nanostructures based on functionalized fullerene 131

3.1 Introduction 132

3.2 Results and discussion 134

3.2.1 Functionalization of fullerene C_{60} 136

3.2.2 Synthesis of Ru nanostructures based on functionalized fullerene@$C_{66}(COOH)_{12}$ 142

3.3 Conclusions 157

3.4 Experimental section 158

3.5 References 167

Chapter 4 Catalytic applications of ruthenium@fullerene nanostructures 170

4.1 Introduction 172

4.2 Results and discussion 173

4.2.1 Hydrogenation of nitrobenzene 173

4.2.2 Hydrogenation of *trans*-cinnamaldehyde 188

4.3 Conclusions 192

4.4 Experimental section 193

4.5 References 197

General conclusions and perspectives 204

Chapitre 5 Résumé 208

5.1 Introduction 209

5.2 Synthèse et caractérisation des nanostructures Ru@C_{60} et T-Ru@C_{60}. 210

5.2.1 Synthèse des nanostructures Ru@C_{60}.....210

5.2.2 Caractérisation des nanostructures Ru@C_{60}.....213

5.3 Synthèse et caractérisation des nanostructures à base de ruthénium et de fullerène fonctionnalisé.....216

5.3.1 Effet du solvant et du rapport Ru/$C_{66}(COOH)_{12}$.....217

5.3.2 Caractérisation des nanostructures Ru@$C_{66}(COOH)_{12}$ 218

5.4 Applications catalytiques des nanostructures ruthénium@fullerène 222

5.4.1 Hydrogénation du nitrobenzène.....222

5.4.2 Hydrogénation du *trans*-cinnamaldéhyde.....226

5.5 Conclusions.....228

General introduction and objectives

Catalysis is the essential technology for precisely transforming the chemical structure of matter on a large scale, and catalysts are the key enabler in 90% of chemical manufacturing processes. One of the main challenges for catalysis science in the 21st century is ***to further understand and design catalyst structures to better control catalytic activity, selectivity and stability***.[1] In that context, investigations on porous materials with tailored pore structures, composition, and nano-environment for catalytic sites are of strategic importance; and it is obvious that any new branches of catalysis science, such as nanocatalysis,[2] should be considered as a potential spur to reach the objectives. Among the different nanocatalysts, nanostructured carbon materials are gaining more and more visibility.[3] The development of new carbon nanostructures over the last decades enables control of carbon materials at multiple length scales in very new manners. The versatility of these materials and the complexity of carbon physical chemistry make the design of structurally controlled catalysts a highly challenging task. Designing catalytic nano-architectures offers the promise of higher activity, selectivity and stability,[4] provided the following specifications are followed: i) a control of nanoparticle size or shape, ii) a control of the direct environment of the nanoparticle, and ii) a robust and controlled (covalent) metal-support interaction.

The objective of this PhD thesis is to produce groundbreaking metal@carbon nanostructures with such specifications that will open new routes and opportunities for modern catalysis science. Thus, a new carbon (surface) chemistry will be developed to synthesize a new type of metal@carbon architectures consisting in organized networks of fullerenes and ruthenium nanoparticles (NPs). We will apply them to a strategic domain of catalysis in industrialized countries: fine chemical synthesis. Two reactions of industrial interest have been selected for which catalytic activity, selectivity and stability are genuine challenges: i) the hydrogenation of

nitrobenzene to aniline and/or cyclohexylamine, and ii) the hydrogenation of cinnamaldehyde.

The functionalization of nanostructured carbon materials with metal particles is a large field of research. Metallic NPs have been now associated to carbon nanotubes,[5] graphene,[6] fullerenes,[7] and even detonation nanodiamonds.[8] While the control of NP size has been sometimes achieved,[9] the main limitation of these materials is, as for activated carbon support, the almost complete absence of a control of their organization: *i.e*. the metallic NPs are randomly distributed on the carbon surface, and the NPs/carbon anchoring is not homogeneous due to the presence of different types of anchoring sites.[10] Considering the fundamental importance of metal-support interaction on heterogeneous catalyst activity, selectivity, and stability, this is clearly detrimental to their performances. Additionally, the distance between NPs being not controlled, their properties are far from being optimized. Indeed, it has been recently evidenced that close proximity of NPs may strongly affect their catalytic performances, including their stability.[11,12,13,14] Finally, it is often extremely difficult to achieve a high metal loading with small metal NP size, and this is detrimental to many catalytic applications. Inspired by Metal-Organic Frameworks (MOFs), and Covalent Organic Frameworks (COFs), we propose to develop a totally original family of hybrid materials, associating in a controlled manner and through covalent bonds, sp^2–C nanostructured carbon materials with metallic NPs. The nanostructured materials selected include pristine and functionalized C_{60} fullerenes. Specifically for catalysis, this material should combine: i) a controlled NP size, ii) an atomically-defined environment for the NPs, iii) a covalent interaction with the support, and iv) a high porosity and a highly dense surface area availability of the catalytic centers. To reach this objective an interdisciplinary approach is necessary: *i*) functionalization of C_{60}, *ii*) synthesis and characterization of Ru metallic NPs, *iii*) the controlled assembly of hybrid structures, and *iv*) a computational approach aimed at modeling and understanding the formation of such mixed edifices construction.

References

1. Derouane, E. G., Catalysis in the 21st century, lessons from the past, challenges for the future. *Cattech* **2001,** *5* (4), 214-225.

2. Chaudret, B.; Somorjai, G. A.; Serp, P.; Philippot, K., in *Nanomaterials in catalysis*. John Wiley & Sons: 2013, pp 1-54.

3. Serp, P.; Machado, B., *Nanostructured carbon materials for catalysis*. Royal Society of Chemistry, Catalysis series N°23: 2015.

4. Rolison, D. R., Catalytic nanoarchitectures the importance of nothing and the unimportance of periodicity. *Science* **2003,** *299* (5613), 1698-1701.

5. Georgakilas, V.; Gournis, D.; Tzitzios, V.; Pasquato, L.; Guldi, D. M.; Prato, M., Decorating carbon nanotubes with metal or semiconductor nanoparticles. *J. Mater. Chem.* **2007,** *17* (26), 2679-2694.

6. Yin, P. T.; Kim, T.-H.; Choi, J.-W.; Lee, K.-B., Prospects for graphene–nanoparticle-based hybrid sensors. *Phys. Chem. Chem. Phys.* **2013,** *15* (31), 12785-12799.

7. Lim, I.-I. S.; Ouyang, J.; Luo, J.; Wang, L.; Zhou, S.; Zhong, C.-J., Multifunctional fullerene-mediated assembly of gold nanoparticles. *Chem. Mater.* **2005,** *17* (26), 6528-6531.

8. Subramanian, P.; Coffinier, Y.; Steinmüller-Nethl, D.; Foord, J.; Boukherroub, R.; Szunerits, S., Diamond nanowires decorated with metallic nanoparticles: A novel electrical interface for the immobilization of histidinylated biomolecuels. *Electrochim. Acta* **2013,** *110*, 4-8.

9. Rao, C. V.; Viswanathan, B., Monodispersed platinum nanoparticle supported carbon electrodes for hydrogen oxidation and oxygen reduction in proton exchange membrane fuel cells. *J. Phys. Chem. C* **2010,** *114* (18), 8661-8667.

10. Axet, M.; Dechy-Cabaret, O.; Durand, J.; Gouygou, M.; Serp, P., Coordination chemistry on carbon surfaces. *Coord. Chem. Rev.* **2016,** *308*, 236-345.

11. Munnik, P.; De Jongh, P. E.; De Jong, K. P., Control and impact of the nanoscale distribution of supported cobalt particles used in fischer–tropsch catalysis. *J. Am. Chem. Soc.* **2014,** *136* (20), 7333-7340.

12. Prieto, G.; Meeldijk, J. D.; de Jong, K. P.; de Jongh, P. E., Interplay between pore size and nanoparticle spatial distribution: Consequences for the stability of $CuZn/SiO_2$ methanol synthesis catalysts. *J. Catal.* **2013,** *303*, 31-40.

13. Prieto, G.; Shakeri, M.; De Jong, K. P.; De Jongh, P. E., Quantitative relationship between support porosity and the stability of pore-confined metal nanoparticles studied on $CuZn/SiO_2$ methanol synthesis catalysts. *Acs Nano* **2014,** *8* (3), 2522-2531.

14. Prieto, G.; Zečević, J.; Friedrich, H.; de Jong, K. P.; de Jongh, P. E., Towards stable catalysts by controlling collective properties of supported metal nanoparticles. *Nat. Mater.* **2013,** *12* (1), 34-39.

List of abbreviations

AC_{60}	Alkaline metals fullerene C_{60}
$Ag_{(2)}$	Pentagonal-pinch mode
AN	Aniline
ATR IR	Attenuated total reflection infrared
BET	Brunauer-Emmett-Teller
$(Boc)_2O$	Di-tert-butyl dicarbonate
C_{60}	Fullerene C_{60}
$C_{66}(COOH)_{12}$	Fullerenehexamalonic acid
CA	Cyclohexylamine
CAL	Cinnamaldehyde
CBr_4	Tetrabromomethane
CNT	Carbon nanotube
COL	Cinnamyl alcohol
CP-NMR	Cross-Polarization-NMR
DBU	1,8-diazabicyclo[5.4.0]undec-7-ene
DCA	Dicyclohexylamine
DFT	Density functional theory
DMAP	4-dimethylaminopyridine
DMF	Dimethylformamide
Ea	Activation energy
EDX	Energy-dispersive X-ray spectroscopy
EXAFS	Extended X-Ray Absorption Fine Structure
GC	Gas chromatography

GC-MS	Gas chromatography–mass spectrometry
HAADF	High-angle annular dark-field imaging
HCAL	Hydrocinnamaldehyde
HCOL	3-Phenyl-1-propanol
HREM	High-resolution transmission electron microscopy
ICP	Inductively coupled plasma
K1	Reaction rate
Kb	Reaction constant
$MCyNH_2$	4-methylcyclohexan-1-amine
NPs	Nanoparticles
PDF	Pair-distribution function
[Ru(COD)(COT)]	(1,5-cyclooctadiene)(1,3,5-cyclooctatriene)ruthenium
SAXS	Small-Angle X-Ray Scattering
SSNMR	Solid State Nuclear Magnetic Resonance Spectroscopy
STEM	Scanning Transmission Electron Microscopy
T	Temperature
t	Time
TEM	Transmission Electron Microscopy
THF	Tetrahydrofuran
TM	Transition metal
TOF	Turnover frequency
UHV	Ultra-High Vacuum
WAXS	Wide-Angle X-Ray Scattering
XANES	X-Ray Absorption Near Edge Structure

XPS	X-Ray Photoelectron Spectroscopy
XRD	X-Ray Diffraction
1, 2, 3D	One, two, three dimensional

Chapter 1 Introduction

1.1 Introduction

Since 1985, the date of their discovery, fullerene, one carbon allotrope (Figure 1.1), has been widely investigated. The first fullerene to be discovered was the hollow, cage-like C_{60}. Nowadays there are thirty or more forms of fullerenes. C_{60} is the first spherical carbon molecule, with carbon atoms arranged in a soccer ball shape. In the structure there are sixty carbon atoms and a number of five-membered rings isolated by six-membered rings. C_{70}, a slightly elongated, spherical carbon molecule in the same group, resembles a rugby ball, and has seventy carbon atoms. Many other forms of fullerenes, up to and beyond C_{120}, have been characterized. Their particular shapes depend on whether five-membered rings are isolated or not, or whether seven-membered rings are present. Among the fullerenes, spherical fullerene C_{60} is a wonderful unit to synthesize organized nanostructures, which have attracted much attention because of their specific size, shape, and physicochemical properties.[1]

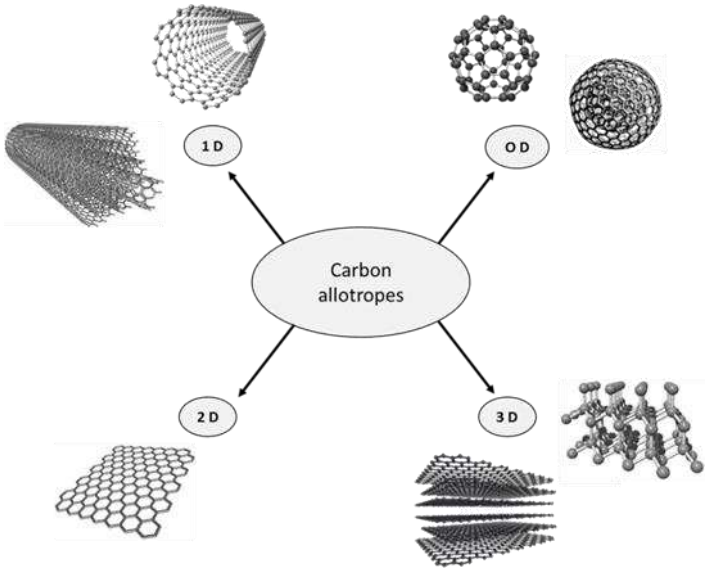

Figure 1.1. The family of carbon allotropes: 0 D, C_{60} fullerene and carbon onion; 1 D, single walled and multi walled carbon nanotubes; 2 D, graphene; and 3 D, graphite and diamond.

To date, fullerenes have found applications in various fields such as the preparation of novel materials for molecular electronic[2] or photovoltaic[3] devices, liquid crystalline materials,[4] materials for medicine,[5] catalysis[6] and others.[7]

C_{60} is a dark needle-like solid, and it is extremely stable even under high temperatures and pressures. Fullerenes are the only present allotrope of carbon that has the property to get dissolved in common organic solvents at room temperature. Thus it is soluble in many organic solvents as shown in Table 1.1,[8] including carbon disulfide, toluene, chlorobenzene, etc. Solutions of pure fullerene usually have a deep purple or violet color.

Table 1.1. Solubility of C_{60}[9]

Solvent	Solubility [C_{60}], mg/mL
n-Pentane	0.005
Decalin	4.6
Dichloromethane	0.26
Chloroform	0.16
Methanol	0.000
Ethanol	0.001
Acetone	0.001
Benzene	1.7
Toluene	2.8
Chlorobenzene	7.0
1,2-dichlorobenzene	27
Bromobenzene	3.3
Nitrobenzene	0.8
Carbon disulfide	7.9

It is worth noting that C_{60} have a low surface area (BET) with 10-20 m^2g^{-1} compare with CNT and graphene (~180-1000 m^2g^{-1}). However, the incorporation of chemical bond such as in metal-C_{60} will lead to increase the surface area of the materials.[6b]

The diameter of fullerene is 7.10 ± 0.07Å. However, when taking in account the π electron-cloud of C_{60}, the outside of C_{60} diameter will increase to 7.10 + 3.35 = 10.45 Å, 3.35 Å being the estimated surrounding π electron-cloud thickness as shown in Figure 1.2.

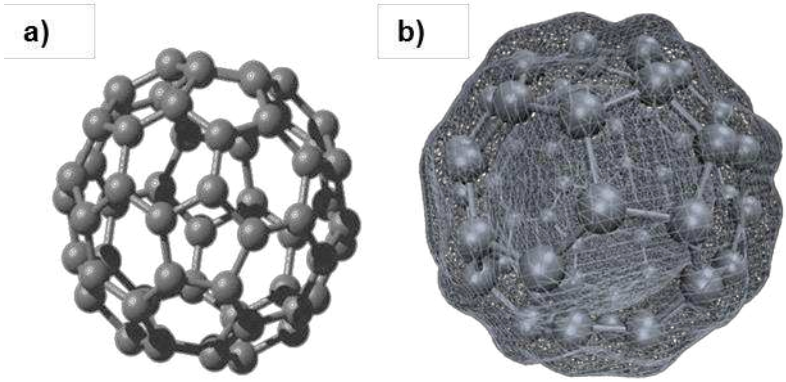

Figure 1.2. a) The ball and stick model structure of C_{60}; and b) C_{60} with isosurface of ground state electron density as calculated with DFT

1.1.1 C_{60} structure

C_{60} has sixty carbon atoms to form an icosidodecagon that consists of twelve pentagons and twenty hexagons as shown in Figure 1.3.[10] There are two manifest features of C_{60}, the first one is that all the pentagons are isolated by hexagons (Figure 1.3b). That means that all the double bonds are located in the hexagons, and there are no double bonds in pentagons. The second one is that the bonds at the junction of [6,6] member rings are shorter (1.38 Å) than the bonds at junction of [6,5] member ring (1.45 Å) (Figure 1.3b).[11]

Besides this, each carbon atom of C_{60} is three-connected to the other two carbon atoms by one double and two single bonds, so the carbon atoms is treated as a sp^2 carbon. Usually, the sp^2 carbon and its three neighbor carbons are coplanar, such as in graphite. The carbon atoms in the spherical C_{60} are not coplanar, but the structure is very stable. Because of the molecule's spherical shape the carbon atoms are highly pyramidalized, which has far-reaching consequences for reactivity. It is estimated that strain energy constitutes 80% of the heat of formation.

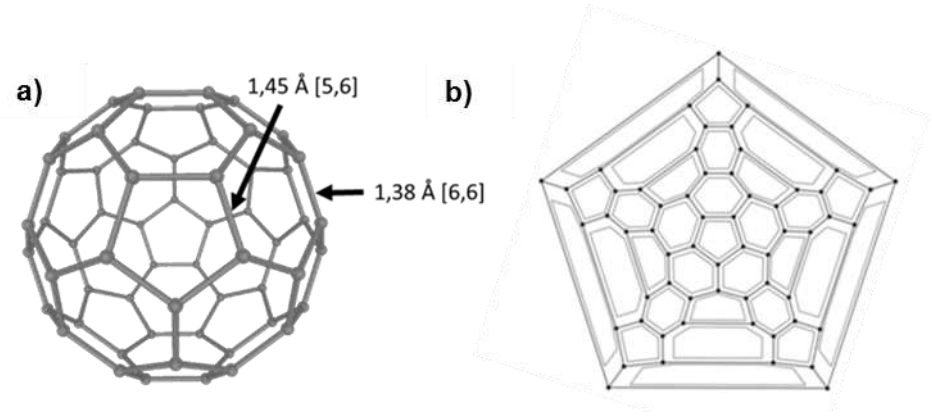

Figure 1.3. a) The schematic representation of C_{60}-I_h fullerene with length of two different bonds in the molecule; and b) Schlegel diagram.

The conjugated carbon atoms respond to deviation from planarity by orbital rehybridization of the sp^2 orbitals and π orbitals to a sp^2 orbital with a gain in *p*-character. The *p* lobes extend further outside the surface than they do into the interior of the sphere, and this is one of the reasons that the fullerene cage has a strong acidic character. The other reason is that the empty low-lying π^* orbitals also have a high *s* character.

The double bonds in fullerene are not all the same. Two groups can be identified: the so-called [6,6] double bonds that connect two hexagons, and the [5,6] double bonds that connect a hexagon and a pentagon. Of the two, the [6,6] bonds are shorter with more double-bond character and therefore a hexagon is often represented as a cyclohexatriene and a pentagon as a pentalene or [5]radialene (Figure 1.4). In other words, although the carbon atoms in fullerene are all conjugated the superstructure, it is not a super-aromatic compound. Indeed, C_{60} fullerene has sixty π electrons but a closed shell configuration requires seventy two electrons. Fullerenes tend to react as electrophiles. An additional driving force is relief of strain when double bonds become saturated. As a result, C_{60} can react readily with electron rich species and behaves like an electron deficient alkene.

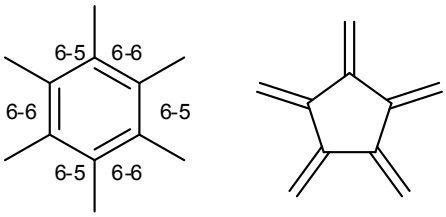

Figure 1.4. Structural fragments of C_{60}: cyclohexatriene (left) and [5]radialene (right).

1.1.2 C_{60} synthesis

Fullerenes do not exist in significant amount naturally, so a lot of efforts have been devoted to synthesize them on a large scale. Generally, resistive heating vaporization, arc vaporization and combustion are the three usual synthesis methods. In 1990, Krätschmer and his colleagues developed a contact arc discharge method for macroscopic production, known as the Krätschmer-Huffman method. They discovered that carbon rods heated resistively in a He atmosphere could generate gram quantities of fullerenes embedded in carbon soot. This method uses graphite electrode contact arcs, passing alternating or direct current through them in an atmosphere of He (approximately 200 torr). The evaporated graphite takes the form of soot, which is dissolved in a nonpolar solvent. The solvent is dried away and the C_{60} and C_{70} fullerenes can be separated from the residue by several methods like chromatography, crystallization or chemical complexation. The optimal current, helium pressure and flow rate allow to reach up to 70% and 15% yield of C_{60} and C_{70}, respectively. This was the first method to produce gram-sized samples. The method was later on modified by Smalley who established an eletric arc between two graphite electrodes, where most of the power dissipate in the arc. This modification granted higher yields. Due to these developments a lot of new fullerene types were rapidly discovered within the next years.

The common used process for mass-production is the “Combusting Process”, which was invented by Howard in 1991. In this process, fullerenes are produced in sooting flames with premixed benzene, oxygen and argon under low pressure. The relative

low percentage of fullerenes in the soot (0.26%) was increased by some changes in the conditions, and up to 20% were obtained when mass production of fullerenes started.

The pace of discovery in fullerene science has continued to accelerate, as above mentioned, and practical applications in catalysis have been investigated.[12] Here, we will only focus on the synthesis, characterization and applications of fullerene catalysts, particularly on metal fullerene complexes, metal fullerides and metallic nanoparticle@fullerene nanostructures.

1.2 Coordination chemistry of fullerene C_{60}

After the preparation of the C_{60} fullerene, many researches have focused on its coordination chemistry.[6c, 13] Due to the hollow structure of fullerene, metal atoms can coordinate inside (endohedral) or outside (exohedral) the cage. Only exohedral metal fullerene C_{60} complexes are discussed here. There are seven possible coordination modes of fullerene C_{60} with metal atoms, which are depicted in Figure 1.5.

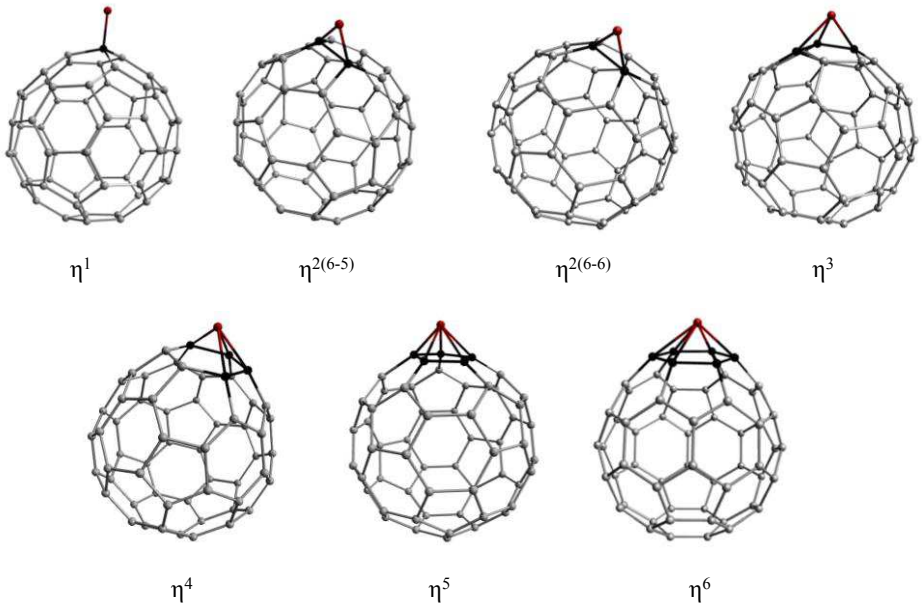

Figure 1.5. Possible metal-C_{60} bonding modes. From ref.[13b]

Since the first preparation of organometallic complexes of fullerene, $[(\eta^2\text{-}C_{60})Pt(PPh_3)_2]$[14] (Figure 1.6) and $[(\eta^2\text{-}C_{70})Ir(CO)Cl(PPh_3)_2]$[15], many organometallic compounds have been prepared and characterized.

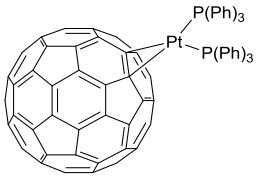

Figure 1.6. First organometallic complex of fullerene C_{60}.

Beside the η^2 coordination, other hapticities are possible (Figure 1.5), where η^1 hapticity is the only one presenting a σ-bond interaction. The η^5 hapticity is the coordination mode more observed after the η^2 coordination; however, it requires the disruption of the conjugated system, modifying the fullerene structure. Nakamura published the first example of this type of compounds.[16] η^1, η^3, η^4 and η^6 are predicted not to be stable, being η^6 much less stable than other hapticities. However, η^1 and η^3 complexes have been produced experimentally.

1.2.1 η^2 coordination

Many researches have suggested that the metal interaction with C-C bonds in fullerene is similar to olefin coordination.[17] The bond between metal and olefin has two components: one consist in donor-acceptor interaction (σ type), and the other (back-bonding) is a dative component (π type). The first interaction is the charge transfer from the filled π orbital of the olefin to the empty *d* orbital of the metal. The second one is the back-donation from an occupied *d*-orbital of the metal to the nonbonding π* molecular orbital of the olefin. To understand this, an excellent theoretical work have been published by Sgamellotti *et al.*[18] It was found that fullerene has a large population of non-bonding π* molecular orbitals, which are very near to the occupied *d*-orbitals of the metal, therefore the interaction of metal and fullerene C_{60} are usually very strong. Compare to metal-ethylene, the bond energies of

the metal-fullerene are higher, but lower than the tetrafluoro- and tetracyanoethylene complexes.

Early theoretical studies of the interaction of C_{60} with transition metals carried out by Lichtemberg,[19] have already shown that the η^2 coordination mode in the [6,6] bonds is the most stable, followed by η^2 coordination to the [6,5] bond. Analogously, Loboda[20] found that the η^2 coordination in the [6,6] bonds is the most stable. The interaction between C_{60} and transition metal atoms of groups 9 and 10 (Co, Rh, Ir, Ni, Pd and Pt) has been studied in this latter work; showing, for instance, that palladium bond dissociation energies at different sites of the fullerene cage followed this trend: η^2 (6-6) > η^2 (6-5) > η^5 > η^6.

A plethora of coordination metal complexes shows this kind of coordination mode including Mo,[21] W,[22,23] Fe,[24] Co,[25,26], Rh,[27] Ir,[27,28] Ni,[29,30,31,32,33] and Pd.[34,35] Table 1.2 presents some recently published organometallic complexes of fullerenes coordinated through a η^2 bond.

Table 1.2. η^2- fullerene C_{60} organometallic complexes

Complex	Ref.	Complex	Ref.
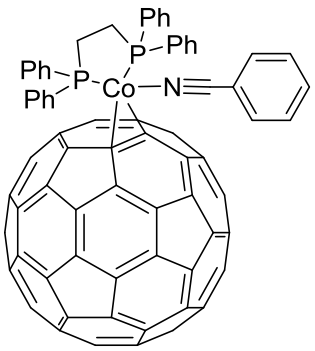	25	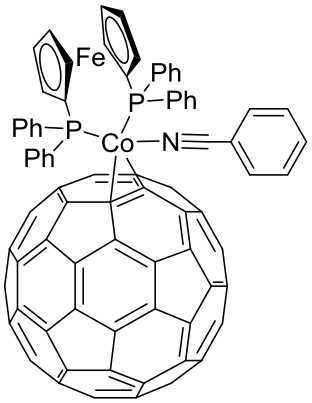	25

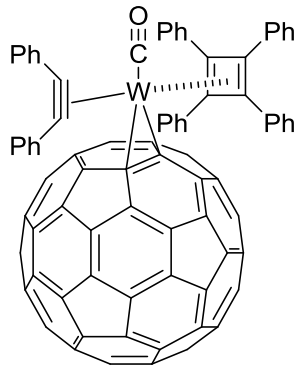

36

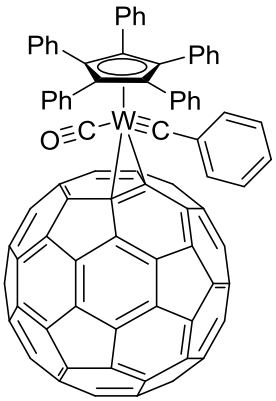

36

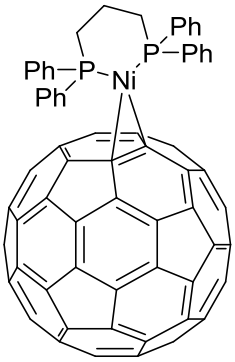

37

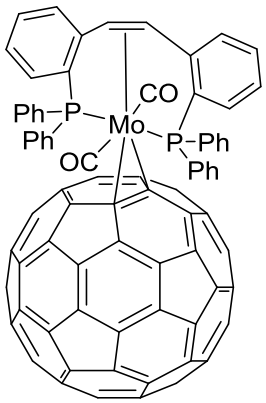

21

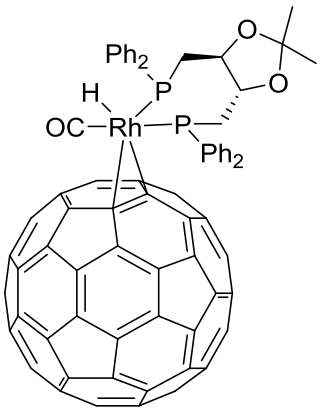

27

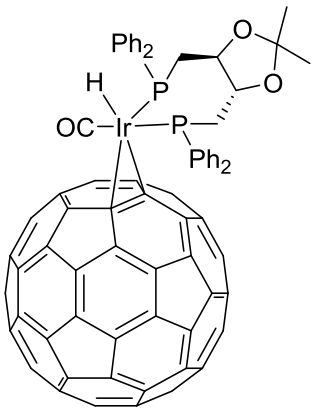

27

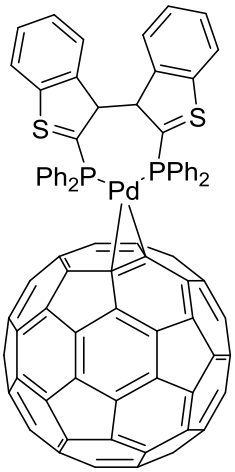	34	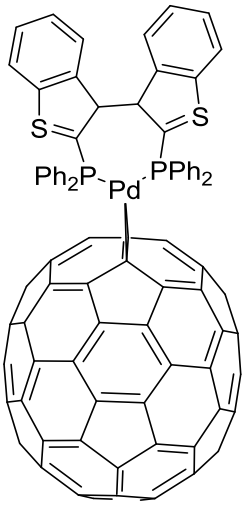	34
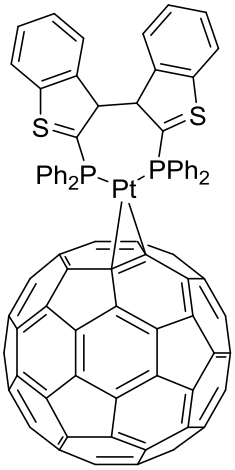	34	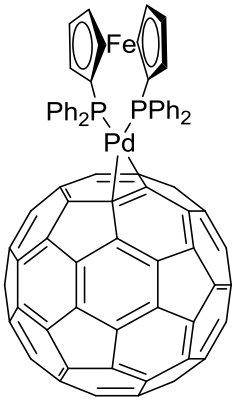	35
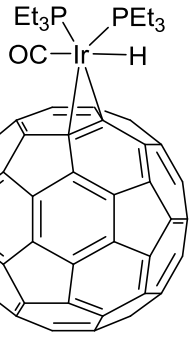	28	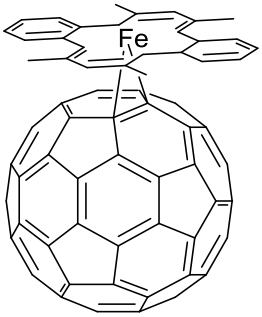	24

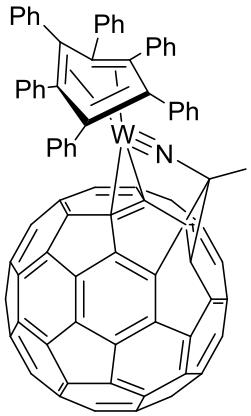

22-23

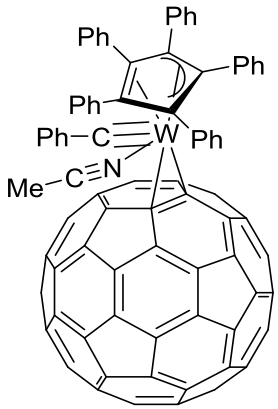

22-23

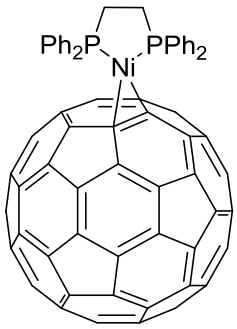

30

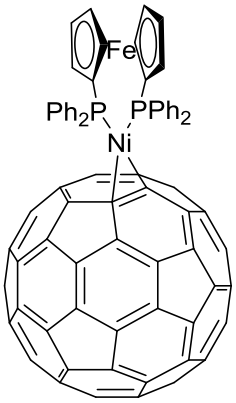

30

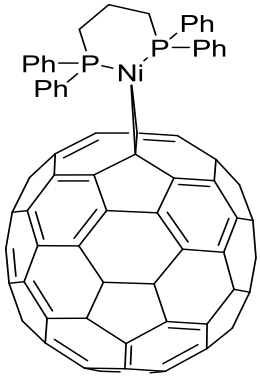

31

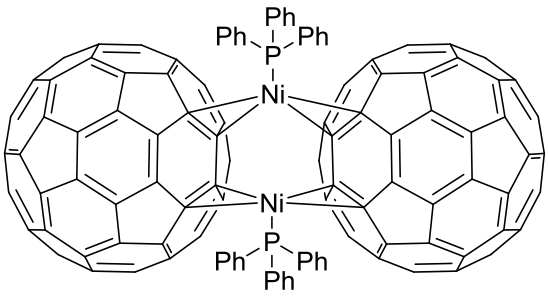

32

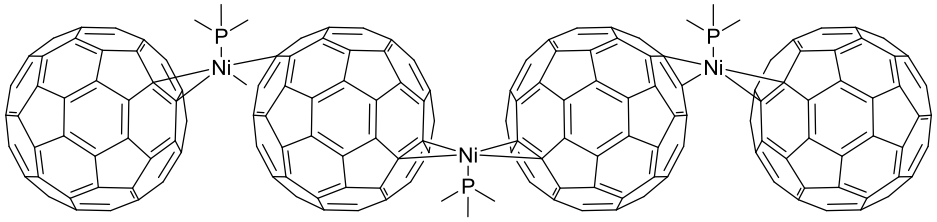

33

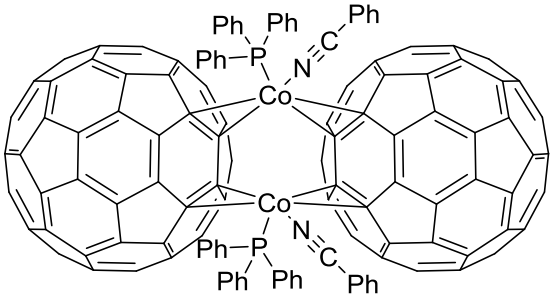

26

Metallic clusters also prefer to coordinate to C_{60} fullerene through η^2 coordination mode (Table 1.3). The coordination chemistry of clusters to C_{60} is dominated by the triosmium and triruthenium clusters coordinated in μ^3-η^2,η^2,η^2 to C_{60}. Usually, these compounds are modified on the metal coordination sphere, but some examples can be found were the fullerene cage has been also modified (see Table 1.2). The first example of cluster coordinated to fullerene, $[Ru_3(CO)_9(\mu^3\text{-}\eta^2,\eta^2,\eta^2\text{-}C_{60})]$, was synthesized in 1996 by thermal decarbonylation of $[Ru_3(CO)_{12}]$ in the presence of C_{60}.[38] X-ray diffraction shows that Ru atoms are η^2 coordinated and positioned over the short C-C bonds, the Ru-C distances are in between 2.324(9) and 2.213(9) Å (Figure 1.8).

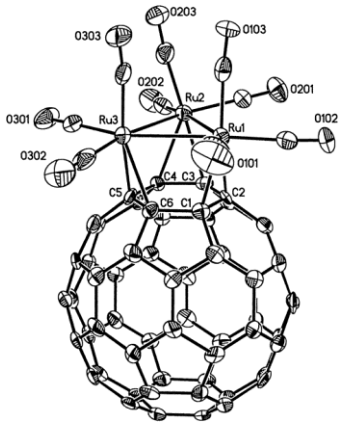

Figure 1.8. Crystal structure of $[Ru_3(CO)_9(\mu^3\text{-}\eta^2,\eta^2,\eta^2\text{-}C_{60})]$. From ref.[38]

Rhodium clusters $[Rh_6(CO)_9(dppm)_2(\mu^3\text{-}\eta^2,\eta^2,\eta^2\text{-}C_{60})]$ and $[Rh_6(CO)_5(dppm)_2(CNR)(\mu^3\text{-}\eta^2,\eta^2,\eta^2\text{-}C_{60})2]$ can also coordinate to one or two fullerene cages *via* $\mu^3\text{-}\eta^2,\eta^2,\eta^2$ coordination mode.[39] The reaction of the Ir cluster $[Ir_4(CO)_8(PMe_3)_4]$ with C_{60} allows to obtain the $[Ir_4(CO)_3(\mu^4\text{-}CH)(PMe_3)_2(\mu\text{-}PMe_2)(CNR)(\mu\text{-}\eta^2,\eta^2\text{-}C_{60})(\mu^4\text{-}\eta^1,\eta^1,\eta^2,\eta^2\text{-}C_{60})]$ compound, where the Ir_4 cluster is mainly coordinated to the C_{60} fullerene *via* η^2 bonds, together with η^1 bonds.[40]

Table 1.3. η^2, η^2, η^2 complexes of fullerene

Complex	Ref.	Complex	Ref.
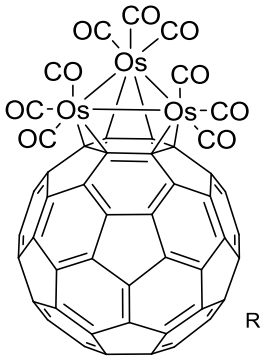 R = CO, $P(CH_3)_3$	43	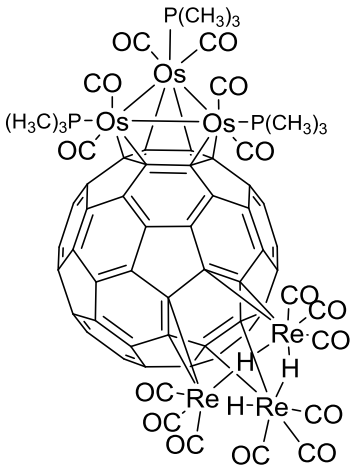	44
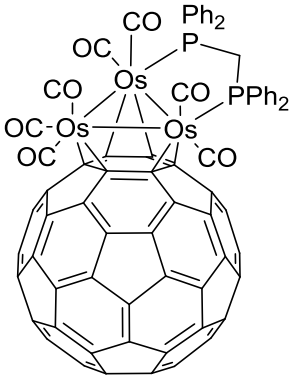	45	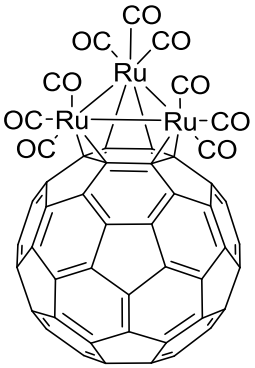	38

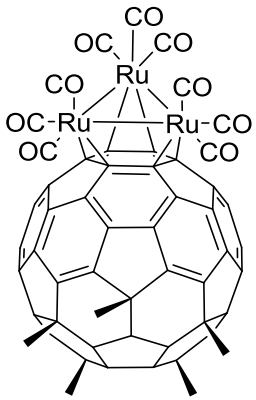

46

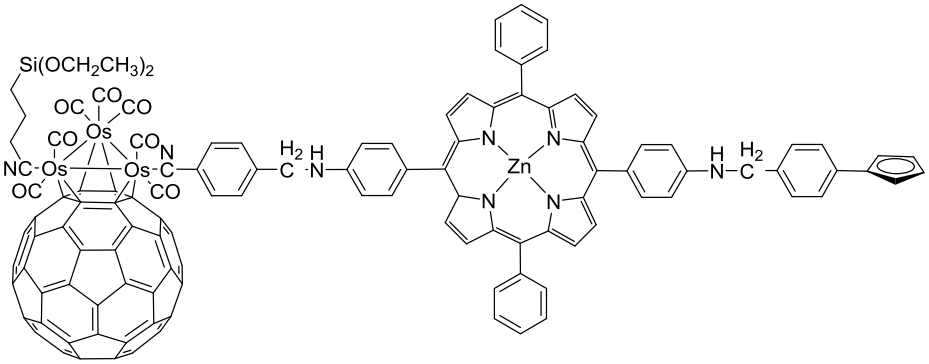

47

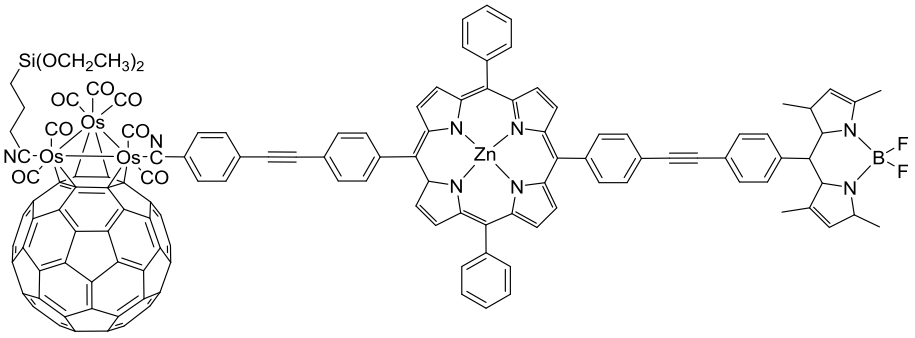

48

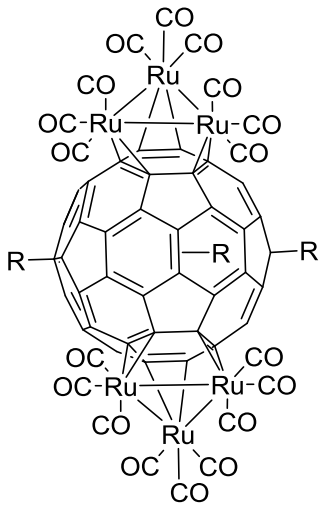

R = $C(COOC_2H_5)_2$

49

Theoretical studies have shown that the η^2 coordination mode is usually the most stable for metallic clusters, as observed for mononuclear complexes. For instance, small cluster of Ru_2[41] and Rh_2[41] coordinate to the fullerene *via* one atom displaying a η^2 hapticity. DFT calculations on osmium clusters $[Os_3(CO)_9(\mu^3\text{-}\eta^2,\eta^2,\eta^2\text{-}C_{60})]$ and $[Os_3(CO)_8(P(CH_3)_3)(\mu^3\text{-}\eta^2,\eta^2,\eta^2\text{-}C_{60})]$ show that all three osmium atoms are η^2 coordinated for neutral, mono- and di-anions. However, the addition of more electrons to produce the trianions produces a change in the coordination mode, obtaining $[Os_3(CO)_9(\mu^3\text{-}\eta^2,\eta^2,\eta^1\text{-}C_{60})]^{-3}$ and $[Os_3(CO)_8(P(CH_3)_3)(\mu^3\text{-}\eta^2,\eta^2,\eta^1\text{-}C_{60})]^{-3}$. The fourth electron reduction produces the $[Os_3(CO)_9(\mu^3\text{-}\eta^2,\eta^1,\eta^1\text{-}C_{60})]^{-4}$ and $[Os_3(CO)_8(P(CH_3)_3)(\mu^3\text{-}\eta^2,\eta^1,\eta^1\text{-}C_{60})]^{-4}$ complexes.[42] Other DFT studies on coordination chemistry of C_{60} to Pd, Au and Co clusters also point out that usually the $\eta^{2(6\text{-}6)}$ is the preferred one, nevertheless $\eta^{2(6\text{-}5)}$ coordination was also found possible.

The η^2 coordination in the [6,6] bonds is the most common between metal and fullerene.[26, 33, 50] One reason could be that the non-planarity surface of fullerene makes that the orbitals are located well outside the plane, thus the η^5 and η^6 fashion is much more difficult to develop. Moreover, it is worth noting that most of C_{60} complexes of various metals have a η^2-structure with metal bonding to [6,6] rather than [6,5] ring. In a theoretical work, Sheu and Su[51] have found that the [6,6]-attack is more favorable than the [6,5]-one, both kinetically and thermodynamically under the same reaction conditions. Figure 1.9 presents some typical coordination η^2 complexes. The first fullerene metal complex are $[\eta^2\text{-}C_{60}Pt(PPh_3)_2]$[52] and $[\eta^2\text{-}C_{60}Pd(PPh_3)_2]$[53] in which the metal center attach to one double bond of the [6,6] member ring. In $[Ru_5C(CO)_{11}(PPh_3)(\mu^3\text{-}\eta^2,\eta^2,\eta^2\text{-}C_{60})]$ the metal cluster coordinates with three double bonds in the six member ring.[54] In $[Ni(Me_3P)_2(\mu\text{-}\eta^2,\ \eta^2\text{-}C_{60})]$, the metal center is bonded to two fullerene cages to form a polymeric like structure.[33]

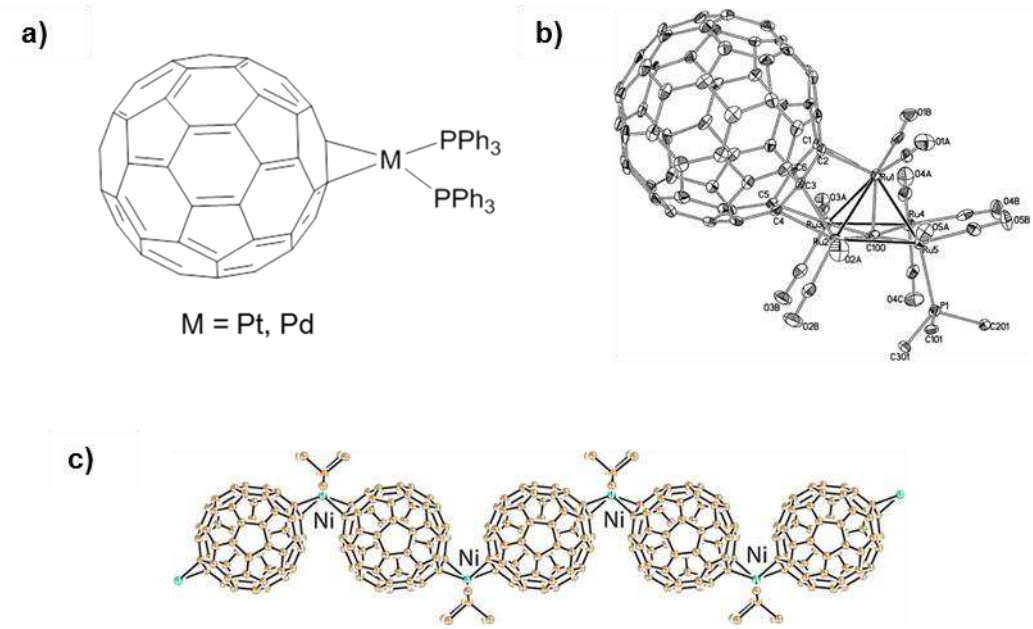

Figure 1.9. The coordination η^2 mode of metal fullerene C_{60}: a) η^2- metal complex, from ref.[52-53]; b) η^2,η^2,η^2- metal cluster complex (From ref.[54]); and c) η^2- metal polymer complex (From ref.[33]).

Computational studies[55] on $[MX(CO)(PH_3)_2(C_{60})]$ (M = Rh or Ir; X= H or Cl) have demonstrated that the binding energy depends on several factors, including *d*-orbital energy, *d*-orbital expansion, the presence of an empty *d*-orbital, and the distortion energy of the metal fragment induced by the complexation. For example, $[IrH(CO)(PH_3)_2(C_{60})]$ is more stable than $[RhH(CO)(PH_3)_2(C_{60})]$ because of the larger *d*-orbital energy.

On the other hand, the η^2 coordination is less stable than the η^1 one under certain conditions. For instance, the η^1 mode has been computed to be more stable for LMC_{60} (L = ligand) with -3 anions.[56] The interpretation is that the electron addition to C_{60} leads to a decrease of π interactions with the *d*-orbital of the metal, whereas it has little effect on the σ type interactions.

Furthermore, the transformation of the σ and π bonds has been reported in the case of a C_{60}-Os cluster by controlling the steric and electronic properties of the metal center.[57] In Scheme 1.1, **1** and **2** can reversibly be obtained, and the reaction of **2** and PPh_3 will form a new π-type complex **3**.

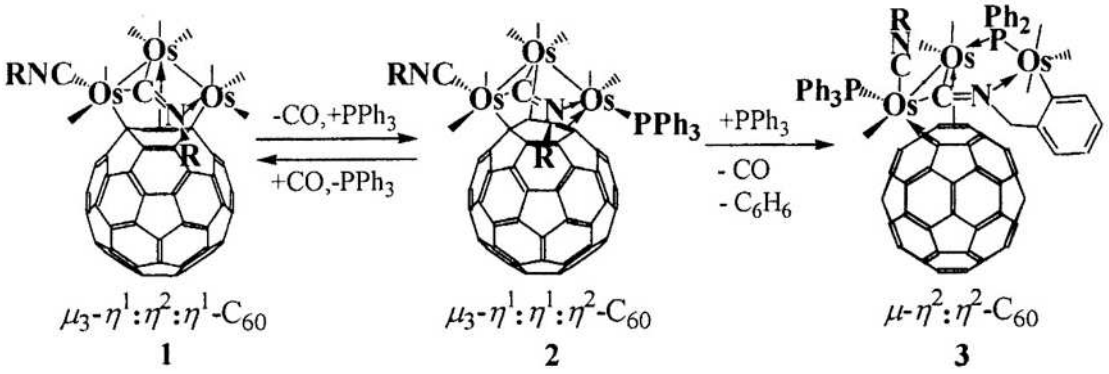

Scheme 1.1 The transformation between the σ and π bonds. From ref.[57]

1.2.2 η^5 coordination

The delocalization of the π-electron density on the C_{60} fullerene makes that the formation of stable η^5 complexes is highly improbable. The metal-C_{60} interaction in Cp-M-C_{60} complexes (M = Fe, Ru and Os) is calculated to be weaker than the M-Cp bonds in ferrocene, ruthenocene, and osmocene.[58] Nevertheless, calculations on $C_{60}R_5M$ (R = H, Ph; M = Ti, In) complexes predict that the addition of substituents in the α-position of the five membered ring, to form half-sandwich metallocene embedded in the C_{60} skeleton, allows the existence of stable η^5 complexes.[59] DFT calculations of a ferrocene analogue with a C_{60} ligand, Cp-Fe-$C_{60}Me_5$, show that this complex is stable.[60] Similarly, the comparison of the coordination mode of osmium complexes and clusters to C_{60} fullerene or five substituted C_{60} predicts a change in the coordination mode of the metal from $\eta^{2(6-6)}$ to η^5 coordination.[61]

The first example of this kind of coordination was reported in 2000;[16] where a rhodium atom is coordinated to a 5 membered ring, where all the α-positions are substituted with methyl groups (Figure 1.10). Since then, many examples of this type of coordination can be found in the literature including Rh,[16] Co,[62,63,64,65] Ru,[66,67,68,69] and Fe[67] complexes. Table 1.4 presents recently published η^5 complexes of fullerene.

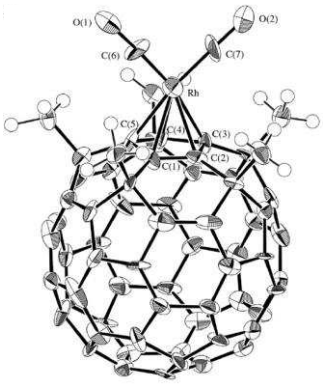

Figure 1.10. Molecular structure of [Rh(η^5-MeFCp)$(CO)_2$] determined by X-ray diffraction. Selected bond lengths (Å): Rh−C(1), 2.27(4); Rh−C(2), 2.22(3); Rh−C(3), 2.12(4); Rh−C(4), 2.19(4); Rh−C(5), 2.13(4). From ref.[16]

Table 1.4. η^5 metal complexes of fullerene

Complex	Ref	Complex	Ref
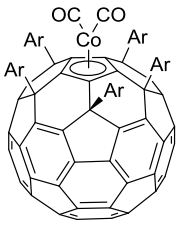 Ar = 4-nBuC$_6$H$_4$, 4-tBuC$_6$H$_4$	62	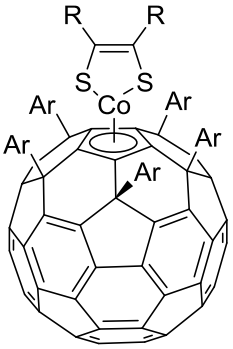 R = CO_2Me, CN Ar = 4-nBuC$_6$H$_4$	62
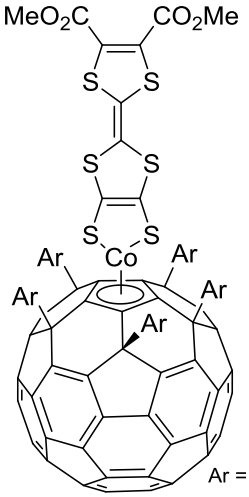 Ar = 4-nBuC$_6$H$_4$			62

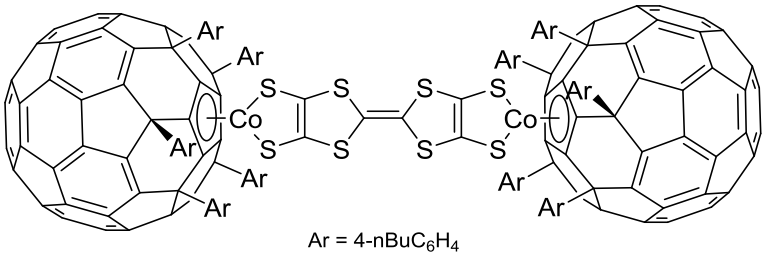

Ar = 4-nBuC$_6$H$_4$

62

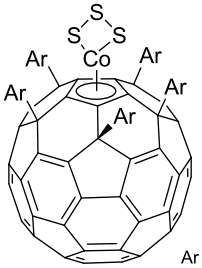

Ar = 4-nBuC$_6$H$_4$, 4-tBuC$_6$H$_4$

63

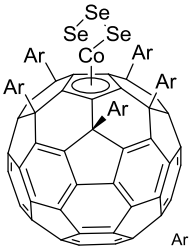

Ar = 4-nBuC$_6$H$_4$, 4-tBuC$_6$H$_4$

63

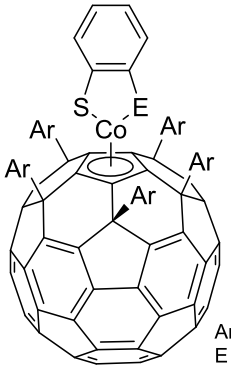

Ar = 4-tBuC$_6$H$_4$
E = S, NH

64

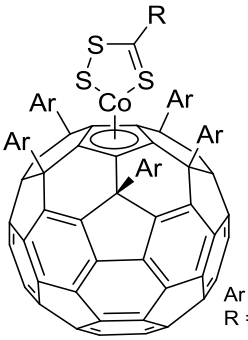

Ar = 4-tBuC$_6$H$_4$
R = p-tol, Ph, NPr

64

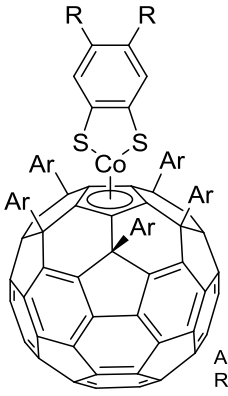

Ar = 4-nBuC$_6$H$_4$
R = F, tBu

65

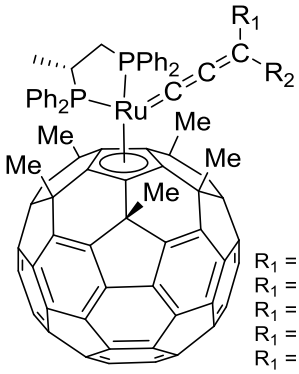

R$_1$ = Ph, R$_2$ = Ph
R$_1$ = H, R$_2$ = Ph
R$_1$ = H, R$_2$ = 4-OMeC$_6$H$_4$
R$_1$ = H, R$_2$ = Fc
R$_1$ = H, R$_2$ = 4-NMe$_2$C$_6$H$_4$

66

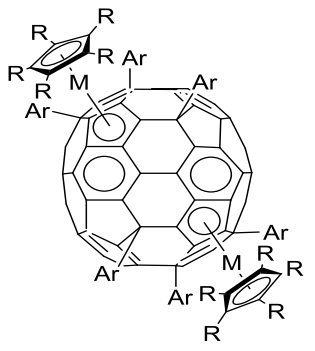

M = Ru, Fe
Ar = p-tol
R = H, Me

67

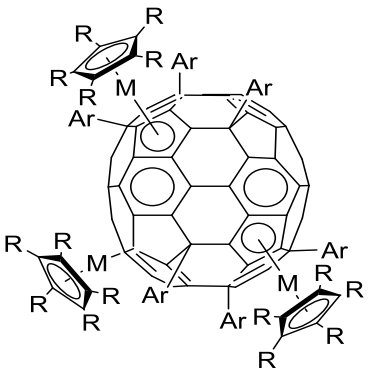

M = Ru, Fe
Ar = p-tol
R = H, Me

67

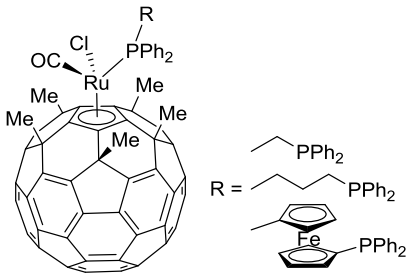

68

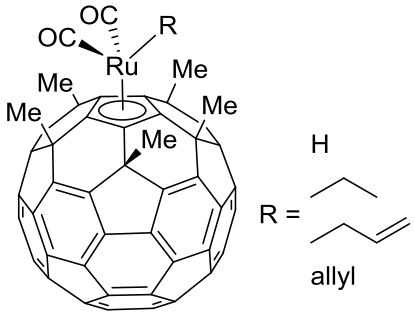

69

1.2.3 η^1 coordination

In the η^1 coordination, the metal atoms directly attach to carbon of fullerene by a σ bond. It exists theoretical and experimental examples that have shown that the σ bond between the metal and fullerene cage is possible.[17,70] Lee and co-workers[40] first reported η^1 C_{60} coordination in a new C_{60}-Ir_4 metal sandwich cluster with a novel μ^4-η^1, η^1, η^2, η^2-C_{60} bonding. The σ-C_{60} metal complex {(μ^3-η^1, η^2, η^1-C_{60})[$Os_3(CO)_8$-($CNCH_2Ph$)]} (Figure 1.7) was reported by Song *et al.*[57, 71], and it was prepared by ligand-induced Os-Os bond cleavage.

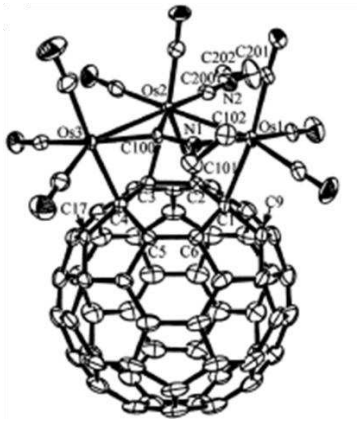

Figure 1.7. Crystallographic structure of (μ^3-η^1, η^2, η^1-C_{60})[$Os_3(CO)_8(CNCH_2Ph)$]. From ref.[57, 71]

The σ-bond between a fullerene and a metal atom seems to be neither stable, nor strong. It is considered more as a possible step in a reaction or a fluxional process.[19,72] DFT calculations on various L_nMC_{60} (M = Cr, Mo, W, Mn, Tc, Re, Fe, Ru, Os, Co, Rh, Ir; L= H, CO) complexes have been carried out in order to understand the differences between η^1 and η^2 coordination modes. As previously observed in osmium

clusters $[Os_3(CO)_9(\mu^3\text{-}\eta^2,\eta^2,\eta^2\text{-}C_{60})]$ and $[Os_3(CO)_8(P(CH_3)_3)(\mu^3\text{-}\eta^2,\eta^2,\eta^2\text{-}C_{60})]$;[42] neutral M-$C_{60}$ complexes prefer $\eta^{2(6\text{-}6)}$ followed by $\eta^{2(6\text{-}5)}$ and finally η^1, while the -3 anions bound stronger in η^1.[70] The reason of this behavior is due to the π-type interactions. The addition of an electron significantly decreases the π-type interaction of both the $\eta^{2(6\text{-}6)}$ and $\eta^{2(6\text{-}5)}$ modes, whereas it has little effect on σ-type interactions. Because of the large proportion of π-character of $\eta^{2(6\text{-}6)}$ coordination, the stability decreases by the addition of electrons to the system, becoming the η^1 coordination the most stable. Experimentally, this bond has been observed in ionic derivatives of Co[73] and Au[74](Figure 1.11).

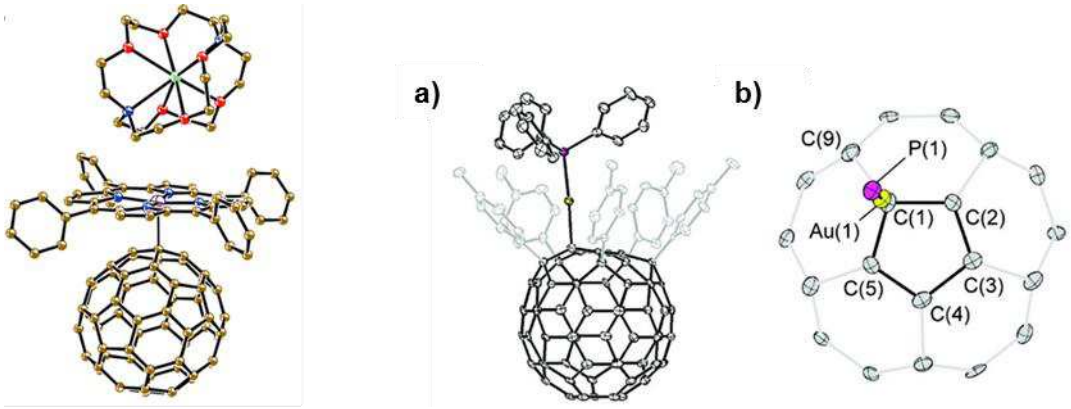

Figure 1.11. Left, Crystal structure of $[CoTPP\cdot(C_{60}^{-})][cryptand[2,2,2]\cdot(Na^{+})]$. From ref.[73]. Right, crystal structure of $[(4\text{-}MeC_6H_4)_5C_{60}][Au(PPh_3)]$: a) ORTEP drawing (thermal ellipsoids at 50% probability); and b) partial structure showing the ligand-metal bonding. From ref.[74]

Recently, it has been demonstrated that neutral fullerenes of silver[75] and ruthenium[76] bind also trough a σ-bond. The silver complex coordinates to fullerene to give polymeric chains (Figure 1.12).[75] The ruthenium complex was obtained by reaction of $[(\eta^5\text{-}C_5H_5)Ru(CO)_2]$ (Figure 1.13) with C_{60} in toluene solution under thermal or photolytic conditions. The X-ray diffraction of $[\eta^1\text{-}C_{60}Ru(CO)_2(\eta^5\text{-}C_5H_5)_2]$ shows two ruthenium atoms bound to the surface of the fullerene in a η^1 fashion (Ru-C bond distances are 2.206(18) Å and 2.201(13) Å).[76]

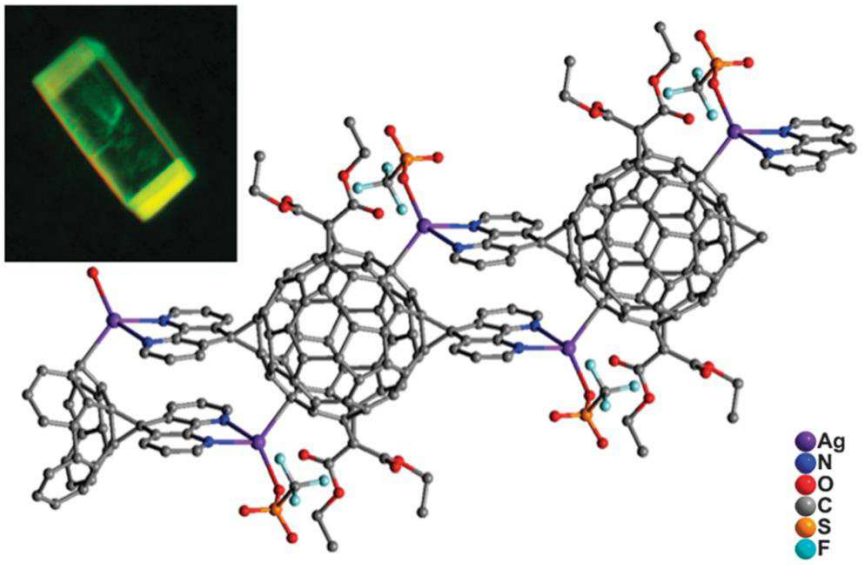

Figure 1.12. View of the structure of a 1D polymer Front and back malonate addends have been omitted for clarity. The inset shows a photograph of a crystal of the polymer. The inset shows a photograph of a crystal of the polymer. From ref.[75]

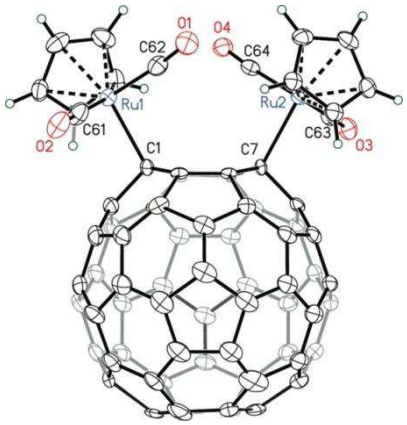

Figure 1.13. Crystallographic structure of [C_{60} η^1-Ru(CO)$_2$(η^5-C_5H_5)$_2$] with thermal ellipsoids shown at 50%. Only the major orientation of the cage is shown with fractional occupancy of 0.68. From ref. [76]

The Ir cluster $Ir_4(CO)_3(\mu^4\text{-CH})(PMe_3)_2(\mu\text{-}PMe_2)(CNR)(\mu\text{-}\eta^2,\eta^2\text{-}C_{60})(\mu^4\text{-}\eta^1,\eta^1,\eta^2,\eta^2\text{-}C_{60})$[40] displays a σ-π mixed type $\mu^4\text{-}\eta^1,\eta^1,\eta^2,\eta^2\text{-}C_{60}$ bonding mode as evidenced by XRD analysis (Figure 1.14).

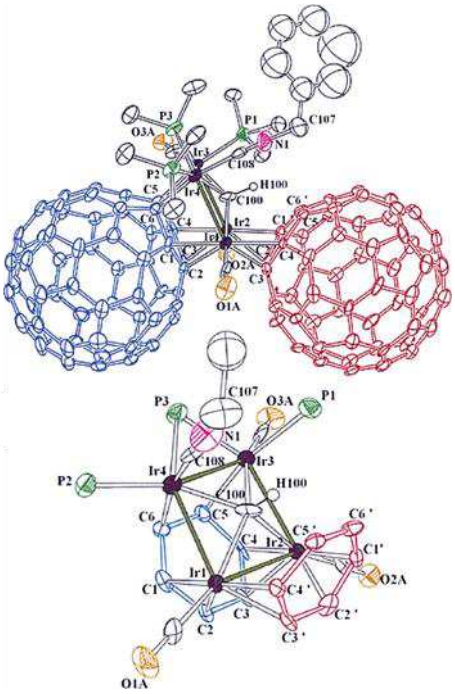

Figure 1.14. $Ir_4(CO)_3(\mu^4\text{-}CH)(PMe_3)_2(\mu\text{-}PMe_2)(CNR)(\mu\text{-}\eta^2,\eta^2\text{-}C_{60})(\mu^4\text{-}\eta^1,\eta^1,\eta^2,\eta^2\text{-}C_{60})$. From ref.[40]

1.2.4 η^3 and η^4 coordinations

Transition metal complexes displaying η^3 or η^4 coordination are not stable. However, as predicted for η^5 coordination complexes, the modification of the fullerene cage could allow the formation of this kind of coordination complexes.[13a]

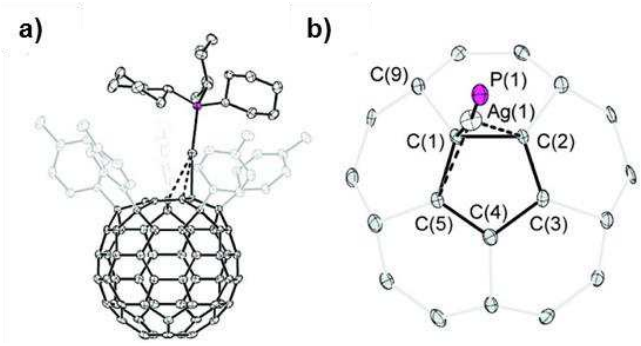

Figure 1.15. Crystal structure of $[(4\text{-}MeC_6H_4)_5C_{60}][Ag(PCy_3)]$: a) ORTEP drawing (thermal ellipsoids at 50% probability); and b) Partial structure showing the ligand-metal bonding. From ref.[74]

Experimentally, this kind of coordination has been observed in silver compounds of fullerene anions ($[(4\text{-}MeC_6H_4)_5C_{60}^-]$) where the α-positions have substituted aryl rings

(Figure 1.15). The bond distances between Ag and fullerene are 2.259(4) Å for the principal interaction and 2.525(4) Å and 2.894(4) Å for the secondary interactions.[74]

1.2.5 η^6 coordination

Early theoretical calculations have shown that metal coordination to fullerenes in a η^6 fashion is much less stable than other hapticities.[19-20] The binding energies and stability of η^6-M-C_{60} complexes have been predicted to be weaker than the respective benzene complexes.[58, 77] Nevertheless, some theoretical studies have shown that Cr can form moderately stable species with C_{60}[78] and C_{80}.[79] In addition, η^6 sandwich type early transition metal complexes have been computed to be more stable than η^5 complexes due to the lower number of *d* electrons.[80] The introduction of six R groups in the α sites with respect to the common hexagon of C_{60} favors the formation of η^6 complexes as observed for η^5 and η^3 complexes.[81] DFT calculations of V-C_{60} polymeric complexes show that polymers are more stable than the corresponding mononuclear complex. The formation of the polymer also implies the changing mode of the metal to fullerene: η^5-V-C_{60} complex is more stable than η^6-V-C_{60}; however, in the polymeric complexes the metal prefers to bind in a η^6 fashion.[82]

1.3 Metal-C_{60} polymers

The incorporation of fullerene into nanostructures has always attracted the attention of the chemists, because fullerene based nanostructures have many potential applications.[6c] Up to now, many C_{60}-based nanostructures have been developed using different methods. Here, we are mainly focusing on the transition metal fullerene-C_{60} nanostructures. Some transition metal fullerides have been prepared in the past, based on Pd, Pt, Ru, etc.; however, the structure of these fullerides is still uncertain.[83] It was found that these polymers are insoluble in many solvents and present good conducting properties. Some of them are air stable, for instance, Pd_nC_{60} can be kept in air for several weeks. Figure 1.16 shows the proposed metal polymer chain model, in which the metal atoms coordinates with fullerene cages in a η^2 fashion.

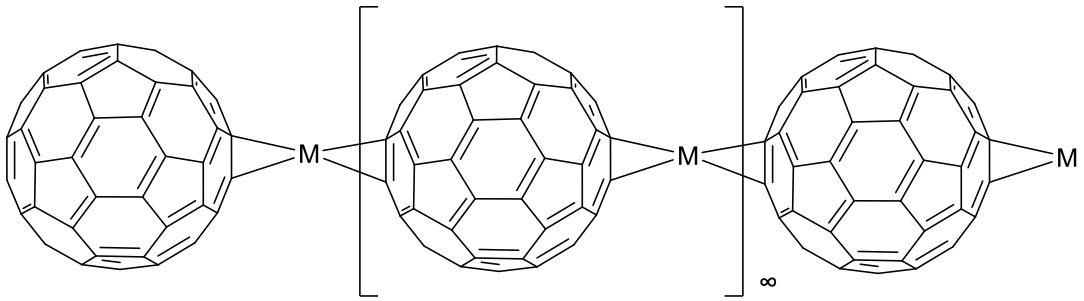

M = Pd, Pt, Ir, Rh, Au, Ag

Figure 1.16. Transition metal-fullerene C_{60} polymer coordinated in η^2 mode.

The synthesis of metal fullerene polymers can be performed either by chemical synthesis, co-evaporation or by electro-chemical procedures.[6b] The synthesis of bulk amounts of palladium and platinum fullerides was reported by solution reaction methods, and Pd_nC_{60} can be also prepared by electrochemical synthesis. Thin films of some other metal fulleride phases have been obtained under ultra-high vacuum (UHV) conditions by co-evaporation of C_{60} with carbide-forming transition metals such as Ti, Fe, Co and Nb. In the following section, the preparation methods of transition metal fullerene polymer is described.

1.3.1 Synthesis of transition metal-fullerene polymers

1.3.1.1 Chemical solution method

The chemical solution method is a rapid, and simple and typical way to produce metal fullerene polymers (such as, Pd, Pt, Ru, Rh, and Ag). It involves a metal complex that reacts with C_{60} in solution. The decomposition of the metal precursor in the presence of C_{60} is depicted on Scheme 1.2.

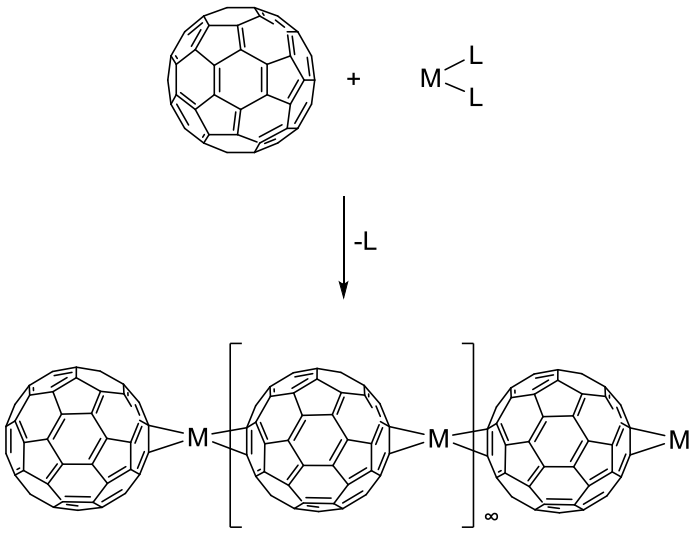

Scheme 1.2. The possible formation process of metal fullerene[C_{60}] polymer.

1.3.1.1.1 Pd(0) and Pt(0) fullerene polymers

The first organometallic polymer of fullerene Pd_nC_{60} was reported by Hideo and co-workers.[84] Pd_nC_{60} is a black air-stable solid, insoluble in common organic solvent, which was synthesized from C_{60} and $[Pd_2(dba)_3]$ (dba=dibenzylideneacetone) as depicted on Scheme 1.3. The composition of Pd_nC_{60} (n=1-7) depends on the reaction conditions.

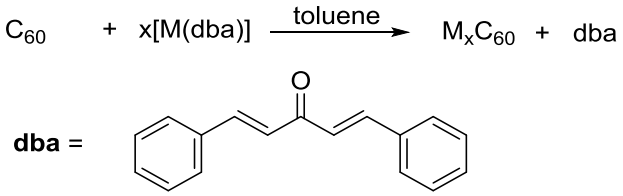

Scheme 1.3. The preparation of Pd fullerene[C_{60}] polymer. From ref.[84]

The ratio of Pd/C_{60} increases from 1 to 7 in the polymer when increasing the $Pd_2(dba)_3/C_{60}$ ratio, or if the palladium polymer ($C_{60}Pd_1$) was refluxed in toluene for several days. Indeed, a long-time refluxing could remove part of the C_{60} from Pd_1C_{60}, thus increasing the ratio of Pd to C_{60}. The authors propose a possible Pd_nC_{60} formation mechanism, as depicted in scheme 1.4. In the Pd_nC_{60} (n>3) polymers, there are two types of Pd atoms: one is coordinated between the C_{60} molecules (polymer),

and the excess of palladium atoms is deposited on the surface of the C_{60}. Pd_3C_{60} is thermodynamically more stable than the other polymers (Pd_1C_{60}, Pd_2C_{60}, $Pd_{n>3}C_{60}$).[85]

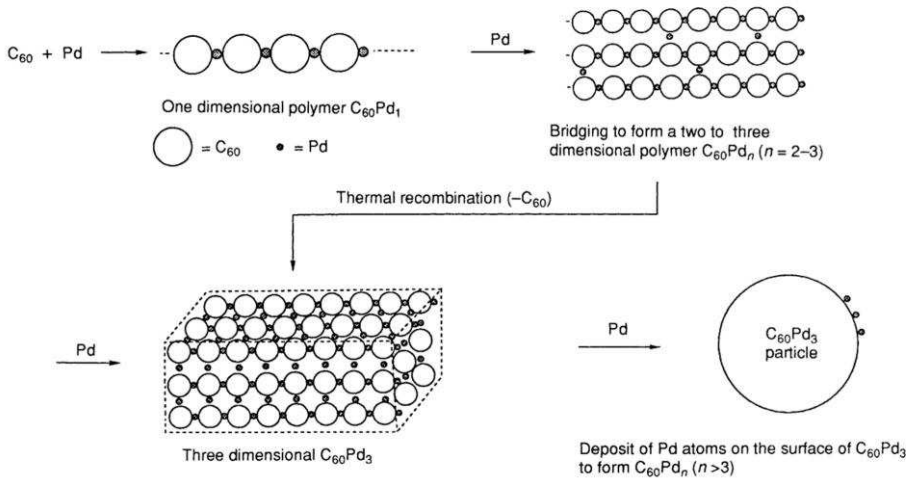

Scheme 1.4. The possible structure of Pd fullerene (Pd_nC_{60}) polymer with different ratio of Pd precursor and C_{60}. From ref. [84]

Using the same procedure, Nagashima[86] found that the reaction of C_{60} and $[Pt(dba)_2]$ was slower than with $[Pd_2(dba)_3]$. A similar preparation of Pt_nC_{60} polymer was achieved using the $[Pt(cod)_2]$ complex.[87] If a phosphine ligand was added to a suspension of $[PtC_{60}]$, the Pt-C_{60} bond cleaved, giving rise to the $[Pt(\eta^2\text{-}C_{60})(L\text{-}L)]$ complex as shown on Scheme 1.5.

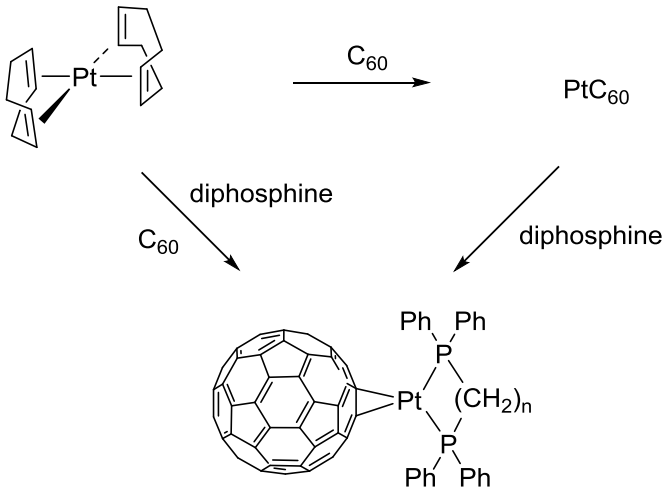

Scheme 1.5. The reaction of phosphine ligand and PtC_{60}. From ref. [87]

1.3.1.1.2 Fe (0) and Ru(0) fullerene C_{60} polymers

Carbonyl metal complexes are efficient precursors to synthesize metal-fullerene compounds.[88] In Scheme 1.5, the formation of metal carbonyl fullerene and metal fullerene polymer structures are shown. This process probably involves ligand exchange between C_{60} and CO.[89] In some cases, the CO ligand is not completely eliminated, as shown in Scheme 1.6a. With continuous thermal treatment or photolysis, the Fe fullerene polymer is formed as depicted in Scheme 1.6b.[83]

$$[Fe_2(CO)_9] + C_{60} \xrightarrow[\text{benzene}]{\text{Heat}} Fe(CO)_{n-1}C_{60} + CO \quad (a)$$

$$[Fe(CO)_5] + C_{60} \xrightarrow[\text{toluene}]{\text{photoysis}} Fe_nC_{60} + 5nCO \quad (b)$$

Scheme 1.6. Iron fullerene compounds synthesized from iron carbonyl complexes and fullerene: a) thermal reflux leading to $C_{60}Fe(CO)_{n-1}$; and b) photolysis leading to Fe_nC_{60}.

A Ru_nC_{60} compound was prepared by reaction of $[Ru_3(CO)_{12}]$ and C_{60} with ratio 1/1 under argon in refluxing toluene for 7 days.[90] From the TEM image (Scheme 1.7), ruthenium particles (2-5 nm) embedded in an amorphous matrix was formed.

$$Ru_3(CO)_{12} + C_{60} \xrightarrow[\text{reflux, 7 days}]{\text{toluene}} Ru_3C_{60}$$

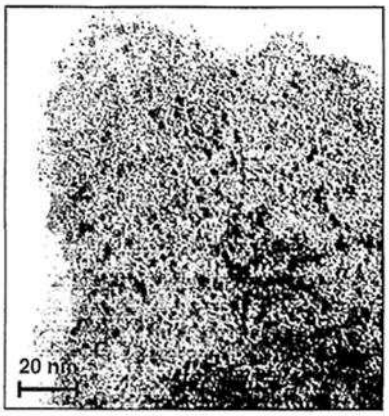

Scheme 1.7. The Ru_3C_{60} synthesis. From ref.[90]

1.3.1.2 Co-evaporation

Many transition metal of the 3d and 4d series (Sc, Ti, V, Ni, Y, Nb, Pd, etc), when evaporated in the presence of fullerene, can react to produce the corresponding metal fullerene polymer. Specifically, for Co_xC_{60}[91], pure fullerene and Co were co-evaporated to achieve a atomic composition of Co and C_{60} 2/1 in the same vacuum chamber. The C_{60}-Co films were grown up at room temperature. The process of deposition was performed in a UHV chamber. HREM analyses (Figure 1.17) evidenced the polymer chain structure, and the measured distance (11~12 Å) between two neighboring fullerenes corresponds to the theoretical value 10.9 Å (1.9 × 2 + 7.1 = 10.9 Å, 1.9 Å is the Co-C length,[92] 7.1 Å is the C_{60} diameter).

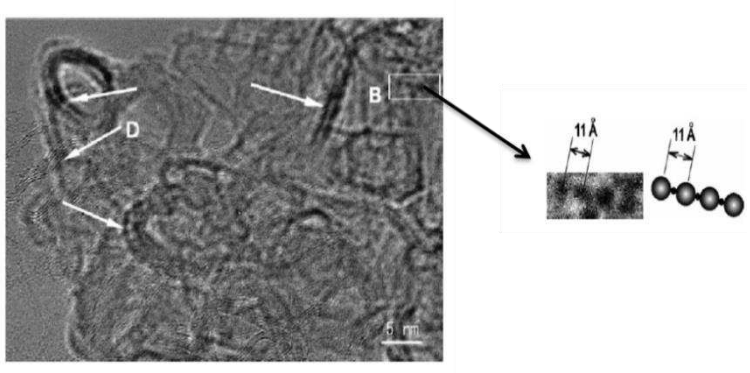

Figure 1.17. TEM and HREM image of CoC_{60} polymer showing the polymer chain (scale bar 5 nm). From ref.[92]

Ag-C_{60} nanostructured films were also prepared by the vapor deposition method, the decomposition rate of Ag/C_{60} was fixed at 2/1. The Ag-C_{60} film was disclosed by Hou *et al*.,[93] and in this film, Ag nano-crystallites are well dispersed in a C_{60} matrix (Figure 1.18), and the mean size of Ag nanocrystallites is 15.88 nm.

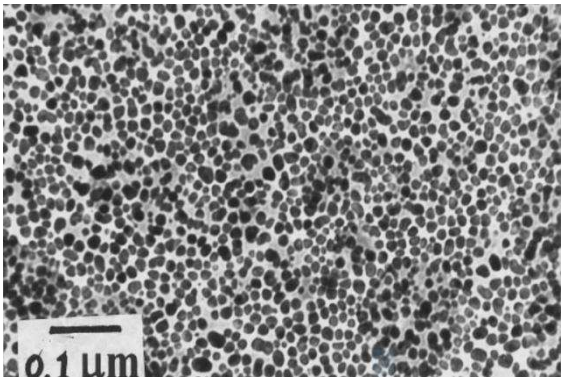

Figure 1.18. TEM image of a AgC_{60} nanostructured film. From ref.[93]

1.3.1.3 Electrochemical reduction method

Electrochemical reduction is another method to produce PdC_{60} films. It involves the use of C_{60} solution in toluene/acetonitrile in the presence of metal precursors such as $[(PhCN)_2PdCl_2]$, $[Pd(ac)_2]$ (ac=acetate) or $[Pd(CF_3COO)_2]$.[94] The electro-reduction of $[(PhCN)_2PdCl_2]$ was described by Hayashi *et al*. as depicted in Scheme 1.8. [94a]

$$C_{60} + e^- \longrightarrow [C_{60}]^-$$

$$[C_{60}]^- + (PhCN)_2Pd^{II}Cl_2 \longrightarrow (PhCN)_2Pd^{II}Cl(C_{60}^-) + Cl^-$$

$$(PhCN)_2Pd^{II}Cl(C_{60}^-) + [C_{60}]^- \longrightarrow Pd^{II}(C_{60}^-)_2 + 2(PhCN) + Cl^-$$

$$Pd^{II}(C_{60}^-)_2 = Pd^0(C_{60})_2$$

$$nPd^0(C_{60})_2 \longrightarrow Pd_n(C_{60}) + 2n\text{-}1C_{60}$$

Scheme 1.8. Electro-reduction synthesis of Pd_nC_{60} polymer film. From ref.[94a]

The structure and composition of the $C_{60}Pd$ films were affected by the Pd precursor/C_{60} ratio. This method can produce uniform and smooth polymer films, when using a high ratio of Pd to C_{60}. In this material, the polymer chain $[\text{-}C_{60}\text{-}Pd\text{-}]_n$ was separated by Pd nanoclusters. The existence of Pd nanoclusters (4-8 nm) in the film was confirmed by HREM (Figure 1.19).[95]

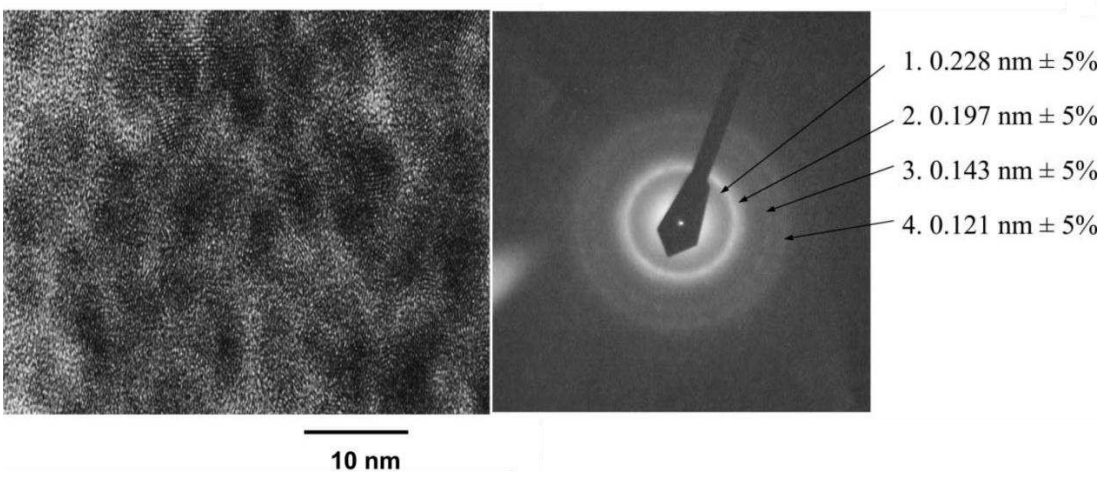

Figure 1.19. HREM image of Pd nano-clusters in the film (scale bar 10 nm). From ref.[95]

As discussed in section 1.3.1.1, the Pd nanoclusters, formed by the excess of Pd and connected to the polymer chain will improve the electrical properties of PdC_{60} polymers.

It seems from these results that, according to the experimental conditions, the formation of a metal-C_{60} polymer can be accompanied by the formation of the metallic nanoparticles.

1.3.2 Characterization of metal-fullerene polymers

To investigate the structure of metal fullerene polymers, many techniques have been used including TEM, Raman, XRD, XPS and SSNMR. However, the understanding of the fullerene-metal interaction is still not very clear.

1.3.2.1 TEM

TEM is a simple and effective way to observe the metal fullerene polymer. No metallic nanoparticles(NPs) were detected in the PdC_{60} polymer in Figure 1.20. However, nanoparticles (4-8 nm) were observed in sample Pd_2C_{60}, or for syntheses performed by electro-reduction and co-evaporation.

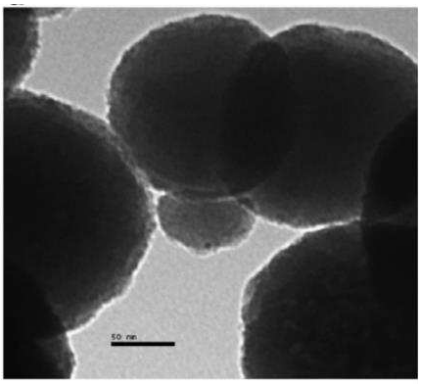

Figure 1.20. TEM images of Pd_nC_{60} polymer synthesized with a ratio of $[Pd_2(dba)_3]$ and C_{60} = 2/1 From ref.[96]

1.3.2.2 Raman and IR spectroscopies

Raman is an informative tool to analyse metal fullerides. As far as we know, both of metal-C_{60} polymer and C_{60} polymer will lead to the pentagonal pinch $A_g(2)$ mode modification, which is active in Raman. On the other hand, compared to metal C_{60} fullerides, C_{60} polymer have been intensively investigated by Raman spectroscopy. Thus it is very useful to make a comparison of metal fulleride and fullerene polymer, so there are some features of C_{60} polymer that we will discuss first.

It is known that the fullerene cage can be polymerizated by 2+2 cycloaddition to form four member rings under high temperature and pressure (Figure 1.21). Table 1.5 shows the peaks of the Raman spectra of fullerene polymer. Pristine C_{60} shows a band at 1469 cm^{-1} that corresponds to pentagonal pinch $A_g(2)$ mode, linear chains are characterized by a band at 1457-1460 cm^{-1}, branched chains at 1454-1455 cm^{-1} and tetragonal polymer at 1446-1449 cm^{-1}.[97]

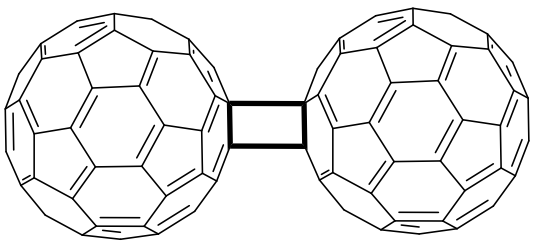

Figure 1.21. Fullerene C_{60} polymer linear structure.

Table 1.5. Raman data of a C_{60} polymer synthesized under photo or pressurized conditions. From ref.[97]

Photo-polymerized	Percentage of total peak area	Pressure polymerized	Percentage of total peak area	Assigned to
1434.2 cm^{-1}	4.53	1434.6 cm^{-1}	1.49	Polymeric planes
1446.3 cm^{-1}	4.50	1447.0 cm^{-1}	5.00	Polymeric planes
1454.0 cm^{-1}	24.9	1454.8 cm^{-1}	6.12	Branched chains
1460.5 cm^{-1}	45.0	1459.6 cm^{-1}	50.5	Linear chains
1464.6 cm^{-1}	14.4	1464.7 cm^{-1}	21.6	Dimers
1469.6 cm^{-1}	6.7	1468.8 cm^{-1}	15.4	Prisine C_{60}

The first comparison between the Pd fulleride and pure fullerene was carried out by Talyzin.[96] In this work, all the Pd_nC_{60} have a main peak at 1458 cm^{-1} (Figure 1.22a). However, it was found that at high Pd content, the main peak has two components: at 1449 and 1458 cm^{-1}. The peak at 1458 cm^{-1} can be assigned to linear chain or branched polymer and the peak at 1449 cm^{-1} to tetragonal polymer with four intermolecular connections. The structure of Pt_nC_{60} (n=1, 2, 3) with different ratio has been analyzed by Herbst *et al.*,[98] the observation of Raman peaks at 527 and 566 cm^{-1} suggests that a dimer/oligomer-like structure was formed under the fullerene polymer Raman features.

Talyzin *et al*. also presented a Raman comparison of several metal fullerides: Fe, Nb, Pd, Pt and Ti (Figure 1.22b).[99] Previously, it was found that the $A_g(2)$ mode of fullerene pentagonal pinch (1469 cm^{-1}) is sensitive to the modification of fullerene. Here, a strong peak (1400-1500 cm^{-1}) was observed (Figure 1.22b). However, it shows a downshift compared with the pure fullerene (1469 cm^{-1}). For the alkali metal fullerides, it is commonly accepted that, in ionic fulleride compounds, this mode is downshifted by approximately 6 cm^{-1} per electron transferred to C_{60}. The downshift of Pd_2C_{60} and Pt_2C_{60} is approximately of 14 cm^{-1}. Raman analysis have shown that the downshift of η^2-Pd and Pt of Pd_2C_{60} and Pt_2C_{60} is approximately 7-10 cm^{-1}, which is

similarly to the shift observed with the well know complexes [$PdPPh_3$ (η^2-C_{60})] and [$PtPPh_3$(η^2-C_{60})]. Thus, it is logical to believe that the Pd and Pt coordinate with two neighboring fullerene with η^2-bonding, which lead to a shift of approximately 14 cm^{-1}. Concerning the Raman spectra of these metal fullerides, it is commonly accepted that the same type of bonding occurs between the metal and the fullerene. For Fe_xC_{60}, the down shift is 24 cm^{-1}, so it is reasonable to conclude that the x is equal to 3-4.

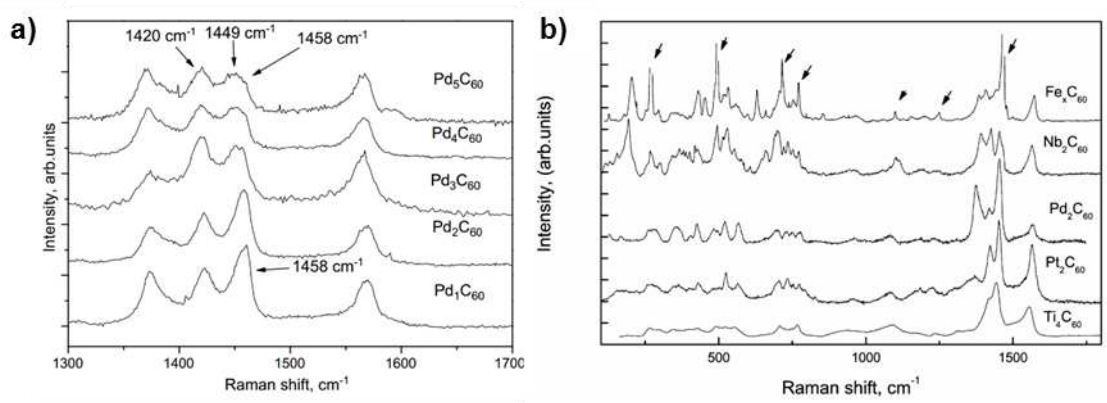

Figure 1.22. Raman spectra of metal C_{60} polymer: a) Pd_nC_{60} polymer with different ratio (n= 1, 2, 3, 4 and 5) of Pd and C_{60}; and b) different metal fullerides Ti, Pt, Pd, Nb and Fe (from the bottom to up). From ref. [96] and ref. [97]

The IR transmission spectra of some alkali metal fullerides were examined.[100] For example, the vibrations of M_xC_{60} (M = K and Rb) are presented in Table 1.6. Pristine C_{60} has four characteristic bands at 527, 576, 1182, and 1427 cm^{-1} (v_1, v_2, v_3, v_4 modes). For the Rb_xC_{60}, the v_2 and v_4 are more intense, so they are more useful for identifying the metal C_{60} polymer. The v_1 and v_3 mode have weaker absorptions compared with v_2 and v_4. Moreover, from C_{60} to M_6C_{60}, the peak of v_2 and v_4 will be enhanced, while the frequency of v_2 and v_4 will downshift: 576 to 565 and 1428 to 1340 cm^{-1}, respectively.

Table 1.6. IR intramolecular vibrations of M_xC_{60} (M =Rb and K, x = 0, 3, 4, 6). From ref.[100]

		C_{60}	M_3C_{60}	M_4C_{60}	M_6C_{60}
	ω_0 (cm^{-1})	526		472	467
v_1	S	0.02		0.008	0.03
	Γ (cm^{-1})	2.5		1.5	3
	ω_0 (cm^{-1})	576	573	570	565
v_2	S	0.008	0.019	0.022	0.17
	Γ (cm^{-1})	2.7	3	3.7	2.8
	ω_0 (cm^{-1})	1182			1182
v_3	S	0.0018			0.003
	Γ (cm^{-1})	4.2			5.8
	ω_0 (cm^{-1})	1428	1393	1363	1340
v_4	S	0.001	0.012	0.016	0.08
	Γ (cm^{-1})	4.5	20.8	23	7.2

[a] ω_0 is the center frequency, K_4C_{60} is 1369cm^{-1}, S is the strength and Γ is the width of each vibrational mode

1.3.2.3 XRD, XPS, and EXAFS

Considering that the structure of metal-fullerene polymer is amorphous, the XRD analysis usually provides a few informations. Figure 1.23a shows the XRD diagram of Pd_nC_{60} polymers.[96] Interestingly, some peak of metallic Pd(111) or Pd carbide are founded in Pd_2C_{60} and Pd_3C_{60}, and these peaks are weak and broad, which is attributed to the formation of small Pd nanoparticles in the samples.

X-ray photoelectron spectroscopy (XPS) analysis is a surface-sensitive spectroscopic technique that measures the elemental composition, chemical state and electronic state of the elements that exist within a material. The XPS analysis of the Pd 3d binding energy in Pd_2C_{60} was reported by Hayashi *et al*.[95] In the Figure 1.23b, the binding energy of Pd was increased compared to the Pd(0), which means that there is an electron transfer from Pd to C_{60}. It is easy to understand because the Pd electron flowing in the polymer chain will stabilize the structure. It have been suggested from

EXAFS analyses that the Pd atoms coordinated with fullerene in $\eta^2(6,6)$ mode,[101] which is similar to a fullerene polymer linked with the carbon of two hexagonal rings by 2+2 cyclo-addition.

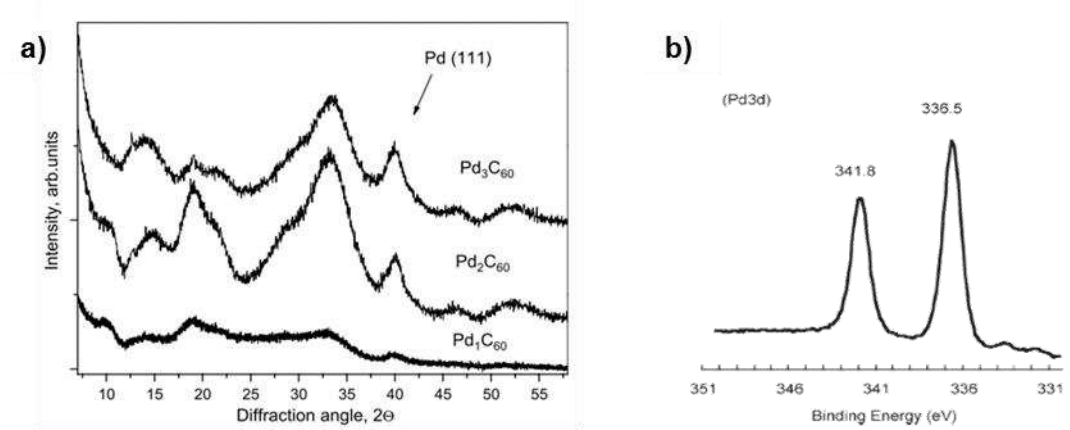

Figure 1.23. a) XRD diagram of Pd_nC_{60}(n=1, 2, 3), from ref [96]; and b) XPS spectrum of Pd_2C_{60} 3d. From ref.[95]

1.4 Metal nanoparticles/fullerene C_{60}

Based on the assembly of C_{60}, it is easy to understand that C_{60} would be a potential building block for well-defined nano-architectures design. However, there are limited reports that studied the interaction of metallic nanoparticles and fullerene.

1.4.1 Metallic nanocluster/C_{60}

Hsu *et al*. reported the first hexahapto $[Ru_3(CO)_9(\mu_3\text{-}\eta^2,\eta^2,\eta^2\text{-}C_{60})]$ complex,[38] which was synthesized with 40 % yield by mixing $[Ru_3(CO)_{12}]$ and C_{60} in refuxing hexane solution. In Figure 24a, we can see the six member ring of C_{60} coordinates with triruthenium cluster in η^2. Being each metal atom coordinated in a η^2 fashion to one benzene ring.

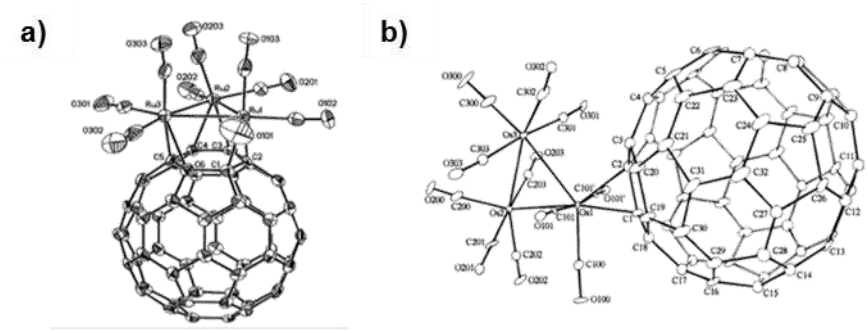

Figure 1.24. Crystal structure of a) $[Ru_3(CO)_9(\mu_3\text{-}\eta^2,\eta^2,\eta^2\text{-}C_{60})]$, from ref.[38]; and b) $\eta^2\text{-}C_{60}[Os_3(CO)_{11}(NCMe)]$. From ref.[43].

After the Ru carbonyl complex, Joon *et al*. investigate the reaction of the osmium $[Os_3(CO)_{11}(NCMe)]$ complex with C_{60}.[43] It was found that the C_{60} and the osmium cluster can coordinate in different ways: not only C_{60} can bond with one Os in η^2 (Figure 24b), but it also can bond with triosmium cluster in three η^2 mode.

Later, Joon *et al*. have prepared the two fullerene metal sandwich complexes $[Rh_6(CO)_9(dppm)_2(\mu_3\text{-}\eta^2,\eta^2,\eta^2\text{-}C_{60})]$[39] and $[Ir_4(CO)_3(\mu_4\text{-}CH)(PMe_3)_2(\mu\text{-}PMe_2)(CNR)(\mu\text{-}\eta^2,\eta^2\text{-}C_{60})\text{-}(\mu_4\text{-}\eta^1,\eta^1,\eta^2,\eta^2\text{-}C_{60})]$,[40] in which the metal atoms bind with two neighboring C_{60} cages (Figure 1.25). It was also found that metal cluster center will enhance electronic communication between two fullerene cages.

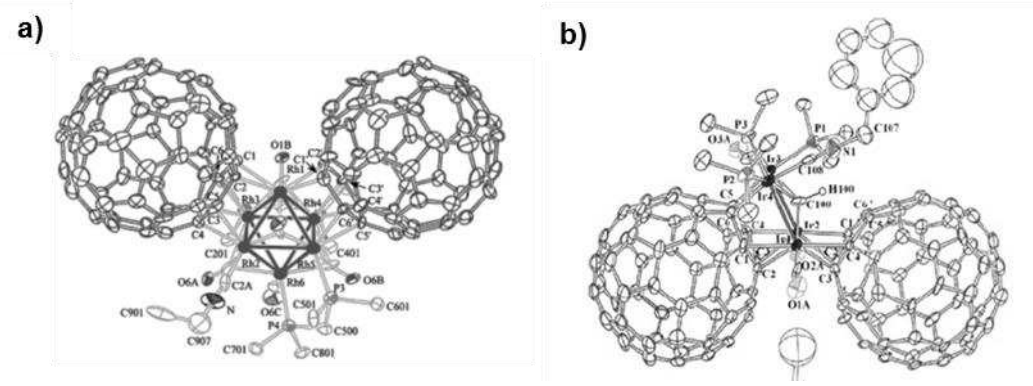

Figure 1.25. Crystal structure of a) $[Rh_6(CO)_9(dppm)_2(\mu_3\text{-}\eta^2,\eta^2,\eta^2\text{-}C_{60})]$, from ref.[39]; and b) $[Ir_4(CO)_3(\mu_4\text{-}CH)(PMe_3)_2(\mu\text{-}PMe_2)(CNR)(\mu\text{-}\eta^2,\eta^2\text{-}C_{60})\text{-}(\mu_4\text{-}\eta^1,\eta^1,\eta^2,\eta^2\text{-}C_{60})]$. From ref.[40]

1.4.2 Metallic nanoparticles/C_{60}

Usually, the conventional way to prepare deposited metal nanoparticles onto the surface of C_{60} is using the impregnation-reduction technique. The use of performed

metal nanoparticles has also been proposed. Recently, Pd or Ru doped C_{60} were synthesized by Saha and Deng[102] using a classic impregnation/activation technique with a mixture of [$Pd(acac)_3$] or [$Ru(acac)_3$] and C_{60}. In the TEM images, the Pd/C_{60} have a small particles size with a range of 5-6 nm (Figure 1.26).

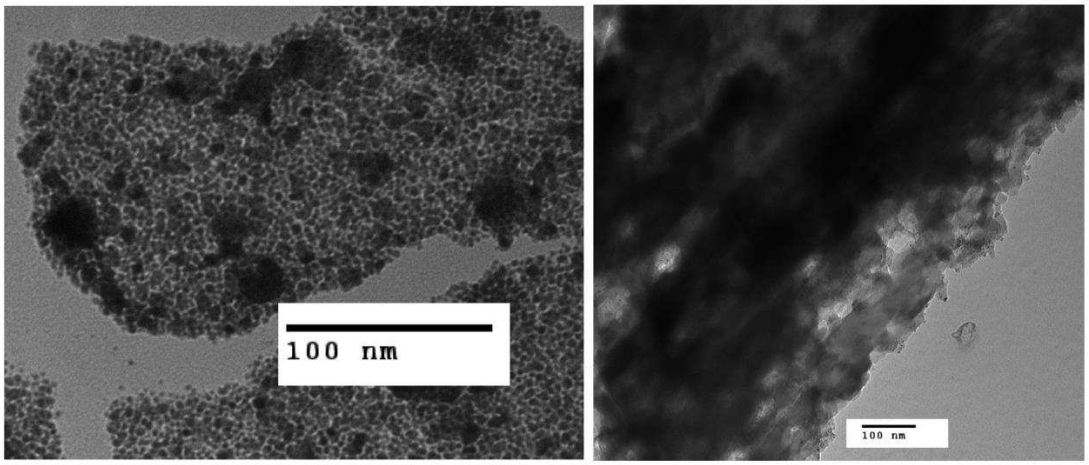

Figure 1.26. TEM image of Pd/C_{60} (left) and Ru/C_{60} (right) synthesized by impregnation method (scale bar = 100 nm). From the ref.[102]

Very few and small ruthenium nanoparticles (Figure 1.26 right) were observed in the Ru-C_{60}. A different morphology was observed with Ru_3C_{60} (Ru particles 2-5nm), which was synthesized by refluxing a toluene solution of C_{60} and [$Ru_3(CO)_{12}$]. Probably, the interaction of fullerene with the two Ru precursors is different, which caused this difference.

It is worth mention that the methods used to prepare metallic nanoparticles are very similar to the chemical solution way used for metal-C_{60} polymer synthesis. Thus, the presence of metal-C_{60} polymer in these materials cannot be excluded.

For the gold fullerene compounds, some works have revealed that C_{60} can be treated as a stabilizing reagent for gold nanoparticles. In 1998, Brust and co-workers developed C_{60} mediated aggregation of gold nanoparticles.[103] In the TEM images(Figure 1.27), small gold particles (3-6 nm) were detected, in a composite of aggregated clusters with size 50-100 nm.

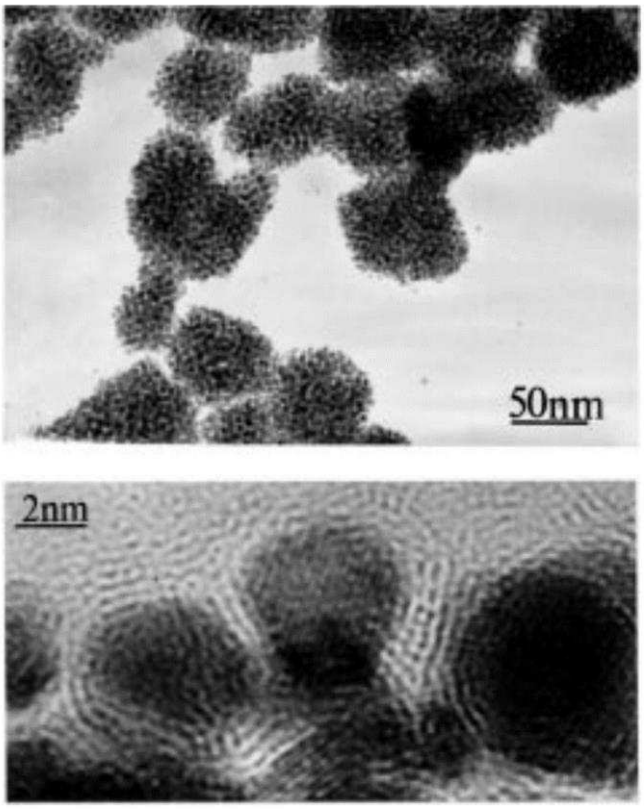

Figure 1.27. TEM (right, scale bar = 50 nm) and HREM (left, scale bar = 2 nm) image of AuC_{60}, from ref.[103]

A similar induced nanoparticle aggregation was described by Liu *et al*.[104] It was found that C_{60} is able to induce the aggregation of thiolated γ-cyclodextrin (CD) capped gold nanoparticles (Figure 1.28). The aggregation is attributed to the formation of a new complex between C_{60}, and γ-CD that attached to gold nanoparticles (Figure 1.29).

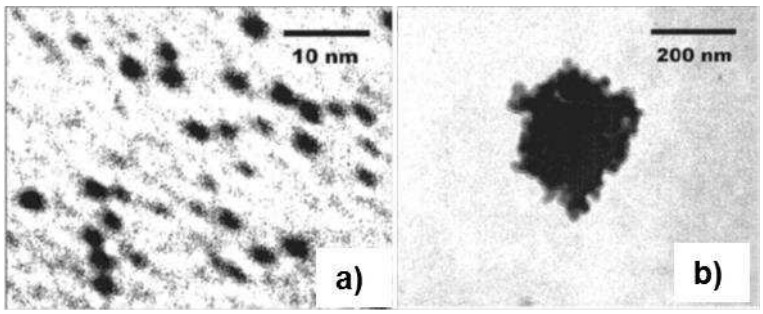

Figure 1.28. TEM image of a) γ-CD-Au nanostructure (scale bar = 10 nm) and b) Au nanoparticles aggregation induced by C_{60} (scale bar = 200 nm). From ref.[104]

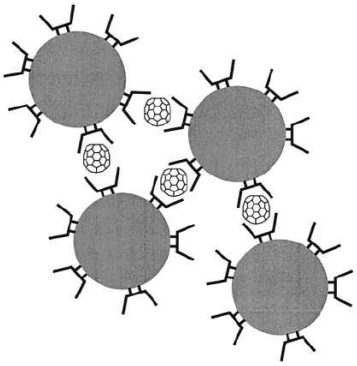

Figure 1.29. C_{60} induced network of γ-CD-Au nanostructures. From ref.[104]

Li *et al.*[105] reported a novel Ag/C_{60} nanocomposite synthesis method, with a mean size of Ag NPs of 5 nm, which is formed by adding $AgNO_3$ (as metal precursor) to a solution of C_{60}^- (Scheme 1.9).

$$AgNO_3 + C_{60}^- \xrightarrow[THF,\ H_2O]{r.t.} Ag + C_{60} \xrightarrow{growth} Ag/C_{60}\ NCC$$

Scheme 1.9. The preparation of Ag/C_{60} nanocomposite.

The TEM image show that the Ag nanoparticles are partially embedded in a C_{60} matrix (Figure 1.30).

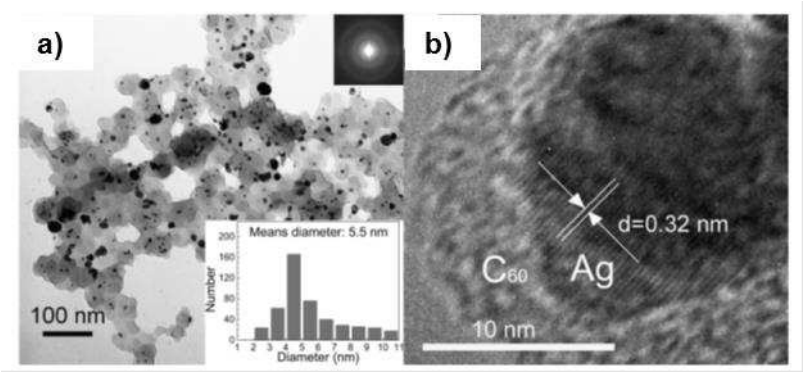

Figure 1.30. a) TEM image of Ag/C_{60} nanocomposite catalyst (scale bar = 100 nm); and b) HREM image of Ag/C_{60}. From ref.[105]

1.4.3 Metallic nanoparticles/functionalized C_{60}

Functionalized fullerenes,[106,107] have attracted the attention of many researchers as building blocks for the assemblies of metallic NPs. As far as we know, the first[108] new

thiol-functionalized fullerene/gold nanoparticles (C_{60}-Au nanoparticles) structure was reported by Fujihara and Naaki in 2001. Then the self-assembly reaction of functionalized fullerene with a thiol derivative and gold NPs was disclosed by Sudeep and co-workers.[109] Later, many fullerene thiol derivative as linker to stabilize Au NPs were used.[110,111,112,113] In addition to the thiol functionalized fullerenes, few examples on N-containing functionalized fullerenes C_{60} associate with metal NPs have been studied.[114,115,116] Generally, the nanostructures Au NPs/N-functionalized fullerene were prepared from gold NPs and a C_{60}-pyrrolidine derivatives.

Up today, however, few examples were focus on ordered three dimensional nanostructures. Lim *et al.*[117] described the assembly of gold NPs mediated by a multifunctional fullerene (Scheme 1.10).

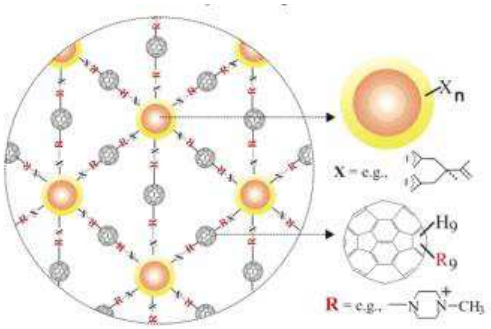

Scheme 1.10. Network of stabilized-Au nanoparticles linked by functionalized C_{60}. From ref.[117]

They show that fullerene can mediate assembly of gold NPs into 3D architectures. It is also addressed that the driving force of the nano-assembly formation was attributed to the interaction between the negatively charged Au NPs and positively charged functionalized fullerenes.

Rousseau *et al.*[118] reported that the use of a hexaadduct of C_{60} (Figure 1.31) as a unit to form three dimensional networks of gold NPs (Figure 1.32). It was revealed that the gold NPs (size 3 nm) were homogenous and strongly coordinated with the sulfur atoms in the C_{60} hexaadducts. The interparticular distance of the NPs is around 2.3 nm as verified by XRD, which is consistent with the ligands they used.

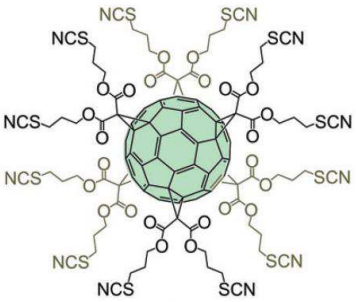

Figure 1.31. C_{60} hexaadduct.

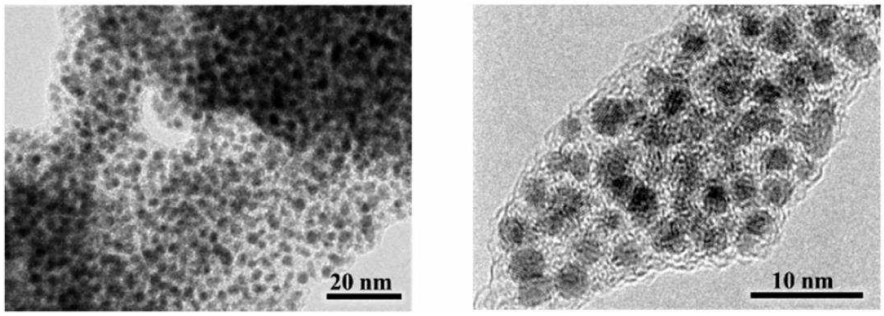

Figure 1.32. TEM image of Au NPS@C_{60} nanostructures. From ref.[118]

1.4.4 Metallic nanoparticles/C_{60} crystals

Fullerene nano or microcrystals have been synthesized by solution based approaches.[4] For example, the Liquid-Liquid Interfacial Precipitation (LLIP) method was developed by Miyazawa and co-worker,[119] in which the liquid/liquid interface acts as a nucleation site to synthesize fullerene crystals with different morphology such as sphere nanowhiskers and nano-rods (Figure 1.33).

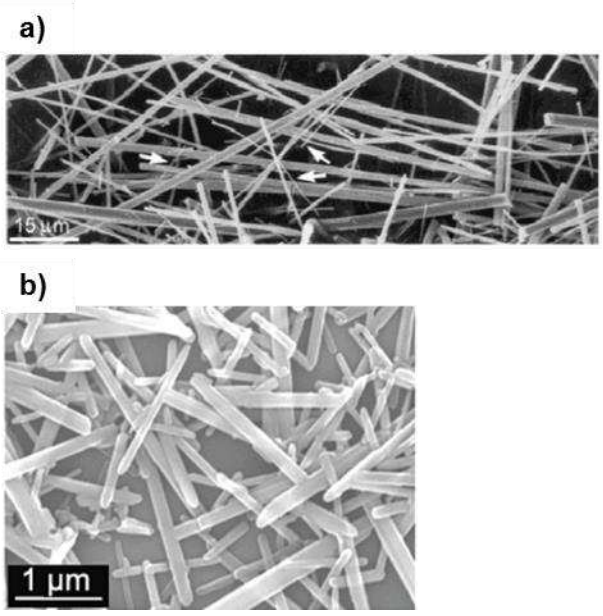

Figure 1.33. a) SEM micrographs of the needlelike crystals of C_{60} formed in a beaker by the liquid–liquid interfacial precipitation method. C_{60} nanowhiskers are indicated by arrows; and b) SEM of C_{60} nanorod obtained by mixed polygon (from TBA/benzene). From ref.[119]

Concerning the development of fullerene crystal preparation, some metallic NPs caped on fullerene crystals were studied. Tan *et al.*[120] developed a novel solution method to deposit gold NPs on the surface of C_{60} microcrystal with various shapes (Figure 1.34). As described above, the unique shape of C_{60} microcrystal can be controlled by the LLIP solution process named liquid-liquid re-precipitation. The hetero-structure C_{60}-Au NPs (a core shell nanostructure) with mean Au NPs size of 21.4 nm, was further valued for their use in catalysis.

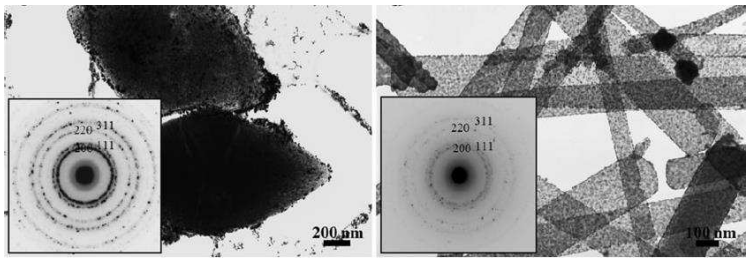

Figure 1.34. TEM image of Au Nanoparticles caped on C_{60} nanocrystals. From ref.[120]

Chong *et al.*[121] described a one-pot and rapid LLIP method to prepare Pd-C_{60} composite. They use isopropanol to induce the co-crystalization of the solution of C_{60}

and [$Pd(PPh_3)_4$]. Small Pd nano-clusters in the range of 1.4-5.6 nm were observed by TEM (Figure 1.35).

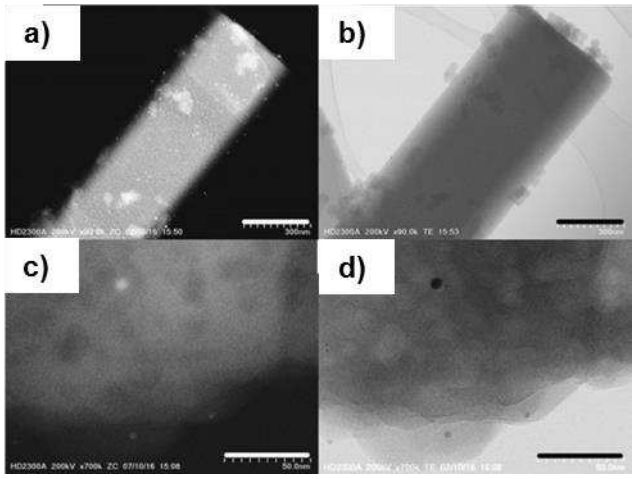

Figure 1.35. SEM image of η^2-$C_{60}Pd(PPh_3)_4$ complex, a) Dark and b) bright field 200 K STEM z-contrast image of fullerite with 300 nm scale bars and high angle annular c) dark and d) bright field images of palladium clusters with 50 nm scale bars. From ref.[121]

1.5 Catalysis with metal/C_{60}

Fullerene and fullerene-based materials have shown interesting catalytic activity and selectivity in heterogeneous catalysis[122,123,6b,124,83,125] because of their specific properties, such as thermal stability[126], high capacity for hydrogen adsorption[127,128,129,130] and the ability of various coordination.[13a,131,13b] The fullerene-based materials, typically the transition metal and fullerene compounds, have been studied in many catalystic reaction.[6b] One of these is the hydrogenation reaction of functional groups including nitro[132,105, 133,133,134], C=C[83] and C=O[135].

1.5.1 Catalysis with metal/C_{60} polymers

The catalytic activity of Pd_nC_{60} polymer was first investigated by Nagashima *et al*.[84,136] They show that Pd_nC_{60} catalyzed the hydrogenation of olefins and acetylenes. This reaction proceeds in cyclohexane at room temperature under an hydrogen atmosphere.[136] Using amines as co-catalysts, one can stop hydrogenation of acetylenes at the stage of alkene formation. It is worth to note that the aromatic rings and the ketone and ester groups are not hydrogenated by this catalyst. Palladium

fulleride is also an efficient catalyst to reduce NO_2 to NH_2 in aromatic nitrocompounds.

The reason for the high activity of Pd_nC_{60} catalyst was the good dispersion of Pd on C_{60} and the strong interaction of Pd nano-cluster and C_{60}. Moreover, Pd_nC_{60} ($n<3$) and Pd_nC_{60} ($n>3$) have a different activity in hydrogenation because of the different organization of metal atoms in the fulleride. When using Pd_nC_{60} ($n<3$) as catalyst, no activity was oberserved in the hydrogenation of diphenylacetylene.[136] The more effective catalytic sites were Pd clusters localized on the fullerene surface and not the metal polymer. However, the complex $C_{60}Pd(PPh_3)_2$[137] have a good catalytic activity for acetylenic alcohols hydrogenation. The interpretation could be that the phosphine ligands have a strong effect on metal electron density. Thus both of PdC_{60} and Pd_nC_{60} could have a good catalytic activity with appropriate modifications.

The alkali metal (M = Cs, K, Na) fullerides exhibit remarkable catalytic activity in the H_2-D_2 exchange reaction, which is similar to that obtained with a noble metal catalyst.[138] The mechanism involved the dissociative chemisorption of H_2 on the metal framework to form fullerene hydride. Later, Chen *et al.*[139] found that the alkali metal is the catalytic center for the dissociative-adsorption of H_2 in the case of Li, K/MWCNT.

In another work reported by Li *et al.*,[133] fullerenes were employed in the catalytic hydrogenation of nitrobenzene to aniline under UV light. These reactions were carried out at 140-160 °C and 4-5 MPa of H_2 pressure and it is worth to note that the active species appears to be not C_{60} itself but rather $[C_{60}]^-$ (Scheme 1.11). The authors also described a cooperative effect between $C_{60}/[C_{60}]^-$, which gave enhanced product selectivity. Although the mechanistic nature of H_2 activation is unclear, these authors reported that irradiation of the mixture led to clean reduction, even under ambient conditions using C_{60}, $[C_{60}]^-$, C_{70}, or $[C_{70}]^-$ as catalysts in the photolysis.

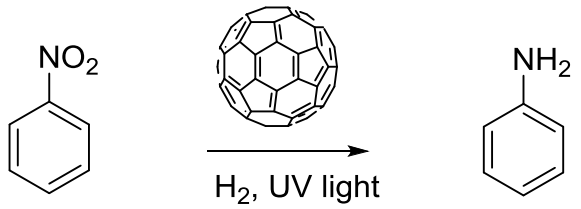

Scheme 1.11. C_{60} catalyzed hydrogenation of nitrobenzene under UV light.

Although the dissociation of H_2 using C_{60} as catalyst has been realized under some specific conditions, it will be very difficult for fullerene to dissociate H_2 when fullerene are associated to a metal cluster. A DFT calculation of the $C_{60}Pt_n$ model was used to investigate the diffusion and migration of H_2 on metal cluster and carbon.[140] The result showed that the hydrogen diffusion is very easy on the surface of both free-standing and C_{60}-supported Pt_n clusters, and the H-atom migration on the carbon surface is very unlikely.

Furthermore, it is worth noting that C_{60} fullerene can be relatively easily hydrogenated by transition metals in the presence of H_2.[141]

1.5.2 Catalysis with metal nanoparticles/C_{60}

The catalytic properties of Pd/C_{60} nano-composite has been investigated by Yu *et al.*[142] in two typical reactions: the hydrogenation of phenylacetylene and of cyclohexene (Figure 1.36). The Pd/C_{60} catalyst was synthesized from C_{60} and [$Pd(OAc)_2PPh_3$], followed by H_2 treatment. A comparison of Pd/C_{60} and Pd/C showed that they provide a similar conversion but that the maximum conversion is obtained at a lower rate with the Pd/C catalyst. The possible reason is that the spherical nature of C_{60} provides an effective surface support for a number of metal fragments, at which the active catalytic sites are found. In additional, the good dispersion of Pd/C_{60} was also contributed to the high activity.

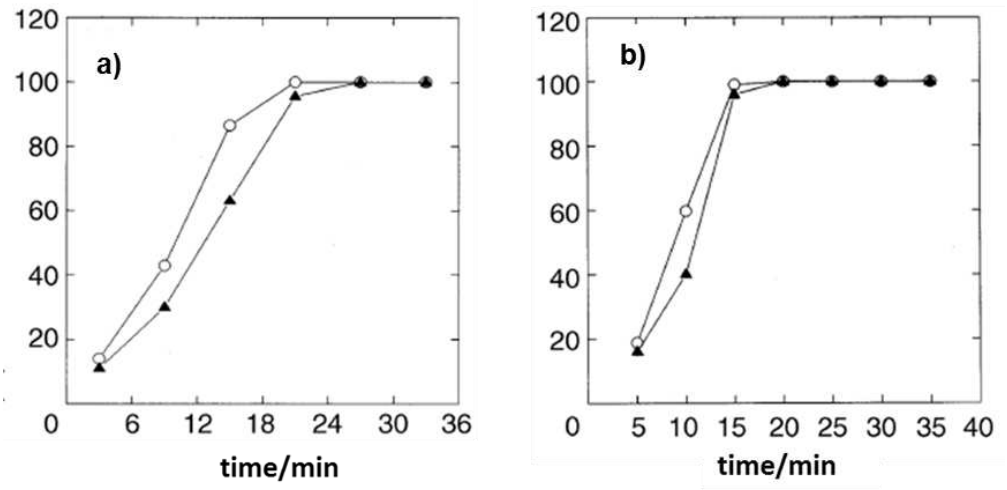

Figure 1.36. Hydrogenation of substrates: a) cyclohexene; and b) diphenylacetylene over the catalyst, Pd/C_{60} (O) and Pd/C (▲) in methanol under a H_2 atmosphere at room temperature. From ref.[142]

The cinnamaldehyde hydrogenation on Ru/C_{60} (Scheme 1.12) was investigated by Lashdaf *et al.*[135] The catalysts were synthesized using impregnation of ruthenium complexes on fullerene and then reduction by H_2 at 573K. It was shown that the support has a dramatic effect on the selectivity to cinnamayl alcohol COL (Figure 1.37). The selectivity for COL is more than 60% with fullerene, while it is only of 30% on conventional carbon supports. The author points out that the Ru cluster size and the bond between Ru and fullerene cage favor the adsorption of cinnamaldehyde and lead to the preferential hydrogenation of the C=O bond.

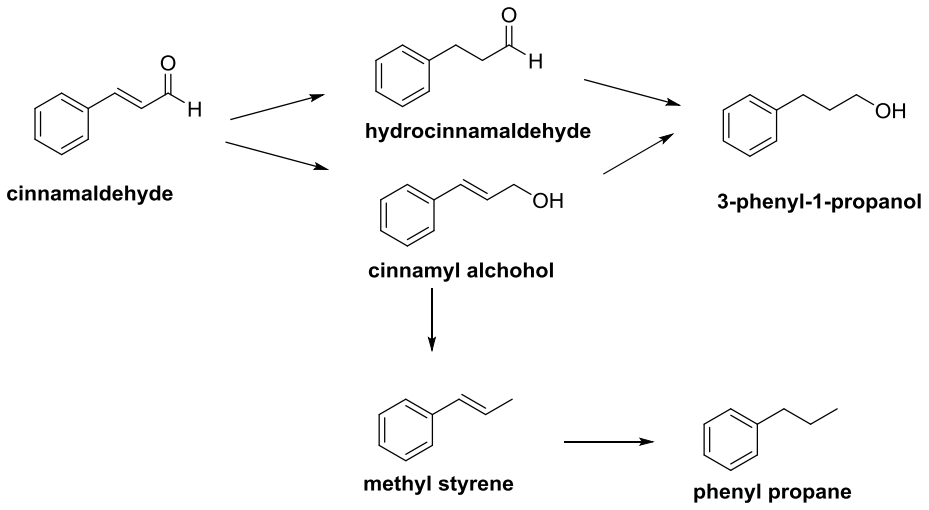

Scheme 1.12. Hydrogenation of *trans*-cinnamaldehyde.

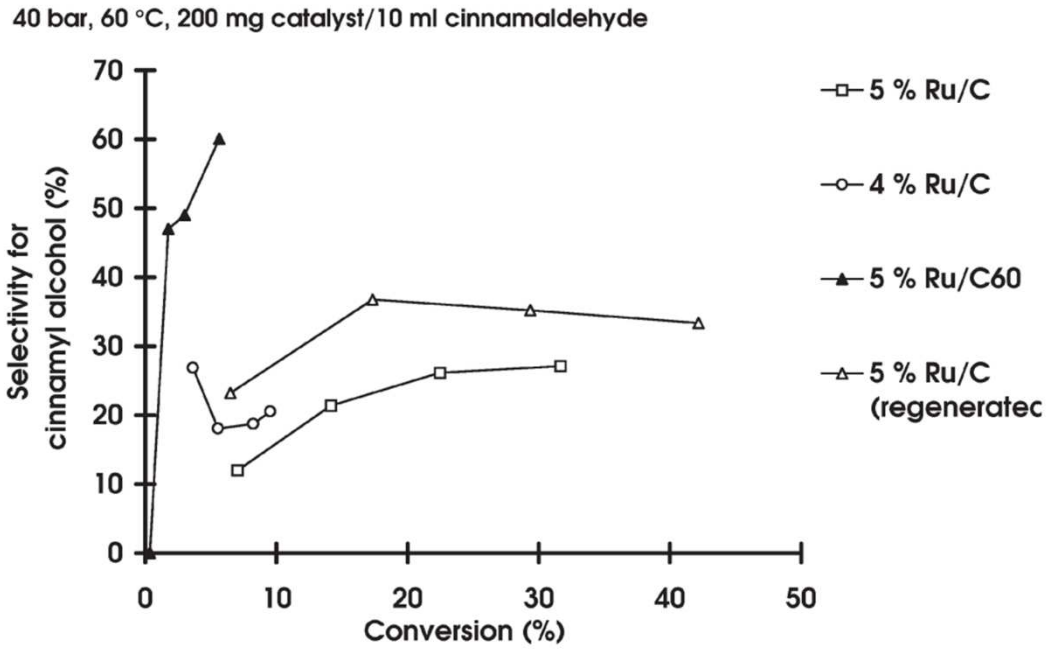

Figure 1.37. The selectivity of hydrogenation of cinnamaldehyde over Ru/C (activated carbon) and Ru/C_{60}. From ref.[135]

Braun *et al.* have evaluated the activity of Ru_3C_{60} and ruthenium deposited on carbon support (including raw fullerene black, extracted fullerene and graphite) catalysts for the CO hydrogenation reaction.[143] The authors suggested that there is no obvious change of the Ru_3C_{60} with annealing to 820K. However, compare to Ru on the fullerene black, the activity of the Ru_3C_{60} in the hydrogenation of CO is decreasing with the increase of the temperature from 470K to 570K (Table 1.7).

Table 1.7. The hydrogenation of CO over Ru_3C_{60} and Ru/C_{60} catalyst. From ref.[143]

	Ru_3C_{60}					**5% Ru on fullerene black**				
	470 K	495 K	520 K	545 K	570 K	470 K	495 K	520 K	545 K	570K
CO_2			0.7	2.9	7.9			0.5	1.9	5.5
CH_4	82.3	91.3	96.4	96.4	91.6	83.9	94.4	98.0	97.7	94.2
C_2H_4	2.6	0.8	0.1	0.1	0.1	2.1	0.5			
C_2H_6	3.5	3.7	1.5	0.4	0.3	3.3	2.8	1.1	0.3	0.2
C_3-C_6	11.6	4.2	1.3	0.2	0.1	10.7	2.3	0.4	0.1	0.1

Next, a comparison of the catalytic performances of Ru_3C_{60}, Ru/C and Ru/C_{60} catalysts, the latter two being synthesized by impregnation/activation procedure from $[Ru_3(CO)_{12}]$, was made.[144] Compared to conventional Ru/C catalysts, Ru_3C_{60} and Ru/C_{60} exhibited a higher selectivity for hydrocarbons in the CO hydrogenation reaction at 473 K. However, this selectivity and the activity of Ru_3C_{60} and Ru/C_{60} decrease at higher reaction temperatures due to the transformation of the initially active $Ru_x(CO)_y$ clusters into metal. In contrast with this, after reductive treatment of the pristine Ru_3C_{60} and Ru/C_{60} catalysts at elevated temperatures (annealing in vacuo), these catalysts exhibited strikingly higher activities in the hydrogenation of 2-cyclohexenone than the initially present $Ru_x(CO)_y$ clusters. The reductive treatment will lead to the loss of residual CO ligands but no extensive crystallization of metal was observed. This finding suggests that the catalytic properties can be enhanced by appropriate pre-treatment, which might multiply the possible applications for Ru_3C_{60} and Ru/C_{60} catalysts.

Finally, Li *et al.*[105] have developed a novel catalyst Ag/C_{60}, which is synthesized by $AgNO_3$ and C_{60}^-. The catalyst exhibited a good activity and selectivity in hydrogenation of nitroarene to amino-arene (Scheme 1.13).

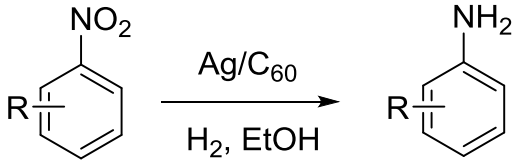

Scheme 1.13. Catalytic selective hydrogenation of nitroarene over Ag/C_{60}.

1.6 Conclusions

With the development of fullerene chemistry, fullerene materials have been investigated for a large variety of purposes, such as catalyst supports, battery anodes, and proton transport membranes.[6c] In this chapter, the synthesis and characterization of transition metal fullerene polymers and nanostructures as well as their applications in catalysis have been described.

Metal fullerene C_{60} polymers have been prepared by three different methods, including, chemical solution synthesis, co-evaporation and electro-reduction method. Among these three procedures, chemical solution synthesis is a costly and effective method to produce metal fullerene polymers. However, the organization of the metal atoms and the fullerene is difficult to control. As far as we know, up to now, there is no examples suggesting the possibility of simple, efficient controlled assembly of metal and C_{60}. For instance, only the amorphous metal fullerides PdC_{60} and PtC_{60} were currently obtained. Although the co-evaporation is able to fabricate well-ordered metal fullerene nanocomposites, high temperatures and high vacuum are necessary during the synthesis.

For the characterization techniques, TEM is a direct way to examine the metal fullerides structure. Raman analysis was thought to be an effective tool to identify the fullerene C_{60} modification. For example, the A_g (2) mode of fullerene pentagonal pinch downshift of PdC_{60} is 7 cm^{-1}, and 14 cm^{-1} for Pd_2C_{60}. Analogously, IR spectra are useful to identify the metal fullerides, with shifting of v_2 and v_4 bands. Beside, XPS analyses can provide the state of metal (charges transfer) and other techniques also give useful information like EXAFS.

In contrast with metal-C_{60} polymer, metallic nanoparticles/C_{60} materials were less investigated. Although the primary carbonyl metal nanocluster coordinated fullerenes C_{60} were synthesized, organized nanostructures of metal nanoparticles and fullerene are rare. The progress on these nanostructures is mainly related to metallic NPs associated with functional fullerene and fullerene crystals. For instance, it has been proposed that a fullerene hexa-adducts may mediated sub-gold nanoparticles to form a three dimensional structure.

Numerous publications demonstrated that transition metal fullerene species present have high catalytic activity. The M_nC_{60} (M = Pd, Pt, Ru.) materials can catalyze many reactions involving molecular hydrogen activation, hydrogenation of olefins and

acetylenes, reduction of CO and NO_2 groups, etc. Comparing the catalytic performances of the metal fullerene and metal particles deposit on fullerene, it was found that the Pd/C_{60} material is better than Pd/C, whereas the ruthenium material behave as their counterparts on activated carbon. Additionally, metal particles play an important role in the catalytic process. For example, in the Pd_nC_{60} ($n>3$) material, there are two types of palladium atoms in the polymers as described above, it is the presence of an excess of palladium atoms on the surface of fullerene (formation of metallic NPs) that make that they present high catalytic activity for specific reactions.

1.7 References

1. (a) Kroto, H. W.; Allaf, A.; Balm, S., C_{60}: Buckminsterfullerene. *Chem. Rev.* **1991,** *91* (6), 1213-1235; (b) Dresselhaus, M. S.; Dresselhaus, G.; Eklund, P. C., *Science of fullerenes and carbon nanotubes: Their properties and applications*. Academic press: 1996.

2. Martin, C. A.; Ding, D.; Sørensen, J. K.; Bjørnholm, T.; van Ruitenbeek, J. M.; van der Zant, H. S., Fullerene-based anchoring groups for molecular electronics. *J. Am. Chem. Soc.* **2008,** *130* (40), 13198-13199.

3. Thompson, B. C.; Frechet, J. M., Polymer–fullerene composite solar cells. *Angew. Chem. Int. Ed.* **2008,** *47* (1), 58-77.

4. Shrestha, L. K.; Shrestha, R. G.; Hill, J. P.; Ariga, K., Self-assembled fullerene nanostructures. *J. Oleo. Sci.* **2013,** *62* (8), 541-553.

5. Montellano, A.; Da Ros, T.; Bianco, A.; Prato, M., Fullerene C_{60} as a multifunctional system for drug and gene delivery. *Nanoscale* **2011,** *3* (10), 4035-4041.

6. (a) Georgakilas, V.; Perman, J. A.; Tucek, J.; Zboril, R., Broad family of carbon nanoallotropes: Classification, chemistry, and applications of fullerenes, carbon dots, nanotubes, graphene, nanodiamonds, and combined superstructures. *Chem. Rev.* **2015,** *115* (11), 4744-4822; (b) Goldshleger, N. F., Fullerenes and fullerene-based materials in catalysis. *Fullerene Sci. Technol.* **2001,** *9* (3), 255-280; (c) Lebedeva, M. A.; Chamberlain, T. W.; Khlobystov, A. N., Harnessing the synergistic and complementary properties of fullerene and transition-metal compounds for nanomaterial applications. *Chem. Rev.* **2015,** *115* (20), 11301-11351; (d) Schaetz, A.; Zeltner, M.; Stark, W. J., Carbon modifications and surfaces for catalytic organic transformations. *ACS Catal.* **2012,** *2* (6), 1267-1284.

7. (a) Prato, M., [C_{60}] fullerene chemistry for materials science applications. *J. Mater. Chem.* **1997,** *7* (7), 1097-1109; (b) Li, Z.; Liu, Z.; Sun, H.; Gao, C., Superstructured assembly of nanocarbons: Fullerenes, nanotubes, and graphene. *Chem. Rev.* **2015,** *115* (15), 7046-7117.

8. Hirsch, A., *The chemistry of the fullerenes*. Wiley Online Library: 1994.

9. Ruoff, R.; Tse, D. S.; Malhotra, R.; Lorents, D. C., Solubility of fullerene (C_{60}) in a variety of solvents. *J. Phys. Chem.* **1993,** *97* (13), 3379-3383.

10. Hirsch, A.; Brettreich, M., *Fullerenes: Chemistry and reactions*. John Wiley & Sons: 2006.

11. Yannoni, C.; Bernier, P.; Bethune, D.; Meijer, G.; Salem, J., NMR determination of the bond lengths in C_{60}. *J. Am. Chem. Soc.* **1991,** *113* (8), 3190-3192.

12. (a) Giacalone, F.; Martin, N., Fullerene polymers: Synthesis and properties. *Chem. Rev.* **2006,** *106* (12), 5136-5190; (b) Balch, A. L.; Olmstead, M. M., Reactions of transition metal complexes with fullerenes (C_{60}, C_{70}, etc.) and related materials. *Chem. Rev.* **1998,** *98* (6), 2123-2166.

13. (a) Soto, D.; Salcedo, R., Coordination modes and different hapticities for fullerene organometallic complexes. *Molecules* **2012,** *17* (6), 7151-7168; (b) Axet, M.; Dechy-Cabaret, O.; Durand, J.; Gouygou, M.; Serp, P., Coordination chemistry on carbon surfaces. *Coord. Chem. Rev.* **2016,** *308*, 236-345.

14. Fagan, P. J.; Calabrese, J. C.; Malone, B., The chemical nature of buckminsterfullerene (C_{60}) and the characterization of a platinum derivative. *Science* **1991,** *252*, 1160-1161.

15. Balch, A. L.; Catalano, V. J.; Lee, J. W.; Olmstead, M. M.; Parkin, S. R., (η^2-C_{70})Ir(CO)Cl(PPh_3)$_2$: The synthesis and structure of an iridium organometallic derivative of a higher fullerene. *J. Am. Chem. Soc.* **1991,** *113*, 8953-8955.

16. Sawamura, M.; Kuninobu, Y.; Nakamura, E., Half-sandwich metallocene embedded in a spherically extended π-conjugate system. Synthesis, structure, and electrochemistry of Rh(η^5-$M_{60}Me_5$)$(CO)_2$. *J. Am. Chem. Soc.* **2000,** *122,* 12407-12408.

17. Zhang, S.; Brown, T. L.; Du, Y.; Shapley, J. R., Metalation of fullerene (C_{60}) with pentacarbonylrhenium radicals. Reversible formation of $C_{60}\{Re(CO)_5\}_2$. *J. Am. Chem. Soc.* **1993,** *115* (15), 6705-6709.

18. Nunzi, F.; Sgamellotti, A.; Re, N.; Floriani, C., A density functional study of C_{60} transition metal complexes. *Organometallics* **2000,** *19* (9), 1628-1634.

19. (a) Lichtenberger, D. L.; Wright, L. L.; Gruhn, N. E.; Rempe, M. E., Electronic structure and bonding of C_{60} to metals. *Synth. Met.* **1993,** *59*, 353-67; (b) Lichtenberger, D. L.; Wright, L. L.; Gruhn, N. E.; Rempe, M. E., Electronic structure of exohedral interactions between C_{60} and transition metals. *J. Organomet. Chem.* **1994,** *478*, 213-221.

20. Loboda, O., A DFT study on exohedral metallofullerenes: Structural and electronic properties. *Fullerenes, Nanotubes, Carbon Nanostruct.* **2009,** *17*, 457-475.

21. Chen, C.-S.; Lin, C.-S.; Yeh, W.-Y., Synthesis of $Mo(CO)_2(\eta^3$-$PPh_2(o$-$C_6H_4)C(O)H)_2$ and its reaction with C_{60}. *J. Organomet. Chem.* **2011,** *696*, 1474-1478.

22. Yeh, W.-Y., C_{60}-induced alkyne-alkyne coupling and alkyne scission reactions of a tungsten tris(diphenylacetylene) complex. *Chem. Commun.* **2011,** *47*, 1506-1508.

23. Yeh, W.-Y., Unusual thermal reactivity of [W(CPh)(NCMe)(η^2-C_{60})(η^5-C_5Ph_5)] in chlorobenzene involving activation of all ligands. *Angew. Chem., Int. Ed.* **2011,** *50*, 12046-12049.

24. Malic, N.; Nichols, P. J.; Makha, M.; Raston, C. L., Assembling C_{60} molecules involving Fe(II)-η^2 bonding to a saddle-shaped macrocycle. *Cryst. Growth Des.* **2009,** *9*, 863-866.

25. Konarev, D. V.; Khasanov, S. S.; Troyanov, S. I.; Nakano, Y.; Ustimenko, K. A.; Otsuka, A.; Yamochi, H.; Saito, G.; Lyubovskaya, R. N., Mononuclear coordination complexes of fullerene C_{60} with zerovalent cobalt having s = 1/2 spin state: Co(η^2-C_{60})(L)(C_6H_5CN)·(*o*-$C_6H_4Cl_2$) (L = 1,2-bis(diphenylphosphino)ethane and 1,1'-bis(diphenylphosphino)ferrocene). *Inorg. Chem.* **2013,** *52*, 13934-13940.

26. Konarev, D. V.; Troyanov, S. I.; Nakano, Y.; Ustimenko, K. A.; Otsuka, A.; Yamochi, H.; Saito, G.; Lyubovskaya, R. N., Magnetic coupling in the fullerene dimer [Co(Ph_3P)(C_6H_5CN)]$_2$(μ^2-η^2:η^2-C_{60})$_2$ with two zerovalent cobalt atoms as bridges. *Organometallics* **2013,** *32* (15), 4038-4041.

27. Tsikalova, M. V.; Zheludkov, S. V.; Vorontsov, E. I.; Bashilov, V. V.; Babievskii, K. K.; Sokolov, V. I.; Novikov, Y. N., Optically active rhodium and iridium C_{60} complexes containing the enantiomeric ligand(+)DIOP: (η^2-C_{60})MH(CO)[(+)DIOP] (M=Rh, Ir). *Mendeleev Commun.* **2011,** *21*, 256-258.

28. Lee, C. Y.; Lee, G.; Kang, H.; Park, B. K.; Park, J. T., Synthesis and characterization of $Ir(H)(CO)(PEt_3)_2(\eta^2\text{-}C_{60})$. *Bull. Korean Chem. Soc.* **2007,** *28*, 1958-1962.

29. Konarev, D. V.; Khasanov, S. S.; Yudanova, E. I.; Lyubovskaya, R. N., The η^2 complex of nickel bis(diphenylphosphanyl)propane with fullerene: $[Ni(dppp)(\eta^2\text{-}C_{60})\}$(solvent) obtained by reduction. *Eur. J. Inorg. Chem.* **2011**, 816-820.

30. Konarev, D. V.; Zorina, L. V.; Khasanov, S. S.; Lyubovskaya, R. N., The formation of 3D fullerene packing in molecular complexes of C_{60} and C_{70} with metal diethyl dithiophosphates: $[M(dedtp)_2][C_{60(70)}]_3$ ($M = Ni^{II}$, Co^{II}, and $V^{IV}O$). *Eur. J. Inorg. Chem.* **2013,** *2013*, 309-314.

31. Konarev, D. V.; Simonov, S. V.; Khasanov, S. S.; Lyubovskaya, R. N., Preparation of η^2-complexes of fullerenes by reduction. Crystal structure and optical properties of $\{Ni(dppp)(\eta^2\text{-}C_{70})\}(C_6C_4Cl_2)_{0.5}$. *Dalton Trans.* **2011,** *40*, 9176-9179.

33. Konarev, D. V.; Troyanov, S. I.; Nakano, Y.; Otsuka, A.; Yamochi, H.; Saito, G.; Lyubovskaya, R. N., Molecular structure and spectroscopic properties of a nickel-bridged $[\{Ni(Ph_3P)\}_2(\mu^2\text{-}\eta^2, \eta^2\text{-}C_{60})_2]$ dimer. *Dalton Trans.* **2014,** *43*, 17920-17923.

33. Konarev, D. V.; Khasanov, S. S.; Nakano, Y.; Otsuka, A.; Yamochi, H.; Saito, G.; Lyubovskaya, R. N., Linear coordination fullerene C_{60} polymer $[\{Ni(Me_3P)_2\}(\mu^2\text{-}\eta^2, \eta^2\text{-}C_{60})]$ infinity bridged by zerovalent nickel atoms. *Inorg. Chem.* **2014,** *53* (22), 11960-11965.

34. Sokolov, V. I.; Bashilov, V. V.; Dolgushin, F. M.; Abramova, N. V.; Babievsky, K. K.; Ginzburg, A. G.; Petrovskii, P. V., Novel optically active organometallic derivatives of fullerenes with non-central types of chirality in addends: Synthetic and CD studies. *Tetrahedron Lett.* **2009,** *50*, 5347-5350.

35. Sokolov, V. I.; Bashilov, V. V.; Abramova, N. V., Fullerene-metallocene composite molecules: Different types. *Fullerenes, Nanotubes, Carbon Nanostruct.* **2008,** *16*, 285-292.

36. Wang, S.-J.; Yeh, W.-Y., C_{60}-induced alkyne cycloaddition with $W(CO)(PhC{\equiv}CPh)_3$. *Organometallics* **2012,** *31*, 6491-6495.

37. Konarev, D. V.; Khasanov, S. S.; Yudanova, E. I.; Lyubovskaya, R. N., The η= complex of nickel bis(diphenylphosphanyl)propane with fullerene: $\{Ni(dppp)(\eta^2\text{-}C_{60})\}$(solvent) obtained by reduction. *Eur. J. Inorg. Chem.* **2011,** *2011* (6), 816-820.

38. Hsu, H.-F.; Shapley, J. R., $Ru_3(CO)_9(\mu^3\text{-}\eta^2,\eta^2,\eta^2\text{-}C_{60})$: A cluster face-capping, arene-like complex of C_{60}. *J. Am. Chem. Soc.* **1996,** *118* (38), 9192-9193.

39. Lee, K.; Song, H.; Kim, B.; Park, J. T.; Park, S.; Choi, M.-G., The first fullerene-metal sandwich complex: An unusually strong electronic communication between two C_{60} cages. *J. Am. Chem. Soc.* **2002,** *124* (12), 2872-2873.

40. Lee, G.; Cho, Y.-J.; Park, B. K.; Lee, K.; Park, J. T., Two metal centers bridging two C_{60} cages as a wide passage for efficient interfullerene electronic interaction. *J. Am. Chem. Soc.* **2003,** *125* (46), 13920-13921.

41. Rogachev, A. Y.; Sevryugina, Y.; Filatov, A. S.; Petrukhina, M. A., Corannulene vs. C_{60}-fullerene in metal binding reactions: A direct DFT and X-ray structural comparison. *Dalton Trans.* **2007,** , 3871-3873.

42. Kim, K. H.; Jung, J.; Han, Y.-K., Geometric and electronic structures of $Os_3(CO)_9(\mu^3\text{-}\eta^2,\eta^2,\eta^2\text{-}C_{60})$, $Os_3(CO)_8(P(CH_3)_3)(\mu^3\text{-}\eta^2,\eta^2,\eta^2\text{-}C_{60})$, and their anions (q = -1 to -4): Reduction-induced conversion of π to σ-C_{60}-metal complexes. *Organometallics* **2004,** *23*, 3865-3869.

43. Park, J. T.; Song, H.; Cho, J.-J.; Chung, M.-K.; Lee, J.-H.; Suh, I.-H., Synthesis and characterization of η^2-C_{60} and μ^3-η^2,η^2,η^2-C_{60} triosmium cluster complexes. *Organometallics* **1998,** *17* (2), 227-236.

44. Park, B. K.; Lee, C. Y.; Jung, J.; Lim, J. H.; Han, Y.-K.; Hong, C. S.; Park, J. T., $[Os_3(CO)_6(PMe_3)_3](\mu^3\text{-}\eta^2,\ \eta^2,\eta^2\text{-}C_{60})[Re_3(\mu\text{-}H)_3(CO)_9]$: A fullerene[$C_{60}$] coordinated to two different trinuclear clusters. *Angew. Chem., Int. Ed.* **2007,** *46*, 1436-1439.

45. Jun, T.; Park, B. K.; Lee, C. Y., Synthesis, characterization, and electrochemical study of $Os_3(CO)_7$(1,2-dppm)(μ^3-η^2:η^2:η^2-C_{60}) and $Os^3(CO)_7$(1,1-dppm)(μ^3-η^2:η^2:η^2-C_{60}). *J. Organomet. Chem.* **2014,** *763-764*, 20-25.

46. Yeh, W.-Y., Synthesis and characterization of face-capping triruthenium cluster complexes of pentamethylfullerenes. *J. Organomet. Chem.* **2014,** *751*, 351-355.

47. Lee, M. H.; Kim, J. W.; Lee, C. Y., [C_{60}]fullerene-porphyrin-ferrocene triad self-assembled monolayers (sams) for photovoltaic applications. *J. Organomet. Chem.* **2014,** *761*, 20-27.

48. Lee, C. Y.; Jang, J. K.; Kim, C. H.; Jung, J.; Park, B. K.; Park, J.; Choi, W.; Han, Y.-K.; Joo, T.; Park, J. T., Remarkably efficient photocurrent generation based on a [C_{60}]fullerene-triosmium cluster/Zn-porphyrin/boron-dipyrrin triad sam. *Chem. Eur. J.* **2010,** *16*, 5586-5599.

49. Chen, C.-H.; Aghabali, A.; Suarez, C.; Olmstead, M. M.; Balch, A. L.; Echegoyen, L., Synthesis and characterization of bis-triruthenium cluster derivatives of an all equatorial [60]fullerene tetramalonate. *Chem. Commun.* **2015,** *51*, 6489-6492.

50. (a) Bashilov, V. V.; Magdesieva, T. V.; Kravchuk, D. N.; Petrovskii, P. V.; Ginzburg, A. G.; Butin, K. P.; Sokolov, V. I., A new heterobimetallic palladium-[60]fullerene complex with bidentate bis-1,1'-[P]$_2$-ferrocene ligand. *J. Organomet. Chem.* **2000,** *599* (1), 37-41; (b) Konarev, D. V.; Troyanov, S. I.; Ustimenko, K. A.; Nakano, Y.; Shestakov, A. F.; Otsuka, A.; Yamochi, H.; Saito, G.; Lyubovskaya, R. N., Formation of {Co(dppe)}$_2${μ^2-η^2:η^2-η^2:η^2-[(C_{60})$_2$]} dimers bonded by single C-C bonds and bridging η^2-coordinated cobalt atoms. *Inorg. Chem.* **2015,** *54* (10), 4597-4599; (c) Sparta, M.; Jensen, V. R.; Børve, K. J., Accurate metal–ligand bond energies in the η^2-C_2H_4 and η^2-C_{60} complexes of $Pt(PPh_3)_2$, with application to their bis(triphenylphosphine) analogues. *Mol. Phys.* **2013,** *111* (9-11), 1599-1611; (d) Watanabe, T.; Itoh, M. F.; Komuro, T.; Okada, H.; Sakai, T.; Ono, Y.; Kawachi, K.; Kasama, Y.; Tobita, H., Iridium and platinum complexes of $Li^+@C_{60}$. *Organometallics* **2014,** *33* (3), 608-611; (e) Zanello, P.; Fabrizi de Biani, F.; Cinquantini, A.; Grigiotti, E., Electrochemistry of the metallo-bisfullerene [Mo(η^2-C_{60})$_2$(CO)$_2$(dbc-bipy)] (dbc-bipy=4,4′-di(butylcarboxyl)-2,2′-bipyridine). *C. R. Chim.* **2005,** *8* (9-10), 1655-1659.

51. Sheu, J. H.; Su, M. D., Computational study of cycloaddition reactions of 16-electron d^8 ML_4 complexes with C_{60}. *J. Phys. Chem. A* **2011,** *115* (26), 7664-7672.

52. Fagan, P. J.; Calabrese, J. C.; Malone, B., The chemical nature of buckminsterfullerene (C_{60}) and the characterization of a platinum derivative. *Science* **1991,** *252* (5009), 1160-1161.

53. Bashilov, V. V.; Petrovskii, P. V.; Sokolov, V. I.; Lindeman, S.; Guzey, I.; Struchkov, Y. T., Synthesis, crystal, and molecular structure of the palladium(0)-fullerene derivative $(\eta^2\text{-}C_{60})Pd(PPh_3)_2$. *Organometallics* **1993,** *12* (4), 991-992.

54. Lee, K.; Hsu, H.-F.; Shapley, J. R., Coordination of C_{60} to penta-and hexaruthenium cluster frames. *Organometallics* **1997,** *16* (18), 3876-3877.

55. Ikeda, A.; Kameno, Y.; Nakao, Y.; Sato, H.; Sakaki, S., Binding energies and bonding nature of $M_x(CO)(Ph_3)_2(C_{60})$(M= Rh or Ir; x= H or Cl): Theoretical study. *J. Organomet. Chem.* **2007,** *692* (1-3), 299-306.

56. Han, Y.-K.; Kim, K. H.; Kim, J. C.; Park, B. K.; Park, J. T., [60]fullerene-metal cluster complexes: Understanding novel η^1 and $\eta^{2[6:5]}$ bonding modes of metallofullerenes. *Eur. J. Inorg. Chem.* **2010,** *2010* (10), 1530-1535.

57. Song, H.; Lee, K.; Choi, M.-G.; Park, J. T., [C_{60}] fullerene as a versatile four-electron donor ligand. *Organometallics* **2002,** *21* (9), 1756-1758.

58. Gal'pern, E. G.; Gambaryan, N. P.; Stankevich, I. V.; Chistyakov, A. L., Fullerene C_{60} as a η^5- and η^6-ligand in sandwich-type π-complexes with transition metals. *Russ. Chem. Bull.* **1994,** *43* (4), 547-550.

59. Chistyakov, A. L.; Stankevich, I. V., Cyclopentadienyl type η^5-π-complexes of C_{60} fullerene derivatives with indium and thallium: Simulation of molecular and electronic structure by the MNDO/PM_3 method of C_{60} fullerene derivatives with indium and thallium: Simulation of molecular and electronic structure by the MNDO/PM_3 method. *Russ. Chem. Bull.* **1997,** *46* (11), 1832-1837.

60. Fan, J.; Wang, Y.; Blake, A. J.; Wilson, C.; Davies, E. S.; Khlobystov, A. N.; Shroder, M., Controlled assembly of silver(I)-pyridylfullerene networks. *Angew. Chem., Int. Ed.* **2007,** *46*, 8013-8016.

61. Gal'pern, E. G.; Sabirov, A. R.; Novikov, Y. N.; Stankevich, I. V., Modeling of the molecular and electronic structures of some mono- and biosmium complexes of fullerene C_{60}. *Russ. Chem. Bull.* **2011,** *60*, 1556-1563.

62. Matsuo, Y.; Maruyama, M.; Gayathri, S. S.; Uchida, T.; Guldi, D. M.; Kishida, H.; Nakamura, A.; Nakamura, E., π-conjugated multidonor/acceptor arrays of fullerene-cobaltadithiolene -tetrathiafulvalene: From synthesis and structure to electronic interactions. *J. Am.Chem. Soc.* **2009,** *131*, 12643-12649.

63. Maruyama, M.; Guo, J.-D.; Nagase, S.; Nakamura, E.; Matsuo, Y., Isolation of planar four-membered aromatic systems by using confined spaces of cobalt pentaaryl[60]fullerene complexes. *J. Am. Chem. Soc.***2011,** *133*, 6890-6893.

64. Maruyama, M.; Koenig, M.; Guldi, D. M.; Nakamura, E.; Matsuo, Y., Reactivity of a metastable cobalt(III) trisulfide complex: Multiple C-H functionalization of *p*-xylene and disulfides to afford photofunctional cobalt complexes. *Angew. Chem., Int. Ed.* **2013,** *52*, 3015-3018.

65. Matsuo, Y.; Ogumi, K.; Maruyama, M.; Nakagawa, T., Divergent synthesis and tuning of the electronic structures of cobalt-dithiolene-fullerene complexes for organic solar cells. *Organometallics* **2014,** *33*, 659-664.

66. Zhong, Y.-W.; Matsuo, Y.; Nakamura, E., Chiral ruthenium-allenylidene complexes that bear a fullerene cyclopentadienyl ligand: Synthesis, characterization, and remote chirality transfer. *Chem. - Asian J.* **2007,** *2*, 358-366.

67. Matsuo, Y.; Tahara, K.; Fujita, T.; Nakamura, E., Di- and trinuclear [70]fullerene complexes: Syntheses and metal-metal electronic interactions. *Angew. Chem., Int. Ed.* **2009,** *48*, 6239-6241.

68. Matsuo, Y.; Park, B. K.; Mitani, Y.; Zhong, Y.-W.; Maruyama, M.; Nakamura, E., Synthesis of ruthenium pentamethyl[60]fullerene complexes bearing monodentate diphenylphosphino-methane, -ferrocene, and -butane ligands. *Bull. Korean Chem. Soc.* **2010,** *31*, 697-699.

69. Matsuo, Y.; Uematsu, T.; Nakamura, E., Synthesis and catalytic activity of η^1-allyl and η^3-allyl, ethyl, and hydrido complexes of ruthenium-pentamethyl[60]fullerene. *Eur. J. Inorg. Chem.* **2007,** 2729-2733.

70. Han, Y. K.; Kim, K. H.; Kim, J. C.; Park, B. K.; Park, J. T., [C_{60}] fullerene–metal cluster complexes: Understanding novel η^1 and $\eta^{2[6:5]}$ bonding modes of metallofullerenes. *Eur. J. Inorg. Chem.* **2010,** *2010* (10), 1530-1535;

71. Song, H.; Lee, K.; Lee, C. H.; Park, J. T.; Chang, H. Y.; Choi, M. G., First example of the μ^3-η^1-,η^2-,η^1-C_{60} bonding mode: Ligand-induced conversion of π to σ C_{60}-metal complexes. *Angew. Chem.* **2001,** *113* (8), 1548-1550

72. Oprunenko, Y. F.; Gloriozov, I. P., A study of dynamic behavior of transition metal complexes with fullerene C_{60} using density function theory. *J. Organomet. Chem.* **2013,** *732*, 116-121.

73. Konarev, D. V.; Khasanov, S. S.; Otsuka, A.; Saito, G.; Lyubovskaya, R. N., Effect of the Co-C(C_{60}-) bond formation on magnetic properties of the ionic complex {cryptand [2,2,2](Na^+)}{$Co^{II}TPP(C_{60}^-)$}($C_6H_4Cl_2$)$_2$. *Dalton Trans.* **2009,** *32*, 6416-6420.

74. Halim, M.; Kennedy, R. D.; Suzuki, M.; Khan, S. I.; Diaconescu, P. L.; Rubin, Y., Complexes of gold(I), silver(II), and copper(I) with pentaaryl [60]fullerides. *J. Am. Chem. Soc.* **2011,** *133* (17), 6841-6851.

75. Peng, P.; Li, F.-F.; Bowles, F. L.; Neti, V. S. P. K.; Metta-Magana, A. J.; Olmstead, M. M.; Balch, A. L.; Echegoyen, L., High yield synthesis of a new fullerene linker and its use in the formation of a linear coordination polymer by silver complexation. *Chem. Commun.* **2013,** *49*, 3209-3211.

76. Bowles, F. L.; Olmstead, M. M.; Balch, A. L., Preparation and crystallographic characterization of C_{60}{η^1-Ru(CO)$_2$(η^5-C_5H_5)}$_2$: A locally crowded organometallic fullerene without the usual η^2-bonding. *J. Am. Chem. Soc.* **2014,** *136*, 3338-3341.

77. Rogers, J. R.; Marynick, D. S., Theoretical estimates of the η^6 bonding capability of buckminsterfullerene in transition metal complexes. *Chem. Phys.Lett.* **1993,** *205*, 197-199.

78. Salcedo, R., Fullerenocene. *Polyhedron* **2009,** *28*, 431-436.

79. Molina, B.; Perez-Manriquez, L.; Salcedo, R., On the π coordination of organometallic fullerene complexes. *Molecules* **2011,** *16*, 4652-4659.

80. (a) Zhu, L.; Zhang, T.; Yi, M.; Wang, J., Ab initio study on mixed inorganic/organic ligand sandwich clusters: $BzTMC_{60}$, TM = Sc-Co. *J. Phys. Chem. A* **2010,** *114*, 9398-403; (b) Yang, Z.; Zhang, B.; Liu, X.; Yang, Y.; Li, X.; Xiong, S.; Xu, B., The structural and optical properties of the $CPTMC_{60}$ (TM = Sc-Fe) sandwich cluster. *J. Phys. B: At., Mol. Opt. Phys.* **2013,** *46*, 035101/1-035101/7.

81. Gal'pern, E. G.; Sabirov, A. R.; Stankevich, I. V., C_{60} fullerene as an η^6 ligand in π complexes of transition metals. *Phys. Solid State* **2007,** *49*, 2330-2334.

82. Zhang, X.; Wang, J.; Zeng, X. C., Ab initio study of structural, electronic, and magnetic properties of $V_n(C_{60})_m$ complexes. *J. Phys. Chem. A* **2009,** *113* (18), 5406-5413.

83. Ivanova, V., Fullerene compounds with transition metals M_nC_{60}: Preparation, structure, and properties. *J. Struct. Chem.* **2000,** *41* (1), 135-148.

84. Nagashima, H.; Nakaoka, A.; Saito, Y.; Kato, M.; Kawanishi, T.; Itoh, K., $C_{60}Pd_n$: The first organometallic polymer of buckminsterfullerene. *J. Chem. Soc., Chem. Commun.* **1992,** 377-379.

85. Cowley, J.; Liu, M.; Ramakrishna, B.; Peace, T.; Wertsching, A.; Pena, M., A new type of metal-fulleride structure: $C_{60}Pd_3$. *Carbon* **1994,** *32* (4), 746-748.

86. Nagashima, H.; Kato, Y.; Yamaguchi, H.; Kimura, E.; Kawanishi, T.; Kato, M.; Saito, Y.; Haga, M.; Itoh, K., Synthesis and reactions of organoplatinum compounds of C_{60}, $C_{60}Pt_n$. *Chem. Lett.* **1994,** (7), 1207-1210.

87. Wijnkoop, M.; Meidine, M.; Avent, A.; Darwish, A.; Kroto, H.; Walton, D. M., Platinum(0)–[60] fullerene complexes with chelating diphosphine ligands. Syntheses and characterisation of $[Pt(\eta^2\text{-}C_{60})(l\text{-}l)][l\text{-}l= Ph_2 P(CH_2)_nPPh_2$, n= 2 or 3]. *J. Chem. Soc., Dalton Trans.* **1997,** (4), 675-678.

88. (a) Li, J.; Schreckenbach, G.; Ziegler, T., A reassessment of the first metal-carbonyl dissociation energy in $M(CO)_4$ (M= Ni,Pd, Pt), $M(CO)_5$(M= Fe, Ru, Os), and $M(CO)_6$ (M= Cr, Mo, W) by a quasirelativistic density functional method. *J. Am. Chem. Soc.* **1995,** *117* (1), 486-494; (b) Ehlers, A. W.; Frenking, G., Structures and bond energies of the transition-metal carbonyls $M(CO)_5$ (m= Fe, Ru, Os) and $M(CO)_4$ (m= Ni, Pd, Pt). *Organometallics* **1995,** *14* (1), 423-426.

89. Douthwaite, R. E.; Green, M. L.; Stephens, A. H.; Turner, J. F., Transition metal-carbonyl,-hydrido and-η-cyclopentadienyl derivatives of the fullerene C_{60}. *J. Chem. Soc., Chem. Commun.* **1993,** (19), 1522-1523.

90. Wohlers, M.; Herzog, B.; Belz, T.; Bauer, A.; Braun, T.; Rühle, T.; Schlögl, R., Ruthenium-C_{60} compounds: Properties and catalytic potential. *Synth. Met.* **1996,** *77* (1), 55-58.

91. (a) Lavrentiev, V.; Abe, H.; Naramoto, H.; Sakai, S.; Narumi, K., Polymeric chains in C_{60} and Co mixture. *Chem. Phys. Lett.* **2006,** *424* (1-3), 101-104; (b) Lavrentiev, V.; Abe, H.; Yamamoto, S.; Naramotoand, H.; Narumi, K., Co and C_{60} interaction under conditions of mixture. *Mol. Cryst. Liq. Crys.* **2002,** *386* (1), 139-143.

92. Branz, W.; Billas, I.; Malinowski, N.; Tast, F.; Heinebrodt, M.; Martin, T., Cage substitution in metal-fullerene clusters. *J. Chem. Phys.* **1998,** *109* (9), 3425-3430.

93. Hou, J.; Wang, Y.; Xu, W.; Zhang, S.; Jian, Z.; Zhang, Y., Synthesis and characterization of Ag-C_{60} nanostructure film. *Appl. Phys. Lett.* **1997,** *70*, 3110-3112.

94. (a) Balch, A. L.; Costa, D. A.; Winkler, K., Formation of redox-active, two-component films by electrochemical reduction of C_{60} and transition metal complexes. *J. Am. Chem. Soc.* **1998,** *120* (37), 9614-9620; (b) Winkler, K.; de Bettencourt-Dias, A.; Balch, A. L., Charging processes in electroactive C_{60}/Pd films: Effect of solvent and supporting electrolyte. *Chem. Mater.* **1999,** *11* (8), 2265-2273; (c) Winkler, K.; de Bettencourt-Dias, A.; Balch, A. L., Electrochemical studies of C_{60}/Pd films formed by the reduction of C_{60} in the presence of palladium(II) acetate trimer. Effects of varying C_{60}/Pd(II) ratios in the precursor solutions. *Chem. Mater.* **2000,** *12* (5), 1386-1392; (d) Hayashi, A.; de Bettencourt-Dias, A.; Winkler, K.; Balch, A. L., Redox-active films formed by electrochemical reduction of solutions of C_{60} and platinum complexes. *J. Mater. Chem.* **2002,** *12* (7), 2116-2122.

95. Winkler, K.; Noworyta, K.; de Bettencourt-Dias, A.; Sobczak, J. W.; Wu, C.-T.; Chen, L.-C.; Kutner, W.; Balch, A. L., Structure and properties of C_{60}-Pd films formed by electroreduction of C_{60} and palladium(II) acetate trimer: Evidence for the presence of palladium nanoparticles. *J. Mater. Chem.* **2003,** *13* (3), 518-525.

96. Talyzin, A. V.; Dzwilewski, A.; Pudelko, M., Formation of palladium fullerides and their thermal decomposition into palladium nanoparticles. *Carbon* **2007,** *45* (13), 2564-2569.

97. Wågberg, T.; Jacobsson, P.; Sundqvist, B., Comparative Raman study of photopolymerized and pressure-polymerized C_{60} films. *Phys. Rev. B* **1999,** *60* (7), 4535.

98. Herbst, M. H.; Pinhal, N. M.; Demétrio, F. A.; Dias, G. H.; Vugman, N. V., Solid-state structural studies on amorphous platinum-fullerene [60] compounds [Pt_nC_{60}](n= 1, 2). *J. Non-Cryst. Solids* **2000,** *272* (2), 127-130.

99. Talyzin, A. V.; Jansson, U., A comparative raman study of some transition metal fullerides. *Thin Solid Films* **2003,** *429* (1-2), 96-101.

100. (a) Martin, M. C.; Koller, D.; Mihaly, L., In situ infrared transmission study of Rb-and K-doped fullerenes. *Phys. Rev. B* **1993,** *47* (21), 14607; (b) Martin, M. C.; Koller, D.; Rosenberg, A.; Kendziora, C.; Mihaly, L., Infrared and raman evidence for dimers and polymers in RbC_{60}. *Phys. Rev. B* **1995,** *51* (5), 3210-3213.

101. Chernov, V.; Ivanova, V.; Kozhevnikova, A.; Mardezhova, G.; Nikitenko, S.; Nikiforov, A., Exafs study of the organometallic polymers Pd_nC_{60} structure. *Nuclear Instruments and Methods in Physics Research Section A: Accelerators, Spectrometers, Detectors and Associated Equipment* **1995,** *359* (1), 250-253.

102. Saha, D.; Deng, S., Hydrogen adsorption on Pd-and Ru-doped C_{60} fullerene at an ambient temperature. *Langmuir* **2011,** *27* (11), 6780-6786.

103. Brust, M.; Kiely, C. J.; Bethell, D.; Schiffrin, D. J., C_{60} mediated aggregation of gold nanoparticles. *J. Am. Chem. Soc.***1998,** *120*, 12367-12368.

104. Liu, J.; Alvarez, J.; Ong, W.; Kaifer, A. E., Network aggregates formed by C_{60} and gold nanoparticles capped with γ-cyclodextrin hosts. *Nano Lett.* **2001,** *1* (2), 57-60.

105. Li, B.; Li, H.; Xu, Z., Experimental evidence for the interface interaction in Ag/C_{60} nanocomposite catalyst and its crucial influence on catalytic performance. *J. Phys. Chem. C* **2009,** *113* (52), 21526-21530.

106. Pierrat, P.; Vanderheiden, S.; Muller, T.; Brase, S., Functionalization of hexakis methanofullerene malonate crown-ethers: Promising octahedral building blocks for molecular networks. *Chem. commun.* **2009,** (13), 1748-50.

107. Afreen, S.; Muthoosamy, K.; Manickam, S.; Hashim, U., Functionalized fullerene (C_{60}) as a potential nanomediator in the fabrication of highly sensitive biosensors. *Biosens. Bioelectron.* **2015,** *63*, 354-364.

108. Fujihara, H.; Nakai, H., Fullerenethiolate-functionalized gold nanoparticles: A new class of surface-confined metal-C_{60} nanocomposites. *Langmuir* **2001,** *17* (21), 6393-6395.

109. Sudeep, P.; Ipe, B. I.; Thomas, K. G.; George, M.; Barazzouk, S.; Hotchandani, S.; Kamat, P. V., Fullerene-functionalized gold nanoparticles. A self-assembled photoactive antenna-metal nanocore assembly. *Nano Lett.* **2002,** *2* (1), 29-35.

110. Hirayama, D.; Takimiya, K.; Aso, Y.; Otsubo, T.; Hasobe, T.; Yamada, H.; Imahori, H.; Fukuzumi, S.; Sakata, Y., Large photocurrent generation of gold electrodes modified with [60] fullerene-linked oligothiophenes bearing a tripodal rigid anchor. *J. Am. Chem. Soc.* **2002,** *124* (4), 532-533.

111. Shon, Y.-S.; Choo, H., [60] fullerene-linked gold nanoparticles: Synthesis and layer-by-layer growth on a solid surface. *Chem. Commun.* **2002,** (21), 2560-2561.

112. Lu, F.; Xiao, S.; Li, Y.; Song, Y.; Liu, H.; Li, H.; Zhuang, J.; Liu, Y.; Gan, L.; Zhu, D., Fullerene-functionalized gold core–shell nanoparticles: Preparation and optical limiting properties. *Inorg.Chem. Commun.***2004,** *7* (8), 960-962.

113. Piotrowski, P.; Pawłowska, J.; Pawłowski, J.; Więckowska, A.; Bilewicz, R.; Kaim, A., Nanostructured films of in situ deprotected thioacetyl-functionalized C_{60}-fullerenes on a gold surface. *J. Mater. Chem. A* **2014,** *2* (7), 2353-2362.

114. Zhang, P.; Li, J.; Liu, D.; Qin, Y.; Guo, Z.-X.; Zhu, D., Self-assembly of gold nanoparticles on fullerene nanospheres. *Langmuir* **2004,** *20* (4), 1466-1472.

115. Lim, I. I. S.; Ouyang, J.; Luo, J.; Wang, L.; Zhou, S.; Zhong, C.-J., Multifunctional fullerene-mediated assembly of gold nanoparticles. *Chem. Mater.* **2005,** *17* (26), 6528-6531.

116. Lim, I.-I. S.; Pan, Y.; Mott, D.; Ouyang, J.; Njoki, P. N.; Luo, J.; Zhou, S.; Zhong, C.-J., Assembly of gold nanoparticles mediated by multifunctional fullerenes. *Langmuir* **2007,** *23* (21), 10715-10724.

117. Lim, I.-I. S.; Ouyang, J.; Luo, J.; Wang, L.; Zhou, S.; Zhong, C.-J., Multifunctional fullerene-mediated assembly of gold nanoparticles. *Chem. Mater.* **2005,** *17* (26), 6528-6531.

118. Rousseau, G.; Lavenn, C.; Cardenas, L.; Loridant, S.; Wang, Y.; Hahn, U.; Nierengarten, J.-F.; Demessence, A., One-pot synthesis of sub-3 nm gold nanoparticle networks connected by thio-based multidentate fullerene adducts. *Chem. Commun.* **2015,** *51* (31), 6730-6733.

119. (a) Miyazawa, K.; Kuwasaki, Y.; Obayashi, A.; Kuwabara, M., C_{60} nanowhiskers formed by the liquid-liquid interfacial precipitation method. *J. Mater. Res.* **2002,** *17* (01), 83-88; (b) Sathish, M.; Miyazawa, K. i., Size-tunable hexagonal fullerene (C_{60}) nanosheets at the liquid-liquid interface. *J. Am. Chem. Soc.* **2007,** *129* (45), 13816-13817; (c) Sathish, M.; Miyazawa, K. i.; Hill, J. P.; Ariga, K., Solvent engineering for shape-shifter pure fullerene (C_{60}). *J. Am. Chem. Soc.* **2009,** *131* (18), 6372-6373; (d) Shrestha, L. K.; Yamauchi, Y.; Hill, J. P.; Miyazawa, K. i.; Ariga, K., Fullerene crystals with bimodal pore architectures consisting of macropores and mesopores. *J. Am. Chem. Soc.* **2012,** *135* (2), 586-589.

120. Tan, Z.; Masuhara, A.; Ohara, S.; Kasai, H.; Nakanishi, H.; Oikawa, H., Facile deposition of gold nanoparticles on C_{60} microcrystals with unique shapes. *J. Nanopart. Res.* **2013,** *15* (11), 1-10.

121. Chong, L. C.; Stolojan, V.; Wagner, G.; Silva, S. R. P.; Curry, R. J., One-pot rapid low-cost synthesis of Pd-fullerite catalysts. *J. Mater. Chem.* **2008,** *18* (40), 4808-4813.

122. Niemeyer, J.; Erker, G., Fullerene-mediated activation of dihydrogen: A new method of metal-free catalytic hydrogenation. *ChemCatChem* **2010,** *2* (5), 499-500.

123. Coq, B.; Planeix, J. M.; Brotons, V., Fullerene-based materials as new support media in heterogeneous catalysis by metals. *Appl. Catal., A* **1998,** *173* (2), 175-183.

124. Serp, P.; Figueiredo, J. L., *Carbon materials for catalysis*. John Wiley & Sons: 2009.

125. Malhotra, R.; Hirschon, A.; McMillen, D.; Bell, W. In *Catalytic properties of fullerene materials*, MRS Proceedings, Cambridge Univ Press: 1997; p 137.

126. Stetzer, M.; Heiney, P.; Fischer, J.; McGhie, A., Thermal stability of solid C_{60}. *Phys. Rev. B* **1997,** *55* (1), 127-131.

127. Pupysheva, O. V.; Farajian, A. A.; Yakobson, B. I., Fullerene nanocage capacity for hydrogen storage. *Nano lett.* **2007,** *8* (3), 767-774.

128. Schur, D. V.; Zaginaichenko, S. Y.; Savenko, A. F.; Bogolepov, V. A.; Anikina, N. S.; Zolotarenko, A.; Matysina, Z. A.; Veziroglu, T. N.; Skryabina, N. E., Experimental evaluation of total hydrogen capacity for fullerite C_{60}. *Int. J. Hydrogen Energy* **2011,** *36* (1), 1143-1151.

129. Zhao, Y.; Kim, Y.-H.; Dillon, A.; Heben, M.; Zhang, S., Hydrogen storage in novel organometallic buckyballs. *Phys. Rev. Lett.* **2005,** *94* (15), 155504-1/155504-4.

130. Chandrakumar, K.; Ghosh, S. K., Alkali-metal-induced enhancement of hydrogen adsorption in C_{60} fullerene: An ab initio study. *Nano Lett.* **2008,** *8* (1), 13-19.

131. Lebedeva, M. A.; Chamberlain, T. W.; Khlobystov, A. N., Harnessing the synergistic and complementary properties of fullerene and transition-metal compounds for nanomaterial applications. *Chem. Rev.* **2015,** *115* (20), 11301-11351.

132. Pacosová, L.; Kartusch, C.; Kukula, P.; van Bokhoven, J. A., Is fullerene a nonmetal catalyst in the hydrogenation of nitrobenzene? *ChemCatChem* **2011,** *3* (1), 154-156.

133. Niemeyer, J.; Erker, G., Fullerene-mediated activation of dihydrogen: A new method of metal-free catalytic hydrogenation. *ChemCatChem* **2010,** *2* (5), 499-500.

134. Keypour, H.; Noroozi, M.; Rashidi, A.; Shariati Rad, M., Application of response surface methodology for catalytic hydrogenation of nitrobenzene to aniline using ruthenium supported fullerene nanocatalyst. *Iranian Journal of Chemistry and Chemical Engineering (IJCCE)* **2015,** *34* (1), 21-32.

135. Lashdaf, M.; Hase, A.; Kauppinen, E.; Krause, A., Fullerene-based ruthenium catalysts in cinnamaldehyde hydrogenation. *Catal. Lett.* **1998,** *52* (3-4), 199-204.

136. Nagashima, H.; Nakaoka, A.; Tajima, S.; Saito, Y.; Itoh, K., Catalytic hydrogenation of olefins and acetylenes over $C_{60}Pd_n$. *Chem. Lett.* **1992,** (7), 1361-1364.

137. Sulman, E.; Matveeva, V.; Semagina, N.; Yanov, I.; Bashilov, V.; Sokolov, V., Catalytic hydrogenation of acetylenic alcohols using palladium complex of fullerene C_{60}. *J. Mol. Catal. A: Chem.* **1999,** *146* (1), 257-263.

138. Serizawa, S.; Gabrielova, I.; Fujimoto, T.; Shido, T.; Ichikawa, M., Catalytic behaviour of alkali-metal fullerides, $C_{60}M_6$ and $C_{70}M_6$ (M= Cs, K, Na), in H_2-D_2 exchange and olefin hydrogenation. *J. Chem. Soc., Chem. Commun.* **1994,** (7), 799-800.

139. Chen, P.; Wu, X.; Lin, J.; Tan, K., High H_2 uptake by alkali-doped carbon nanotubes under ambient pressure and moderate temperatures. *Science* **1999,** *285* (5424), 91-93.

140. Méndez-Camacho, R.; Guirado-López, R., Adsorption and diffusion of hydrogen on C_{60}-supported Pt_n clusters. *J. Phys.Chem. C* **2013,** *117* (19), 10059-10069.

141. Becker, L.; Evans, T. P.; Bada, J. L., Synthesis of [hydrogenated fullerene] $C_{60}H_2$ by rhodium-catalyzed hydrogenation of C_{60}. *J. Org. Chem.* **1993,** *58* (27), 7630-7631.

142. Yu, R.; Liu, Q.; Tan, K.-L.; Xu, G.-Q.; Ng, S. C.; Chan, H. S.; Hor, T. A., Preparation, characterisation and catalytic hydrogenation properties of palladium supported on C_{60}. *J. Chem. Soc., Faraday Trans.* **1997,** *93* (12), 2207-2210.

143. Braun, T.; Wohlers, M.; Belz, T.; Nowitzke, G.; Wortmann, G.; Uchida, Y.; Pfänder, N.; Schlögl, R., Fullerene-based ruthenium catalysts: A novel approach for anchoring metal to carbonaceous supports. I. Structure. *Catal. Lett.* **1997,** *43* (3-4), 167-173.

144. Braun, T.; Wohlers, M.; Belz, T.; Schlögl, R., Fullerene-based ruthenium catalysts: A novel approach for anchoring metal to carbonaceous supports. II. Hydrogenation activity. *Catal. Lett.* **1997,** *43* (3-4), 175-180.

Chapter 2 Synthesis and characterization of Ru@C_{60} nanostructures

Part of the work descrided in chapter 2 has been published in: F. Leng; I. C. Gerber; P. Lecante; W. Bacsa; J. Miller; J. R. Gallagher; S. Moldovan; M. Girleanu; M. R. Axet and P. Serp, Synthesis and structure of ruthenium-fullerides, *RSC Adv*., **2016**, *6*, 69135-69148

2.1 Introduction

Extensive investigations of fullerene C_{60}, both in its pristine form as well as in its doped or intercalated variants, have definitively confirmed the strong tendency toward polymerization of this molecule.[1] The combination of fullerenes and metals offers exciting perspectives for the production of novel fullerene-based architectures with unprecedented properties for catalysis,[2] batteries,[3] sensors[4] or nanoelectronic devices.[5] The metal fullerides have been the subject of intensive investigations over the past 20 years and mostly compounds of C_{60} with alkali and alkaline metals (AC_{60}) have been synthesized.[6] Metals in these compounds usually occupy interstitial sites in the octahedral or tetrahedral holes of the C_{60} structure. The bonding in these fullerides is ionic and the C_{60} molecules rotate free. Li_4C_{60}, one of the best representatives of lithium intercalated fullerides, features an unusual type of two-dimensional polymerization.[7] In contrast, only a few reports claiming the existence of fullerides with transition metals are known;[8] and despite the progress in the study of AC_{60} polymerization,[9] knowledge about this phenomenon in the transition metal-fullerene systems is scarce. Transition metal fullerides or organometallic fullerene derivatives can be prepared by chemical reactions in solution between a suitable metal complex and C_{60},[10] through electrochemical reduction from solutions of C_{60} and selected transition metal complexes,[11] or by co-evaporation of metal and C_{60} from separate sources under ultra-high vacuum (UHV) conditions.[12] Up to now, organometallic fullerene derivatives of Pd,[10] Pt,[13] Co,[14] Ru,[15] Fe,[16], Rh,[17] and Ti[12] have been reported. Although an understanding of the structure and bonding of the proposed compounds is highly desirable, the structure of these phases is still under discussion due to the poor crystallinity of the obtained samples, but it is believed that metal atoms serve as bridges connecting neighboring C_{60} molecules. Depending on the amount of metal, the suggested structure is polymeric with chain-like, two- or three-dimensional coordination.

The first and the most studied, organometallic fullerene derivatives, Pd_nC_{60}, was reported in 1992 by Nagashima *et al.*[10] This compound, insoluble in most organic solvents, precipitated by mixing $[Pd_2(dba)_3]$ (dba = dibenzylideneacetone) and C_{60} benzene solutions at room temperature. Two and three-dimensional amorphous polymeric structures were proposed already in early studies from electron probe microanalysis for Pd_nC_{60}, but the exact nature of these polymers remains unclear, and no systematic study of Pd_nC_{60} with various compositions is available in the literature. Additionally, various transmission electron microscopy (TEM) studies on the Pd_nC_{60} compound suggest the possible presence of Pd nanoparticles in the material.[18] The presence of metallic clusters was also evidenced for Ru_nC_{60} compounds produced at higher temperatures from $[Ru_3(CO)_{12}]$.[15, 19] An organo-soluble C_{60} hexaadduct bearing twelve thiocyanate functions has been successfully used as a stabilizing agent to assemble homogeneous 3 nm gold nanoparticles into extended tridimensional networks.[20] In addition, Lavrentiev *et al*. have observed the polymeric chains in the $ConC_{60}$ mixture using TEM, which inner structure has been evaluated as (-C_{60}-Co-C_{60}-) order.[21] It is worth mentioning that most of these structural studies have used single characterization techniques such as Raman spectroscopy,[16] X-ray photoelectron spectroscopy (XPS),[12] or TEM.[18a]

Theoretical studies, using Density Functional Theory (DFT), on exohedral fullerenes have been mainly devoted to the interaction between C_{60} and alkali atoms: Na, K,[22,23,24,25] and to a less extent with TM, mainly V,[26,30] Ni,[27] Au,[28,29] and Ta,[30,31] and more recently with Pd and Pt atoms.[32] To our knowledge, no theoretical studies on the existence or the possible structures of -C_{60}-TM-C_{60}- linear chains have been reported.

Considering the possible applications of these supramolecular architectures, it is of paramount importance to have a better knowledge of their structure for the establishment of structure/properties relationships. In this context, we decided to study the case of ruthenium. Ill-defined structures were reported for this metal, consisting in poorly dispersed Ru NPs

deposited on a C_{60} containing material.[12] In this chapter, we describe an original synthesis to produce well defined materials, which have been characterized with a large variety of complementary characterization techniques, including TEM in high resolution, scanning and electron tomography modes, attenuated total reflection infrared spectroscopy (ATR-IR), nuclear magnetic resonance (NMR), Raman spectroscopy, Wide-Angle X-Ray Scattering WAXS, Extended X-Ray Absorption Fine Structure (EXAFS) and XPS, as well as DFT calculations.

2.2 Results and discussion

Ru@C_{60} nanoarchitectures have been synthesized by decomposing [Ru(COD)(COT)] (COD = 1,5 cyclooctadiene, COT= 1,3,5-cyclooctatriene) in the presence of C_{60} under 3 bar of H_2 at room temperature.[33] The control of the reaction conditions allows to synthesize C_{60}-Ru-C_{60}-polymers, spherical Ru-C_{60} nanoparticles, and Ru NPs decorating nanospherical Ru-C_{60} polymer nanoparticles.

The effect of the solvent and the Ru/C_{60} ratio used during the reaction, on the nanostructures obtained have been studied in detail and is discussed below. The Ru@C_{60} nanostructures have been mainly characterized by microscopic techniques; however, in order to shed some light on the formation and nature of Ru-C_{60} interactions in some of the nanostructures synthesized, a large variety of complementary characterization techniques, including TEM in high resolution, scanning and electron tomography modes, IR, NMR, Raman, WAXS, EXAFS and XPS, as well as DFT calculations has been used. Scheme 2.1 shows the synthetic pathway; initially, [Ru(COD)(COT)] decomposes under dihydrogen and forms metallic atoms.

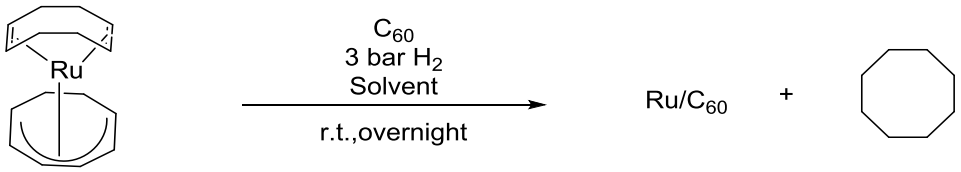

Scheme 2.1. Synthesis of Ru@C_{60} nanoarchitectures.

Then these atoms may either: i) nucleate as small Ru NPs in the presence of the C_{60} ligand (further, the NPs will grow bigger and become more thermodynamically stable); or ii) coordinate directly to C_{60}, so a Ru-C_{60} complex polymer compounds will be form instead of Ru NPs. Kinetic or thermodynamic control should dictate the course of the reaction (Table 2.1).

Table 2.1 Thermodynamic products based on either Ru-Ru bonds (Ru NPs) or Ru-C bonds (DFT calculations).

Systems	Energy gain (kcal/mol)
C_{60}-Ru	-48
$(C_{60})_2$-Ru	-92
$(C_{60})_3$-Ru	-103
…-C_{60}-Ru-C_{60}-…	-86
…-C_{60}-Ru_2-C_{60}-…	-94
…-C_{60}-Ru_3-C_{60}-…	-106
…-C_{60}-Ru_4-C_{60}-…	-76
Ru_{13}	-96
Ru_{55}	-123
Ru bulk	-153

Energy stabilization per Ru atom

From the thermodynamic point of view, DFT calculations performed on different systems involving either Ru-Ru bonds (Ru NPs) or Ru-C bonds (Ru molecular or polymeric species)

clearly show that the preferred tendency is the formation of metal-metal bonds (Table 2.1), so the thermodynamic product of the reaction should consists in Ru NPs.

2.2.1 Solvent effect

First, we studied the effect of the solvent fixing the Ru/C_{60} ratio to 2/1. Several solvents were studied including toluene, chlorobenzene, 1,2-dichlorobenzene, dichloromethane, chloroform and decalin using the same dilutions with the exception of $CHCl_3$ and CH_2Cl_2, for which higher dilutions were used because of the low solubility of C_{60} in these solvents (see Table 2.2).[34]

As depicted in Table 2.2, the solubility of fullerene C_{60} depends on several solvent properties such as refraction, dielectric constant, molecular size and H-bonding. C_{60} have low solubility in polar or H-containing solvents, and increasing molar volume and solvent polarity will diminish the solubility of C_{60}, whereas electron pair donation ability and polarizability enhanced solubility. Initially, we choose the solvent based on these factors, so dichloromethane, chloroform, decalin, toluene, bromobenzene, and chlorobenzene were tested for the synthesis. The structure of Ru@C_{60} synthesized in different solvents is shown in Figure 2.1. TEM analyses of the Ru@C_{60} compounds show that the solvent has a significant effect on the synthesized nanostructures (Figures 2.1 and 2.2 and Table 2.3). When the synthesis was performed in decalin, structures with irregular shapes decorated with small Ru NPs (1.23 ± 0.22 nm) were obtained. Toluene led to smaller shapeless structures with mean diameters of *ca*. 175 nm. Spherical particles were obtained using chlorinated solvents: chlorobenzene (285 ± 3 nm), 1,2-dichlorobenzene (200 ± 3 nm), $CHCl_3$ (229 ± 1.5 nm), and CH_2Cl_2 (40 ± 0.7 nm). The nanospheres synthesized in CH_2Cl_2 shown a significantly smaller mean diameter and narrower size distribution. In addition, in CH_2Cl_2, these nanospheres were decorated with small Ru NPs (1.15 ± 0.02 nm).

Table 2.2. Solubility of fullerene in some organic solvents.[34-35]

Solvent	[C_{60}] mg/mL	Solvent	[C_{60}] mg/mL
n-pentane	0.005	benzene	1.7
decalins	4.6		
cis-decalin	2.2	toluene	2.8
trans- decalin	1.3		
dichloromethane	0.26	xylene	5.2
chloroform	0.16	bromobenzene	3.3
1,1,2,2-tetrachloroethane	5.3	chlorobenzene	7.0
methanol	0.000	1,2-dichlorobenzene	27
acetone	0.001	tetrahydrofuran	0.000

The HREM analyses (Figure 2.2) confirmed that the structures synthesized in toluene and 1,2-dichlorobenzene do not contain Ru NPs. STEM-EDX mappings of the structures synthesized in toluene, 1,2-dichlorobenzene and dichloromethane confirm that they are composed of Ru and C even if Ru NPs are not observed (Figure 2.3).

The absence of metal nanoparticles in several nanostructures synthesized pointed out the possible formation of C_{60}-Ru-C_{60}- polymers, as previously suggested for Pd_nC_{60} compounds.[10] It is known that polymeric spheres of uniform size can be produced using mechanical methods.[37] The mechanism of formation of such spheres consists in three steps: in the first step the polymers form long threads, which in a second time break up into smaller droplets of uniform size due to Rayleigh instability. The resulting droplets can again break up into daughter droplets, however, this third step is much slower and not always observed. The size of the spheres is mainly determined by the applied stress, and weakly affected by the viscosity ratio between the dispersed and the continuous phases.[38] The polymer concentration is also an

important factor that affects the structure formation.[39] If we assume that all the Ru@C_{60} spheres are polymeric and present similar properties (*i.e.* viscosity), we can correlate the self-assembly of the polymer in spheres with the solvent viscosity and permittivity (Figure 2.4).

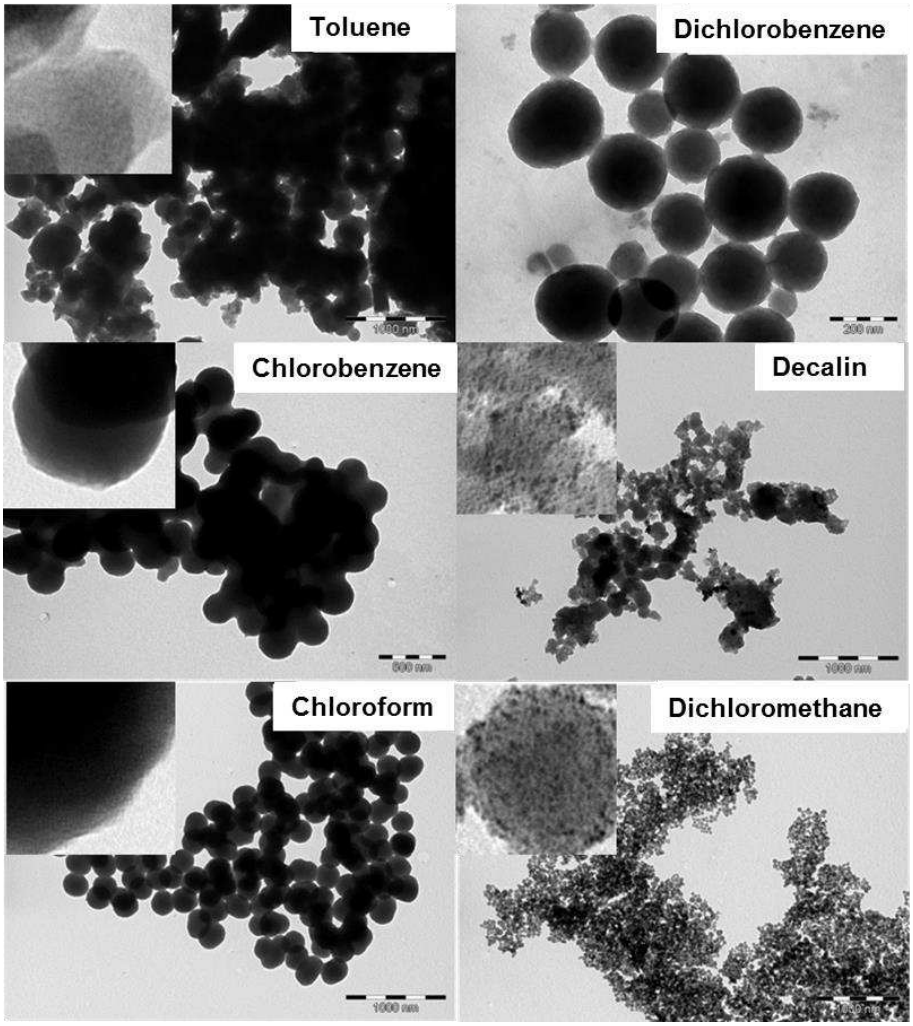

Figure 2.1. TEM micrographs of Ru@C_{60} structures with Ru/C_{60}=2/1 synthesized in different solvents: toluene (scale bar 1000 nm), dichlorobenzene (scale bar 200 nm), chlorobenzene (scale bar 500 nm), decalin (scale bar 1000 nm), chloroform (scale bar 1000 nm) and dichloromethane (scale bar 1000 nm).

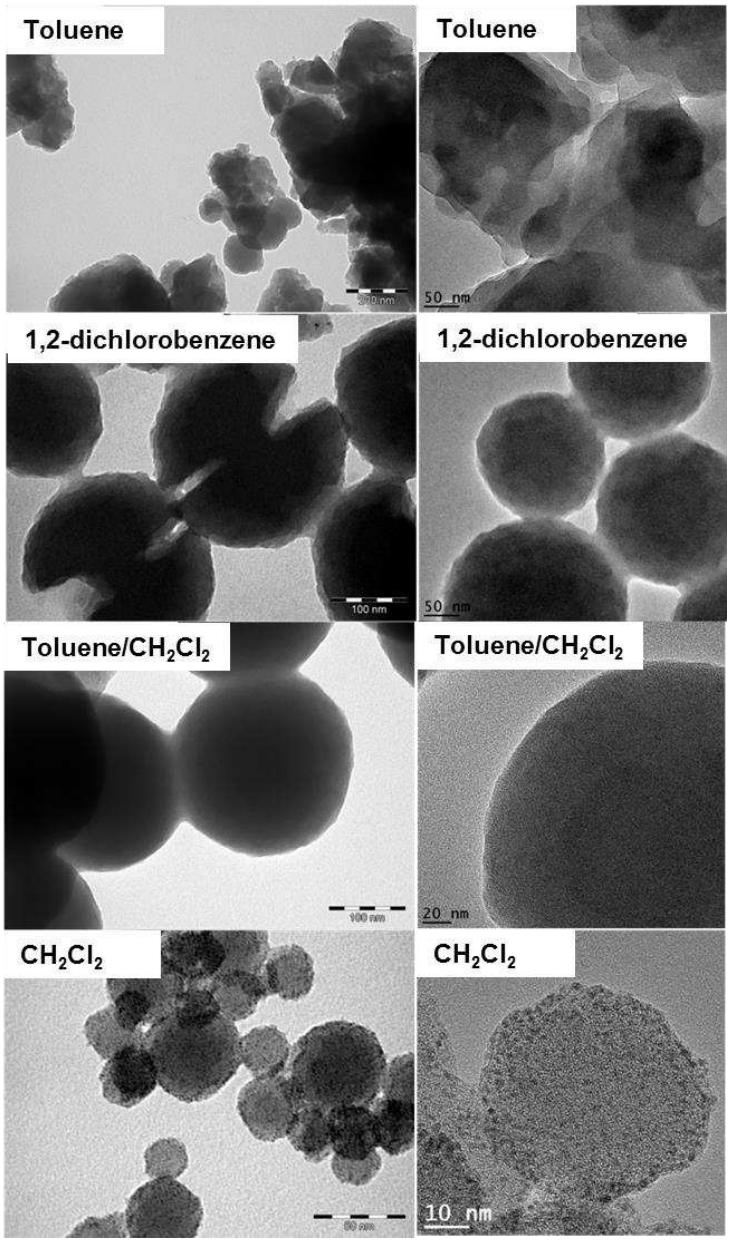

Figure 2.2. TEM (left) and HREM (right) micrographs of Ru@C_{60} assemblies (Ru/C_{60} = 2/1) produced in different solvent.

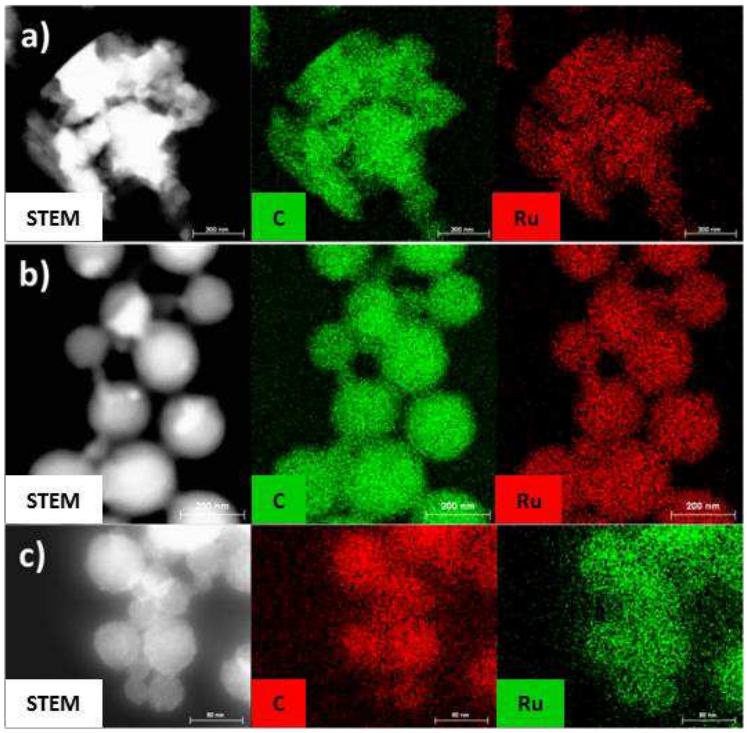

Figure 2.3. STEM-EDX mappings of Ru@C_{60} (2/1) structures synthesized in a) toluene (scale bar 300 nm); b) 1, 2-dichlorobenzene (scale bar 200 nm); and dichloromethane (scale bar 50 nm).

During the synthesis carried out in decalin, which has the higher viscosity and the lower permittivity (see Table 2.3), no shape control is achieved, while in CH_2Cl_2 (lower viscosity and high permittivity), small spherical particles are produced. The other solvents, showing intermediate viscosity, allow obtaining spheres as well, however, with larger mean diameters. The only exception is the nanomaterial synthesized in toluene, which has, as decalin, a low permittivity. Mixtures of solvents were also tested in order to corroborate this hypothesis. First, a mixture of solvents, 1, 2-dichlorobenzene and dichloromethane, was used in several ratios (Figure 2.5 and Table 2.4). The nanosphere size clearly decreases at higher CH_2Cl_2 concentration and correlate with the estimate viscosity of the solvent mixture (see Table 2.4), *i.e.* small nanospheres are obtained with lower viscosity of the solvent mixture.

Table 2.3. Solvent properties related to the TEM analyses obtained for the Ru@C_{60} structures.

Solvent	Viscosity (mPa.s)[36]	C_{60} solubility ([C_{60}], mg/mL)[34-35]	Relative permittivity (ε_r)[36]	TEM analyses
cis-decalin *trans*-decalin	3.042 1.948	4.6	2.22 2.18	no shape controlled structures decorated with Ru NP of 1.23 ± 0.22 nm
1,2-dichlorobenzene	1.324	27	10.12	spheres of 200 ± 3 nm
chlorobenzene	0.753	7	5.70	spheres of 285 ± 3 nm
toluene	0.560	2.8	2.38	no shape control of the structures of ca. 175 nm
chloroform	0.537	0.16	4.81	spheres of 229 ± 1.5 nm
dichloromethane	0.413	0.26	8.93	spheres of 39.6 ± 0.7 nm decorated with Ru NP 1.15 ± 0.02 nm
methanol	0.545	0	32.7	n.a.

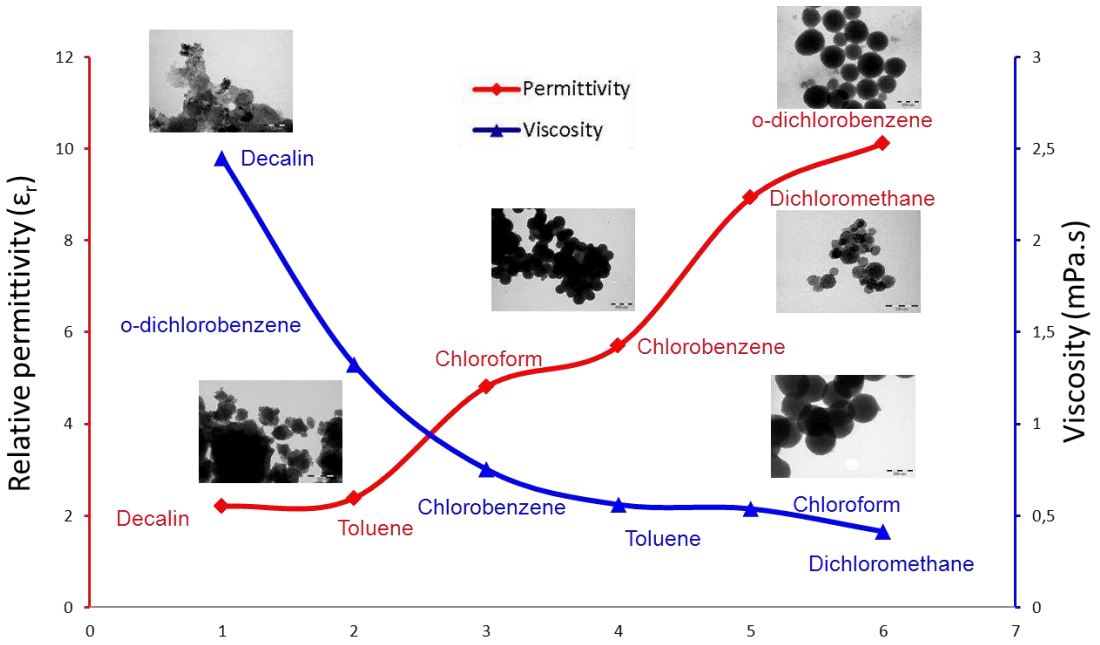

Figure 2.4. Effect of solvent viscosity and permittivity on Ru@C_{60} assemblies (Ru/C_{60} = 2/1). Reaction conditions: [Ru(COD)(COT)] 2.0 eq, C_{60} 1.0eq, solvent, 3 bar H_2, r.t., overnight.

Table 2.4. Solvent mixture viscosity related to the TEM analyses obtained for the Ru@C_{60} structures.

Solvent		Ratio	Viscosity (mPa.s)[36, a]	Relative permittivity (ε_r)[36, b]	TEM analyses
1,2-dichlorobenzene	-	-	0.753	10.12	spheres of 197.0 ± 1.9 nm
1,2-dichlorobenzene	CH_2Cl_2	95/5	0.73	10.1	spheres of 133.0 ± 1.9 nm
1,2-dichlorobenzene	CH_2Cl_2	17/83	0.46	9.1	spheres of 47.4 ± 0.7 nm
1,2-dichlorobenzene	CH_2Cl_2	9/91	0.44	9.0	spheres of 44.0 ± 1.4 nm
1,2-dichlorobenzene	CH_2Cl_2	2/98	0.42	8.9	spheres of 37.6 ± 0.7 nm
-	CH_2Cl_2	-	0.413	8.93	spheres of 39.6 ± 0.7 nm
Toluene	-	-	0.56	2.38	no shape control of the structures of *ca*. 175 nm
Toluene	CH_2Cl_2	50/50	0.48	5.6	spheres of 220.5 ± 3.4 nm
Toluene	CH_2Cl_2	25/75	0.45	7.3	spheres of 182.2 ± 1.8 nm
Toluene	CH_2Cl_2	9/91	0.43	8.3	spheres of 119.0 ± 1.8 nm
Toluene	MeOH	95/5	0.56	3.8	spheres of 214.7 ± 1.5 nm

[a]Estimated viscosity of the solvent mixture using the following equation: $v^{1/3}=x_a v_a^{1/3}+x_b v_b^{1/3}$ (v = viscosity, x = mass fraction)[40], [b]Estimated relative permittivity of the solvent mixture using the following equation: $\varepsilon=x_a\varepsilon_a+x_b\varepsilon_b$ (ε = permittivity, x = mass fraction) [41]

Interestingly, the mixture toluene/CH_2Cl_2 allows also obtaining nanospheres while the use of pure toluene led to shapeless structures. Here also, the decrease of the viscosity of the solvent mixture also induces a decrease of the sphere size (Figure 2.6 and Table 2.4). Finally, in order to understand the role of the solvent permittivity, methanol was used as co-solvent with toluene. The toluene/methanol 95/5 mixture displaying a similar viscosity than pure toluene but higher permittivity also allows to obtain nanospheres of 214 nm diameter (Figure 2.6), pointing out that permittivity plays a crucial role on the formation of the nanospheres.

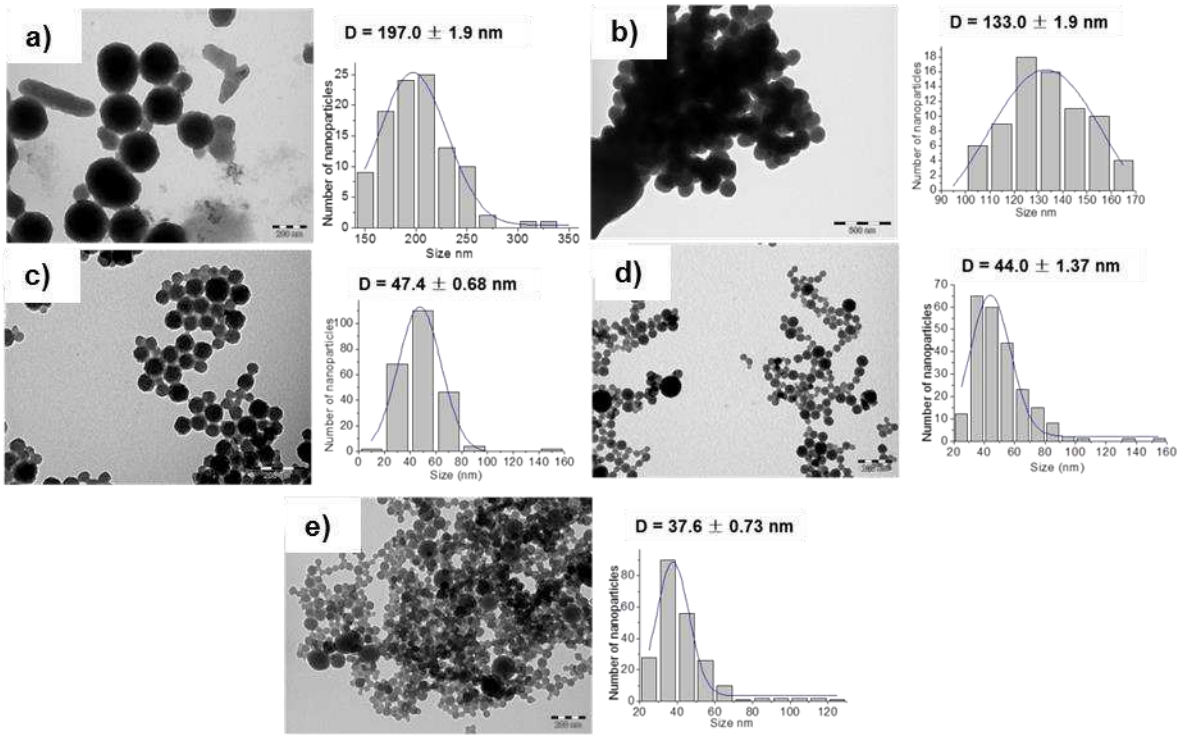

Figure 2.5 TEM micrographs of Ru@C_{60} structures with Ru/C_{60}=2/1 synthesized in a mixture of solvents: a) 1, 2-dichlorobenzene (scale bar 200 nm), b) 1, 2-dichlorobenzene/CH_2Cl_2 = 20/1 (scale bar 200 nm), c) o-dichlorobenzene/CH_2Cl_2 = 1/5 (scale bar 500 nm), d) *o*-dichlorobenzene/CH_2Cl_2 = 1/10 (scale bar 200 nm), and e) 1, 2-dichlorobenzene/CH_2Cl_2 = 1/50 (scale bar 200 nm).

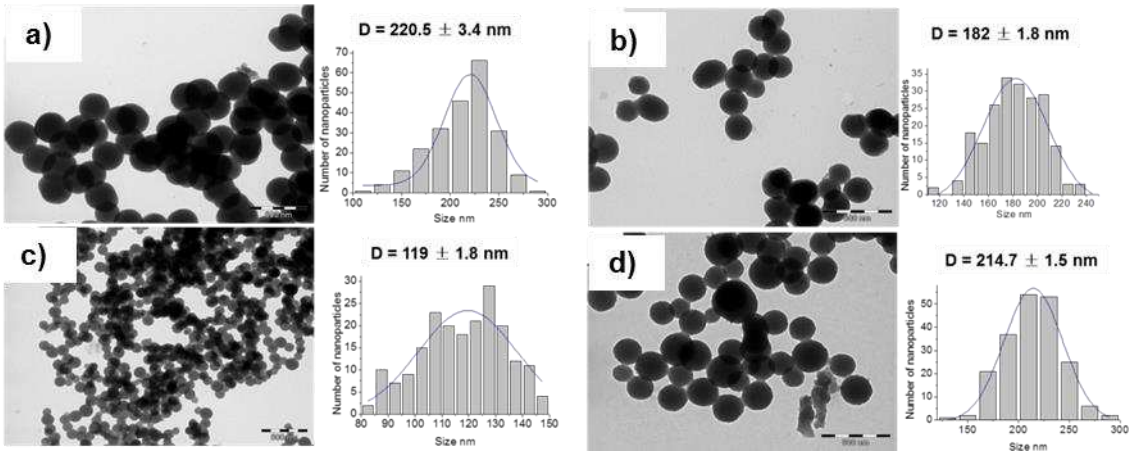

Figure 2.6. TEM micrographs of Ru@C_{60} structures with Ru/C_{60}=2/1 synthesized in a mixture of solvents: a) toluene/CH_2Cl_2 = 1/1 (scale bar 500 nm), b) toluene/CH_2Cl_2 = 1/3 (scale bar 500 nm), c) toluene/CH_2Cl_2 = 1/10 (scale bar 500 nm), and d) toluene/methanol = 20/1 (scale bar 500 nm).

In order to unravel the growth mechanism of the spherical nanoobjects the reaction was monitored by *ex-situ* TEM analyses (Figure 2.7). The synthesis was realized in CH_2Cl_2 using

a Ru/C_{60} ratio of 2/1 at low temperature (-20°C) because of the fast formation of the spheres at room temperature. TEM micrographs of samples taken at different reaction times are displayed in Figure 2.7.

The TEM analyses show that the nanosphere growth mechanism in CH_2Cl_2 is divided in three steps, as observed for the synthesis of polymeric spheres.[42] In the early stages of the reaction, long threads are formed: at 5 min of reaction, mainly elongated objects (with sizes ranging from 300 to 1000 nm) are observed together with some spherical particles with diameters of *ca*. 130 nm. At 10 min, the size of these objects ranged between 20 and 400 nm. In a second step, large nanospheres are formed from the elongated nanostructures. Large spheres of *ca*. 290 nm are observed after 40 min. of reaction, which are clearly formed from the elongated objects (see Figure 2.7). The solution was stirred overnight in order to see if the third step of the growth mechanism is active. The TEM images revealed the formation of smaller nanospheres (37.0 ± 0.3 nm) together with the larger ones (*ca*. 330 nm) and clearly show that the small spheres are formed from the large ones.

The STEM-EDX mappings of the Ru@C_{60} structures synthesized at -20°C in CH_2Cl_2 (see Figure 2.8) confirm that the structures observed in the early stages of the reaction are constituted by Ru and C, as well as the spheres observed at 40 min of reaction. This result indicates that a second step towards the formation of smaller spheres is indeed active and, as observed in the formation of polymer nanospheres, that this step is much slower. After overnight, the small Ru NPs was also observed in the TEM.

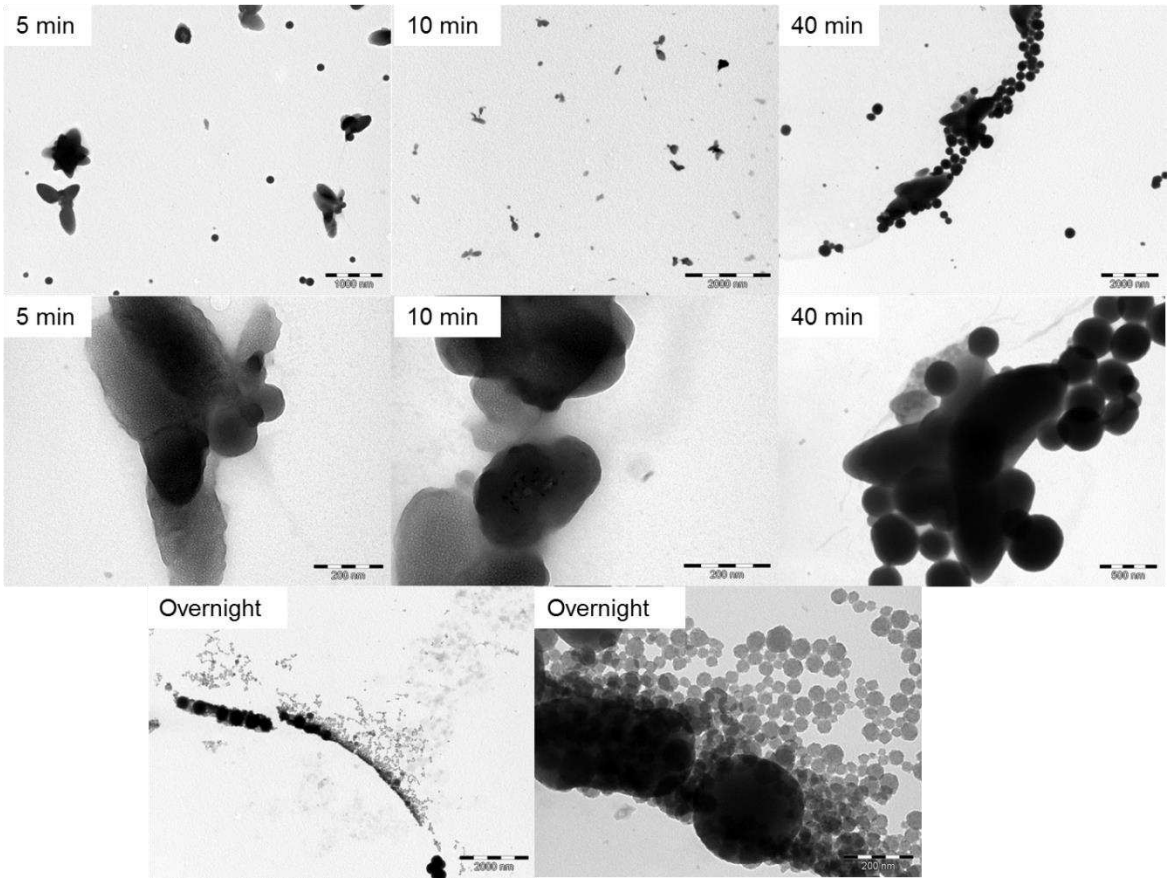

Figure 2.7. TEM micrographs of Ru@C_{60} structures synthesized in CH_2Cl_2 using a Ru/C_{60} ratio of 2/1 at -20°C (scale bar: 5 min, 2000 et 200 nm; 10 min, 2000 et 500 nm; 40 min, 2000 et 500 nm; and overnight, 1000 et 200 nm).

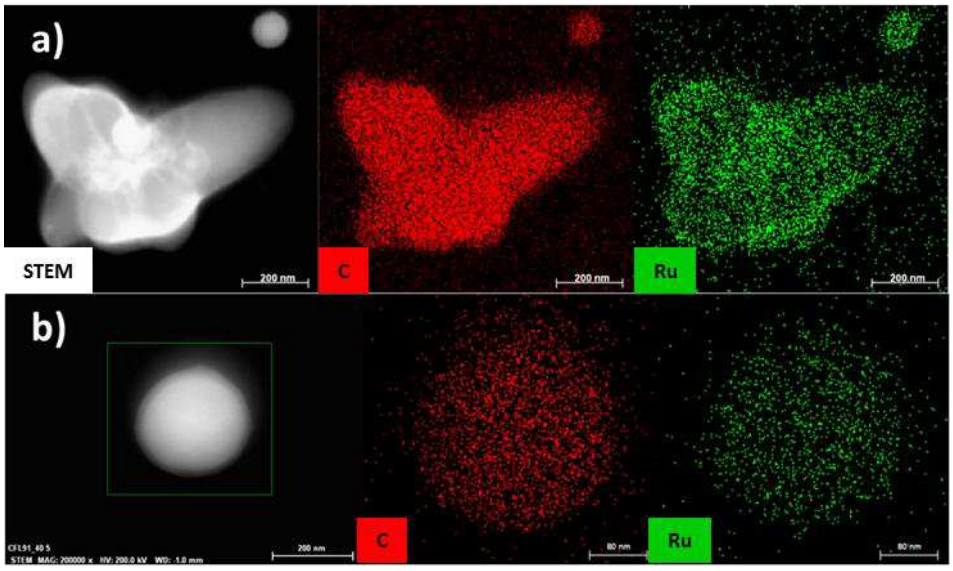

Figure 2.8. STEM-EDX mappings of Ru/C_{60} (Ru/C_{60} = 2/1) nanostructures synthesized in dichloromethane a) at -20°C at 5 min of reaction (scale bar 200 nm); and b) at -20°C at 40 min of reaction (scale bar 200 and 80 nm).

In conclusion, using mild reaction conditions Ru@C_{60} nanostructures are synthesized in a straightforward manner. The careful choice of the solvent allows to obtain different nanostructures: i) Ru-C_{60} polymers in pure toluene; nanospherical Ru-C_{60} polymers in 1, 2-dichlorobenzene, chlorobenzene, chloroform and in several solvent mixtures (1, 2-dichlorobenzene/dichloromethane, toluene/dichloromethane and toluene/methanol); ii) Ru NPs decorated Ru-C_{60} polymeric nanospheres in dichloromethane; and iii) Ru NPs supported on a C_{60} or Ru-C_{60} matrix in decalin. The shape of the nanostructure is determined mainly by the viscosity of the solvent but also by its permittivity. Indeed, controlling the viscosity of the solvent (using solvent mixtures) permits a precise control of the nanosphere size, which open the way to the synthesis of tailored nanostructures. The preferential formation of polymeric structure at the beginning of the reaction points to the fact that the reaction should be kinetically driven.

2.2.2 Ru/C_{60} ratio effect

The synthesis of Pd fulleride have shown that the final product Pd_nC_{60} was determined by the ratio of metal to C_{60}.[43] From microprobe analyses, a possible mechanism for the Pd_nC_{60} formation was proposed, which consists in one dimensional polymer PdC_{60} at the first stage. Then, the addition of Pd atoms will make bridges to connected the polymer chains and form Pd_nC_{60} ($1 < n < 3$). Besides, an excess of Pd atoms would be deposited on the surface of the Pd_nC_{60} if the ratio of Pd to C_{60} is fixed beyond 3.[44] In order to better understand the structure of the nanospheres, several nanostructures were synthesized using CH_2Cl_2 as solvent and changing the Ru/C_{60} ratio with a fixed C_{60} concentration. The Ru/C_{60} ratios investigated are the following: 2/3, 1, 2, 5, 10, 20, 30 and 50. The TEM images of the synthesized materials are shown in Figures 2.9 and 2.10. TEM analyses show that Ru@C_{60} 2/3 and 1/1 do not contain Ru NPs, in agreement with HREM (see above Figure 2.2). Increasing the Ru content,

Ru NPs are observed. Ru NPs display in all cases a small mean diameter, even at high Ru/C_{60} ratios, ranging from 1.10 to 1.35 nm (see Figure 2.9 and Table 2.5).

Table 2.5. Mean size diameters of Ru NPs and spheres of Ru@C_{60} according to the Ru/C_{60} ratio.

Ru/C_{60}[a]	Ru load[b] (%)	Nanoparticles mean size (nm)[c]	Spheres mean size (nm)[c]
2/3	6.4	Not observed	35.1 ± 1.1 nm
1/1	10.6	Not observed	36.2 ± 1.2 nm
2/1	16.7	1.16 ± 0.02 nm	31.6 ± 0.6 nm
5/1	35.6	1.31 ± 0.03 nm	42.6 ± 1.0 nm
10/1	48.7	1.26 ± 0.03 nm	32.4 ± 0.3 nm
20/1	50.4	1.10 ± 0.01 nm	39.8 ± 1.1 nm | 85.2 ± 2.9 nm
30/1	54.7	1.34 ± 0.01 nm	56.4 ± 4.7 nm | 103.2 ± 1.0 nm
50/1	61.9	1.35 ± 0.02 nm	63.3 ± 0.8 nm

[a]Synthesized by decomposing [Ru(COD)(COT)] under H_2 (3bar) in the presence of C_{60} at r.t. in CH_2Cl_2. [b]by ICP analyses [c]Manual measurement from enlarged micrographs of at least 200 objects.

Secondly, TEM images reveal that there is no significant change of the Ru@C_{60} nanosphere size from Ru/C_{60} ratios 1/1 to 10/1 ($\approx$ 40 nm, Figure 2.11). For higher Ru content (20/1 and 30/1) a bimodal size distribution is observed with small and large nanospheres (39.8 ± 1.1 nm | 85.2 ± 2.9 nm, and 56.4 ± 4.7 nm | 103.2 ± 1.0 nm, respectively). At 50/1 ratio, only one mean diameter of large spheres was measured (63.3 ± 0.8 nm, Table 2.5). A few aggregated Ru NPs was found in the ratio 30/1, and more particularly in the 50/1 nanostructures, and these aggregated Ru NPs are very similar to the one obtained by decomposition of the [Ru(COD)(COT)] precursor in the absence of C_{60} (Figure 2.10).

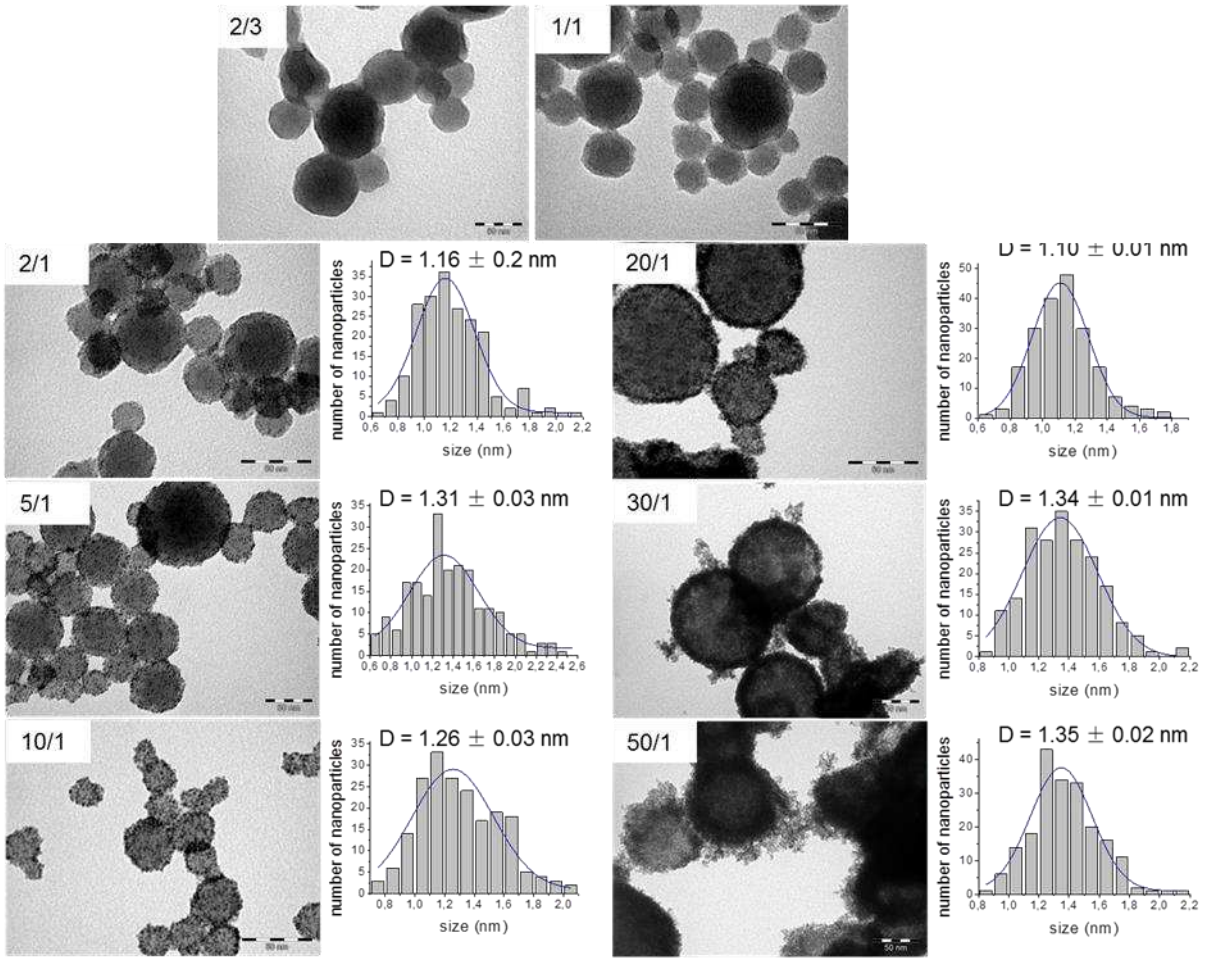

Figure 2.9. TEM images of Ru@C_{60} structures synthesized in CH_2Cl_2 using a Ru/C_{60} ratio of 2/3, 1/1, 2/1, 5/1, 10/1, 20/1, 30/1 and 50/1 (scale bar 50 nm).

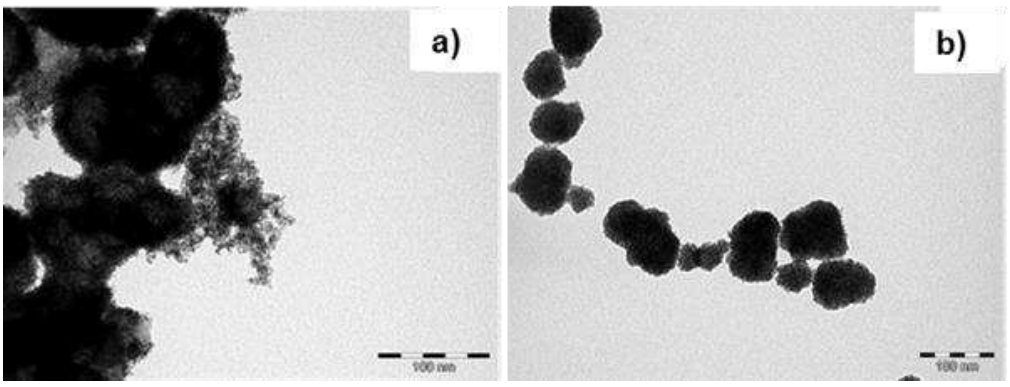

Figure 2.10. TEM micrographs of a) Ru@C_{60} structures for Ru/C_{60} = 50/1, scale bar 100 nm, and b) aggregated Ru NPs obtained by decomposition of [Ru(COD)(COT)] in the absence of C_{60}.

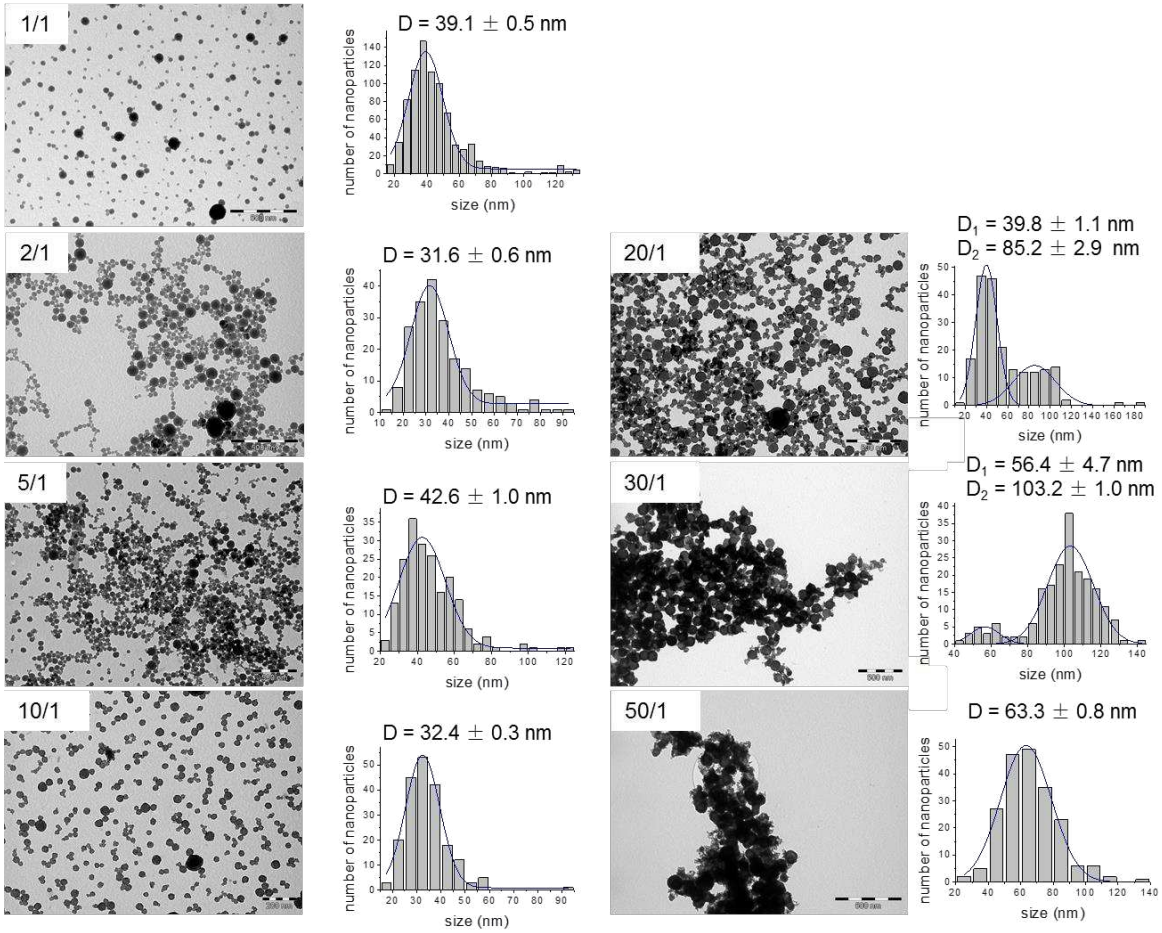

Figure 2.11. TEM images of Ru@C_{60} structures synthesized in CH_2Cl_2 using a Ru/C_{60} ratio of 1/1, 2/1, 5/1, 20/1, 30/1, 50/1 (scale bar 500 nm) and 10/1(scale bar 200 nm).

For comparative purposes, the Ru/C_{60} ratio effect was also studied for the nanostructures produced in toluene. Several Ru/C_{60} ratios (1/1, 10/1, 20/1 and 55/1) were investigated using toluene as reaction solvent (T-Ru@C_{60}). Similarly, low Ru/C_{60} ratios do not produce Ru NPs, which are only observed in the T-Ru@C_{60} 20/1 and 55/1 samples in conventional TEM (Figure 2.12). The structures with no regular shape were observed for all ratios, indicating no effect of the ruthenium content on the structure shape.

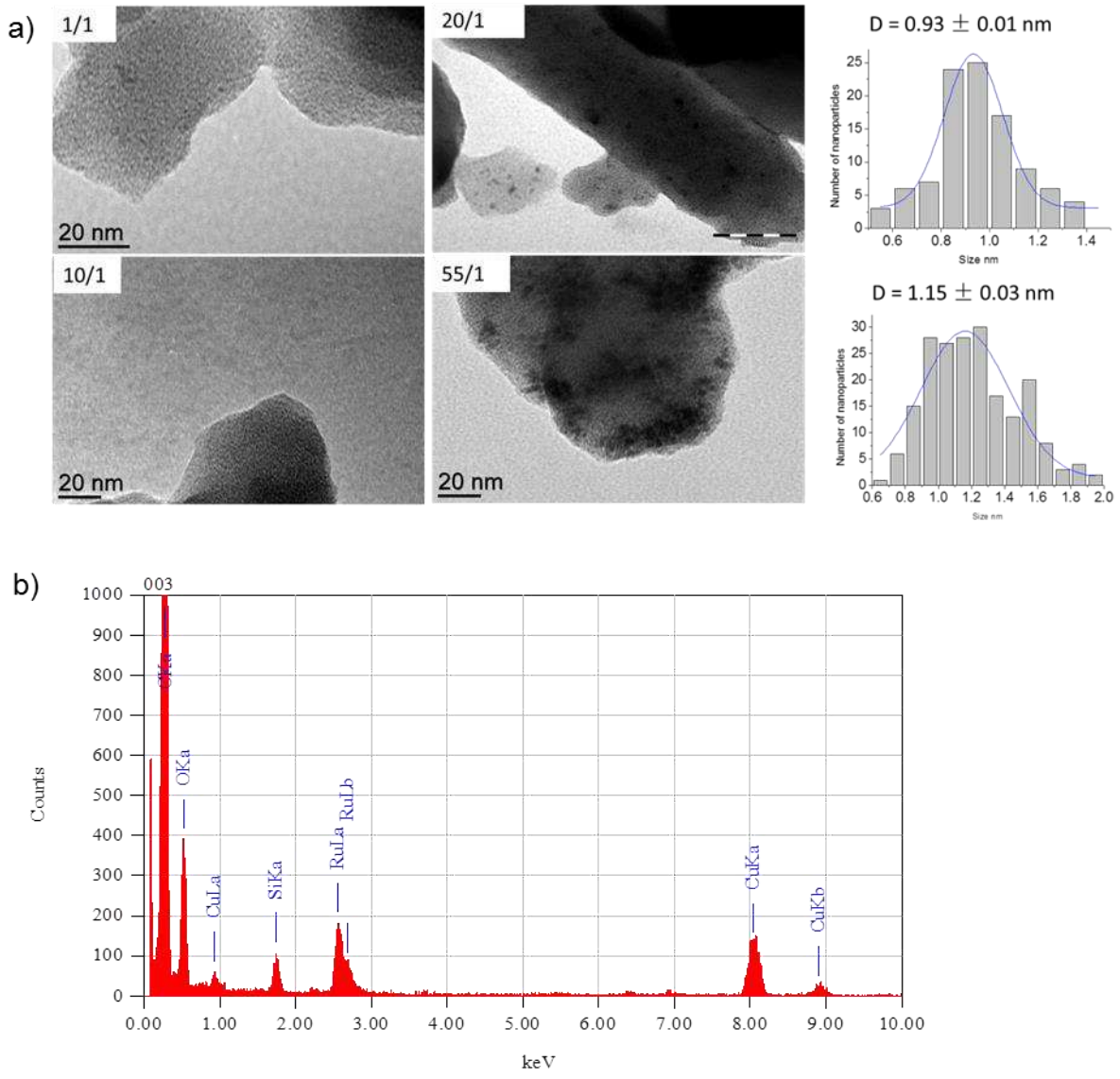

Figure 2.12. a) Ru@C_{60} synthesized in toluene with different ratio of Ru and C_{60}; Ru@C_{60} 1/1 (scale bar 20 nm), Ru@C_{60} 10/1 (scale bar 20 nm), Ru/C_{60} 20/1 (scale bar 50 nm), and Ru@C_{60} 55/1 (scale bar 20 nm); and b) EDX spectrum of Ru@C_{60} 10/1.

HREM analysis confirmed the TEM observations. HREM images of T-Ru@C_{60} 10/1 (Figure 2.13) only revelead very small Ru NPs (with size less than 1 nm). Ultrasmall Ru NPs were observed in the T-Ru@C_{60} 20 /1 sample (0.93 ± 0.01 nm). In contrats to the Ru@C_{60} samples synthesized in CH_2Cl_2, the increase of the Ru content in T-Ru@C_{60} samples indicate a increase of the Ru NP size. The EDX analysis confirmed that Ru and C are distributed homogeneously in the structures.

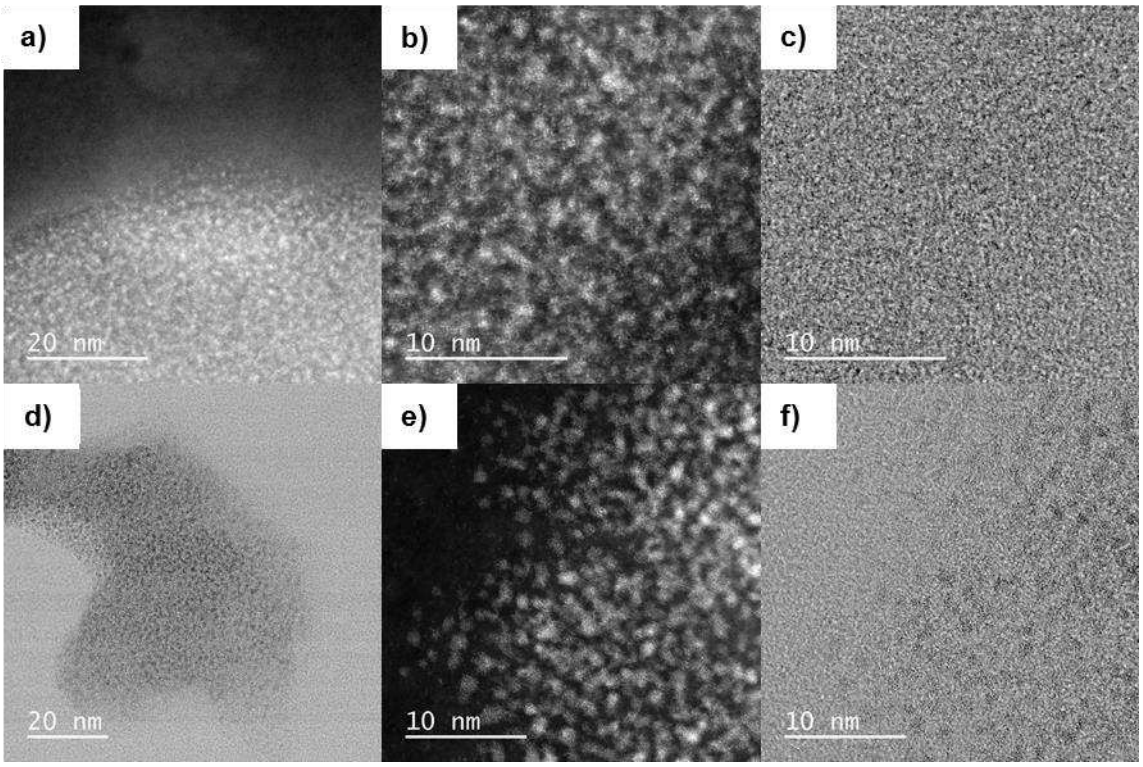

Figure 2.13. HREM images of T-Ru@C_{60} synthesized with different ratio a), b); and c) 10/1; and d), e); and f) 20/1.

Table 2.6. Mean size diameters of Ru NPs according to the Ru/C_{60} ratio.

T-Ru/C_{60}[a]	Ru % ICP[b]	Ru NPs[c]
1/1	6.8	Not observed
10/1	15.7	Not observed (< 1 nm)
20/1	35.4	0.93 ± 0.01 nm
55/1	47.5	1.15 ± 0.03 nm

[a]Synthesized by decomposing [Ru(COD)(COT)] under H_2 (3bar) in the presence of C_{60} at r.t. in toluene. [b]By ICP analyses. [c]Manual measurement from enlarged micrographs of at least 200 objects.

2.2.3 Characterization of the Ru@C_{60} nanostructures

In order to better understand structure of the Ru/C_{60} nanostructures synthesized in CH_2Cl_2 several techniques have been used including: TEM, HREM, Raman, ATR-IR, WAXS, EXAFS and XPS, in addition to DFT calculations.

2.2.3.1 Electron microscopy

Conventional TEM images revealed that some of the nanostructures prepared do not contain Ru nanoparticles (Figure 2.14), even if both Ru and C_{60} are present in these samples (Figure 2.15).

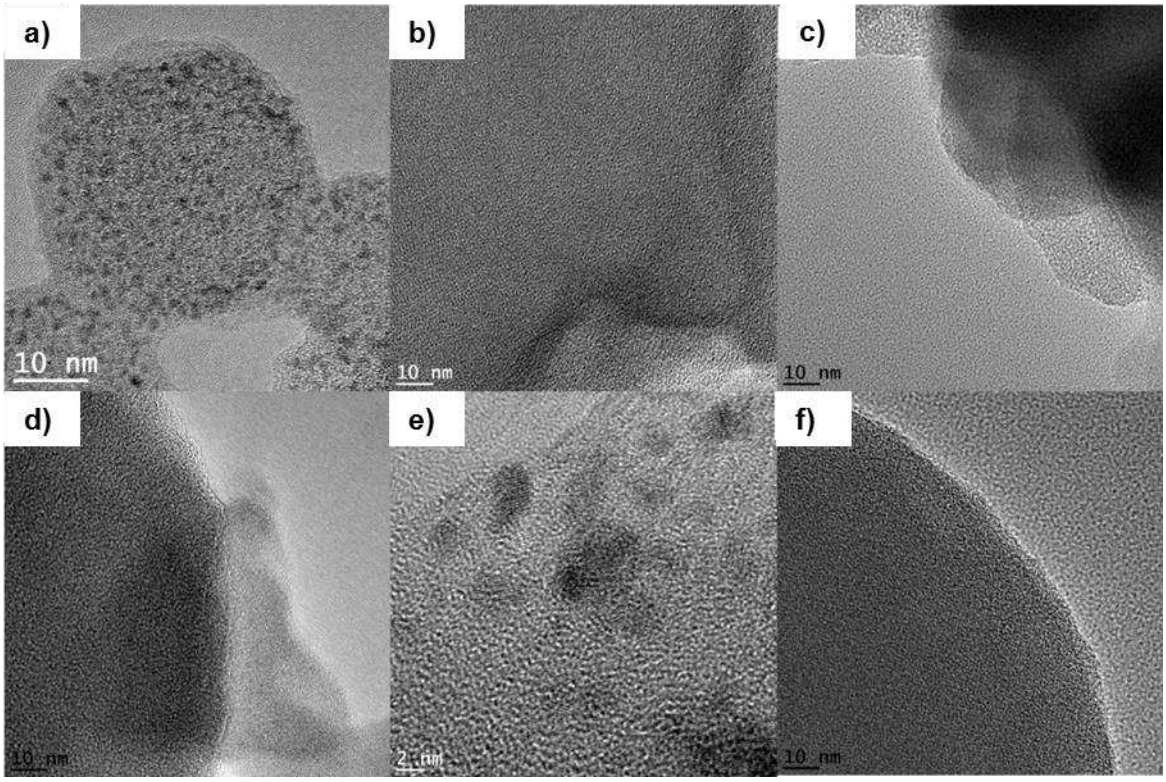

Figure 2.14. HREM images of Ru@C_{60} 2/1 synthesized in different solvents a) dichloromethane; b) chloroform; c) toluene; d) dichlorobenzene; e) decalin; and f) toluene/CH_2Cl_2 = 1/1, (all scale bar is 10 nm except e-2 nm).

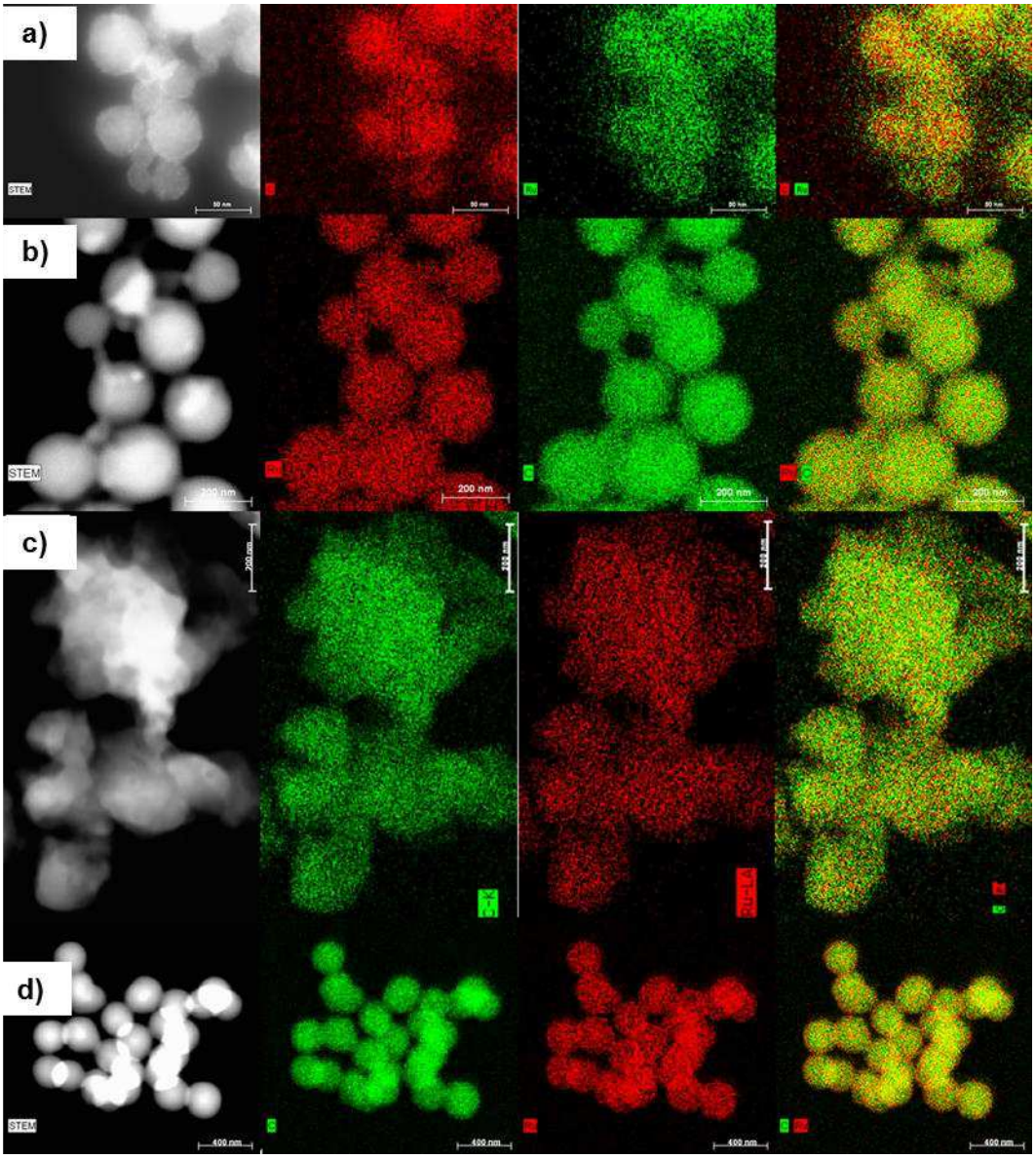

Figure 2.15. STEM-EDX images of Ru@C_{60} 2/1 structures synthesized in different solvents: a) dichloromethane; b) dichlorobenzene; c) toluene; and d) toluene/CH_2Cl_2 1/1.

Even if HREM (Figure 2.16a) confirmed the absence of NPs for the sample Ru@C_{60} 1/1 prepared in dichloromethane, and the presence of carbon and ruthenium in the nanostructures, the extremely small size of the Ru species possibly present in the Ru-C_{60} matrix is a drawback for a classical TEM analysis. To overcome this, a scanning TEM in high-angle annular dark field (STEM-HAADF) approach, based on the Z-contrast dependence, can be useful to identify the small metallic species supported in/on the lighter matrix. These analyses have

been performed in collaboration with S. Moldovan and M. Girleanu of *Institut de Physique et Chimie des Matériaux de Strasbourg, UMR 7504 CNRS-UdS, Strasbourg, France*.

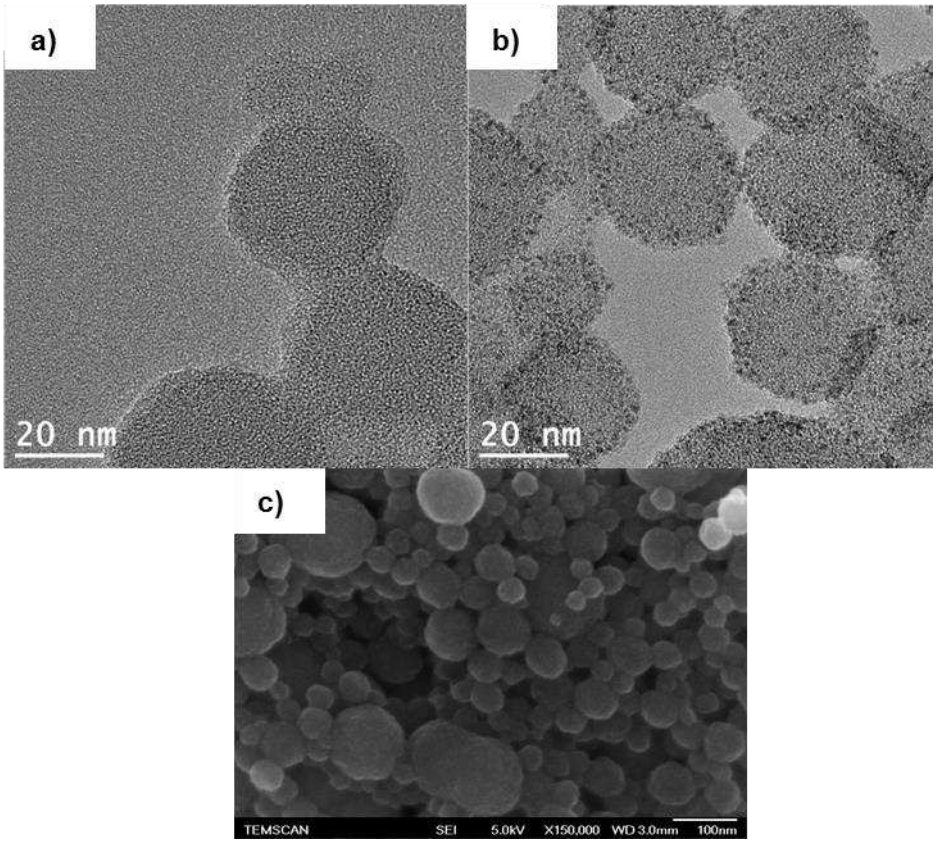

Figure 2.16. HREM of the Ru@C_{60} a) 1/1; and b) 2/1; and c) SEM of Ru@C_{60} 1/1.

The STEM-HAADF micrographs of the Ru@C_{60} 1/1 sample synthesized in CH_2Cl_2 reveal that all the surface of the spheres was coated by Ru atoms and/or clusters (Figure 2.17a and 2.17b). The Ru clusters size does not exceed 0.6 nm. Higher resolution images obtained on a ARM-200F microscope, on which Ru atoms are clearly visible are depicted on Figure 2.18.

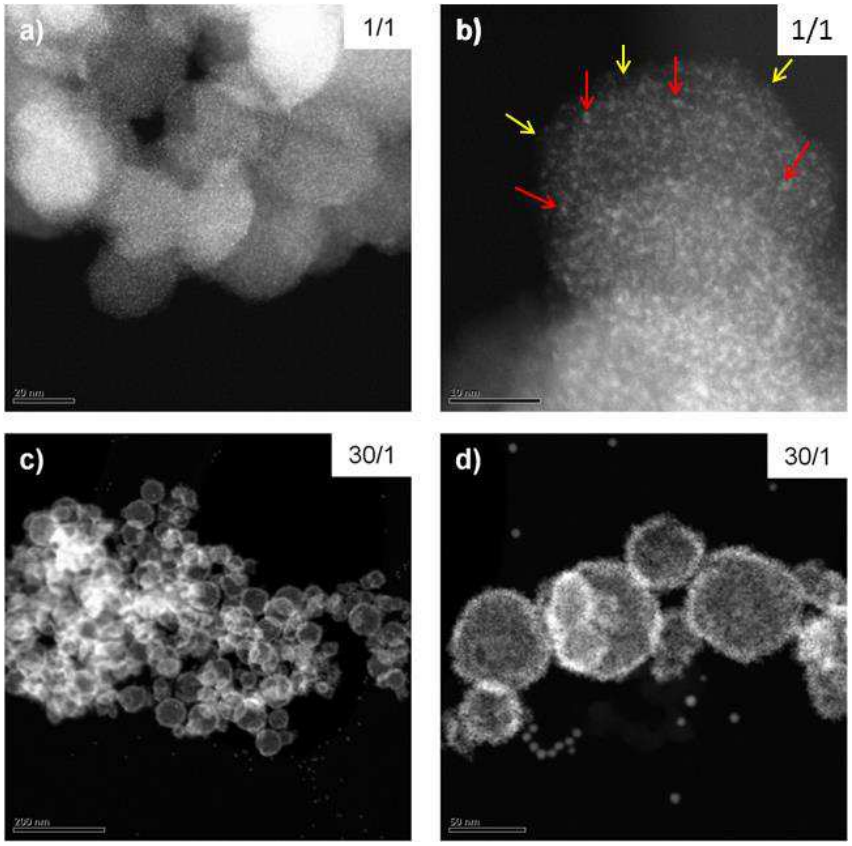

Figure 2.17. STEM-HAADF micrographs of Ru@C_{60} 1/1 (a, b) and 30/1 (c, d) nanostructures. In b), the yellow and red arrows point to the Ru few atom clusters and larger clusters, respectively (scale bars a) 20 nm, b) 10 nm, c) 200 nm; and d) 50 nm).

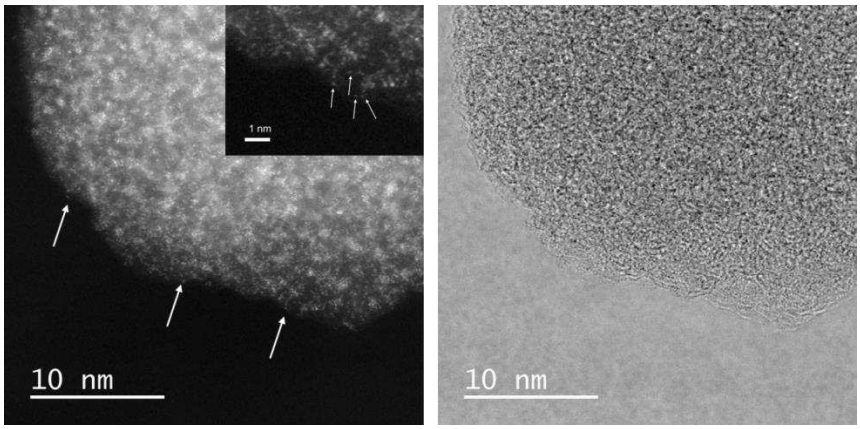

Figure 2.18. ARM-HREM and STEM micrographys of Ru@C_{60} 1/1.

In contrast, for the ratio 30/1 ratio (Figure 2.17c and 2.19e,f), the HAADF micrographs shown small Ru NPs (~1.5nm) on the surface of the spheres. The distribution of the Ru signal, acquired in STEM-EDX along a line scan (Figure 2.19), confirms the presence of Ru NPs on

the outer sphere surface within the 30/1 sample, whereas a more uniform distribution of Ru is observed for the 1/1 sample.

The above TEM or STEM analyses on the 2D projections of the object, do not provide clear information on the possible presence of Ru species (clusters or small NPs) in the interior of the spheres. Electron tomography analysis allowed the investigation within the volume of theses spheres. Figure 2.19 shows the results obtained for the 30/1 Ru/C_{60} ratio. From the slices views of 3D reconstructed volumes (Figures 2.20-b and 2.20-c) the presence of small Ru NPs is obvious on the surface of the sphere, creating a Ru NP shell with a thickness around 7 nm, which correspond to a multilayered NP structure. This is in agreement with the Ru signal distribution observed in Figure 2.19, as the heavier elements appear most contrasted in STEM-HAADF (Figure 2.19h). It is thus clear that no crystallized Ru NPs are present inside the spheres, but this analysis does not exclude the presence of atomic Ru inside the polymeric matrix. The analysis was also performed for the Ru@C_{60} sample with a 1/1 ratio, but the very small size of the clusters prevents their localization (see Figure 2.20d), the size of the clusters being below the resolution limit for the electron tomography analysis.

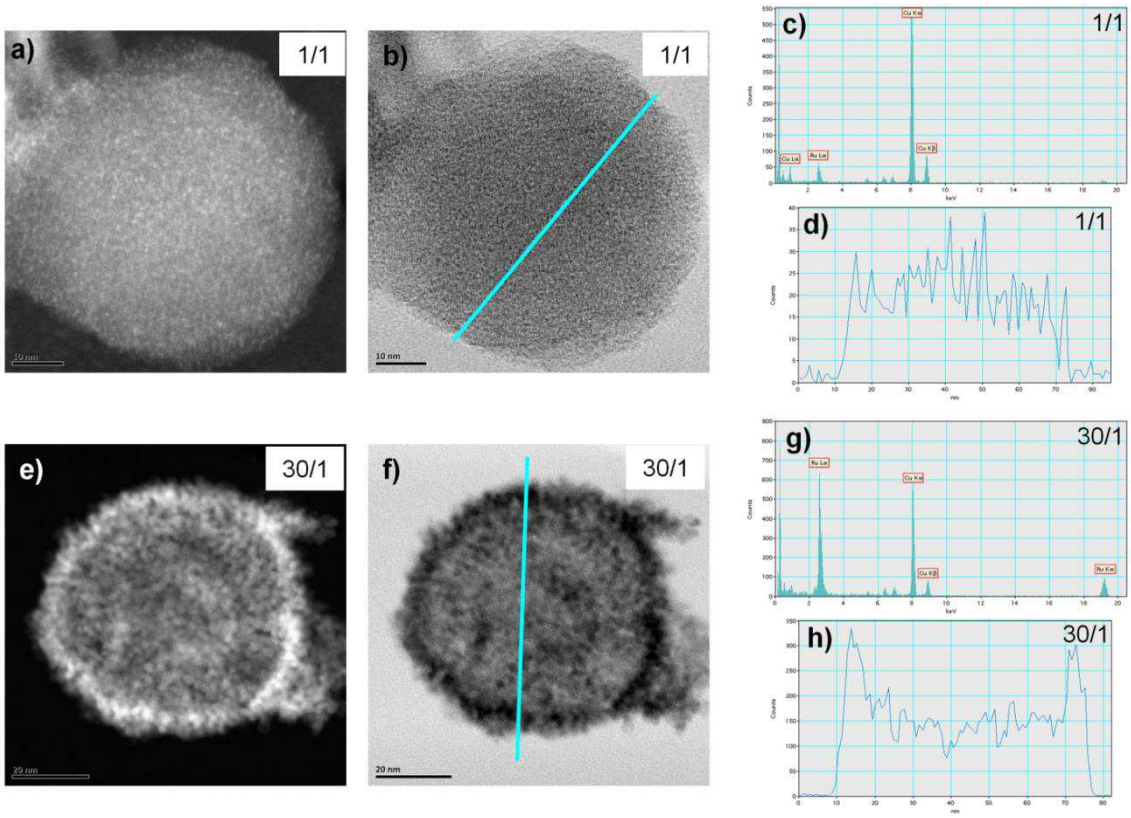

Figure 2.19. HAADF and BF STEM imaging of Ru@C_{60} 1/1 (a,b) and 30/1 (e,f) nanostructures showing the presence of atomic clusters of Ru on the all surface of C_{60} spheres for 1/1 composition and the presence of Ru small particles on the surface C_{60} spheres for 30/1 composition. Subfigures (c,d) and (g,h) display the cumulated EDX line scans and the Ru signal extracted from the corresponding spectra for the 1/1 and 30/1 specimens, respectively (scale bars a) 10 nm, b) 10 nm, e) 20 nm, and f) 20 nm).

The resolution attained in electron tomography is in the nanometer range, thus it is practically impossible to evidence the presence of any metal atoms and/or few-atom clusters within the spheres. It is therefore reasonable to propose that, in CH_2Cl_2, the decomposition of the [Ru(COD)(COT)] precursor leads to the formation of polymeric spheres containing Ru atoms or small clusters and fullerenes at low Ru/C_{60} ratio ($\leqslant$ 1), and that further increase of the Ru/C_{60} ratio leads to Ru atoms, clusters or NPs deposition on the surface of these polymeric spheres.

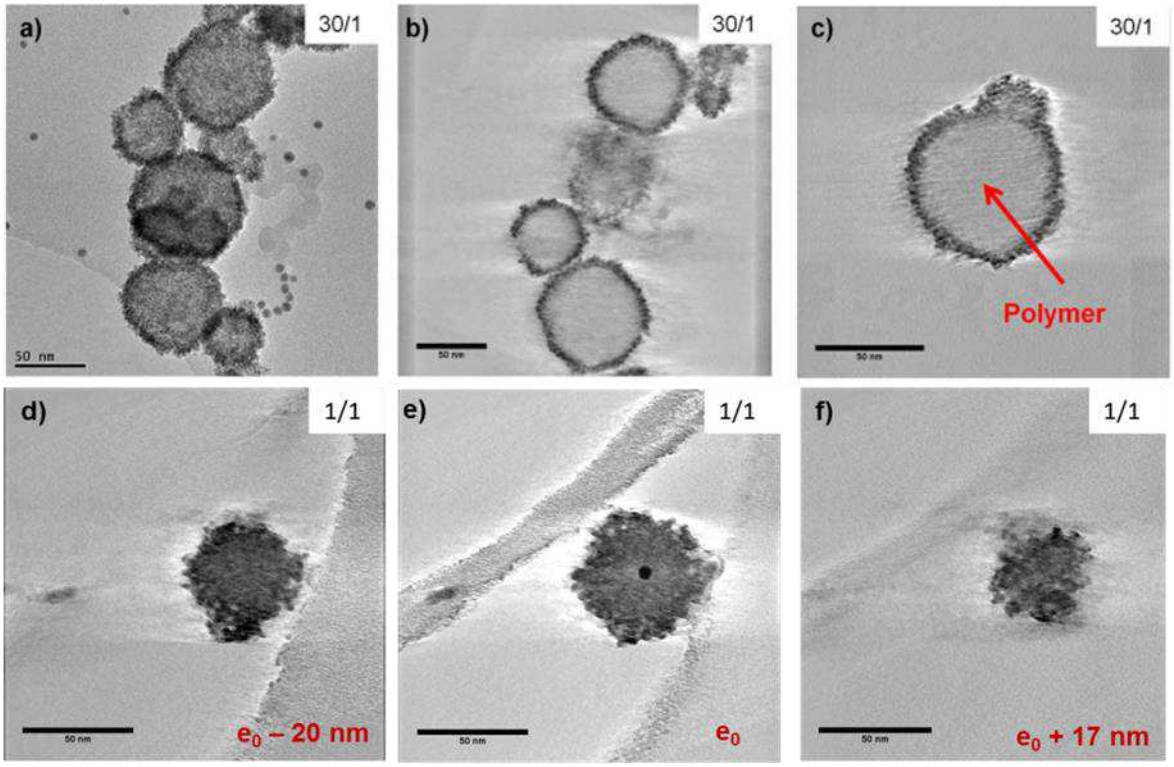

Figure 2.20. a) Electron tomography analysis of Ru@C_{60} 30/1 a) at 0° tilt from the tilt series, b) and c) representative cross-sectional slices along one direction in the plane of 3D reconstructed the volume and d) Ru@C_{60} 1/1, at e_0 -20nm, e) at e_0 +17nm f) (scale bars 50 nm).

The deposition of Ru NPs on the polymer surface might be due to diffusional limitations, which prevent the addition of extra Ru atoms in the polymeric spheres. We checked independently that the decomposition of an excess of [Ru(COD)(COT)] on the Ru@C_{60} 1/1 sample, to reach a 10/1 ratio, leads to NP deposition outside the Ru@C_{60} 1/1 spheres (Figure 2.21). In addition, TEM images reveal that the new nanoparticles are not all of them deposited on the surface, pointing out that fullerene C_{60} plays an important role in the stabilization of the Ru NPs in the Ru@C_{60} nanostructures.

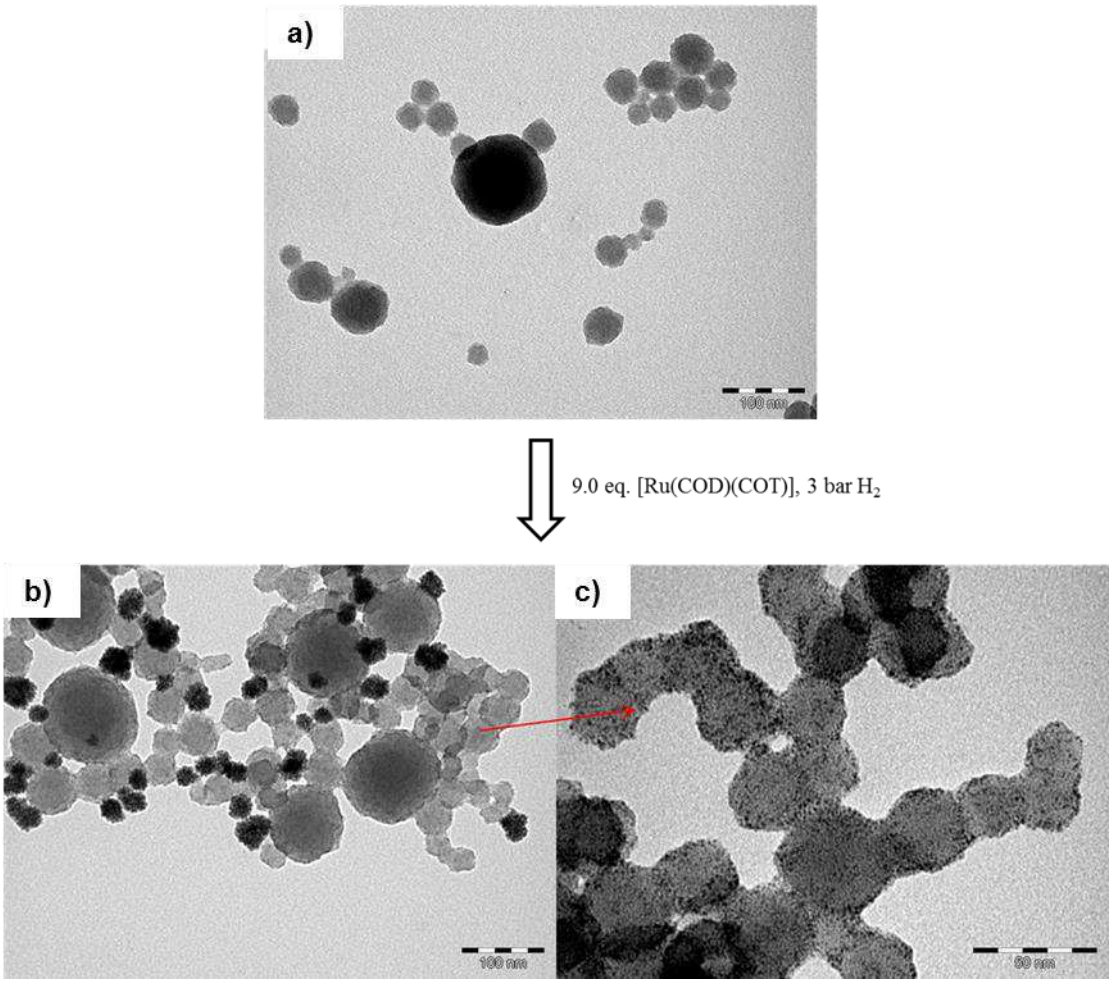

Figure 2.21. TEM micrographs of a) Ru@C_{60} 1/1 (scale bar 100 nm); b) Ru@C_{60} 10/1 synthesized by adding 9.0 eq. extra [Ru(COD)(COT)] to the obtained Ru@C_{60} 1/1. (scale bar 100 nm); and c) enlargement of b) (scale bar 50 nm).

2.2.3.3 WAXS

WAXS analyses were done in collaboration with Pierre Lecante of the *Centre d'élaboration des matériaux et d'études structurales UPR CNRS 8011, Toulouse, France*. Samples sealed in Lindemann glass capillaries were measured by WAXS using a diffractometer dedicated to pair-distribution function (PDF) studies (low background, Mo radiation). For the samples with high Ru/C_{60} ratio, the obtained diffractograms are very close and fully consistent with metallic Ru in the *hcp* system (Figure 2.22) with no significant contribution of C_{60}. After corrections and Fourier Transforms, the related PDF functions are as expected also very close,

and consistent with metallic Ru NPs with low structural disorder and sizes (from coherence length) reaching 2.5 nm. From the shape of the envelope characterized by a rapid initial decrease and a secondary maximum for a larger value (*ca*. 1.5 nm) before the final decrease, size dispersion is likely, with a large proportion of NPs much smaller than the 2.5 nm value.

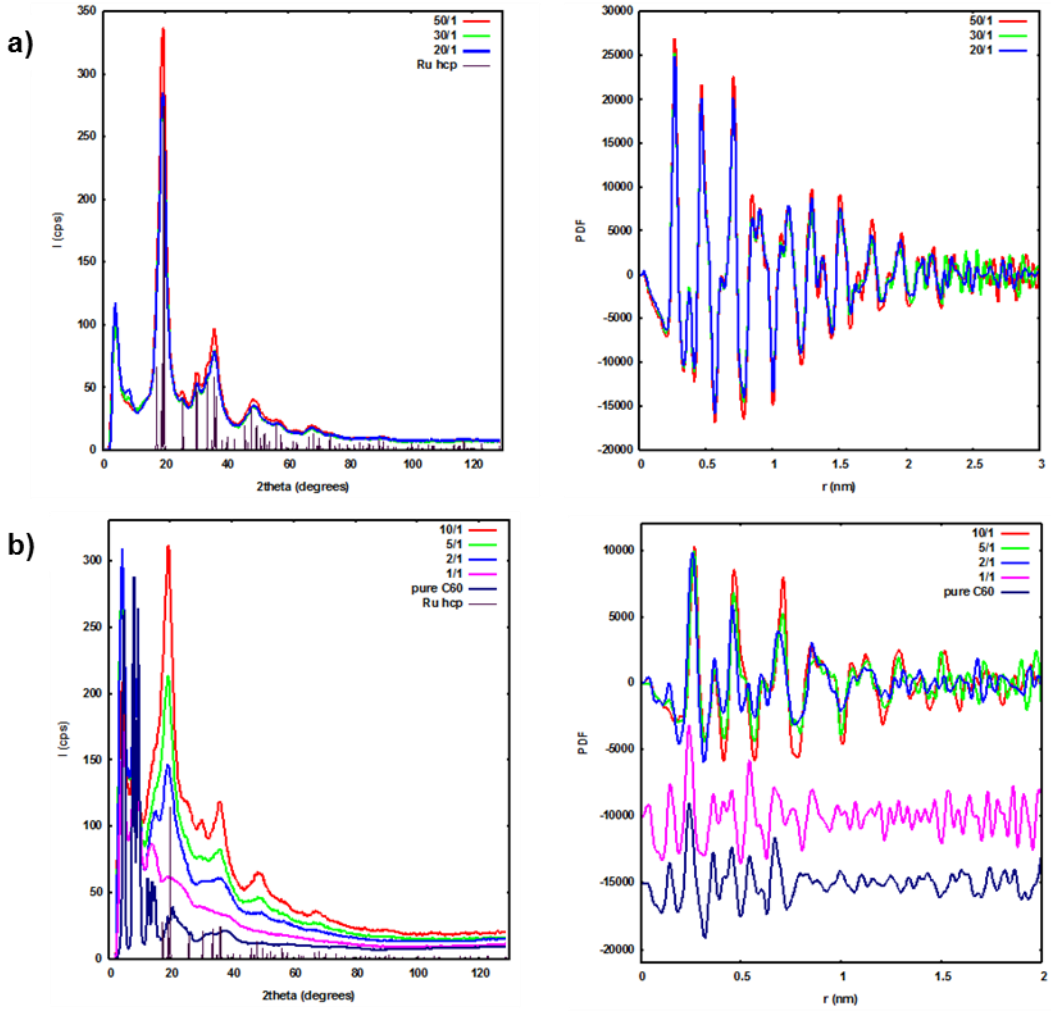

Figure 2.22. a) Left – diffractograms for high Ru/C_{60} ratio together with Ru *hcp* reference data, right – related PDF; b) Left – diffractograms for lower Ru/C_{60} ratio with Ru *hcp* reference data, right – related PDF.

This is in agreement with TEM measurements. Evolution is much different for smaller Ru/C_{60} ratios: for 10/1, 5/1 and 2/1, we first observe (Figure 2.22b) a gradual decrease of the peaks characteristic of the Ru *hcp* structure, then for the 1/1 ratio the *hcp* crystalline signature totally vanishes and the diffractogram is closer to the one obtained for pure C_{60}, excepted for the

sharp peaks at low angle observed only for the highly ordered pure C_{60} sample. The main interest of PDF analysis is the ability to go beyond crystalline order and to analyze characteristic distances in the material, related to crystalline periodicity or not. In the present case, we observe on the PDF a decrease of the metallic Ru order, however mostly marked for the longer distances for the 10/1, 5/1 and 2/1 ratios, actually indicating Ru NPs with a more single size distribution and an average diameter close to 1.5 nm for the 2/1 ratio.

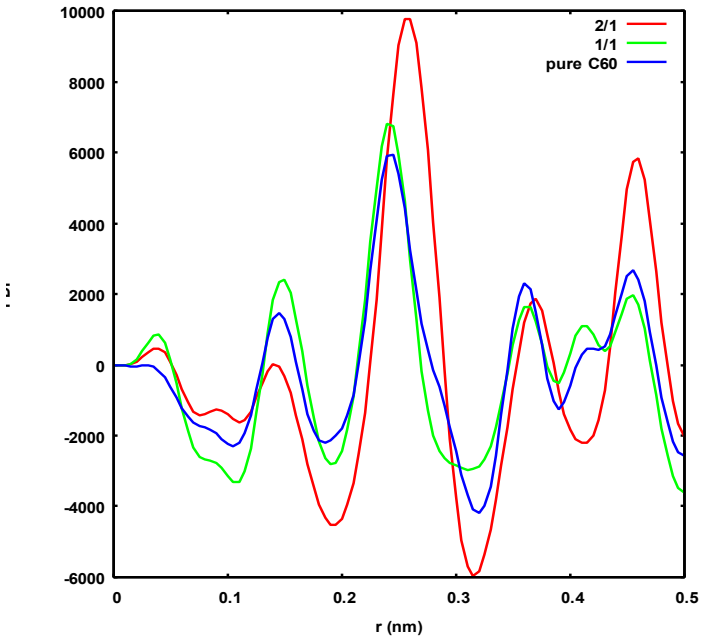

Figure 2.23. PDF for ratio Ru/C_{60} 1/1, 2/1 and pure C_{60}.

For the 1/1 ratio (Figure 2.23), we observe a drastic change for the distances compare with the high Ru/C_{60} ratio. There is still Ru-Ru bond in ratio 2/1, however, it disappeared completely for the 1/1 sample. The PDF results in Figure 2.23 show that the range of distance (0.2~0.4nm) of 1/1 is very close to the pure C_{60} but a slight shorter. As we know, many Ru-light elements have this kind of distance distribution such as Ru-O, Ru-C and Ru-N. Concerning the reaction conditions, the distance distribution could be assigned to the Ru-C because many references have disclosed the general Ru-C distance at around 0.21-0.23 nm.[45] In addition, *ab initio* calculations, as well as the results of our DFT calculations, show a significant contraction of the bond lengths for Ru clusters (n < 13): Ru-Ru bonding distance between 0.21 and 0.24 nm.

However, owing to non-bonding C-C distances from C_{60} obviously also pile up in this range, thus there is still not a very clear evidence of Ru-C or Ru-Ru bonds identification by these techniques.

From the above discussion, all the analysis of ratio 1/1 have displayed that there is no Ru nanoparticles in this sample, regardless of some possible Ru-Ru bonds in small clusters. Order is dominated by the C_{60} structure for short distances, but discrepancies for distances above 0.7 nm strongly indicate more extended ordering, however it is difficult to safely characterize. Short distances are also in good agreement with eventual Ru-C bonding.

For the 2/1 ratio, small Ru NPs (*ca.* 1.5 nm) can be observed. For the 5/1 ratio and above, these small NPs can still be observed but associated to an increasing proportion of larger NPs (2.5 nm from coherence length), which suggests increasing coalescence from small NPs. Besides, in the view of tomography results at high Ru/C_{60} ratio, we know that the structure has two components, one is Ru@C_{60} polymer inside, and one is a Ru NP shell.

2.2.3.4 Raman

C_{60} is a well-known electron acceptor and Raman spectroscopy can give valuable information on charge transfer. Figure 2.24a shows Raman spectra of Ru@C_{60} 1/1, 2/1, 5/1 and 10/1 samples at 532 nm. These analyses were performed in collaboration with Prof. Wolfgang Bacsa of the *Centre d'élaboration des matériaux et d'études structurales UPR CNRS 8011, Toulouse, France*. The spectral range is mainly focus on the pentagonal pinch mode Ag(2), because it have been proven that this mode is a reliable probe of metal fullerides polymer states. It is known that the energy of the Ag(2) mode (1468 cm^{-1} for pure C_{60}) is sensitive to charge transfer when evaporating C_{60} on metal surfaces,[46] or for transition metal fullerides.[47] Generally, the shift of this mode is affected by many factors such as the function of the metal, the number of covalent bonds on the C_{60} molecules and the metal-adsorbate interactions.

It is commonly accepted that the Ag(2) mode is downshifted by approximately 6 cm^{-1} transferred to C_{60} in alkali metal fulleride compounds.[48] The downshift of alkali metal fulleride depends of the number of metal atoms and each metal atom donates one electron to C_{60}, because there are only ionic bonds between C_{60} and alkali atoms. For the transition metal fullerides, the relationship between shift and composition is more complicated since these compounds may exhibit a large proportion of covalent bonding between metal and C_{60}.

From the work function of Ru (4.71 eV) one would expect a similar spectral shift as for Cu (4.70 eV) of -23cm^{-1}. We observe here a spectral shift as large as -10.1 cm^{-1} for the Ru@C_{60} 10/1 sample, and a significant broadening with increasing amount of C_{60} caused by strong electron-phonon interaction, which is in agreement with spectrum of Pd_nC_{60} at high Pd content. For the Ru@C_{60} 1/1 sample, the spectral shift is -6 cm^{-1}. The spectrum of C_{60} without Ru is shown at the bottom of Figure 2.24a for comparison. Unlike the Pd_nC_{60}, which shows an identical signal at 1458 cm^{-1} at different ratio ,[49] here we have a difference in shift with the four ratios (Figure 2.24b).

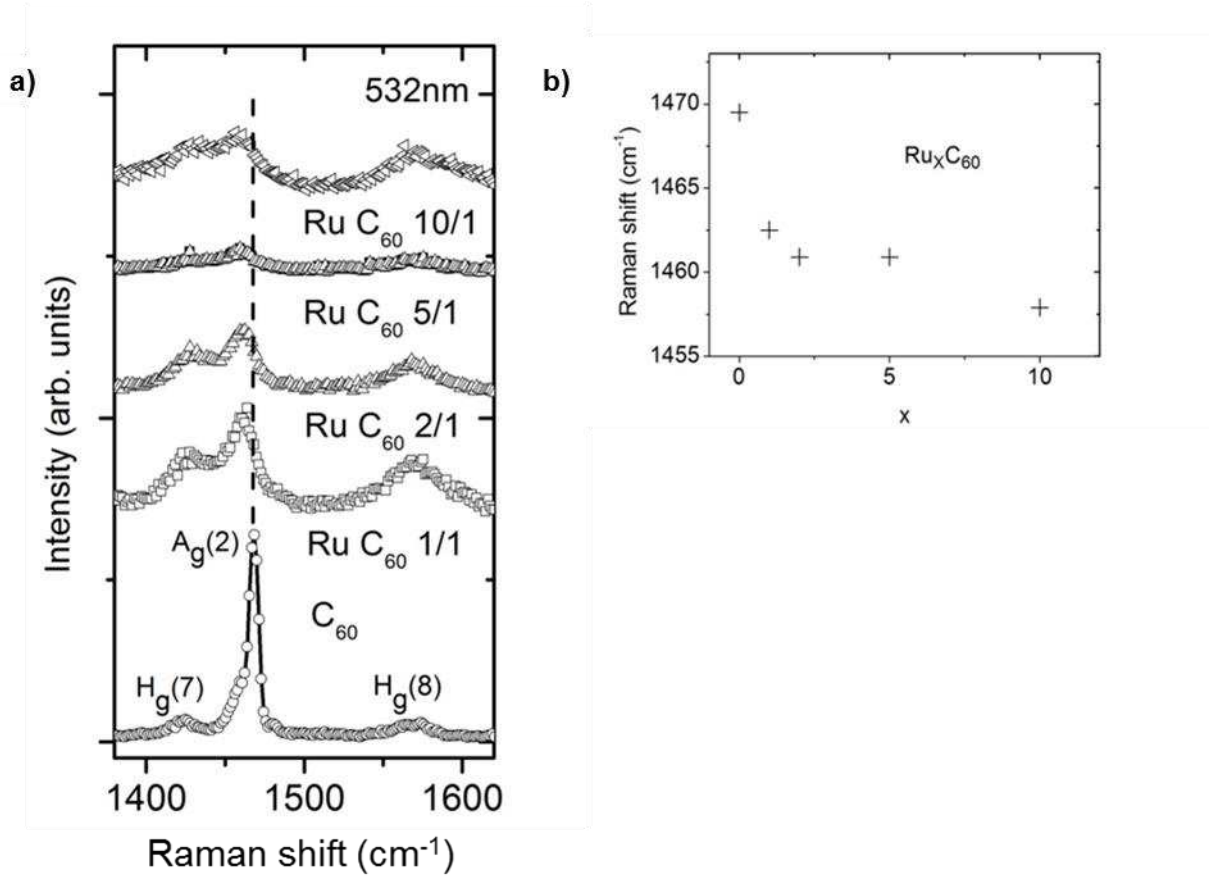

Figure 2.24. a) Raman spectra excited at 532 nm of C_{60} and Ru@C_{60} 1/1, 2/1, 5/1 and 10/1 samples in the spectral range of the pentagonal pinch mode Ag(2); and b) Raman spectral position of the Ag(2) band as a function of molar concentration of C_{60}.

In addition, the spectrum of pentagonal-pinch mode Ag(2) was not superimposed by the high content Ru, demonstrating that the C_{60} is strongly interacting with Ru. It is known that the Ag(2) mode downshift for Pd-C_{60} and Pt-C_{60} fullerides is 15 cm^{-1}, which suggests that these fullerides have a similar coordination η^2-fashion between the metal and C_{60}, such as for the [$Pd(PPh_3)_2(\eta^2$-$C_{60})$] and [$Pt(PPh_3)_2(\eta^2$-$C_{60})$] molecular complexes. The difference of Ag(2) mode downshift among the Ru@C_{60} and Pd-C_{60} and Pt-C_{60} fullerides might be due to a different coordination mode: the η^2-bonding to two neighboring C_{60} for Pd-C_{60} and Pt-C_{60}, and the η^2- and η^6 for the Ru@C_{60} structures(see DFT calculation and EXAFS). Therefore, we concluded that the charge transfer to the C_{60} molecules is not only dependent on the metal but also on the type of covalent bonds. Figure 2.24b shows how the Ag(2) shift progressively

increases at higher molar concentration of Ru. The Hg(7) and Hg(8) modes were not found downshift in the spectra. Only small shifts were observed for C_{60} on Cu (< 7cm^{-1}). Compared to metallic surfaces, the smaller spectral shift (6-10 cm^{-1}) observed for the Ru@C_{60} samples, indicates that the work function of the Ru species is larger than for bulk Ru.

2.2.3.5 ATR-IR

IR gives valuable information to verify the structure of metal fullerides.[50] As reported by Martin *et al*., the mode at 576 and 1427 cm^{-1}(v_2, v_4) are more useful and sensitive for identification of the metal polymer structure. The attenuated total reflectance infrared (ATR-IR) spectra recorded for Ru@C_{60} samples in the solid state are shown in Figure 2.25.

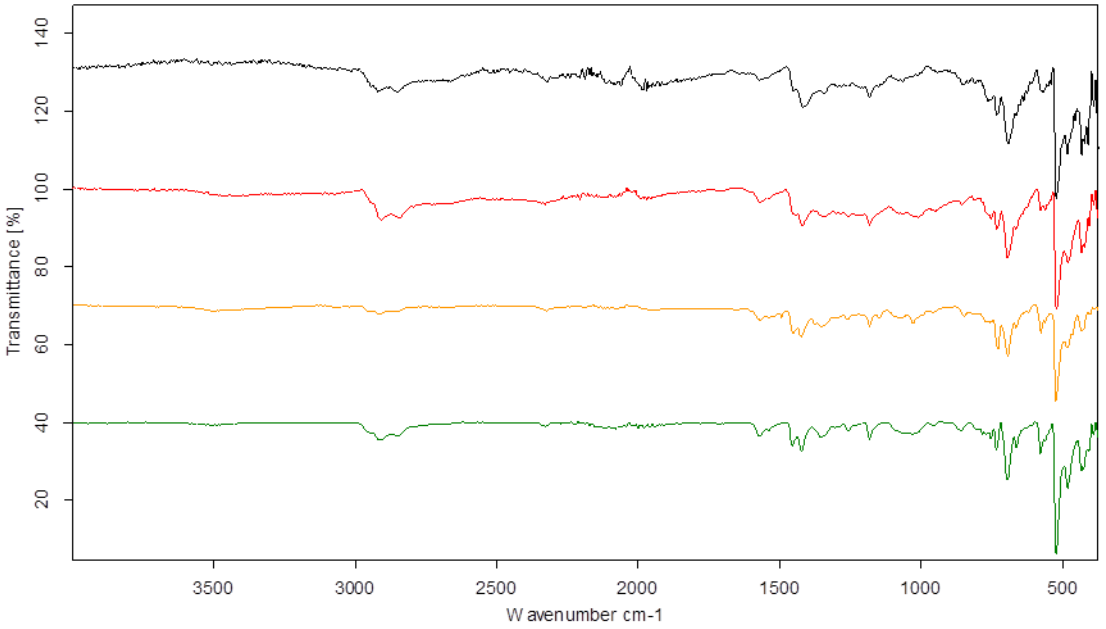

Figure 2.25. ATR-IR spectra of Ru@C_{60} with ratio of 1/1, 2/1, 5/1 and 10/1 from up to down.

The presence of C_{60} was confirmed by the four characteristic peaks at 524, 576, 1182 and 1422 cm^{-1}, together with other vibrations in the range of 2800-3000 cm^{-1} and 400-1600 cm^{-1}. Some of the peaks have been attributed to $C_{60}H_{18}$[51] and $C_{60}H_{36}$[52] species, and the rest of the peaks are probably due to the presence of a mixture of hydrofullerenes with different number of hydrogen atoms.[53] The hydrogenation of C_{60} over Rh/Al_2O_3 catalyst at ambient

temperature and pressure has already been reported by Becker and co-workers,[55] however the reaction have a low yield (15 %). For our Ru@C_{60} materials, it has been verified by solid state NMR (SSNMR) that the hydrogenated C_{60} are only present in a small proportion (see next section). Usually, the mode v_4 at 1422 cm^{-1} for alkali metal fullerides will present a significant shift, such as for K_3C_{60} to 1393 cm^{-1}, and Rb_4C_{60} to 1363 cm^{-1}. However, the down or upshift of v_4 mode at 1422 cm^{-1} was not observed for all Ru@C_{60} samples. That is probably because of the different bonding mode between the Ru@C_{60} and alkali metal fullerides.[54]

Since carbon monoxide is a sensitive probe for studying the surface composition of metal nanoparticles, CO adsorption on the Ru@C_{60} nanostructures was investigated by ATR-IR. Carbon monoxide was reacted with solid samples of Ru@C_{60} in a Fisher-Porter bottle under mild conditions (1.5 bar of CO, r. t., 24 h). Then, ATR-IR spectra were recorded with a spectrometer available in a glove box (Figure 2.26).

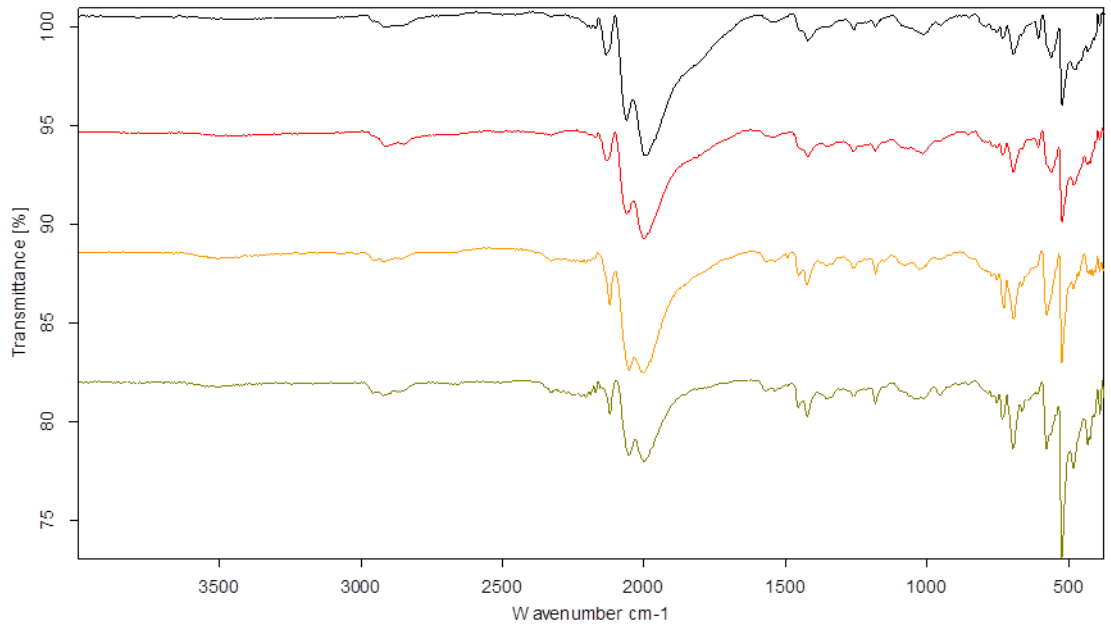

Figure 2.26. ATR-IR spectra of Ru@C_{60} exposed to CO with ratios of 1/1, 2/1, 5/1 and 10/1 from up to down.

After CO exposure, Ru@C_{60} 1/1, 2/1, 5/1 and 10/1 samples display at three new peaks in the range of 1900-2130 cm^{-1}, which are typical of metal terminal CO species. In the Ru@C_{60} 1/1

nanostructure, the peaks appear at 1998, 2053 and 2120 cm^{-1}. In a previously reported coordination nickel-bridged fullerene polymer $[Ni(Me_3P)_2(\mu\text{-}\eta^2,\eta^2\text{-}C_{60})]_\infty$,[56] each nickel atom is linked in the polymer with two fullerene units by η^2-type bonds to the [6,6] fullerene bonds. Taking into account the *cis* coordination of fullerenes to the Ru atom, CO molecules are likely to coordinate to the Ru atom to form species such as $[Ru(CO)_3(\mu\text{-}\eta^2,\eta^2\text{-}C_{60})]_\infty$. The $[Ru(CO)_3(alkene)_2]$ complexes typically show three adsorption bands in the CO stretching region, in particular the $[Ru(CO)_3(C_2H_4)_2]$ complex displays three bands at 2081, 2005 and 1995 cm^{-1}.[57] Considering that fullerene acts as an electron-deficient olefin, the bands should be shifted to highest stretching frequencies in a $[Ru(CO)_3(\eta^2\text{-}C_{60})_2]$ species compared to the $[Ru(CO)_3(C_2H_4)_2]$ complex, fitting with the spectrum obtained for the Ru@C_{60} 1/1 sample. However, species containing more or less CO ligands, as well as a mixture of species, cannot be discarded, as the signals are relatively broad. Ru@C_{60} 2/1, 5/1 and 10/1 samples show the same pattern, although the signal at 1998 cm^{-1} becomes broader when increasing the Ru NPs. We assigned this broad signal, which increases in intensity with the number of Ru nanoparticle present on the sample, to terminal CO adsorbed on the Ru nanoparticles surface as it usually appears in the region of 1970-2000 cm^{-1}.[58] For higher Ru/C_{60} ratios, the ATR-IR signal intensity was too low to be observed.

2.2.3.5 Solid State NMR

To confirm the structure of Ru@C_{60}, ^1H and ^{13}C-NMR spectra were measured; they are presented in Figure 2.27. Figure 2.27b shows the ^{13}C spectra of the Ru@C_{60} with ratio 1/1, 2/1, 5/1 and 10/1, which reveal an intense peak at 143 ppm and small peaks in the range 50-10 ppm. The chemical shift at 143 ppm corresponds to sp^2-carbon of pristine C_{60}, and the 50-10 ppm peaks can be assigned to the hydrogen adduct carbon. Signal enhancement in the 50-10 ppm region with H-C cross polarization disclosed further the signal at 50-10 ppm are hydrogen adducted carbon, as shown in Figure 2.28.

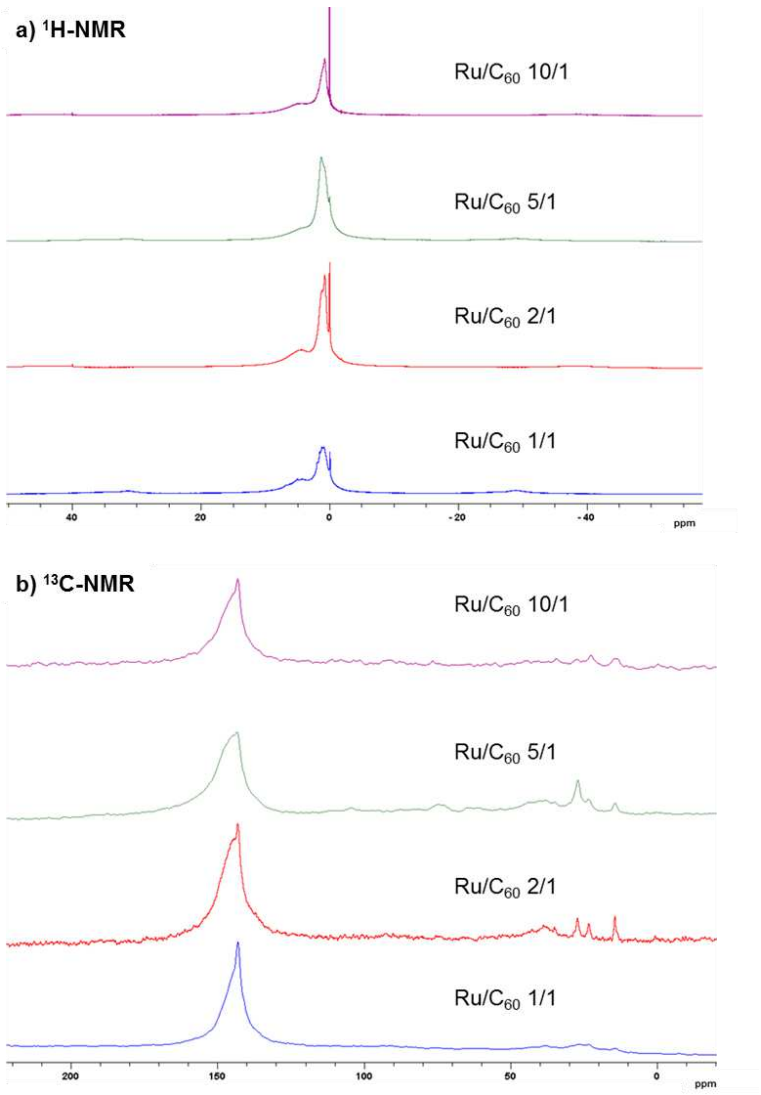

Figure 2.27. SSNMR spectra of Ru@C_{60} with ratio of 1/1, 2/1, 5/1 and 10/1 from bottom to top, a) ^{1}H-NMR; and b) ^{13}C-NMR.

On the basis of the ^{1}H-^{13}C cross polarization NMR spectra, the presence of hydrogen on Ru@C_{60} could be directly verified by ^{1}H-NMR spectra, as shown in the Figure 2.27a. There are two broad peaks at 4.0 and 0.7 ppm, which are accompanied by 4 spinning sidebands. Although hydrogenated C_{60} was detected in our sample, most of the sample consists in non-hydrogenated C_{60} and only a small amount was hydrogenated.

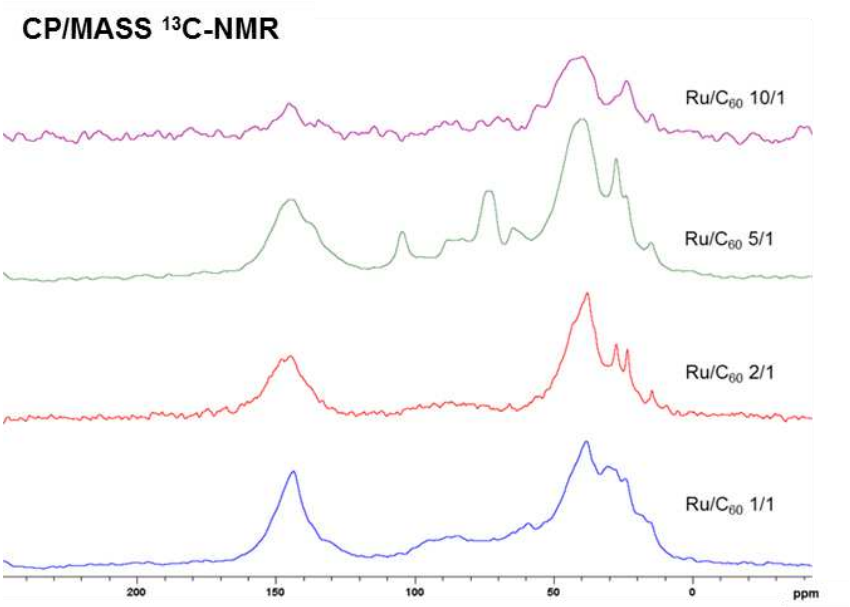

Figure 2.28. CP/MAS-^{13}C SSNMR spectra of Ru@C_{60} with ratio of 1/1, 2/1, 5/1 and 10/1 from bottom to top.

2.2.3.6 EXAFS

The Ru K-edge X-ray absorption spectra of samples Ru@C_{60} 1/1 and 2/1 were obtained in N_2 and after heating in 4% H_2/He for 1h at 150 °C, and the XANES energy is 22.1244 keV for both spectra. Figure 2.29a shows the X-ray absorption near edge (XANES) spectra of Ru@C_{60} 1/1 in N_2 and after high temperature treatment in H_2. It was found that the shape of the XANES does not change, indicating no change in the Ru oxidation state. And there is no obvious change of the structure even after high temperature treatment under H_2. After high temperature treatment under H_2, the magnitude of the Fourier transform of Ru@C_{60} 1/1 shows a peak below about 2 Å (phase uncorrected distance) and a small peak at longer distance in, while the Ru@C_{60} 2/1 have two peaks: one is below 2 Å and one is at 2.5 Å (Figure 2.29b).

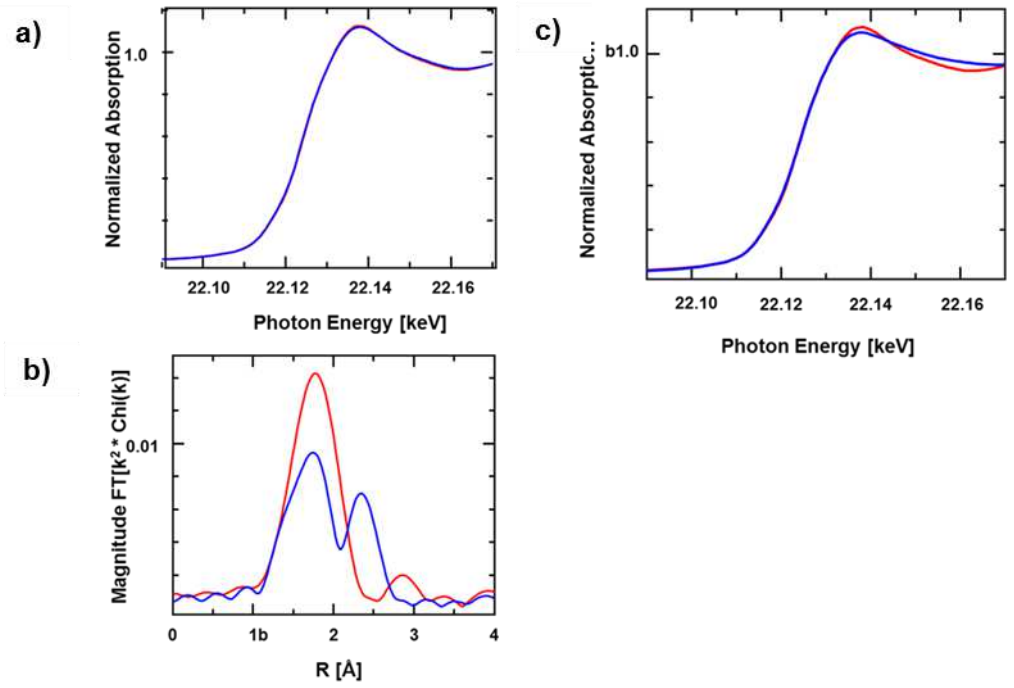

Figure 2.29. a) Ru K-edge XANES from 22.09 to 22.17 keV (red: Ru@C_{60} 1/1 N_2 at RT, and blue: Ru@C_{60} 1/1 H_2 at 150°C); b) Magnitude of the Fourier Transform of k^2-weighted Ru EXAFS (k^2: $\Delta k = 2.8 – 11.3$ Å^{-1}) (blue: Ru@C_{60} 2/1, H_2 at 150°C, red: Ru@C_{60} 1/1, H_2 at 150°C); and c) Ru K-edge XANES from 22.09 to 22.17 keV (blue: Ru@C_{60} 1/1, H_2 at 150°C red: Ru@C_{60} 2/1, H_2 at 150°C).

The fit of the Fourier transform is given in Table 2.7. The low R peak is fit with a Ru-C phase and amplitude functions calculated by FEFF, and gives 8.3 Ru-X bonds at 2.24 Å. Typical Ru-O bonds are below 2.0 Å, while Ru-C are longer at about 2.2 Å; thus it is likely that the light scatter is Ru-C. Within the error of the analysis, the fits of the sample treated in H_2 at 150 °C, is identical to that in N_2 at r.t. For Ru@C_{60} 1/1, in both the N_2 and H_2 spectra there is no indication of Ru-Ru scatters typical of metallic Ru NPs. There is a small peak at about 3 Å, which is likely due to a Ru-C-Ru scatter; however, the peak is too small to fit reliably.

The XANES and magnitude of the Fourier transform of Ru@C_{60} 1/1 and 2/1 heated to 150 °C in H_2 are shown in Figures 2.29c and 2.29b, respectively. The XANES energy of Ru@C_{60} 2/1 is the same as Ru@C_{60} 1/1, *e.g.*, 22.1244 keV; however, the shape of the XANES is slightly different, indicating some small difference in structure. The magnitude of the FT of Ru@C_{60}

2/1 shows that there are fewer light scatters and a new higher R peak at about 2.5 Å (phase uncorrected distance). Fits of the EXAFS spectra indicate there are fewer Ru-C, 5.1 Ru-C at 2.24 Å, compared to sample Ru@C_{60} 1/1. In addition, the scatter at longer R is due to Ru-Ru scatter with a coordination number of 2.2 at 2.63 Å, typical of metallic Ru NPs. Since non-metallic Ru-C has 8 bonds, a coordination number of 5.1 indicates that approximately 61% of the Ru is bonded to C in the Ru@C_{60} 2/1 sample. The remaining Ru is, therefore, metallic, *i.e.*, 39%. For the metallic fraction, the true coordination number is the measured coordination number divided by the fraction of metallic Ru, or 2.2/0.39, or 5.6. For *fcc* and *hcp* metals a coordination number of 5.6 is consistent with a particle size of about 1.5 nm.[59] In summary, sample Ru@C_{60} 1/1 has 8 Ru-C bonds, which are stable to reduction in H_2 at 150°C; while in sample Ru@C_{60} 2/1, approximately one-third of the Ru is present as 1.5 nm metallic Ru NPs. In the latter, the remaining two-thirds Ru-C are identical to those in Ru@C_{60} 1/1 sample.

Table 2.7. Ruthenium EXAFS fits of samples Ru@C_{60} 1/1 and 2/1.

Sample	XANES Energy, keV	Scatter	N	R, Å	$\Delta\sigma^2$ (x 10^3)	Eo, eV
Ru Foil (ref.) Ref	22.1170	Ru-Ru	12	2.68	0.0	8.5
RuO_2	22.1285	Ru-O	5.8	1.97	3.0	0.5
$Ru(NH_3)_6Cl_3$	22.1268					
$Ru(NH_3)_6Cl_2$	22.1248					
Ru@C_{60} 1/1 N_2 at RT	22.1244	Ru-C	8.3	2.21	3.0	7.7
Ru@C_{60} 1/1 H_2 at 150°C	22.1244	Ru-C	8.3	2.21	3.0	8.7
Ru@C_{60} 2/1 H_2 at 150°C	22.1241	Ru-C Ru-Ru	5.1 2.2	2.21 2.63	3.0 4.0	9.4 1.5

The result of EXAFS are thus in good agreement with the tomography and theoretical DFT calculations. In magnitude of the Fourier transform spectra of Ru@C_{60} 1/1 and 2/1 show that these two samples have a different structure as displayed by tomography (polymer structure if

ratio <1, and "core-shell" structure for ratio >1). DFT calculation have confirmed that Ru is bonded to 8 carbon atoms in a stable η^2, η^6 fashion (see below).

2.2.3.7 XPS

XPS measurements were performed to characterize the oxidation state of Ru. Although ruthenium is typically analyzed in XPS by following the strong 3*d* photoelectons, here the Ru-3p region was prefered in order to avoid interferences from the carbon substrates (the binding energy of Ru-3d overlaped with the C-1s). The analysis of the two samples Ru@C_{60} 1/1 and 20/1 (Figure 2.30) shows the presence of three element Ru, C and O. The C and Ru arise from our sample, while the presence of O is probably due to Ru oxidation during sample preparation for the analysis. Compare to the 3p3/2 binding energy of pure Ru metal at 460 ev,[60] the BE of the Ru@C_{60} 1/1 (462.78 ev) and 20/1 (461.68 ev) were clearly higher.

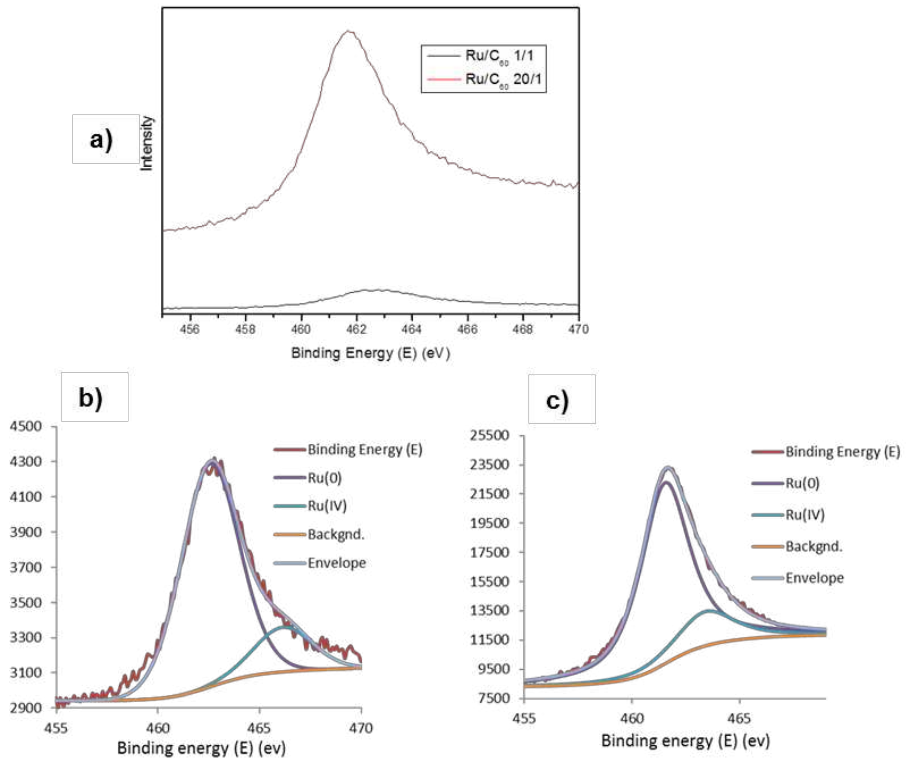

Figure 2.30. XPS spectra of the Ru@C_{60} a) binding energy of ratio 1/1and 20/1; b) Peak fitting of 1/1; and c) Peak fitting of 20/1.

For Ru@C_{60} 1/1, the Ru 3p region was divided into two components in Figure 2.30b,[61] which were indentified as Ru(0) (462.2 ev) and Ru(IV) (464.2 ev). The Ru@C_{60} 20/1 3p pattern was also deconvoluted into two components Ru(0) (461.5 ev) and Ru(IV) (463.2 ev) in Figure 2.310c. Since the sample preparation for XPS analysis is under air, the Ru will be oxided, therefore the presence of RuO_2 in our sample is reasonable. From the shift of the Ru(0) peak we deduced that the combination of Ru and C_{60} lead to a significant charge transfer as shown by Raman.

Table 2.8. Binding energy of Ru3d, C 1s and O1s

Entry	Position	FWHM	Conc.%
Ru 3d	279.9	0.7	2.9
	284.1	1.0	1.9
	280.6	1.3	0.7
	284.8	1.5	0.5
			6.0
C 1s	284.2	1.1	37.0
	285.0	1.1	29.8
	286.3	1.1	8.4
	288.7	1.0	5.7
			80.8
O 1s	531.7	1.4	5.3
	533.1	1.4	5.3
	534.5	1.6	0.7
			11.3
C1 2p			1.9

XPS analyses were also performed for sample Ru@C_{60} 10/1 in a special apparatus allowing to perform all the operation in a glove box under argon atmosphere (Figure 2.31 and Table 2.8). The results of binding energy of Ru 3d and Ru 3p (Figures 2.31-a and b) indicate the Ru is indeed in the metallic state, with only a small propostion that is oxidized, and the binding energy of C 1s (284.2 ev) suggesting the presence of C_{60}.

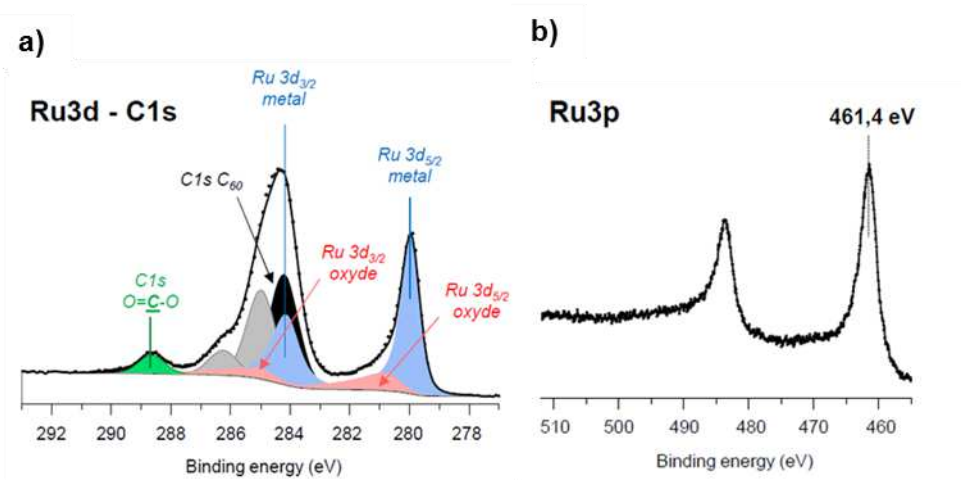

Figure 2.31. XPS spectra of the Ru/C_{60}.

2.2.3.8 DFT Calculations

There are five possible sites on C_{60} surface where Ru atoms may be adsorbed (Figure 2.32): (i) an atop site (η^1) on which the Ru atom is coordinated to a single carbon atom, (ii) a bridge site between two hexagonal rings ($\eta^{2(6\text{-}6)}$), (iii) a bridge site between pentagonal and hexagonal rings ($\eta^{2(6\text{-}5)}$) on which a Ru atom sits on the C–C bond and forms two Ru-C bonds, (iv) a hollow site above the center of a pentagonal ring of C atoms (η^5), and (v) a hollow site above the center of a hexagonal ring of C atoms (η^6).

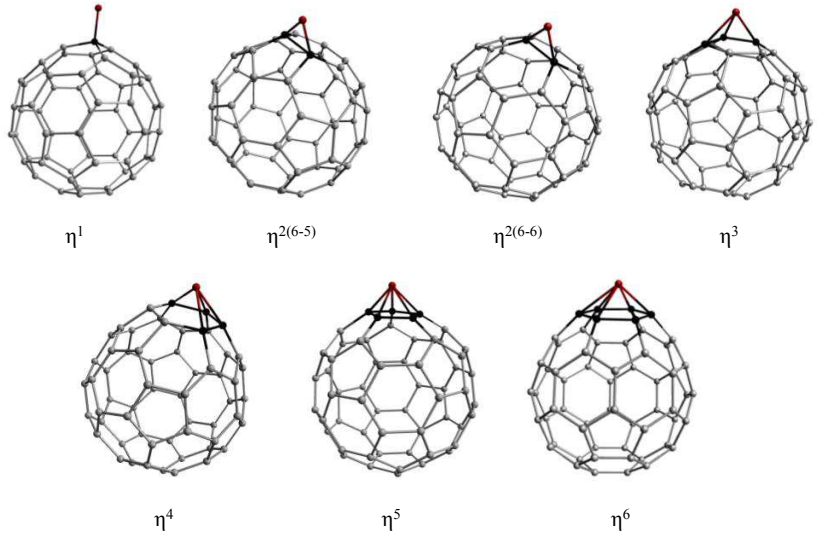

Figure 2.32. Possible metal-C_{60} bonding modes.

For a single Ru atom interacting with one C_{60}, the most stable configuration is $\eta^{2(6)}$, with an adsorption energy of -48 kcal/mol. And the following is $\eta^{2(5)}$, η^6, η^5, with energies of -39, -38, and -35 kcal/mol, respectively, while the top site is instable. The better stability of the $\eta^{2(6)}$ site is not surprising, as the double bond shared by two hexagons corresponds to a maximum of the electronic density of the fullerene. Experimentally, this coordination mode has been observed for Pt complexes and suspected for Ru ones.[62] These adsorption energies are significantly larger than the ones obtained for Ni, Au or Ta atoms for instance, with typical values smaller than -25 kcal/mol,[30, 63] but remain in very good agreement with values obtained for Rh, Ir, Pd and Pt atoms.[64] Using the same computational settings, Pt atoms bind more strongly than Ru ones on C_{60} since the adsorption energy of a Pt atom is already -66 kcal/mol. This value is also in good agreement with previously reported values.[64-65] For the $\eta^{2(6)}$ and $\eta^{2(5)}$ sites, the smallest Ru-C bond lengths are 2.06 Å. Then, the Ru-C bond length increases with the increase of adsorption energy for the different sites. For the η^6 site, two Ru-C bond-lengths are 2.25, two others Ru-C distances are 2.34 when the last ones are 2.42 Å. It means that a single Ru prefers to lie in a displaced hollow site than a highly symmetric site. Finally, the Ru-C distances in the less stable site, *i.e.* in the η^5 position, are 2.21 Å. Interestingly the most stable Ru-C_{60} complex is magnetic with a moment of 2 μ_B.

If now, we take into account the real source of Ru in the calculation, the [Ru(COD)(COT)] precursor, we have to consider that it may coordinate even when it is partially decomposed. The [Ru(COD)] species adsorbs, in a $\eta^{2(6)}$ site, with two short Ru-C bond-lengths of 2.11Å and adsorption energy of -58 kcal/mol. The η^1 site has almost the same energy but with a smaller Ru-C distance, *i.e* 2.04 Å. On the contrary, the [Ru(COT)] species has a preference for the η^1 site, with an adsorption energy of -38 kcal/mol, while the $\eta^{2(6)}$ site is 4 kcal/mol higher. However when using the following energy balances: [Ru(COD)(COT)] + C_{60} → [Ru(COT)]/C_{60} + COD or [Ru(COD)(COT)] + C_{60} → [Ru(COD)]/C_{60} + COT, meaning that we take into account the precursor dissociation energy, the energy differences become largely positive: +21 and +28 kcal/mol, respectively. As a result, the precursor has to be completely decomposed by the action of H_2 in order to allow for the creation of Ru-C_{60} bond, and no partially decomposed Ru complexes can be stabilized on the C_{60} surface. In interaction with 2 fullerenes, a single Ru atom will preferably coordinate in a η^2-η^2 position, bridging two $\eta^{2(6)}$ positions, with 4 Ru-C bond-lengths of 2.07 Å, as shown in Figure 2.33a. This complex adopts then a dumbbell like structure, as for a Ni [63a, 66] or Pt atoms.[64-65] The corresponding stabilization energy of this nonmagnetic complex is large, -44 kcal/mol, when adding a C_{60} to an existing Ru-C_{60} complex. However, this binding energy for a Ru complex is still lower than the value of -65 kcal/mol, obtained at a semi-empirical level, on a C_{60}-Pt-C_{60} complex.[65b] It suggests again that a Ru atom has a little less affinity for C_{60} than a Pt one.

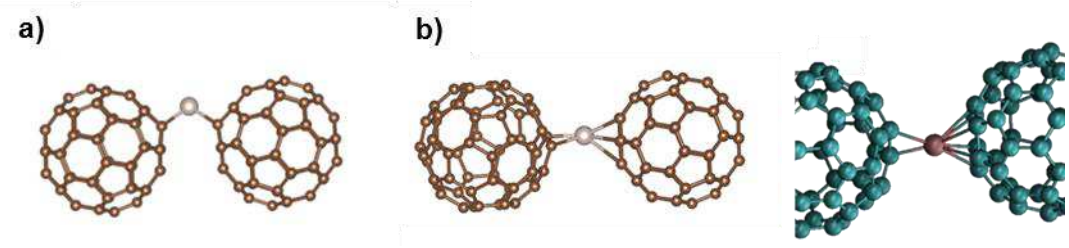

Figure 2.33. Optimized structure of the: a) $\eta^{2(6)}$-$\eta^{2(6)}$ C_{60}-Ru-C_{60} complex; and b) $\eta^{2(6)}$-η^6 C_{60}-Ru-C_{60} complex.

Interestingly, another stable structure that exhibits a $\eta^{2(6)}$-η^6 coordination mode in (Figure 2.33b), lies only 12 kcal/mol higher in energy. The corresponding Ru-C distances are ranging from 2.07 to 2.85 Å for this site that connects 8 carbons to the Ru atom.

This relatively small energy difference between the two coordination modes can be reduced by 5 extra kcal/mol due to the presence of adsorbed hydrogen atoms on the C_{60}, in the vicinity of the Ru atom, as proposed experimentally. Indeed, a significant change of the Ru coordination is observed upon H_2 adsorption since the most stable structure possesses a $\eta^{2(6)}$-η^4 character. The thermodynamics of the hydrogenation of C_{60} have been studied using DFT calculations several years ago.[67,68] Since it has been shown that the 1,2 addition of a [6,6] bond is energetically the most favorable adsorption site of a single H_2 molecule, we have used this configuration through all our calculations. Considering that we have only a partial hydrogenation of the fullerenes, we have limited our study to systems that have been hydrogenated only once, as shown in Figure 2.34. Energetically speaking, the hydrogenation of a single C_{60} is favorable with an adsorption energy of -25 kcal/mol. Since H_2 are in excess during the synthesis, and that a H_2 molecule spontaneously dissociates on the metallic center of a C_{60}-Ru-C_{60}, the presence of C_{60}-Ru$(H)_2$-C_{60} complexes are almost certain since it corresponds to more complete coordination sphere of the metal. The optimized geometry that corresponds to this state is given in Figure 2.34-a. The Ru-H distances are 1.59 Å, when the H-H one is also 1.59 Å, a clear evidence of the H_2 dissociation. The formation energy is negative: -79 kcal/mol, a value that is in the same range of the C_{60}-Ru-C_{60} complex formation energy in its η^2-η^6 configuration (-72 kcal/mol). Without discussing the migration process of the hydrides on the fullerenes, it is noteworthy that a C_{60}-Ru-$C_{60}(H)_2$ complex has almost the same energy (+1.5 kcal/mol), despite the loss of coordination of the metallic center. A side view of the corresponding structure is given in Figure 2.34b.

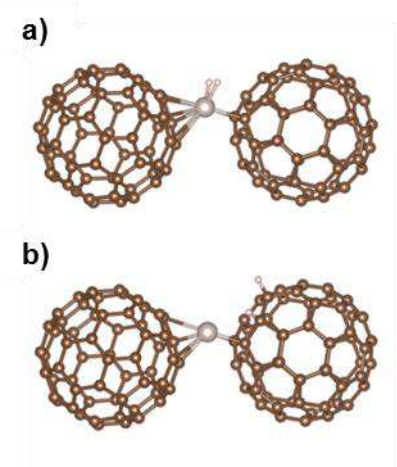

Figure 2.34. a) Optimized structure of the C_{60}-Ru$(H)_2$ -C_{60} complex; and b) Optimized structure of the C_{60}-Ru-$C_{60}(H)_2$ complex.

In the case of the dumbbell like structure (Figure 2.35a) it seems obvious that a third C_{60} can be easily coordinated to the central Ru atom. Due to the η^1 coordination mode of the third fullerene, this reaction is still thermodynamically favorable, but the energy gain is only -11 kcal/mol. This stable Ru$(C_{60})_3$ configuration (Figure 2.35c) might be viewed as a potential linker between ideal linear polymeric chains, as described in the following.

The two C_{60}-Ru-C_{60} complexes (Figure 2.35a, 2.35b) can thus be viewed as elementary bricks for hypothetical 1D chains made of -C_{60}-Ru-C_{60}- with a 1Ru/1C_{60} ratio. Figure 2.35d shows a first model made of a unit cell that contains only 1 Ru and 1 C_{60}. The corresponding optimized lattice constant is around 10.4 Å. In this particular state, the four smallest Ru-C distances are lying in 2.04 to 2.11 Å range and two others are at 2.42 and 2.45 Å, when the next nearest C atoms are 2.66 Å away. As a consequence, the Ru atom has a $\eta^{2(6)}$-η^4 coordination mode in this case. To allow for more flexibility in the coordination mode, we have also used a model made of 2 Ru atoms and 2 C_{60} in the calculation cell. As a result of rotating slightly one of the C_{60} molecule on a vertical axis, a $\eta^{2(6)}$- η^6 coordination mode is stabilized, as shown in Figure 2.35e. In this structure a Ru atom is not having a perfect hollow position with 8 different Ru-C bond-lengths: 2.04, 2.11, 2.14, 2.18, 2.34, 2.44, 2.53 and 2.57

Å. Almost the same values are yielded for the second metallic center. This coordination mode is in good agreement with EXAFS results.

If we now try to complete the coordination sphere of one Ru atom by approaching a H_2 molecule, it spontaneously dissociates and push the Ru to change its coordination to be $\eta^{2(6)}$-η^3 with two additional Ru-H distances are 1.59 Å, see Figure 2.35f. When these two hydrides are transferred to one of the C_{60}, the $\eta^{2(6)}$-η^6 coordination mode is recovered but with a slight elongation of the largest Ru-C distances, that are now between 2.60 and 2.70 Å (Figure 2.35g). In this case, the Ru atoms provide large electronic density to the neighboring C_{60}, with a charge transfer of around 0.6 e^-. This value is not surprising since as already stated C_{60} is a well-known electron acceptor and it is in reasonable agreement with Raman spectroscopy results. From the different microscopy techniques, it seems obvious that outside the spheres that contain the polymeric phase, Ru NPs are formed. To propose an answer at the molecular level of this statement, we have addressed two issues: are the thermodynamics in favor of Ru NPs formation? Could it be the solvent that protects metallic atoms and avoid Ru-Ru formation bonds?

Starting from an ideal 1D polymeric chain (Figure 2.35a), and thus adding a second metal atom or adding 2 other ones is indeed energetically favorable (Table 2.1). An interesting feature is that the lattice parameter values are increased to accommodate the creation of new Ru-C bonds, and thus could be experimentally detected.

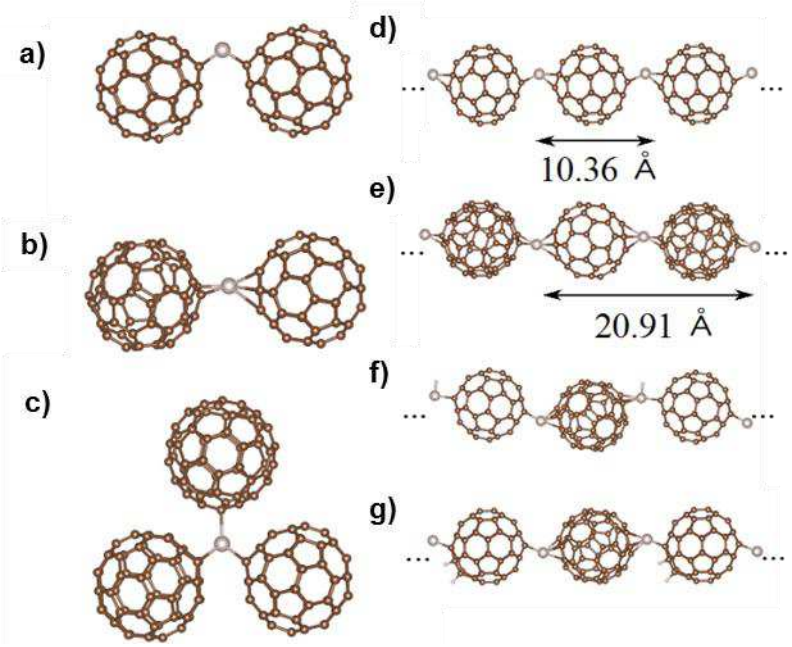

Figure 2.35. Side views of a) C_{60}-Ru-C_{60} complex in the dumbbell like structure; b) in the $\eta^{2(6)}$-η^6 coordination mode; and c)of the most stable Ru-$(C_{60})_3$ complex. Ideal 1D chains and their corresponding lattice parameters for 1 Ru/ 1 C_{60} ratio are also given: in d) for the $\eta^{2(6)}$-η^4 and in e) for the the $\eta^{2(6)}$-η^6 state. In the last two panels are given the partially hydrogenated ideal polymeric chains: in f) one Ru atom is hydrogenated or one C_{60} is in g). Ru atoms are in grey, carbon atoms in brown and H in white.

Moreover, Figure 2.36a shows that the distance between the two Ru_1-Ru_2 atoms is very unusual for metallic bond with a value of 2.28 Å. With 4 Ru atoms, see Figure 2.36b, the Ru_4-Ru_2 bond-length is 2.26 Å, the Ru_1-Ru_2 is slightly elongated (+0.09 Å) when the last one is 2.35 Å. From Table 2.1, where energy gains per Ru atom are compiled in various binding situations, *i.e.* in single complexes with different ratio Ru/C_{60}, in some ideal 1D polymeric chains or even in small cluster models and finally in the bulk, we can provide some interesting insights of the reaction media behavior. Indeed, when comparing the stabilization energies of a Ru atom involved in a 1D chain, and one in small clusters or even worse in the bulk, it is clear that Ru atoms prefer to bind to other Ru atoms. If one considers Ru_{13} cluster formation energy (-96 kcal/mol), the two processes are thermodynamically favorable. At this step, one can assume that the polymeric phase, with a ratio close to 1Ru/1C_{60} without

excluding small clusters of Ru_n ($n \leq 3$) linking fullerenes is the kinetic product of the reaction, and then larger Ru NPs are created, producing the thermodynamic products of the reaction.

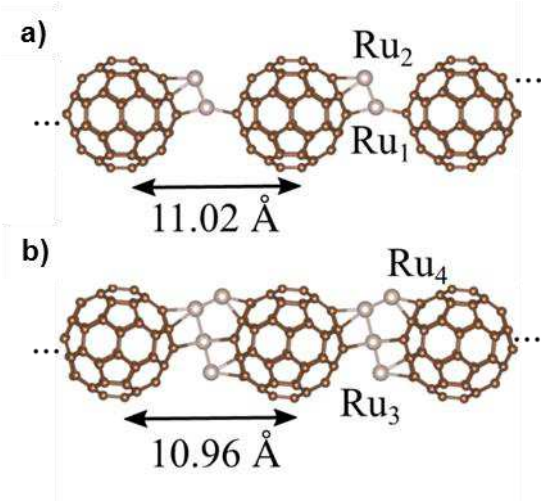

Figure 2.36. Side views and lattice parameters of Ru@C_{60}: a) ratio of Ru/C_{60} = 2/1; and b) ratio of Ru/C_{60} = 4/1. Ru atoms are in grey, carbon atoms in brown.

To support this idea we have also calculated the binding energy of Ru_{13}-$(C_{60})_x$ complexes with x up to 6. The corresponding values are slightly lower than the others values given in Table 2.1: the energy gain per C_{60} is maximal for x = 1 and x = 2, with -87 and -88 kcal/mol, respectively, and decreases when x increases: -77, -74, -61 kcal/mol. See Figure 2.37 for molecular models of the stable Ru_{13}-C_{60}, Ru_{13}-$(C_{60})_2$, and Ru_{13}-$(C_{60})_6$ complexes. It means that when fullerenes are in excess, they have also the possibility to strongly bind metallic NPs.

However, in the present theoretical picture of the system, it is not clear why the polymeric phase is stabilized and has a net preference for the 1Ru/1C_{60} ratio. To propose a reasonable explanation, at the atomic scale, we have further investigated the effects of two different solvent molecules (Figure 2.38 and Table 2.9), *i.e.* toluene and dichloromethane, on the stabilization of the polymeric phase. Since the solvent molecules interact only weakly with the metallic center, the main reason probably is a steric effect to avoid the agglomeration of Ru atoms.

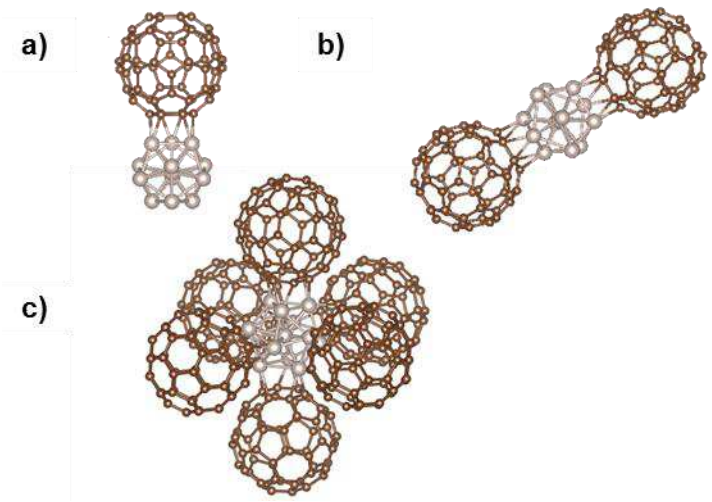

Figure 2.37. Optimized geometries of Ru_{13}-C_{60} (a), Ru_{13}-$(C_{60})_2$(b) and Ru_{13}-$(C_{60})_6$ (c) complexes. Ru atoms are in grey and carbon atoms in brown. Ru-C bonds are represented for values smaller than 2.5 Å. As a result one can identify 3 Ru atoms in η^2 positions for Ru_{13}-C_{60} system, and 3 others Ru atoms having the same coordination mode for the Ru_{13}-$(C_{60})_2$ complex. When 6 fullerenes interact with the Ru_{13} cluster, four C_{60} are bound with 3 Ru atoms, one with 2 Ru atoms and the last one is in atop position.

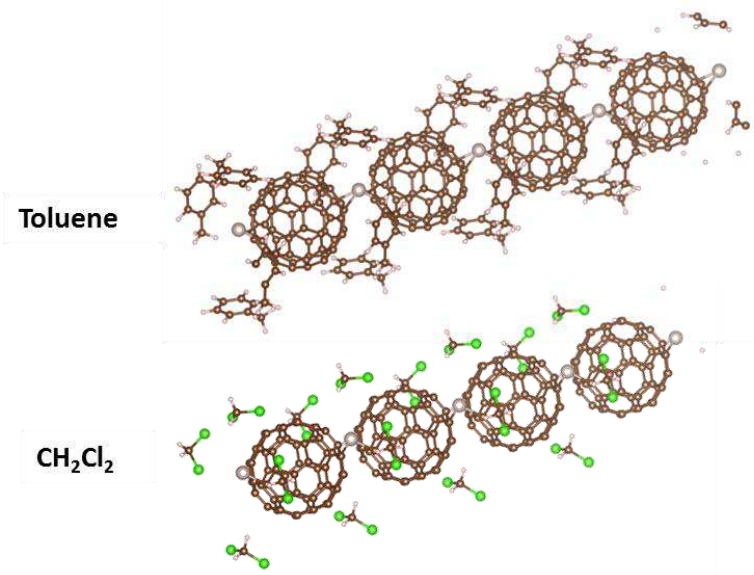

Figure 2.38. Side views of Ru-C_{60} polymer chain structure in toluene and CH_2Cl_2.

A single toluene molecule or a dichloromethane molecule interacts weakly with fullerenes, with adsorption energies of -9 and -4 kcal/mol, respectively. These energies are slightly larger when the molecules are pointing to Ru metallic center of the 1D chain model, with values of -10 and -12 kcal/mol respectively, which are typical of van der Waals interactions. In Figure

2.38-a,b, the optimal geometries with the metallic center decorated by four solvent molecules are shown. The corresponding energetic balances are similar, with binding energies of -45 kcal/mol for the interaction with 4 CH_2Cl_2 molecules and -49 kcal/mol for the toluene molecules. For the dichloromethane case, only one Cl interacts with the Ru atom with a Ru-Cl bond-length of 2.4 Å, the others neighboring atoms being above 4.4 Å. Interestingly, the Ru center is well protected by steric effects from any under-attack, due to the presence of the fullerenes. The bottom molecule has a C center placed at 5.4 Å when the three others have smaller C-Ru distances below 5 Å. This protection is even more pronounced when toluene is the reaction solvent, due to the presence of the methyl groups, stabilizing more the polymeric phase and avoiding the agglomeration of metals.

Table 2.9. Stabilization energy of RuC_{60} polymer chain structure with different numbers of solvent molecules: toluene and dichloromethane

Stabilization Energy (kcal/mol)	**CH_2Cl_2**	**C_7H_8**
Single C_{60}	-4	-9
Polymer Phase model $1C_{60}$-1Ru		
1 molecule of solvent	-10	-12
2 molecules of solvent	-25	-22
4 molecules of solvent	-45	-49

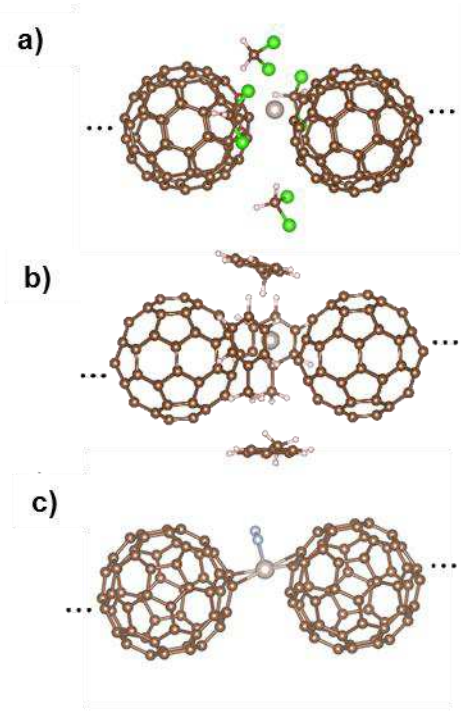

Figure 2.38. Side views of C_{60}-Ru-C_{60} complex in the dumbbell like structure (a) with the metallic center decorated by CH_2Cl_2 molecules, and (b) with toluene molecules. Panel (c) shows the resulting geometry of the adsorption of a N_2 molecule on the Ru center. Ru atoms are in grey and carbon atoms in brown, while Cl are in green, H in white, and Nitrogen in blue.

Finaly, we have also tested the effect of the interaction between the Ru atom and N_2 molecules, to exclude this interaction as a possible explanation for the coordination between 8 light elements and the Ru center as determined by the EXAFS experiments. Indeed the corresponding interaction is weak (-10 kcal/mol), meaning that when the system is heated up, the N_2 molecules should desorb. Since the EXAFS results are not thermally dependent, one can reject this hypothesis too.

2.3 Conclusions

In summary, the decomposition reaction of [Ru(COD)(COT)] in the presence of C_{60} has been investigated, and the products of the reaction characterized. The choice of the solvent affects the course of the reaction. Spherical particles are selectively produced in solvent with low viscosity and high permittivity, such as dichloromethane. The particle size depends on the nature of the solvent. According to the Ru/C_{60} ratio, these spherical particles can be surface

decorated with metallic Ru atoms, clusters (<0.6 nm) or NPs (1.5-2.5 nm), which are stabilized by C_{60}. The structure of the spherical particles has been studied. EXAFS, WAXS, and DFT calculations point to a polymeric structure, in which each Ru atoms is coordinated to two C_{60}, with a $\eta^{2(6)}$-η^6 coordination mode. Solvent molecules contribute to stabilize this fulleride. This polymeric phase is the kinetic product of the reaction. Then, at Ru/C_{60} ratio ≥ 2, larger Ru NPs are created on their surface, producing the thermodynamic products of the reaction. During the decomposition reaction under hydrogen, partial hydrogenation of the fullerene occurs, catalyzed by the ruthenium. Significant charge transfer from ruthenium to fullerene has been evidenced by Raman spectrometry and XPS for all the prepared materials, which is an important factor to take into account, particularly if we consider the possible reactivity of these fullerides. We believe that these results should open the possibility to draw important structure/properties relationships.

2.4 Experimental section

General Methods

All operations were carried out under argon atmosphere using standard Schlenk techniques or in an MBraun glovebox. Solvents were purified by standard methods or by an MBraun SPS-800 solvent purification system. [Ru(COD)(COT)] was purchased from Nanomeps Toulouse, fullerene C_{60} (99.5%) from Sigma-Aldrich, and CO and H_2 from Air Liquid. All these reactants were used as received.

The ruthenium content was established by inductively coupled plasma optical emission spectroscopy (ICP-OES) performed in a Thermo Scientific ICAP 6300 instrument. Solid state NMR (MAS-NMR) with and without ^{1}H-^{13}C cross polarization (CP) were performed at the LCC on a Bruker Avance 400WB instrument equipped with a 4 mm probe with the sample rotation frequency being set at 12 kHz unless otherwise indicated. Measurements were carried

out in a 4 mm ZrO_2 rotor. ATR-IR spectra were recorded on a Perkin-Elmer GX2000 spectrometer available in a glovebox, in the range 4000-400 cm^{-1}. The Raman spectra have been recorded with an Explora (Horiba) spectrometer in backscattering geometry using an opical objective x100 (NA 0.9). The wavelength of the incident laser has been 532nm and the laser power was set to 1mW.

TEM analyses. Some TEM and HREM analyses were performed at the "Centre de microcaracterisation Raimond Castaing, UMS 3623, Toulouse" by using a JEOL JEM 1011 CX-T electron microscope operating at 100 kV with a point resolution of 4.5 Å and a JEOL JEM 1400 electron microscope operating at 120 kV. The high resolution analyses were conduct using a JEOL JEM 2100F equipped with a Field Emission Gun (FEG) operating at 200 kV with a point resolution of 2.3 Å. The approximation of the particles mean size was made through a manual analysis of enlarged micrographs by measuring at least 200 particles on a given grid. Other TEM micrographs were acquired with a JEOL 2100F S/TEM microscope equipped with a FEG operating at 200 kV, a spherical aberration probe corrector and a GATAN Tridiem energy filter. The resolutions attained are od 2 Å and 1.1 Å under parallel TEM mode and scanning STEM modes, respectively. For STEM-HAADF analyses the spot size was of 0.13 nm, a current density of 140 pA, the camera focal length was 10 cm, corresponding to inner and outer detection angle of the annular detector of about 60 mrad and 160 mrad. For tomography experiments, the acquisitions of the tilt images series were performed using a high tilt sample holder, under angles spanning from +72 to -72 degrees, with projections taken every 2° according to Saxton scheme. The irradiation damage was limited by using low electron doses. The images were first roughly aligned using a cross-correlation algorithm. A refinement of this initial alignment and a precise determination of the tilt axis direction were then obtained using the IMOD software where the centers of several Au nanoparticles from the analyzed group were used as fiducial markers.[69] The

volume reconstructions have been computed using an iterative approach consisting of a simultaneous algebraic reconstruction technique implemented using the TOMO3D software,[70] the number of iterations not exceeding 40. Visualization and quantitative analysis of the final volumes were carried out using ImageJ software.

DFT Calculations. DFT calculations were carried out using the Vienna *ab initio* simulation package VASP.[71] The code uses the full-potential projector augmented wave (PAW) framework.[72] Exchange-correlation effects have been approximated using the PBE functional[73] and applied in spin-polarized calculations. Besides to correctly describe weak intermolecular forces between Ru-C_{60} complexes and solvent molecules, we have also used the optB86b-vdW functional.[74] We have checked that this scheme provide accurate geometries when van der Waals forces are the major bonding origin, as for instance in the C_{60} crystalline phase. A kinetic-energy cutoff of 400 eV was found to be sufficient to achieve a total-energy convergence within several meV, considering a k-point sampling with a (1×1×5) grid for the polymeric state or Gamma-point only calculations for isolated molecules and complexes, in conjunction with a gaussian smearing with a width of 0.05 eV. During geometry optimization runs and cell relaxations, all the atoms were fully relaxed until forces on individual atoms were smaller than 0.01 eV/Å. Calculation cells for isolated molecules and complexes were 25×26×27Å, to avoid spurious interactions between periodic images, when the same lattice parameters on (Ox) and (Oy) were kept fixed for the polymeric phase. Figures of the different geometries were produced thanks to the 3D visualization program VESTA.[75]

WAXS, EXAFS, and XPS analyses. Wide Angle X-ray Scattering measurements were performed at CEMES on a diffractometer dedicated to Pair Distribution Function (PDF) analysis: graphite-monochromatized Molybdenum radiation (0.07169nm), solid state detection and low background setup. Samples were sealed in Lindemann glass capillaries (diameter 1.5mm) to avoid any oxidation after filling in a glove box. For all samples data

were collected on an extended angular range (129 degrees in 2theta) with counting times of typically 150s for each of the 457 data points, thus allowing for PDF analysis. Classic corrections (polarization and absorption in cylindrical geometry) were applied before reduction and Fourier transform.

X-ray absorption measurements were made on the bending magnet beam line of the Materials Research Collaborative Access Team (MRCAT) at the Advanced Photon Source, Argonne National Laboratory. The data was collected in step-scan, transmission mode. The 3 pre-edge regions, from -250 to -50 eV, -50 to -10eV and -10 to 30eV, were scanned in 10, 5 and 0.4 eV steps, respectively. The EXAFS was also scanned in 3 regions, to 6, from 6-10 and from 10-13 Å-1. The data acquisition time in each region was increased to give a high signal to noise in the k2-weighted chi. The Ru on C_{60} samples were handled and loaded in the absence of air and water in a glove box. The samples were placed in an environmental cell for data acquisition. The samples were additionally treated in 4% H_2/He at 150°C, cooled to room temperature and data taken without exposure to air. A ruthenium foil spectrum was acquired simultaneously with each measurement for energy calibration. Samples were pressed into a cylindrical holder capable of holding 6 samples with amounts chosen to give a ruthenium edge step of ca. 0.5-1.0. The spectra were obtained at room temperature without treatment and after heating in 4% H_2/He at 150°C for 1h and cooled to RT. RuO_2, $Ru(NH_3)_6Cl_3$, $Ru(NH_3)_6Cl_2$, Ru(IV), Ru(III) and Ru(II), respectively, reference compounds were obtained from Aldrich and used to determine the shift in the XANES energy due to change in oxidation state. Phase shifts, backscattering amplitudes were obtained from reference compounds: RuO_2 (4 Ru-O at 1.99 Å and 2 Ru-O at 1.94 Å, or an average of 6 Ru-O at 1.97 Å) and Ru foil (12 Ru-Ru at 2.68 Å). The XANES edge energy was determined from the inflection point of the leading edge, i.e., the maximum in the first derivative. Standard procedures using WINXAS3.1 software were used to extract the EXAFS data. The coordination parameters

were obtained by a least square fit in k- and r-space of the isolated multiple-shell, k^2–weighted Fourier transform data. The samples were also analyzed by X-ray photoelectron spectroscopy (XPS) using a VG Escalab MKII spectrophotometer, which operated with a non monochromatized Mg K source (1253.6 eV).

Synthesis of Ru@C_{60} nanostructures

In a typical experiment the [Ru(COD)(COT)] complex was introduced in a Fisher-Porter bottle, and a solution of fullerene C_{60} in the desired solvent was then introduced in the reactor. The resulting purple solution was stirred for 30 min at room temperature, after which the bottle was pressurized with 3 bar of H_2. The solution, which turned black after few min of reaction, was kept under stirring overnight at room temperature. After this period of time, excess of H_2 was eliminated and the volume of solvent was reduced under vacuum. Pentane was then added to the colloidal suspension to precipitate the Ru@C_{60} nanostructures. After filtration under argon with a cannula, the black solid powder was washed twice with pentane and filtrated again before drying under vacuum. For each ratio studied, the quantities of reactants are detailed hereafter:

Ru@C_{60} 2/3: 16.3 mg (0.0517 mmol) of [Ru(COD)(COT)]; 55.8 mg (0.0776 mmol) of fullerene C_{60} and 250 mL of CH_2Cl_2. Yield: 52.3 mg. Ru: 6.35 %.

Ru@C_{60} 1/1: 30.0 mg (0.10 mmol) of [Ru(COD)(COT)]; 68.5 mg (0.10 mmol) of fullerene C_{60} and 300 mL of CH_2Cl_2. Yield: 68.1 mg. Ru: 10.6 %.

Ru@C_{60} 2/1: 80 mg (0.25 mmol) of [Ru(COD)(COT)]; 91.3 mg (0.126 mmol) of fullerene C_{60} and 400 mL of CH_2Cl_2. Yield: 100 mg. Ru: 16.7 %.

Ru@C_{60} 5/1: 200 mg (0.63 mmol) of [Ru(COD)(COT)]; 91.3 mg (0.126 mmol) of fullerene C_{60} and 400 mL of CH_2Cl_2. Yield:129 mg. Ru: 35.6 %.

Ru@C_{60} 10/1: 400 mg (1.27 mmol) of [Ru(COD)(COT)]; 91.3 mg (0.126 mmol) of fullerene C_{60} and 400 mL of CH_2Cl_2. Yield: 188 mg. Ru: 48.7 %.

Ru@C_{60} 20/1: 100 mg (0.32 mmol) of [Ru(COD)(COT)]; 11.4 mg (0.016 mmol) of fullerene C_{60} and 50 mL of CH_2Cl_2. Yield: 36.9 mg. Ru: 50.4 %.

Ru@C_{60} 30/1: 150 mg (0.48 mmol) of [Ru(COD)(COT)]; 11.4 mg (0.016 mmol) of fullerene C_{60} and 50 mL of CH_2Cl_2. Yield: 48 mg. Ru: 54.7 %.

Ru@C_{60} 50/1: 250 mg (0.79 mmol) of [Ru(COD)(COT)]; 11.4 mg (0.016 mmol) of fullerene C_{60} and 50 mL of CH_2Cl_2. Yield: 80 mg. Ru: 61.9 %.

T-Ru@C_{60} 1/1: 30 mg (0.10 mmol) of [Ru(COD)(COT)]; 68.5 mg (0.10 mmol) of fullerene C_{60} and 100 mL of toluene. Yield: 67 mg. Ru: 6.8 %.

T-Ru@C_{60} 10/1: 131 mg (0.415 mmol) of [Ru(COD)(COT)]; 30 mg (0.0416 mmol) of fullerene C_{60} and 50 mL of toluene. Yield: 51 mg. Ru: 15.7 %.

T-Ru@C_{60} 20/1: 262 mg (0.820 mmol) of [Ru(COD)(COT)]; 30 mg (0.0416 mmol) of fullerene C_{60} and 50 mL of toluene. Yield: 71 mg. Ru: 35.4 %.

T-Ru@C_{60} 55/1: 240 mg (0.764 mmol) of [Ru(COD)(COT)]; 10 mg (0.0139 mmol) of fullerene C_{60} and 15 mL of toluene. Yield: 55 mg. Ru: 47.5 %.

In situ growth reaction for mechanistic study: The reaction was performed at -20 °C following the standard procedure: 20 mg (0.064 mmol) of [Ru(COD)(COT)]; 23 mg (0.032 mmol) of fullerene C_{60} and 50 mL of CH_2Cl_2. The reaction was followed by sampling the mixture over the time.

Surface reactivity with CO: The adsorption of carbon monoxide on the surface of the nanostructures was performed in the solid state as follows. A purified sample of nanoparticles

was introduced in a Fischer-Porter bottle. The reactor was pressurized with 1.5 bar of CO for 72 h. Then, the CO gas was evacuated under vacuum for 20 min and the ATR-IR spectra were recorded.

Solvent effect of viscosity and permittivity: 20 mg (0.064 mmol) of [Ru(COD)(COT)] were added to a solution of 23 mg (0.032 mmol) fullerene C_{60} in a mixture of solvents, then the resulting purple solution was stirred for 30 min at room temperature, after which the bottle was pressurized with 3 bar of H_2. The solution was stirred overnight at room temperature. After this period of time, excess of H_2 was eliminated and the volume of solvent was reduced under vacuum. Pentane was then added to the colloidal suspension to precipitate the Ru@C_{60} nanostructures. After filtration under argon with a cannula, the black solid powder was washed twice with pentane and filtrated again before drying under vacuum.

The comparison reaction with "core-shell" structure synthesis: The Ru@C_{60} 1/1 was synthesized as described above. The excess of H_2 was eliminated of the reaction mixture after being stirred overnight at room temperature. 9.0 eq [Ru(COD)(COT)] were introduced to the Fisher-Portter bottle and the reaction mixture was treated in an ultrasound bath for 5 min. The bottle was pressurized again with 3 bar of H_2. The black suspension was kept under stirring overnight at room temperature. After this period of time, a sample of the mixture was analysed by TEM.

2.5 References

1. Giacalone, F.; Martín, N.; Wudl, F., Fullerene-containing polymers: An overview. in *Fullerene Polymers*, Wiley-VCH Verlag GmbH & Co. KGaA: 2009; pp 1-14.

2. (a) Coq, B.; Marc Planeix, J.; Brotons, V., Fullerene-based materials as new support media in heterogeneous catalysis by metals. *Appl. Catal., A.* **1998,** *173* (2), 175-183; (b) Goldshleger, N. F., Fullerene and fullerene based materials in catalysis. *Fullerene Sci. Techn.* **2001,** *9* (3), 255-280; (c) Chapter 7 Heterogeneous catalysis on nanostructured carbon material supported catalysts. In *Nanostructured Carbon Materials for Catalysis*, The Royal Society of Chemistry: 2015; pp 312-411.

3. Loutfy, R.; Katagiri, S., Fullerene materials for lithium-ion battery applications. In *Perspectives of Fullerene Nanotechnology*, Õsawa, E., Ed. Springer Netherlands: 2002; pp 357-367.

4. Sherigara, B. S.; Kutner, W.; D'Souza, F., Electrocatalytic properties and sensor applications of fullerenes and carbon nanotubes. *Electroanalysis* **2003,** *15* (9), 753-772.

5. Brosseau, C., Emerging technologies of plastic carbon nanoelectronics: A review. *Surf. Coat. Tech.,* **2011,** *206* (4), 753-758.

6. Rosseinsky, M. J., Recent developments in the chemistry and physics of metal fullerides. *Chem. Mater.* **1998,** *10* (10), 2665-2685.

7. Riccò, M.; Shiroka, T.; Belli, M.; Pontiroli, D.; Pagliari, M.; Ruani, G.; Palles, D.; Margadonna, S.; Tomaselli, M., Unusual polymerization in the Li_4C_{60} fulleride. *Phys. Rev. B* **2005,** *72* (15), 155437.

8. Ivanova, V. N., Fullerene compounds with transition metals M_nC_{60}: Preparation, structure, and properties. *J. Struct. Chem.,* **2000,** *41* (1), 135-148.

9. (a) Rosseinsky, M. J., Fullerene intercalation chemistry. *J. Mate. Chem.* **1995,** *5* (10), 1497-1513; (b) Yildirim, T.; Zhou, O.; Fischer, J. E., Intercalation compounds of fullerenes I: Synthesis, characterization, and solid state properties. In *The Physics of Fullerene-Based and Fullerene-Related Materials*, Andreoni, W., Ed. Springer Netherlands: 2000; Vol. 23, pp 23-66.

10. Nagashima, H.; Nakaoka, A.; Saito, Y.; Kato, M.; Kawanishi, T.; Itoh, K., $C_{60}Pd_n$: the first organometallic polymer of buckminsterfullerene. *J. Chem. Soc., Chem. Commun.* **1992,** 377-379.

11. Winkler, K.; Noworyta, K.; Kutner, W.; Balch, A. L., Study of redox active C_{60} /Pd films by simultaneous cyclic voltammetry and piezoelectric microgravimetry at an electrochemical quartz crystal microbalance. *J. Electrochem. Soc.,* **2000,** *147* (7), 2597-2603.

12. Norin, L.; Jansson, U.; Dyer, C.; Jacobsson, P.; McGinnis, S., On the existence of transition-metal fullerides: deposition and characterization of Ti_xC_{60}. *Chem. Mater.,* **1998,** *10* (4), 1184-1190.

13. Dias, G. H. M., Fullerene-60 and platinafullerene-60. *Quimica Nova* **1995,** *18* (6), 592-596.

14. Lavrentiev, V.; Abe, H.; Yamamoto, S.; Naramotoand, H.; Narumi, K., Co and C_{60} interaction under conditionsof mixture. *Mol. Cryst. Liq. Cryst.*, **2002,** *386* (1), 139-143.

15. Wohlers, M.; Herzog, B.; Belz, T.; Bauer, A.; Braun, T.; Rühle, T.; Schlögl, R., Ruthenium-C_{60} compounds: properties and catalytic potential. *Synth. Met.,* **1996,** *77* (1–3), 55-58.

16. Talyzin, A. V.; Jansson, U., A comparative Raman study of some transition metal fullerides. *Thin Solid Films,* **2003,** *429* (1–2), 96-101.

17. Gurav, A. S.; Duan, Z.; Wang, L.; Hampden-Smith, M. J.; Kodas, T. T., Synthesis of fullerene-rhodium nanocomposites via aerosol decomposition. *Chem. Mater.,* **1993,** *5* (2), 214-216.

18. (a) Cowley, J. M.; Liu, M. Q.; Ramakrishna, B. L.; Peace, T. S.; Wertsching, A. K.; Pena, M. R., A new type of metal-fulleride structure: $C_{60}Pd_3$. *Carbon,* **1994,** *32* (4), 746-748; (b) Talyzin, A. V.; Dzwilewski, A.; Pudelko, M., Formation of palladium fullerides and their thermal decomposition into palladium nanoparticles. *Carbon,* **2007,** *45* (13), 2564-2569; (c) Winkler, K.; Noworyta, K.; de Bettencourt-Dias, A.; Sobczak, J. W.; Wu, C.-T.; Chen, L.-C.; Kutner, W.; Balch, A. L., Structure and properties of C_{60}-Pd films formed by electroreduction of C_{60} and palladium(II) acetate trimer: evidence for the presence of palladium nanoparticles. *J. Mater.Chem.,* **2003,** *13* (3), 518-525.

19. Braun, T.; Wohlers, M.; Belz, T.; Nowitzke, G.; Wortmann, G.; Uchida, Y.; Pfänder, N.; Schlögl, R., Fullerene-based ruthenium catalysts: a novel approach for anchoring metal to carbonaceous supports. I. Structure. *Catal. Lett.,* **1997,** *43* (3-4), 167-173.

20. Rousseau, G.; Lavenn, C.; Cardenas, L.; Loridant, S.; Wang, Y.; Hahn, U.; Nierengarten, J.-F.; Demessence, A., One-pot synthesis of sub-3 nm gold nanoparticle networks connected by thio-based multidentate fullerene adducts. *Chem. Commun.,* **2015,** *51* (31), 6730-6733.

21. Lavrentiev, V.; Abe, H.; Naramoto, H.; Sakai, S.; Narumi, K., Polymeric chains in C_{60} and Co mixture. *Chem. Phys. Lett.,* **2006,** *424* (1-3), 101-104.

22. Östling, D.; Rosén, A., Electronic properties of the C_{60} molecule doped with potassium. *Chem. Phys. Lett.,* **1993,** *202* (5), 389-393.

23. Roques, J.; Calvo, F.; Spiegelman, F.; Mijoule, C., Nucleation of a sodium droplet on C_{60}. *Phys. Rev., B* **2003,** *68* (20), 205412-1/6.

24. Pitarch-Ruiz, J.; Evangelisti, S.; Maynau, D., Ab initio study of the C_{60}+Na system. *J. Mol. Struc-Theochem,* **2004,** *681* (1-3), 203-207.

25. Ramaniah, L. M.; Boero, M., Mobility of a single alkali metal atom on fullerene C_{60}: First principles molecular dynamical study. *J. Chem. Phys.,* **2010,** *133* (13), 134701-1/7.

26. Andriotis, A. N.; Menon, M.; Froudakis, G. E., Contrasting bonding behaviors of 3d transition metal atoms with graphite and C_{60}. *Phys, Rev. B* **2000,** *62* (15), 9867-9871.

27. Andriotis, A. N.; Menon, M., Geometry and bonding in small $(C_{60})_nNi_m$ clusters. *Phys. Rev. B* **1999,** *60* (7), 4521-4524.

28. Shukla, M. K.; Dubey, M.; Leszczynski, J., Theoretical investigation of electronic structures and properties of C_{60}-Gold nanocontacts. *ACS Nano* **2008,** *2* (2), 227-234.

29. Zeng, Q.; Chu, X.; Yang, M.; Wu, D.-Y., Spin–orbit coupling effect on Au-C_{60} interaction: A density functional theory study. *Chem.Phys.,* **2012,** *395*, 82-86.

30. Ramaniah, L. M.; Boero, M.; Laghate, M., Tantalum-fullerene clusters: A first-principles study of static properties and dynamical behavior. *Phys. Rev. B* **2004,** *70* (3), 035411-1/12.

31. Matsubara, M.; Massobrio, C.; Ramaniah, L. M.; Ruiz, E.; Boero, M., Electronic structure and localization properties of $C_{60}Ta_n$ clusters (n = 1, 3): A first-principles study. *Phys. Rev. B* **2010,** *81* (19), 195433-1/7.

32. Loboda, O., *Quantum-chemical studies on Porphyrins, Fullerenes and Carbon Nanostructures, Carbon Nanostructures*. Springer-Verlag Berlin, Heidelberg 2013.

33. Chaudret, B., Organometallic approach to nanoparticles synthesis and self-organization. *C. R. Phys.* **2005,** *6* (1), 117-131.

34. Marcus, Y.; Smith, A. L.; Korobov, M.; Mirakyan, A.; Avramenko, N.; Stukalin, E., Solubility of C_{60} fullerene. *J. Phys. Chem. B* **2001,** *105* (13), 2499-2506.

35. Ruoff, R.; Tse, D. S.; Malhotra, R.; Lorents, D. C., Solubility of fullerene (C_{60}) in a variety of solvents. *J. Phys. Chem.,* **1993,** *97* (13), 3379-3383.

36. Haynes, W. M., *CRC handbook of chemistry and physics*. CRC press: 2014.

37. Vauthier, C.; Bouchemal, K., Methods for the preparation and manufacture of polymeric nanoparticles. *Pharm. Res.* **2009,** *26* (5), 1025-1058.

38. (a) Mabille, C.; Leal-Calderon, F.; Bibette, J.; Schmitt, V., Monodisperse fragmentation in emulsions: Mechanisms and kinetics. *EPL (Europhysics Letters)* **2003,** *61*(5), 708; (b) Paleos, C. M.; Tsiourvas, D., Molecular recognition and hydrogen-bonded amphiphiles. In *Colloid Chemistry II*, Springer: 2003; pp 1-29.

39. Smoukov, S. K.; Tian, T.; Vitchuli, N.; Gangwal, S.; Geisen, P.; Wright, M.; Shim, E.; Marquez, M.; Fowler, J.; Velev, O. D., Scalable liquid shear-driven fabrication of polymer nanofibers. *Adv. Mater.* **2015,** *27* (16), 2642-2647.

40. Gambill, W., How to estimate mixtures viscosities. *Chem. Eng.* **1959,** *66*, 151-152.

41. Jouyban, A.; Soltanpour, S.; Chan, H.-K., A simple relationship between dielectric constant of mixed solvents with solvent composition and temperature. *Int. J. Pharm.* **2004,** *269* (2), 353-360.

42. Schmitt, V.; Leal-Calderon, F.; Bibette, J., Preparation of monodisperse particles and emulsions by controlled shear. *Top. Curr. Chem.* **2003,** *227*, 195-215.

43. Nagashima, H.; Nakaoka, A.; Saito, Y.; Kato, M.; Kawanishi, T.; Itoh, K., $C_{60}Pd_n$: the first organometallic polymer of buckminsterfullerene. *J. Chem. Soc., Chem. Commun.* **1992,** (4), 377-379.

44. Grądzka, E.; Wysocka-Żołopa, M.; Winkler, K., In Situ Conductance Studies of Two-Component C_{60}-Pd Polymer. *J. Phys. Chem. C* **2014,** *118* (26), 14061-14072.

45. (a) Bowles, F. L.; Olmstead, M. M.; Balch, A. L., Preparation and Crystallographic Characterization of $C_{60}\{\eta^1$-Ru $(CO)_2(\eta^5$-$C_5H_5)\}_2$: A Locally Crowded Organometallic Fullerene Without the Usual η^2-Bonding. *J. Am. Chem. Soc.* **2014,** *136* (9), 3338-3341; (b) Lee, K.; Hsu, H.-F.; Shapley, J. R., Coordination of C_{60} to Penta-and Hexaruthenium Cluster Frames. *Organometallics* **1997,** *16* (18), 3876-3877.

46. Chase, S. J.; Bacsa, W. S.; Mitch, M. G.; Pilione, L. J.; Lannin, J. S., Surface-enhanced Raman scattering and photoemission of C_{60} on noble-metal surfaces. *Phys. Rev. B* **1992,** *46* (12), 7873-7877.

47. Talyzin, A.; Jansson, U., A comparative Raman study of some transition metal fullerides. *Thin Solid Films* **2003,** *429* (1), 96-101.

48. Wang, K.-A.; Wang, Y.; Zhou, P.; Holden, J.; Ren, S.-l.; Hager, G.; Ni, H.; Eklund, P.; Dresselhaus, G.; Dresselhaus, M., Raman scattering in C_{60} and alkali-metal-doped C_{60} films. *Phys. Rev. B* **1992,** *45* (4), 1955-1958.

49. Talyzin, A.; Dzwilewski, A.; Pudelko, M., Formation of palladium fullerides and their thermal decomposition into palladium nanoparticles. *Carbon* **2007,** *45* (13), 2564-2569.

50. Martin, M. C.; Koller, D.; Rosenberg, A.; Kendziora, C.; Mihaly, L., Infrared and Raman evidence for dimers and polymers in RbC_{60}. *Phys. Rev. B* **1995,** *51* (5), 3210-3213.

51. Darwish, A. D.; Avent, A. G.; Taylor, R.; Walton, D. R. M., Structural characterization of $C_{60}H_{18}$; a C_{3v} symmetry crown. *J. Chem. Soc., Perkin Trans. 2* **1996,** 2051-2054.

52. Bini, R.; Ebenhoch, J.; Fanti, M.; Fowler, P. W.; Leach, S.; Orlandi, G.; Ruchardt, C.; Sandall, J. P. B.; Zerbetto, F., The vibrational spectroscopy of $C_{60}H_{36}$: an experimental and theoretical study. *Chem. Phys.* **1998,** *232*, 75-94.

53. (a) Talyzin, A. V.; Tsybin, Y. O.; Schaub, T. M.; Mauron, P.; Shulga, Y. M.; Zuettel, A.; Sundqvist, B.; Marshall, A. G., Composition of hydrofullerene mixtures produced by C_{60} reaction with hydrogen gas revealed by high-resolution mass spectrometry. *J. Phys. Chem. B* **2005,** *109*, 12742-12747; (b) Talyzin, A. V.; Tsybin, Y. O.; Purcell, J. M.; Schaub, T. M.; Shulga, Y. M.; Noreus, D.; Sato, T.; Dzwilewski, A.; Sundqvist, B.; Marshall, A. G., Reaction of hydrogen gas with C_{60} at elevated pressure and temperature: hydrogenation and cage fragmentation. *J. Phys. Chem. A* **2006,** *110*, 8528-8534.

54. (a) Luzan, S. M.; Tsybin, Y. O.; Talyzin, A. V., Reaction of C_{60} with hydrogen gas: in situ monitoring and pathways. *J. Phys. Chem. C* **2011,** *115*, 11484-11492; (b) Talyzin, A. V.; Shulga, Y. M.; Jacob, A., Comparative study of hydrofullerides $C_{60}H_x$ synthesized by direct and catalytic hydrogenation. *Appl. Phys. A: Mater. Sci. Process.* **2004,** *78*, 1005-1010.

55. Becker, L.; Evans, T. P.; Bada, J. L., Synthesis of [hydrogenated fullerene] $C_{60}H_2$ by rhodium-catalyzed hydrogenation of C_{60}. *J. Org. Chem.* **1993,** *58* (27), 7630-7631.

56. Konarev, D. V.; Khasanov, S. S.; Nakano, Y.; Otsuka, A.; Yamochi, H.; Saito, G.; Lyubovskaya, R. N., Linear coordination fullerene C_{60} polymer $[\{Ni(Me_3P)_2\}(\mu$-η^2,η^2-$C_{60})]_\infty$ bridged by zerovalent nickel atoms. *Inorg. Chem.* **2014,** *53*, 11960-11965.

57. (a) Wuu, Y. M.; Zou, C.; Wrighton, M. S., Thermal reactions of tricarbonylbis(ethene)ruthenium with acrylic, nonconjugated dienes and photochemistry of $Ru(CO)_4(\eta^2$-diene) complexes. *Inorg. Chem.* **1988,** *27*, 3039-3044; (b) Wuu, Y. M.; Bentsen, J. G.; Brinkley, C. G.; Wrighton, M. S., Photochemical formation of mononuclear bis- and tris(ethylene) complexes from irradiation of iron pentacarbonyl or triruthenium dodecacarbonyl: species involved in catalytic alkene isomerization. *Inorg. Chem.* **1987,** *26*, 530-40; (c) Ingham, S. L.; Magennis, S. W., The synthesis, structure and selected reactivity of a series of tricarbonyl ruthenium complexes with 1,3-dienes and heterodienes. *J. Organomet. Chem.* **1999,** *574*, 302-310.

58. (a) Lara, P.; Ayvali, T.; Casanove, M.-J.; Lecante, P.; Mayoral, A.; Fazzini, P.-F.; Philippot, K.; Chaudret, B., On the influence of diphosphine ligands on the chemical order in small RuPt nanoparticles: combined structural and surface reactivity studies. *Dalton Trans.* **2013,** *42*, 372-382; (b) Qi, X.; Axet, M. R.; Philippot, K.;

Lecante, P.; Serp, P., Seed-mediated synthesis of bimetallic ruthenium-platinum nanoparticles efficient in cinnamaldehyde selective hydrogenation. *Dalton Trans.* **2014,** *43*, 9283-9295.

59. Miller, J. T.; Kropf, A. J.; Zha, Y.; Regalbuto, J. R.; Delannoy, L.; Louis, C.; Bus, E.; van Bokhoven, J. A., The effect of gold particle size on Au-Au bond length and reactivity toward oxygen in supported catalysts. *J. Catal.* **2006,** *240* (2), 222-234.

60. Kötz, R.; Lewerenz, H.; Stucki, S., XPS studies of oxygen evolution on Ru and RuO_2 anodes. *J. Electrochem. Soc.* **1983,** *130* (4), 825-829.

61. Chen, M.-Y.; Huang, Y.-B.; Pang, H.; Liu, X.-X.; Fu, Y., Hydrodeoxygenation of lignin-derived phenols into alkanes over carbon nanotube supported Ru catalysts in biphasic systems. *Green Chem.* **2015,** *17* (3), 1710-1717.

62. Fagan, P. J.; Calabrese, J. C.; Malone, B., The chemical nature of buckminsterfullerene (c_{60}) and the characterization of a platinum derivative. *Science* **1991,** *252* (5009), 1160-1161.

63. (a) Andriotis, A. N.; Menon, M., Geometry and bonding in small $(C_{60})_nNi_m$ clusters. *Phys. Rev. B* **1999,** *60* (7), 4521; (b) Zeng, Q.; Chu, X.; Yang, M.; Wu, D.-Y., Spin–orbit coupling effect on Au-C_{60} interaction: A density functional theory study. *Chem. Phys.* **2012,** *395*, 82-86.

64. Loboda, O., *Quantum-chemical studies on porphyrins, fullerenes and carbon nanostructures*. Springer Science & Business Media: 2012.

65. (a) Nagashima, H.; Kato, Y.; Yamaguchi, H.; Kimura, E.; Kawanishi, T.; Kato, M.; Saito, Y.; Haga, M.; Itoh, K., Synthesis and Reactions of Organoplatinum Compounds of C_{60}, $C_{60}Pt_n$. *Chem. Lett.* **1994,** (7), 1207-1210; (b) Voityuk, A. A., Thermochemistry of Pt-fullerene complexes: semiempirical study. *J. Phys. Chem. A* **2009,** *113* (43), 11801-11808.

66. Huang, Y.; Freiser, B. S., Synthesis of bis (buckminsterfullerene) nickel cation, $Ni(C_{60})^{2+}$, in the gas phase. *J. Am. Chem. Soc.* **1991,** *113* (21), 8186-8187.

67. Okamoto, Y., Ab initio investigation of hydrogenation of C_{60}. *J. Phys. Chem. A* **2001,** *105* (32), 7634-7637.

68. Yi, J.-Y.; Bernholc, J., Hydrogenation effect on the structural transition of C_{60}. *Chem. Phys. Lett.* **2005,** *403* (4), 359-362.

69. Kremer, J. R.; Mastronarde, D. N.; McIntosh, J. R., Computer visualization of three-dimensional image data using IMOD. *J. struct. bio.* **1996,** *116* (1), 71-76.

70. Messaoudii, C.; Boudier, T.; Sanchez Sorzano, C. O.; Marco, S., TomoJ: tomography software for three-dimensional reconstruction in transmission electron microscopy. *BMC Bioinformatics* **2007,** *8*, 288.

71. (a) Kresse, G.; Furthmüller, J., Efficiency of ab-initio total energy calculations for metals and semiconductors using a plane-wave basis set. *Comput. Mater. Sci.* **1996,** *6* (1), 15-50; (b) Kresse, G.; Hafner, J., Ab initiomolecular dynamics for liquid metals. *Phys. Rev. B* **1993,** *47* (1), 558-561; (c) Kresse, G.; Furthmüller, J., Efficient iterative schemes for ab initio total-energy calculations using a plane-wave basis set. *Phys. Rev. B* **1996,** *54* (16), 11169; (d) Kresse, G.; Hafner, J., Ab initiomolecular-dynamics simulation of the liquid-metal-amorphous-semiconductor transition in germanium. *Phys. Rev. B* **1994,** *49* (20), 14251-14269.

72. (a) Blöchl, P. E., Projector augmented-wave method. *Phys. Rev. B* **1994,** *50* (24), 17953-17979; (b) Kresse, G.; Joubert, D., From ultrasoft pseudopotentials to the projector augmented-wave method. *Phys. Rev. B* **1999,** *59* (3), 1758.

73. Perdew, J. P.; Burke, K.; Ernzerhof, M., Generalized gradient approximation made simple. *Phys. Rev. Lett.* **1996,** *77* (18), 3865.

74. (a) Klimeš, J.; Bowler, D. R.; Michaelides, A., Van der Waals density functionals applied to solids. *Phys. Rev. B* **2011,** *83* (19); (b) Roman-Perez, G.; Soler, J. M., Efficient implementation of a van der waals density functional: application to double-wall carbon nanotubes. *Phys. Rev. Lett.* **2009,** *103* (9), 096102; (c) Klimes, J.; Bowler, D. R.; Michaelides, A., Chemical accuracy for the van der Waals density functional. *J. Phys. Condens. Matter.* **2010,** *22* (2), 022201.

75. Momma, K.; Izumi, F., VESTA 3 for three-dimensional visualization of crystal, volumetric and morphology data. *J. Appl. Crystallogr.* **2011,** *44* (6), 1272-1276.

Chapter 3 Synthesis and characterization of ruthenium nanostructures based on functionalized fullerene

3.1 Introduction

Ordered assemblies of metallic nanoparticles have found many applications in different fields including catalysis, and electronics.[1] [2] [3] Uniform nanostructures, which present excellent catalytic and electronic properties because of their size[4] and shape[5], are synthesized in the presence of stabilizing agents. The assembly of metallic nanoparticles with different building blocks has been the subject of intensive work in the past few years. The properties of these hybrid structures are interesting from a fundamental point of view, and these objects are currently envisaged to be applied. Indeed they can address many cutting-edge applications like plasmonic,[6] sensoric,[7] or catalysis,[8] where it has been shown that the proximity of NPs may affect their catalytic performances and their stability.[9]

Functionalized fullerenes are interesting building blocks to create ordered metal NP assemblies due to the directionality of the directing groups present on the fullerene moiety. Thiol-functionalized fullerene/gold nanoparticles (Au NPs/C_{60}) structures have been reported by Fujihara and Naaki in 2001.[10] Also the self-assembly reaction of a thiol functionalized fullerene with gold nanoparticles was disclosed by Sudeep and co-workers.[11] In this work (Figure 3.1), photoelectron-chemical measurements demonstrate that the nanocore (Au NPs) of the nano-assemblies (Au/S-C_{60}) play an important role on mediating the charge transport process.

Other fullerene thiol derivatives have been reported as linker to stabile Au NPs.[12,13] In addition, Geng *et al*. report a novel approach to synthesize metallic NPs/ functionalized fullerene in 2010.[14] In this work, the Au NPs were attached by 4-aminobenzenethiol/1-hexanethiol and then Au/functionalized C_{60} was prepared through the amination reaction of fullerene C_{60} and peripheral amino groups, which were located on the gold surface.

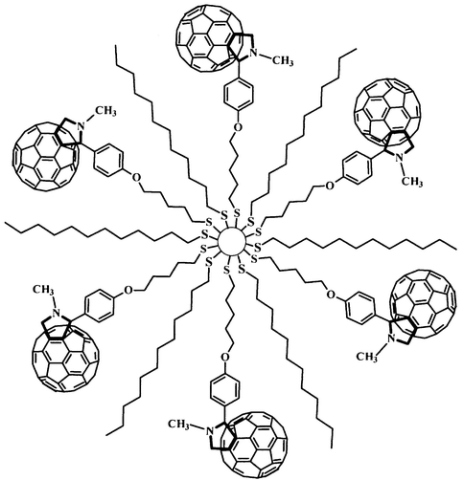

Figure 3.1. Gold Nps/Thiol-functionalized fullerene (Au NPs/C_{60}) structures. From ref.[11]

In contrast with thiol functionalized fullerene that have been intensively studied, there are few examples of N-containing functionalized C_{60} associate with metal nanoparticles. A gold nanostructure Au NPs/N-functionalized fullerene was prepared from gold nanoparticles and a C_{60}-pyrrolidine derivative.[15,16,17] For example, a nano-assembly was synthesized by reduction of aqueous $HAuCl_4$ in presence of the C_{60}-pyrrolidine derivative (Figure 3.2.)[15] Here, the authors attributted the driving force of the formation of the nano-assemblies to the interaction between the negatively charged Au NPs and positively charged functionalized fullerenes.

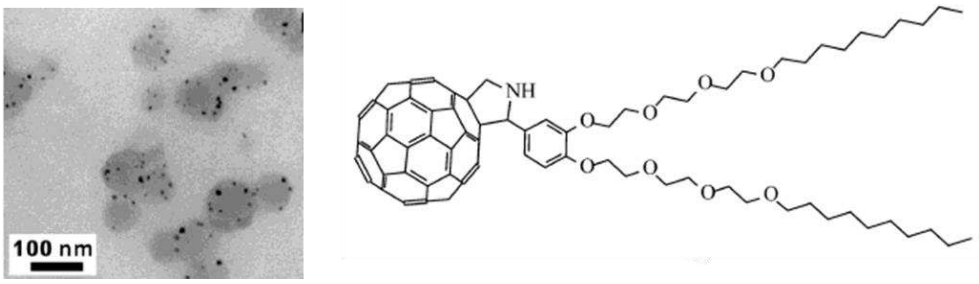

Figure 3.2. Gold nanoparticles/C_{60}-pyrrolidine derivative (Au NPs/C_{60}) structures. From ref.[15]

The T_h-hexa-adduct fullerene compounds, as representative example of symmetrical multi-functional fullerene, are usually treated as potential building blocks to construct nanoobjects.[18,19] However, few examples have been focus on the assembly of symmetrical functional fullerene C_{60} and metal nanoparticles. Recently, a Au

NPs/hexa-adducted-fullerene nanostructure was synthesized by Rousseau and co-workers (Figure 3.3).[20] In this structure, it is proposed that the Au NPs linked by the hexa-adducted-fullerenes formed a three dimensional structures and the inter-particular distance was verified by XRD.

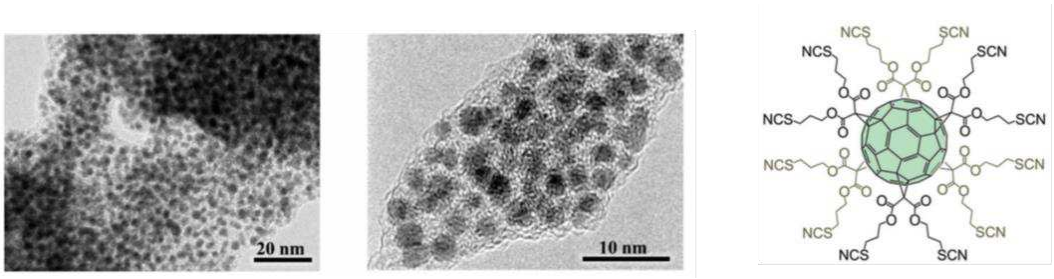

Figure 3.3. TEM image of Au NPs/C_{60} nanostructures. From ref.[20]

Except this, many ordered fullerene materials have been prepared by the assembly of functionalized fullerene C_{60}.[21] With these results in mind and with the objective to synthesise ordered nano-objects we describe here the synthesis of metallic nanoparticles and fullerene hexa-adducted assemblies.

3.2 Results and discussion

With the aim to build ordered hybrid materials containing Ru NPs together with nanometric-sized organic spacers, several hexa-substituted fullerene compounds, which contain amines or carboxylic acids as linking groups have been proposed (Figure 3.4). This work was performed in collaboration (through a scientific mission) with a team internationally recognized for his expertise on fullerene chemistry, the Nazario Martin Group in Madrid, Spain. Compounds **1**-**4** have been synthesized using the Bingel-Hirsch reaction,[22,23] where a bromomalonate compound reacts in the presence of a base with a [6,6] double bonds of the fullerene to give the cyclopropane derivative.

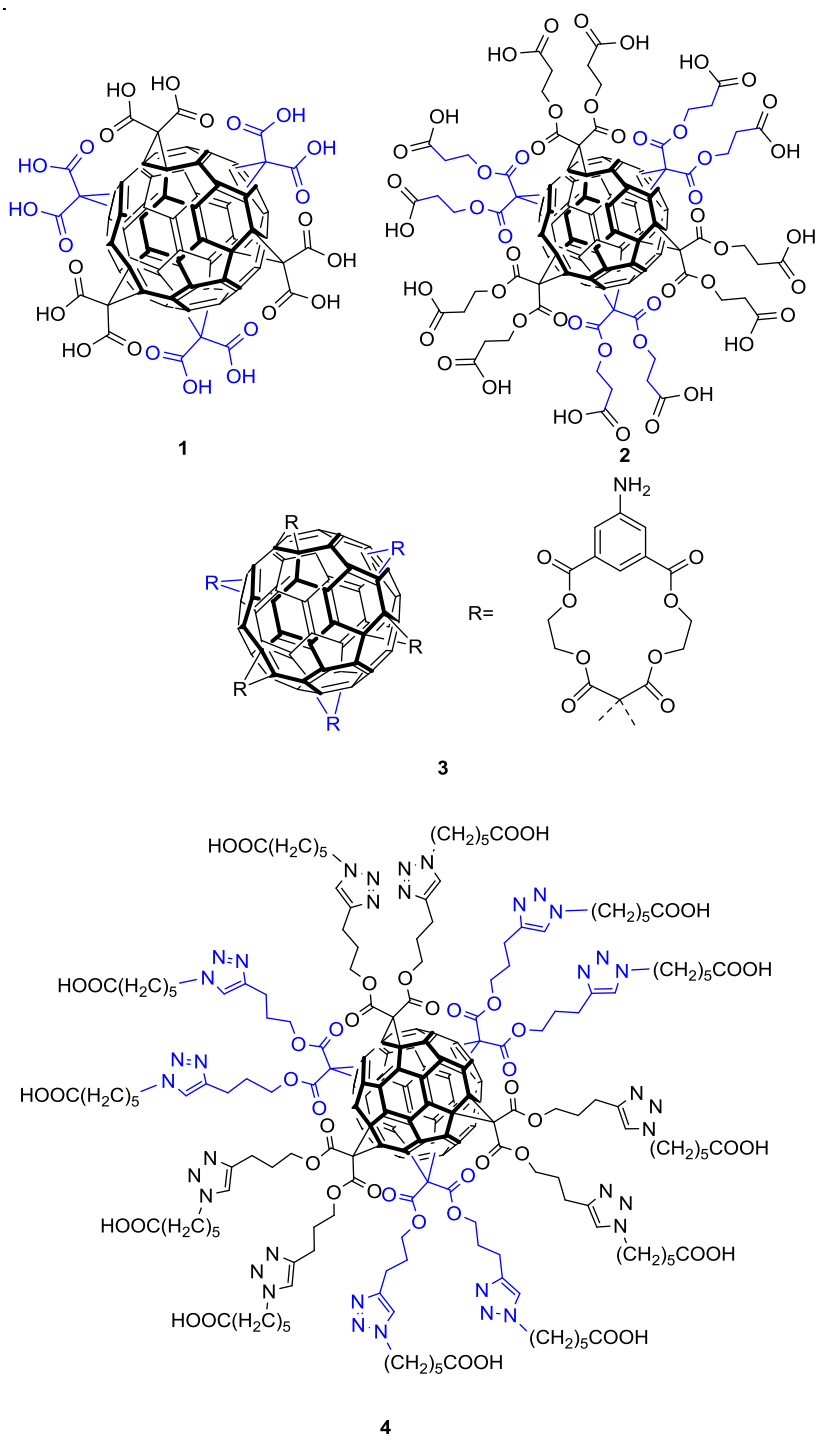

Figure 3.4. Hexa-substituted fullerene C_{60} 1-4.

In this chapter, the synthesis of the hexasubstituted C_{60} fullerenes **1-4** is discussed first. Compounds **1** and **4** were successfully synthesized, unfortunately, for compounds **2** and **3** the complete synthesis was not achieved and only the intermediary

compounds were obtained. Next, the synthesis and characterisation of Ru NPs in the presence of the hexasubstituted fullerene **1** ($C_{66}(COOH)_{12}$) is described.

3.2.1 Functionalization of fullerene C_{60}

A plethora of methods to functionalize fullerenes have been described,[24] and the most employed and well-known is the cycloaddition to [6,6] double bonds of C_{60}. As well as mono-adducts, many stereochemically defined multiple adducts have been synthesized by the Bingel-Hirsh reaction. Of all the possible multiple addition products, hexakis-adducts C_{60} with a T_h-symmetrical octahedral addition are by far the most interesting building block to construct 3D nanostructured nanomaterials.

The cycloaddition reaction of a bromo-derivative of diethyl malonate in the presence of a base (NaH or DBU (1,8-diazabicyclo[5.4.0]undec-7-ene) to C_{60} was first described by Bingel.[22] Later on, the reaction conditions have been improved and several methods have been developed, such as the *in situ* preparation of the halogen malonate with CBr_4[25] or I_2.[26] It has also been found that the addition of a large quantity of CBr_4 plays an important role for the hexa-adducted cycloaddition reactions.[27]

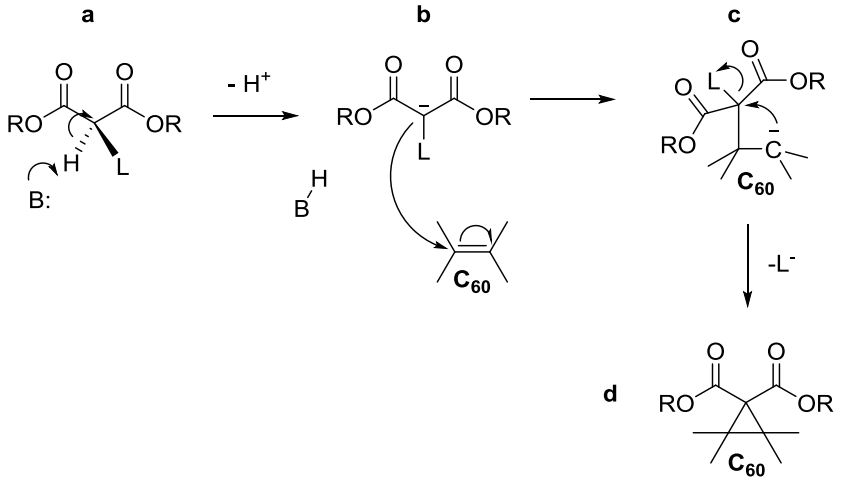

Scheme 3.1. The Bingel-Hirsh reaction mechanism. L leaving goup, B strong base.

Scheme 3.1 depicts the mechanism of the cycloaddition reaction. The bromide malonate reacts first with a base to generate **b**, a negative carbanion. Then, the

negative charged malonate carbanion attacks the [6, 6] double bond of the electron deficient C_{60}. Finally, the second carbanion formed **c** displaces the bromine to gives a cyclopropane ring. Mono- to hexa-substituted fullerenes can be synthesized using this procedure.[18]

In previous studies performed in our group shown that carboxylic groups can coordinate and stabilize Ru NPs.[28] With the purpose of preparing self-assembled nanostructures of Ru NPs several substituted fullerene with carboxylic acid groups have been prepared (**1**, **2** and **4**). Additionally, the compound **3** was also synthesized with six amine groups, as it is known that amine compounds may stabilize well metallic NPs.[29]

3.2.1.1 Synthesis of compound 1 ($C_{66}(COOH)_{12}$)

$C_{66}(COOH)_{12}$ was synthesized by hydrolysis of the T_h-hexa-adducts diethyl malonate fullerene $C_{66}(COOEt)_{12}$, which in turn was synthesized by nucleophilic cyclopropanation of fullerene C_{60} with diethyl bromo-malonate.[22]

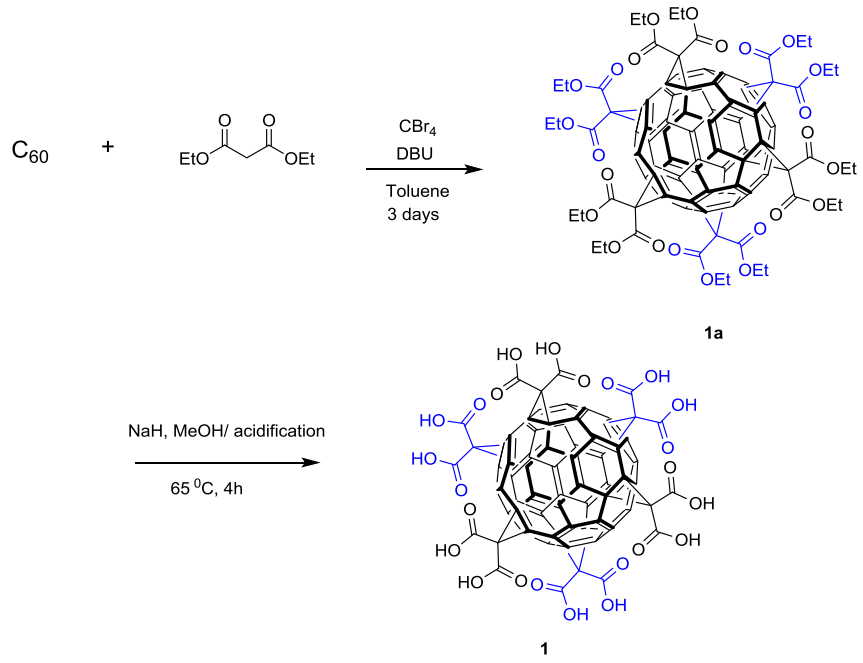

Scheme 3.2. Synthesis of $C_{66}(COOH)_{12}$: 1) synthesis of $C_{66}(COOEt)_{12}$ and 2) hydrolysis and acidification of $C_{66}(COOEt)_{12}$.

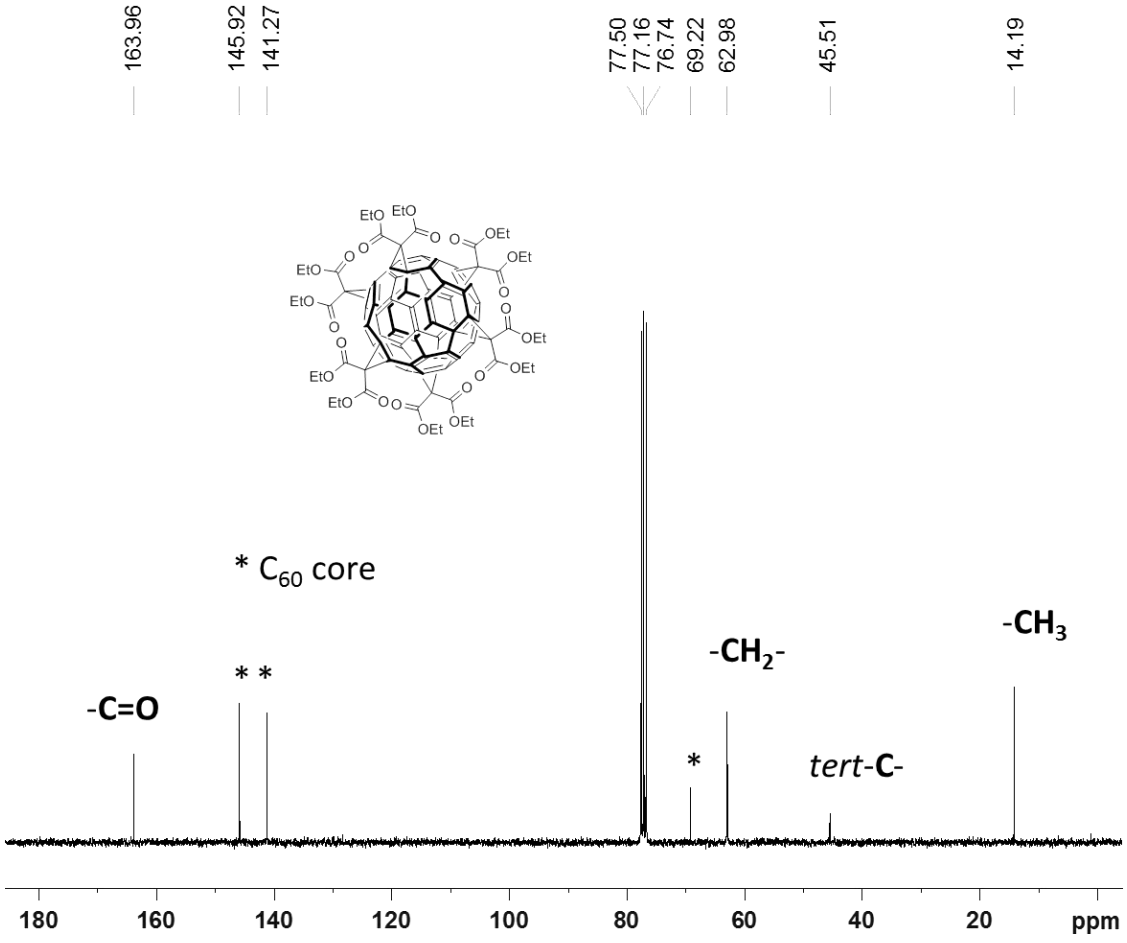

Figure 3.5. ^{13}C-NMR spectrum of $C_{66}(COOEt)_{12}$.

$C_{66}(COOEt)_{12}$ was synthesized as a yellow solid (50 % yield). The ^{13}C-NMR ($CDCl_3$) spectrum of $C_{66}(COOEt)_{12}$ depicted in Figure 3.5 shows the characteristic peaks of the fullerene cage (sp^2-C C_{60}) at 146 and 141 ppm. The peaks at 69 and 45 ppm are assigned to the cyclopropane carbons. The peaks at 62.9 and 14.19 ppm are attributed to the ethyl groups and the peak at 164.0 ppm to the carboxylic group.

$C_{66}(COOH)_{12}$ was synthesized by refluxing **1a** and NaH in toluene, followed by acidification with an ion exchange resin. Figure 3.6 displays the ^{13}C-NMR ($(CD_3)_2CO$) spectrum of **1.** The peaks at 146.3 and 142.5 correspond to the fullerene cage, the cyclopropane carbons appeared at 70.4 and 47.7 ppm which are downfield shifted with respect compound **1a**. Finally the carboxylic group appeared at 164.7 ppm.

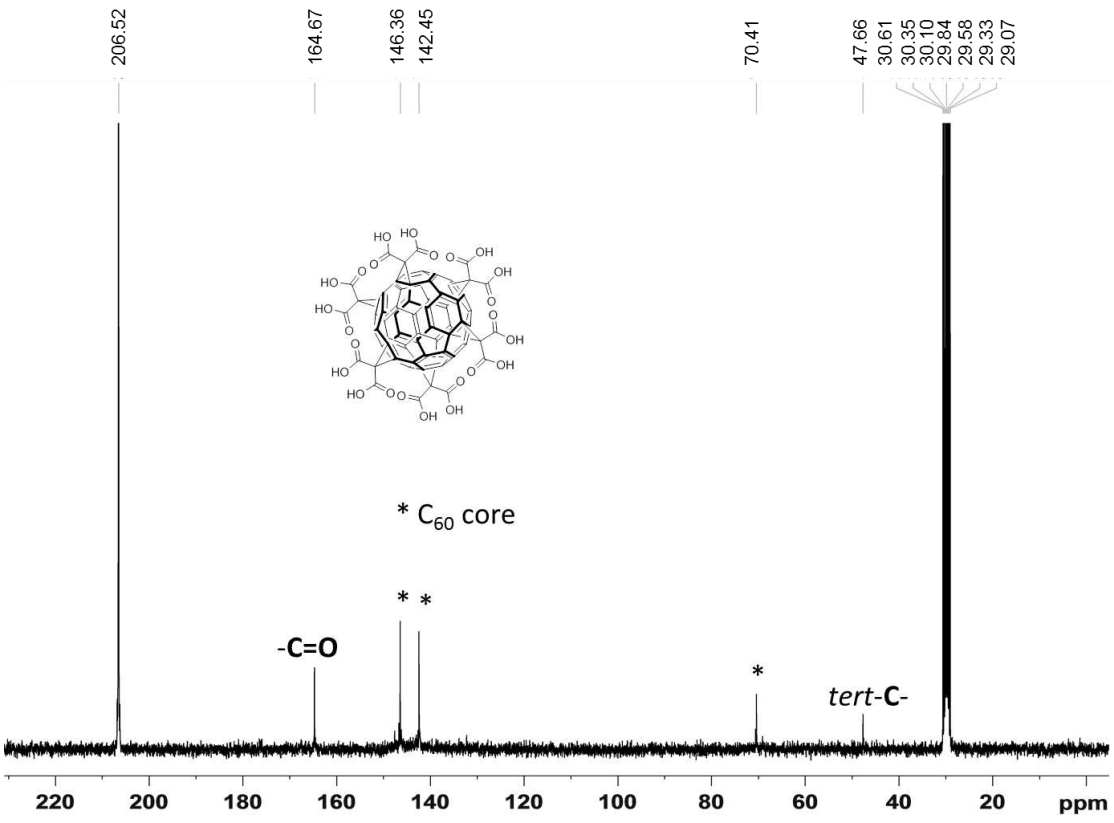

Figure 3.6. ^{13}C-NMR spectrum of $C_{66}(COOH)_{12}$.

2.1.2 Synthesis of compound 2

A long chain carboxylic group of hexaadducts C_{60} was also desired to produce longer building blocks. Scheme 3.3 presents the compound **2** as the target product. A similar compound has been previously reported by Kraft *et al.,*[30] which has a shorter carbon chain. First, the malonyl compound **2a** was successfully synthesized by malonyl chloride and tert-butyl 3-hydroxypropionate with a 20% yield (Scheme 3.3). Next, **2a** was allowed to react with C_{60} to produce the cyclopropane derivative **2b** using similar conditions as described for **1a**. Unfortunately, the reaction gave a complicated mixture of several substituted fullerenes, which was difficult to purify and characterize, and compound **2** was not isolated.

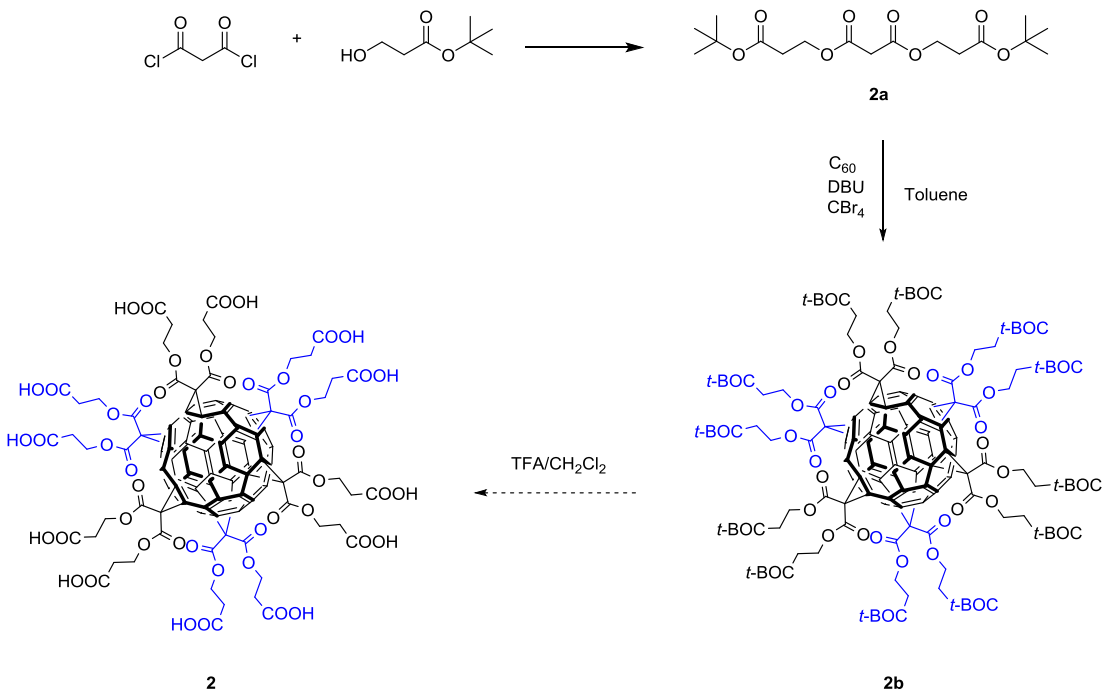

Scheme 3.3. Synthesis of compound 2.

3.2.1.3 Synthesis of compounds 3

The malonate **3d** compound containing a substituted amine was also synthesized as presented in scheme 3.4. The malonate crown ether was synthesized from **3c** and malonyl chloride, which is a typical method to synthesize functionalized malonates.[18] First, **3a** was synthesized from $(Boc)_2O$ and 5-aminoisophthalic acid, and the **3b** was produced from the reaction of ethylene glycol and toluene sulfonyl chloride. **3a** was allowed to react with **3b** using $CsCO_3$ as base to produce **3c** in 49% yield at room temperature. The malonate crown ester **3d** was synthesized with a 27% yield by adding a solution of malonate chloride into the solution of **3c**. The reaction of the malonate crown ester **3d** with fullerene C_{60} in the presence of CBr_4 and DBU allowed to obtain **3e**. However the yield was very low (3.2%), probably due to the high steric hindrance of such malonate compound.

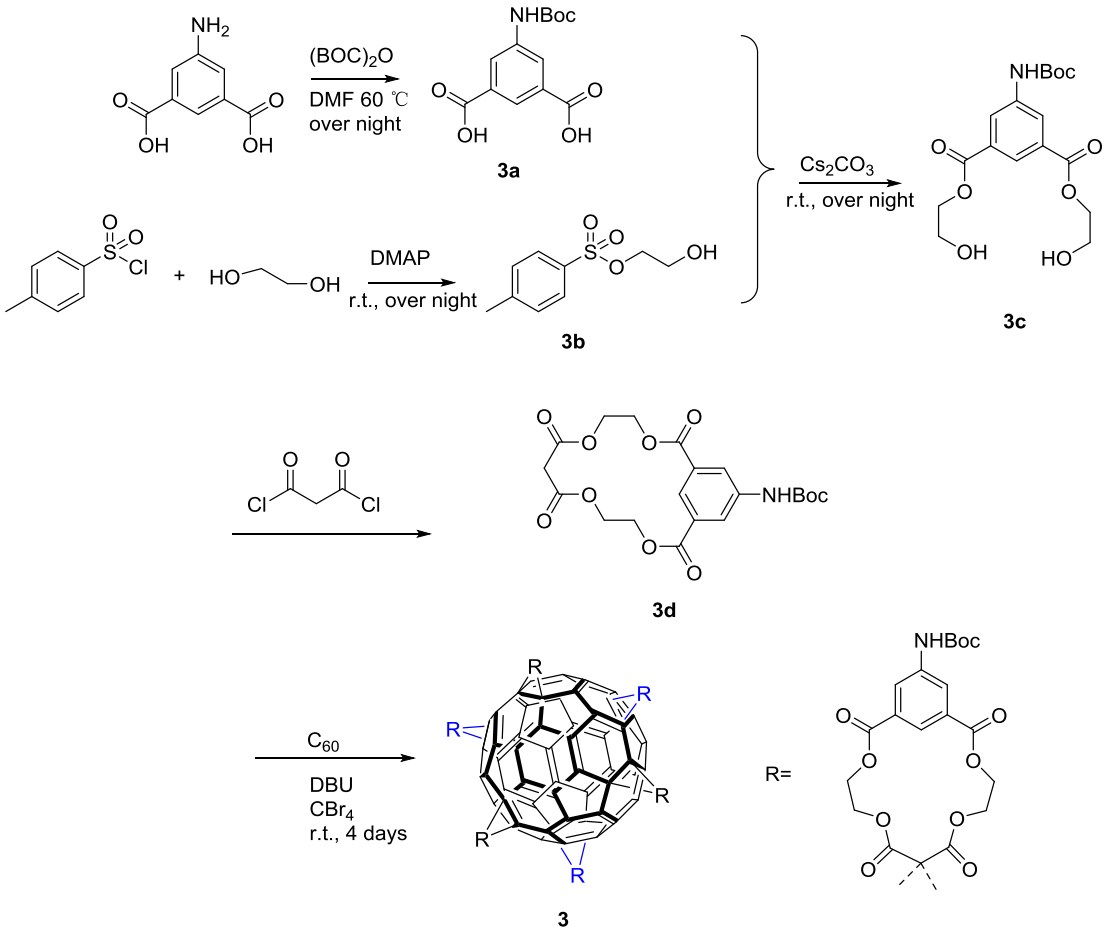

Scheme 3.4 Synthesis of compound 3.

3.2.1.4 Synthesis of compound 4

Using a Bingel-Hirsch hexaadduct and click chemistry,[18] the synthesis of fullerene derivative **4b** was carried out as depicted in Scheme 3.5. Fullerene hexaadduct **4a** was prepared by the addition of dipent-4-ynyl malonate to C_{60} in toluene, employing an excess of CBr_4. For the 1,3-dipolar cycloaddition of compound **4a**, we followed optimised conditions previously reported,[31] in which a $CuBr{\cdot}SMe_2$ was used as catalyst. At the end of the reaction, the product **4** was precipitated by centrifugation and washed. Using this procedure the reaction time was significantly reduced and compound **4** was obtained in 61 % yield.

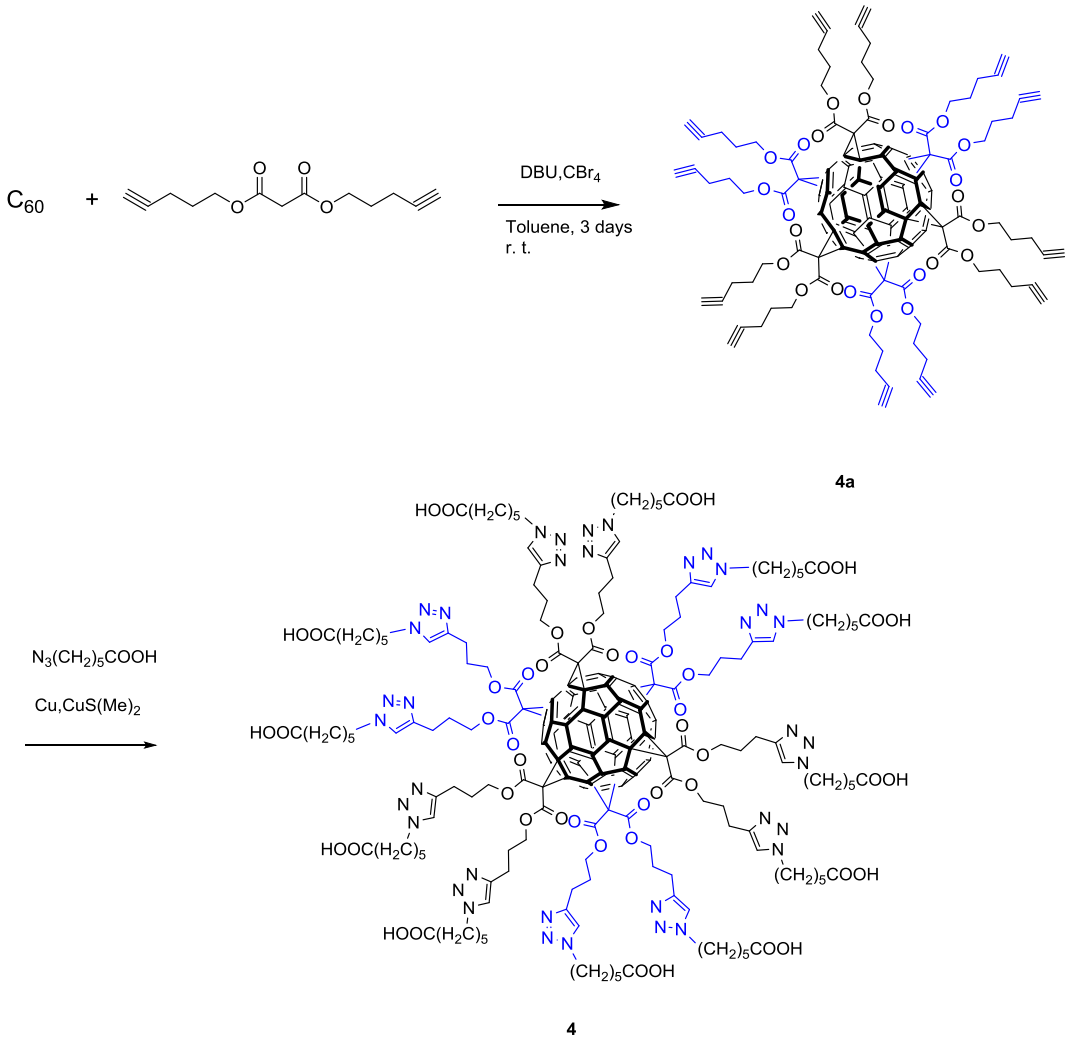

Scheme 3.5. Synthesis of compound 4.

3.2.2 Synthesis of Ru nanostructures based on functionalized fullerene@$C_{66}(COOH)_{12}$

$Ru@C_{66}(COOH)_{12}$ nanostructures have been synthesized using a similar procedure to produce $Ru@C_{60}$ nanostructures, as described in Chapter 2. [Ru(COD)(COT)] (COD= 1,5 cyclooctadiene, COT= 1,3,5-cyclooctatriene) was decomposed in the presence of $C_{66}(COOH)_{12}$ under 3 bar of H_2 at room temperature.[32] The effect of the solvent and the $Ru/C_{66}(COOH)_{12}$ ratio used during the reaction on the nanostructures have been characterized. The nanostructures obtained were studied in details using Transmission Electron Microscopy (TEM) techniques together with Wide-Angle X-Ray Scattering (WAXS), Small Angle X-ray Scattering (SAXS), Solid State NMR

(SSNMR), X-Ray Photoelectron Spectroscopy (XPS) and Attenuated Total Reflection Infrared Spectroscopy (ATR-IR).

3.2.2.1 Solvent effect

The effect of the solvent on the nanostructure was studied by using a Ru/$C_{66}(COOH)_{12}$ ratio of 6/1. The solvents were chosen according to the solubility of $C_{66}(COOH)_{12}$, including THF (tetrahydrofuran), MeOH, DMF(dimethylformamide), and THF/H_2O (10/1) and THF/MeOH (1/1) mixtures. Figure 3.7 shows the TEM images of the Ru@$C_{66}(COOH)_{12}$ synthesized using several solvents.

Table 3.1. Mean size diameters of Ru NPs produced with different solvents.

Solvent	Viscosity (mPa.s)[33]	Relative permittivity(ε_r)[33]	Nanoparticles mean size (nm)[a]
THF	0.46	7.58	1.23 ± 0.02
MeOH	0.54	32.7	1.03 ± 0.06
DMF	0.79	36.7	1.74 ± 0.03
THF/H_2O 10/1	0.49[b]	14.2[c]	2.37 ± 0.04
THF/MeOH 1/1	0.50[b]	20.1[c]	2.25 ± 0.08

[a]Manual measurement from enlarged micrographs of at least 200 objects. [b]Estimated viscosity of the solvent mixture using the following equation: $v^{1/3}=x_a v_a^{1/3}+x_b v_b^{1/3}$ (v = viscosity, x = mass fraction)[34], [c]Estimated permittivity corrected viscosity of the solvent mixture using the following equation: $\varepsilon=x_a\varepsilon_a+x_b\varepsilon_b$ (ε = permittivity, x = mass fraction).[35]

In all cases, matrixes of irregular shapes decorated with Ru NPs were observed, except for the compound synthesized using a THF/MeOH (1/1) mixture, where nanospheres were obtained. The mean size diameters of the metallic NPs are in the range of 1.03 to 2.37 nm (see mean sizes distribution in Figure 3.7 and Table 3.1). The Ru@$C_{66}(COOH)_{12}$ nanostructures synthesized in THF and MeOH contain ultra-small Ru NPs, 1.23 ± 0.02 and 1.03 ± 0.06 nm, respectively. The NPs are close together indicating a certain degree of ordering. In contrast, the synthesis carried out in DMF afforded Ru NPs supported on a matrix that is similar to the one observed in

the TEM images obtained with the Ru@C_{60} polymer. However, no further analyses have been done in order to corroborate this hypothesis. Analogously, THF/H_2O (10/1) and THF/MeOH (1/1) mixtures produced also probably a Ru@$C_{66}(COOH)_{12}$ polymer, see Figure 3.7 d) and e).

3.2.2.2 Ru@$C_{66}(COOH)_{12}$ ratio effect

A series of experiments using Ru/$C_{66}(COOH)_{12}$ ratio from 6/1 to 100/1 were carried out in order to understand better the Ru@$C_{66}(COOH)_{12}$ structures using THF as the reaction solvent. TEM analyses depicted in Figure 3.8 show that in all cases Ru NPs were synthesized and in all cases the NPs were near each other forming bigger superstructures. Interestingly, the narrower mean size distribution of the Ru NPs (Table 3.2) increased with increasing the Ru content while the nanostructure remained almost unchanged, except for Ru/$C_{66}(COOH)_{12}$ ratio 100/1, where the nanostructure slightly vanished maybe due to the high Ru content.

Table 3.2. Mean size diameters of Ru NPs with different Ru/$C_{66}(COOH)_{12}$ ratio.

Ru@$C_{66}(COOH)_{12}$	Ru load[a] (%)	Nanoparticles mean size (nm)[b]
6/1	22.6	1.23 ± 0.02
12/1	40	1.56 ± 0.01
30/1	52.2	1.52 ± 0.02
50/1	---	1.78 ± 0.02
100/1	---	1.67 ± 0.01

[a]ICP analysis. [b]Manual measurement from enlarged micrographs of at least 200 objects.

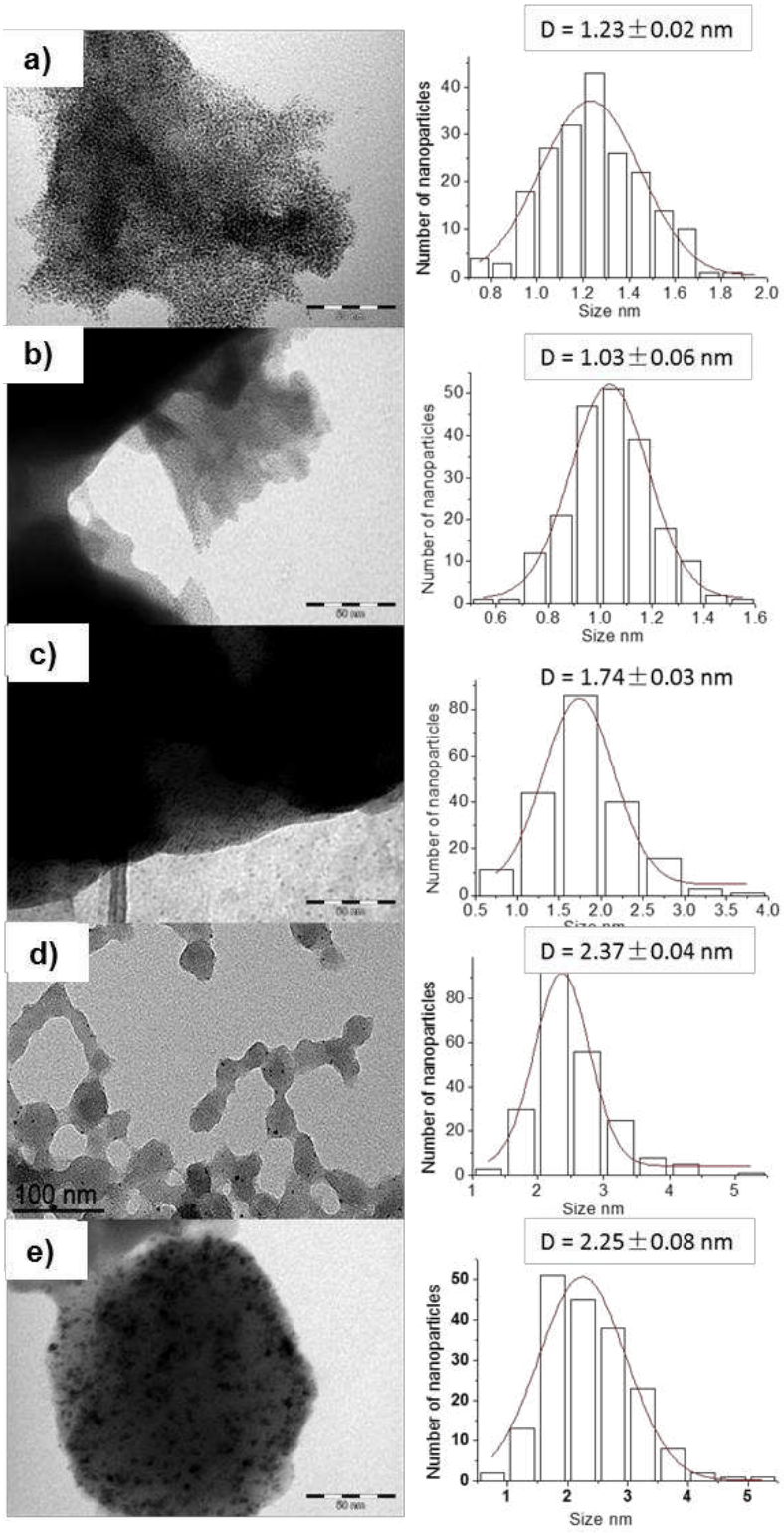

Figure 3.7. TEM micrographs of $Ru@C_{66}(COOH)_{12}$ structures with $Ru@C_{66}(COOH)_{12}$ = 6/1 synthesized in different solvents: a) THF(scale bar 50 nm), b) MeOH(scale bar 50 nm), c) DMF (scale bar 50 nm), d) THF/ H_2O (10/1) (scale bar 100 nm), e) MeOH/THF 1/1 (scale bar 50 nm).

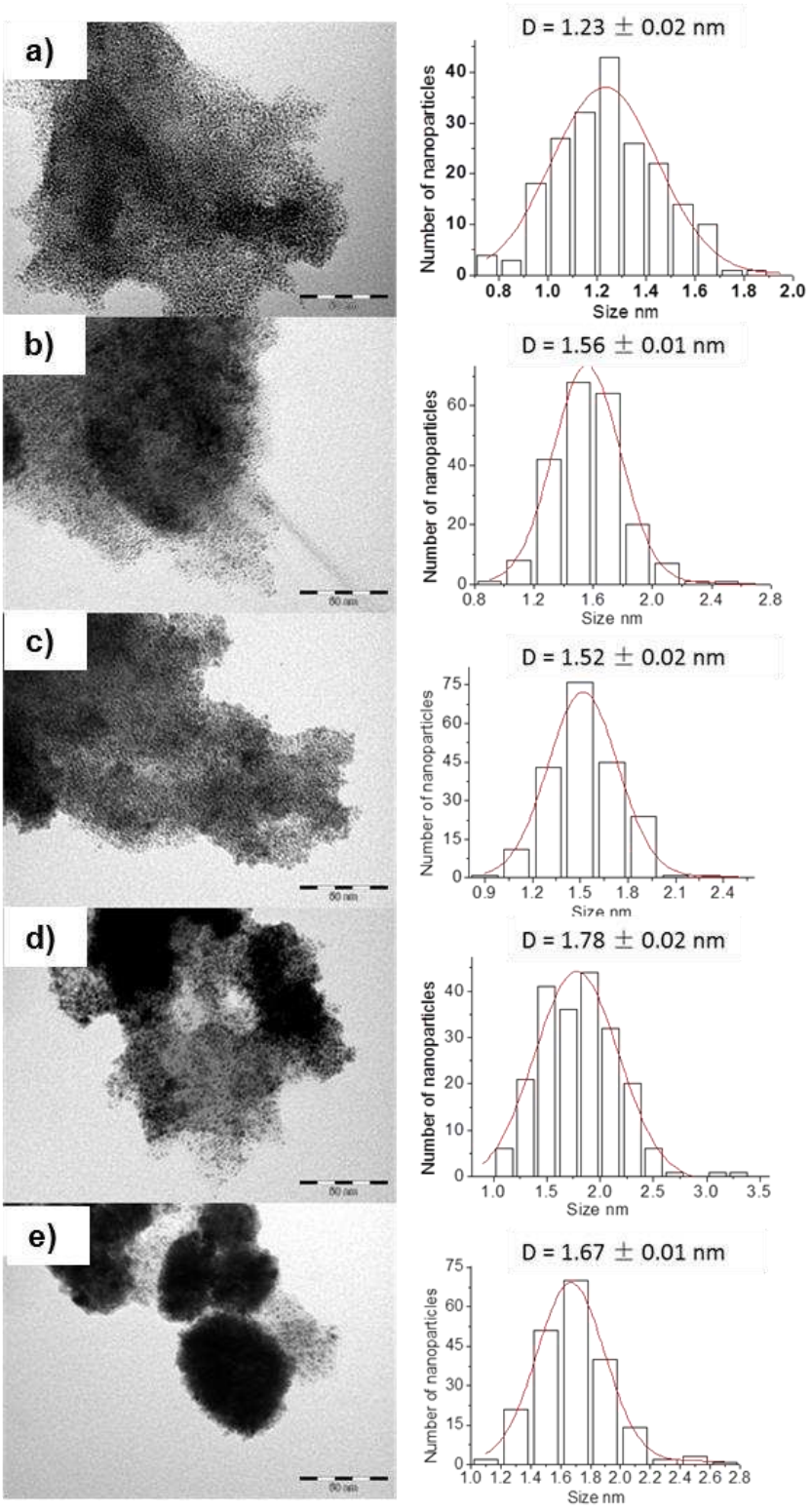

Figure 3.8. TEM micrographs of Ru@$C_{66}(COOH)_{12}$ structures synthesized in THF using a Ru/$C_{66}(COOH)_{12}$ ratio of: a) 6/1, b) 12/1, c) 30/1, d) 50/1; and e) 100/1 (scale bar 50 nm).

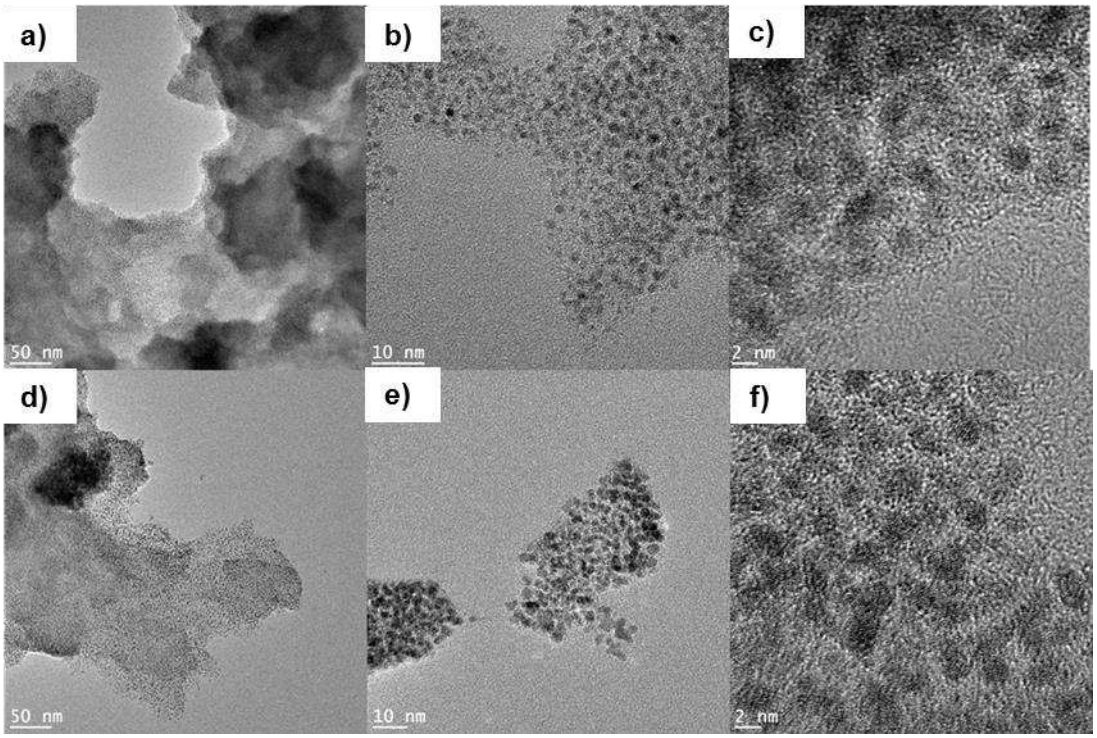

Figure 3.9. HREM micrographs of Ru@C_{66}(COOH)$_{12}$ nanostructures: a), b), c) Ru@C_{66}(COOH)$_{12}$ 6/1; and (d), (e) (f), Ru@C_{66}(COOH)$_{12}$ 30/1.

The HREM images of Ru@C_{66}(COOH)$_{12}$ nanostructures 6/1 and 30/1 are depicted in Figure 3.9. The small Ru NPs are clearly observed in both compounds. Even if HREM points out that no Ru@C_{66}(COOH)$_{12}$ polymer is synthesized and only Ru NPs are produced, further analyses are necessary (*i. e*. tomography) in order to discard the formation of the organometallic polymer. HREM observations (Figure 3.10) show that the Ru NPs are well crystallized with crystal parameters of Ru *hcp*. The EDX analysis conformed that the Ru@C_{66}(COOH)$_{12}$ nanostructures are composed of Ru and C in Figure 3.10b.

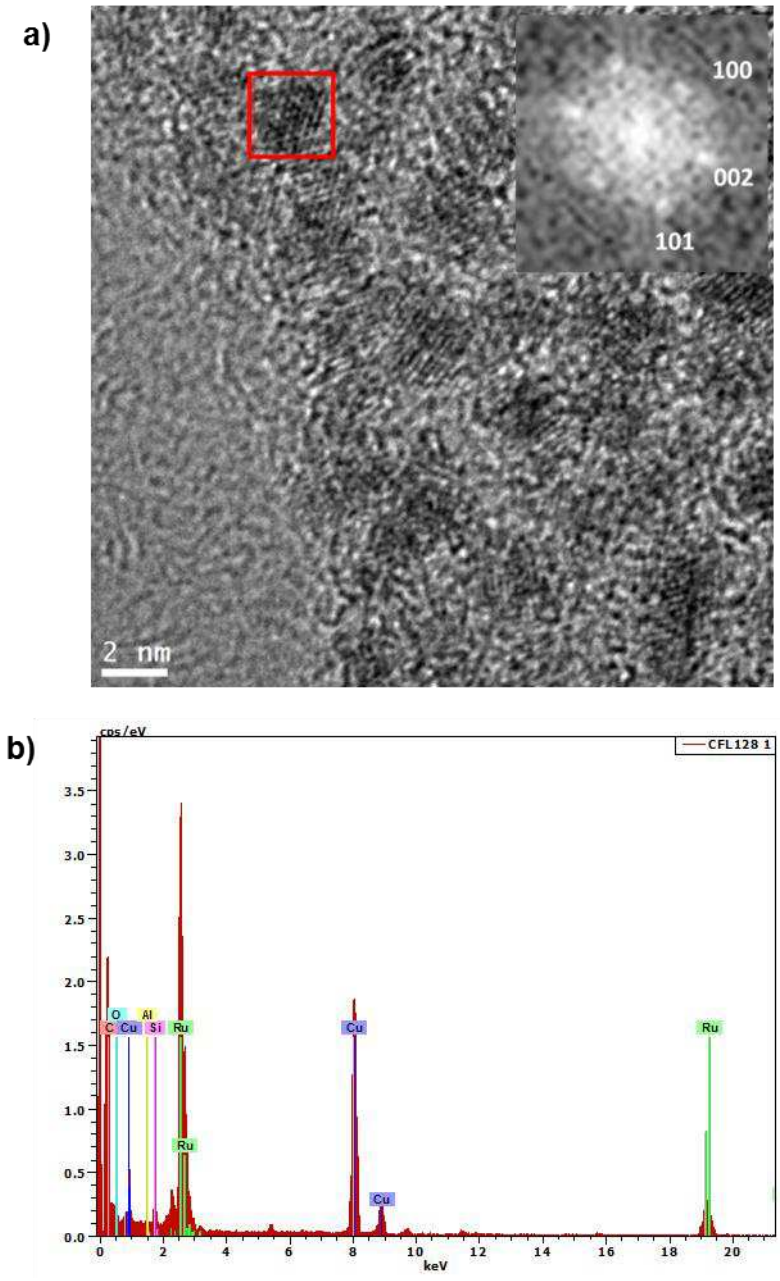

Figure 3.10. a) HREM image of of $Ru@C_{66}(COOH)_{12}$ 6/1; inset: Fast Fourier Transform (FFT) with the corresponding orientation of the Ru lattice; and b) EDX of $Ru@C_{66}(COOH)_{12}$.

3.2.2.3 WAXS analyses

WAXS analyses were done in collaboration with Pierre Lecante of the Centre d'élaboration des matériaux et d'études structurales UPR CNRS 8011, Toulouse, France. Ru@$C_{66}(COOH)_{12}$ samples synthesized in THF sealed in Lindemann glass capillaries were measured by WAXS using a diffractometer dedicated to pair-distribution function (PDF) studies. The diffractograms of Ru@$C_{66}(COOH)_{12}$ 6/1, 12/1 and 30/1 are displayed in Figures 3.11 and 3.12.

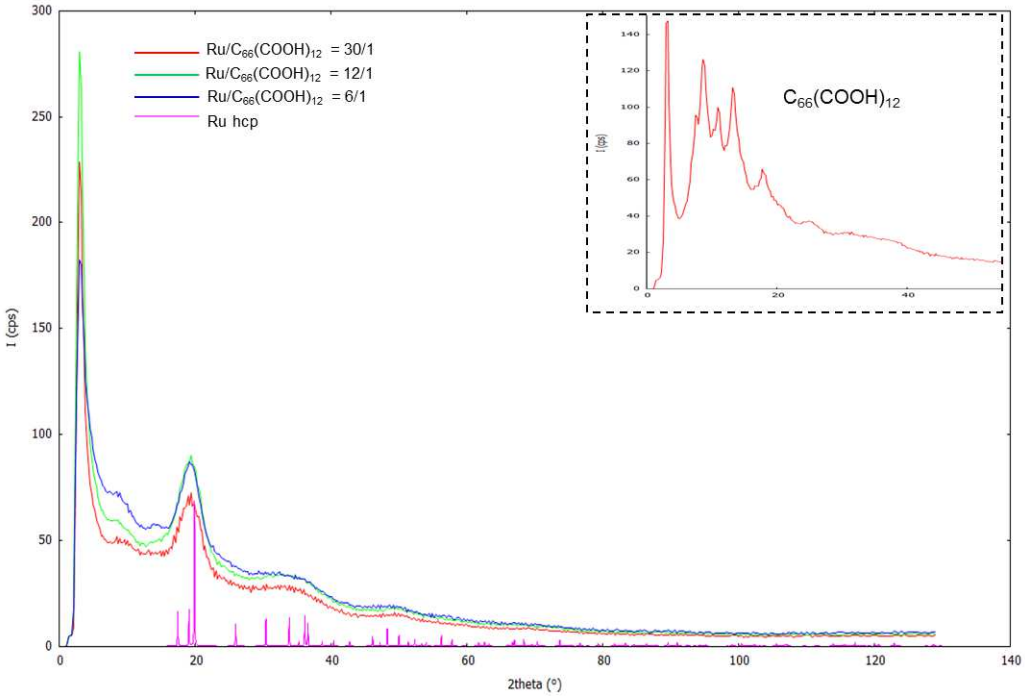

Figure 3.11. Diffractograms for Ru@$C_{66}(COOH)_{12}$ 6/1, 12/1 and 30/1 nanostructures together with Ru *hcp* reference data; inset diffractogram of $C_{66}(COOH)_{12}$.

The three diffractograms of Ru@$C_{66}(COOH)_{12}$ 6/1, 12/1 and 30/1 were very similar, and it is fully consistent with metallic Ru in the *hcp* system (2theta = 20°). The sharp peak signal at small angle could be assigned to the $C_{66}(COOH)_{12}$, which is very close to the feature of pure $C_{66}(COOH)_{12}$.

After corrections and Fourier Transforms (Figure 3.12), the related PDF functions are also very close as expected, and the size (from coherence length) can reach 1.5 nm. In the present case, we do not observe a decrease or increase on the PDF of the metallic

Ru order like in Ru@C_{60}. The PDF also indicate that Ru NPs have a single size distribution and an average diameter close to 1.5 nm, in agreement with the TEM measurements.

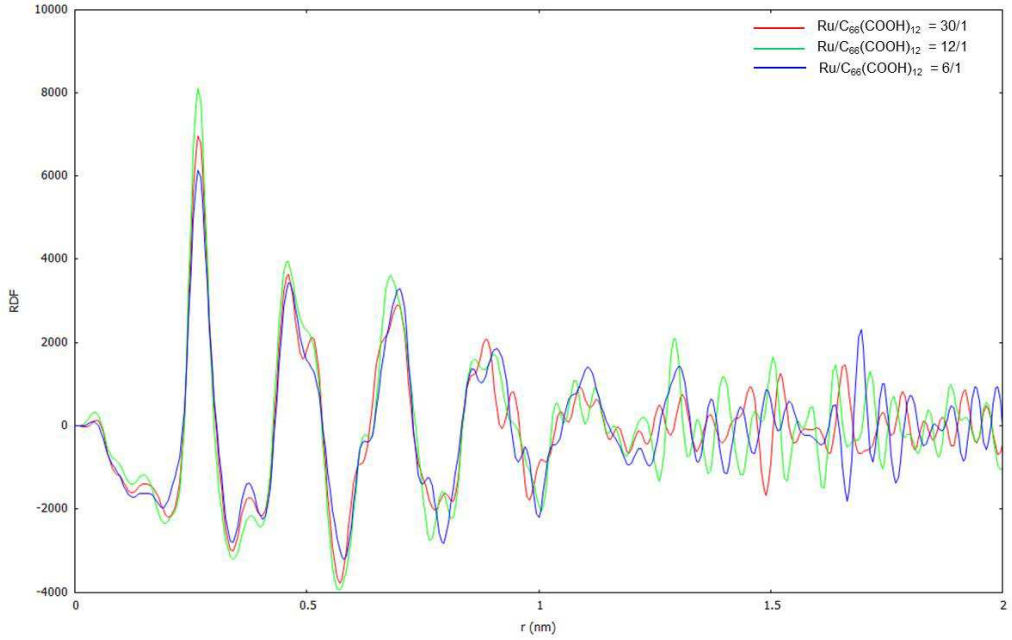

Figure 3.12. Pair-distribution function of Ru@$C_{66}(COOH)_{12}$ 6/1, 12/1 and 30/1 nanostructures.

3.2.3.4 Small Angle X-ray Scattering (SAXS)

SAXS is a useful tool to analyse the nanoscale structure of particle systems in terms of parameters such as average particle sizes, shapes, distribution, and surface-to-volume ratio. To measure the interparticle distance of Ru@$C_{66}(COOH)_{12}$, the Ru@$C_{66}(COOH)_{12}$ 12/1 nanostructure was characterized by SAXS at small angle (Figure 3.13.) in Paul Pascal Research Center-CNRS University of Bordeaux. SAXS patterns are typically represented as scattered intensity as a function of the magnitude of the scattering vector $q = 4\pi\sin\theta/\lambda$. The result shown a small peak at 0.22 $Å^{-1}$ in (Figure 3.13). After calculations ($q = 4\pi\sin\theta/\lambda$, Bragg's law function $2d\sin\theta = n\lambda$), the results give an the interparticle distance of 2.85 nm from Ru NPs center to center.

Taking into account that the Ru NPs mean size diameter is 1.56 nm in Ru@$C_{66}(COOH)_{12}$ 12/1 nanostructure and the diameter of the $C_{66}(COOH)_{12}$ fullerene

is 1.48 nm (calculated by DFT, see DFT calculations section), a Ru NPs distance of 3.04 nm correlates well with the distance (2.85 nm) found by SAXS. In addition, the manual counting of the Ru NPs - Ru NPs distance in TEM images is equal to 2.56 nm (Figure 3.14 and Table 3.3), which is also comparable considering the resolution of

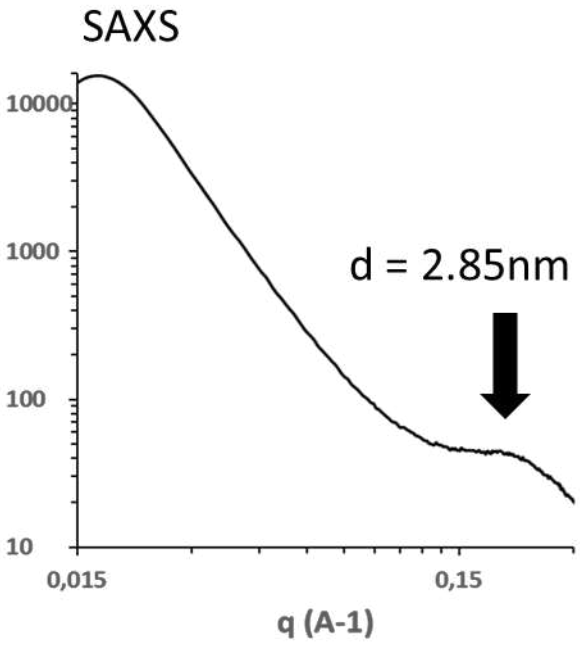

Figure 3.13. The SAXS spectrum of Ru@C_{66}(COOH)$_{12}$ 12/1.

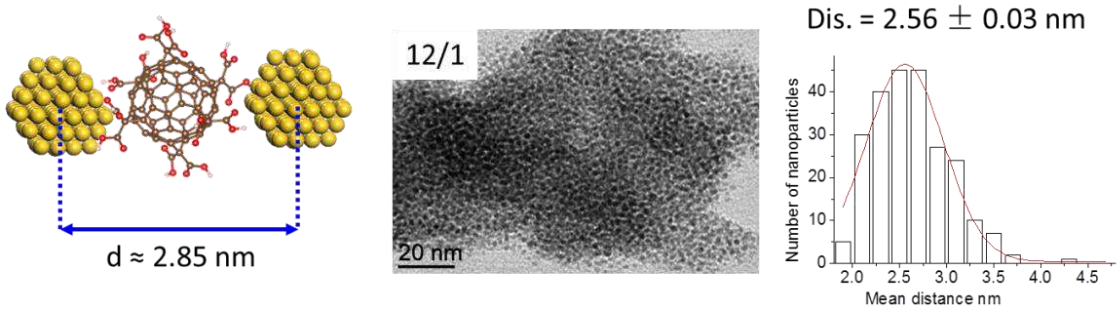

Figure 3.14. Schematic representation of Ru NPs distance center to center found by SAXS, and rigth size histogram (left) and mean distance between to Ru NPs measured by manual measurement from enlarged TEM micrographs of at least 200 objects (right).

TEM. Complementary counting realized in HREM images of the Ru@C_{66}(COOH)$_{12}$ 6/1 sample only using isolated Ru NPs (see Figure 3.15) give a mean distance of 2.87 nm.

Table 3.3. Ru NP- RuNP distance from the TEM and SAXS analyses

Sample	Ru NPs-Ru NPs distance (nm)[a]	Ru NPs diameter (nm)[b]	Ru NPs-Ru NPs distance (nm) (nm)[c]
$Ru@C_{66}(COOH)_{12}$ 12/1	2.85	1.56	2.56

[a]Calculated from SAXS measurement. [b]Manual measurement from enlarged micrographs of at least 200 objects. [c]Manual measurement from enlarged TEM micrographs of at least 200 objects.

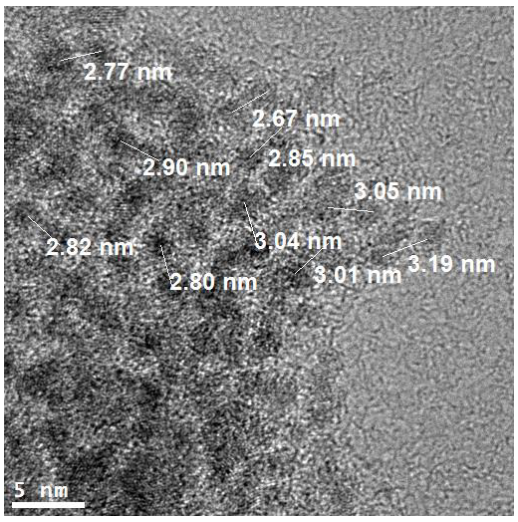

Figure 3.15. HREM image of $Ru@C_{66}(COOH)_{12}$ 6/1 sample displaying Ru NPs - Ru NPs distances.

3.2.3.5 Solid State NMR

^{13}C-NMR and cross polarization magic-angle spinning (CP-MAS) Solid-State NMR (SSNMR) spectroscopy were performed for several $Ru@C_{66}(COOH)_{12}$ nanostructures. ^{13}C-NMR SSNMR spectra of $Ru@C_{66}(COOH)_{12}$ 12/1 and 30/1 are displayed in the Figure 3.16a together with the functionalised fullerene $C_{66}(COOH)_{12}$. ^{13}C-NMR SSNMR spectrum of $C_{66}(COOH)_{12}$ showed a peak at 69 ppm and a broad signal at 141-150 ppm attributed to the fullerene cage. In addition, a peak visible at 45 ppm is attributed to the quaternary carbon and a peak visible at 165 ppm is attributed to the carbon of the carbonyl moiety. The ^{13}C-NMR SSNMR spectra of $Ru@C_{66}(COOH)_{12}$ 12/1 and 30/1 displayed the same number of peaks. The peaks at 69 ppm and 141-150 ppm are attributed to the fullerene cage; they remain unchanged with respect to the $C_{66}(COOH)_{12}$ compound in both nanostructures. In contrast, the peak visible at 45

ppm attributed to the quaternary carbon upfield shifted of 25 ppm and the peak attributed to the COOH downfield shifted to 185 ppm (see Figure 3.13b for CP-MAS ^{13}C-NMR SSNMR), indicating that $C_{66}(COOH)_{12}$ is coordinating to the Ru NPs thought the carbonyl moieties, probably in a carboxylate form, which has been confirmed by IR and DFT calculations (see below).

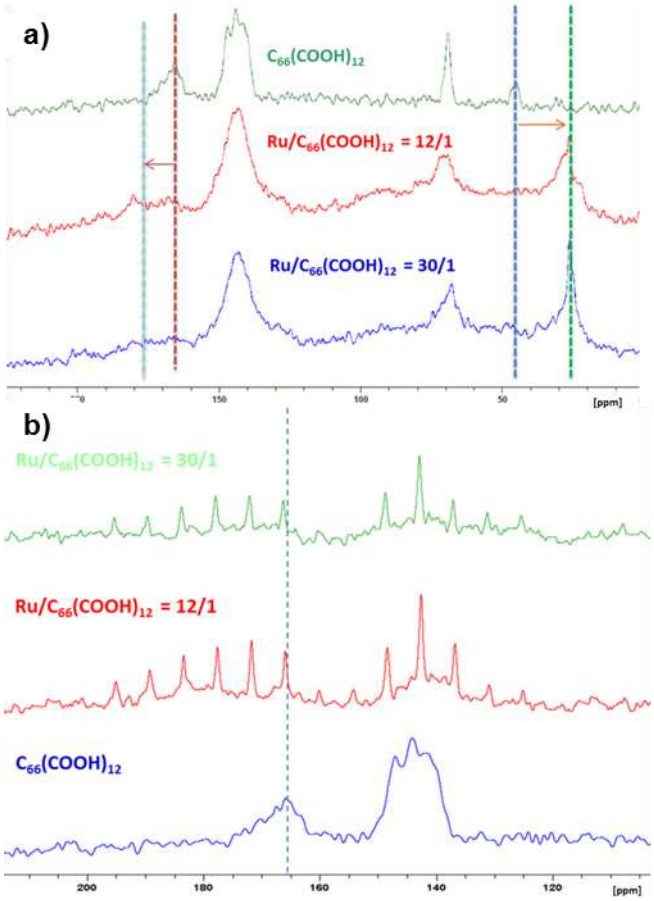

Figure 3.16. ^{13}C-NMR spectrum of a) SSNMR; and b) CP-MAS SSNMR of $C_{66}(COOH)_{12}$, $Ru@C_{66}(COOH)_{12}$ 12/1; and $Ru@C_{66}(COOH)_{12}$ 30/1

3.2.3.6 XPS

X-ray photoelectron spectrometry analyses were realized for several $Ru@C_{66}(COOH)_{12}$ nanostructures. XPS analysis of $Ru@C_{66}(COOH)_{12}$ 12/1 is detailed in Figure 3.17 and Table 3.4. Ru, C and O were identified. The Ru 3d-C1s peak can be divided into several components and the peak fitting assigned to O-C=O, -C_{60}, sp^2-C, sp^3-C, Ru $3d^{3/2}$ and Ru $3d^{5/2}$ bands. O^{1s} binding energy peak is attributed

to O=C-O and RuO_2. The binding energy of Ru $3p^{3/2}$ at 462.5 ev was slightly higher than the one of Ru(0), which normally appears at 462.2 ev.[36]

The peak fitting analyses reveal that Ru is partially oxidized and the Ru atoms bind strongly to O. Additionally, the percentage of C and O found by XPS analyses (74.6% C, 22.2% O) was similar to the one expected for a $Ru@C_{66}(COOH)_{12}$ 12/1 ratio (70.3% C, 28.8% O).

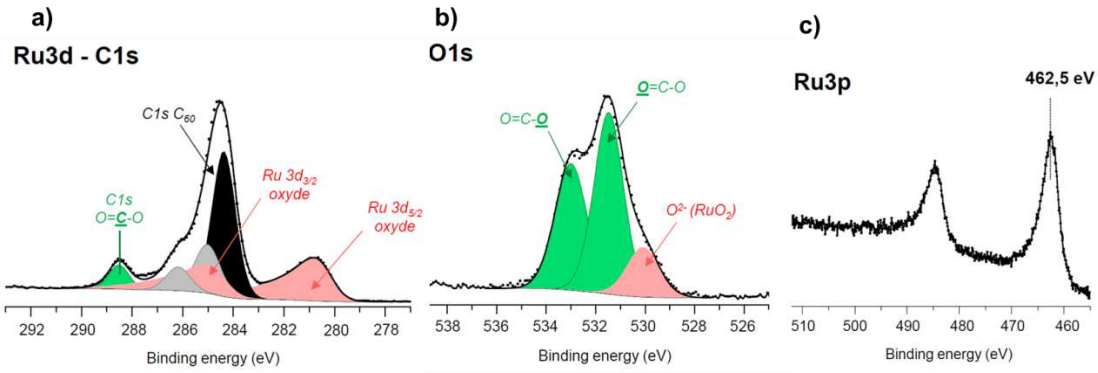

Figure 3.17. Peak fitting of $Ru@C_{66}(COOH)_{12}$ 12/1: a) Ru 3d b) O1s; and c) binding energy of Ru 3p.

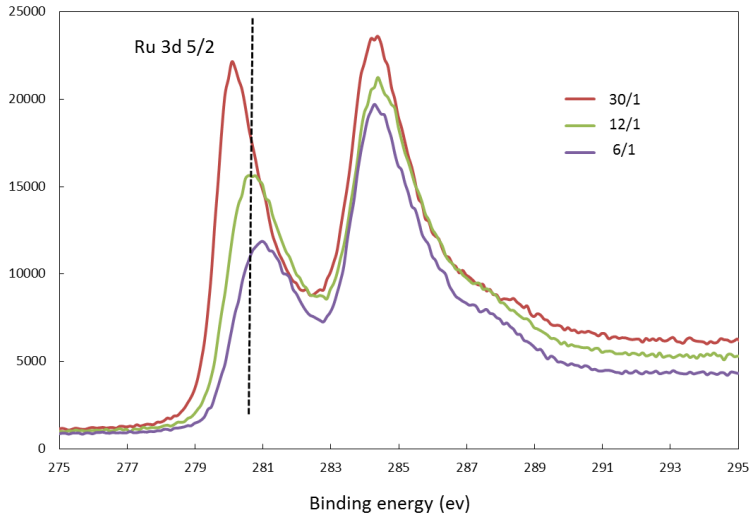

Figure 3.18. Binding energy of Ru 3d of $Ru@C_{66}(COOH)_{12}$ 6/1, 12/1 and 30/1.

The comparison of the Ru $3d^{5/2}$ binding energy peak of $Ru@C_{66}(COOH)_{12}$ 6/1, 12/1 and 30/1 nanostructures is displayed in Figure 3.18. The peak at 281.2 ev shifted with the ratio increase, indicating a more metallic composition of sample in high ratio.

Table 3.4 XPS data (peak fitting, FWHM and atomic concentration) for the Ru@$C_{66}(COOH)_{12}$ 12/1 sample.

Name	Position	FWHM	concentration%
Ru 3d	280.5	1.6	1.9
	284.7	1.7	1.3
			3.3
C1s	284.4	1.1	44.3
	285.0	1.2	16.4
	286.2	1.1	7.4
	288.5	1.0	6.5
			74.6
O1s	530.1	1.5	3.2
	531.5	1.4	10.8
	533.0	1.5	8.1
			22.1

3.2.2.7 ATR-IR

The attenuated total reflectance infrared (ATR-IR) spectra were recorded for $C_{66}(COOH)_{12}$ (top) and Ru@$C_{66}(COOH)_{12}$ 6/1, 12/1 and 30/1 samples in the solid state in a IR available in a glove box (Figure 3.19). The $C_{66}(COOH)_{12}$ ATR-IR spectrum show peaks at 2900, 1700, 1192, 830, 708, 540 and 524 cm^{-1}. The intense vibrations at 2900(COOH), 1700(C=O), 1192 cm^{-1} (C-O) are attributed to the -COOH moiety, while the other peaks are attributed to vibrations of the fullerene cage. Ru@$C_{66}(COOH)_{12}$ 6/1, 12/1 and 30/1 samples gave similar ATR-IR spectra.

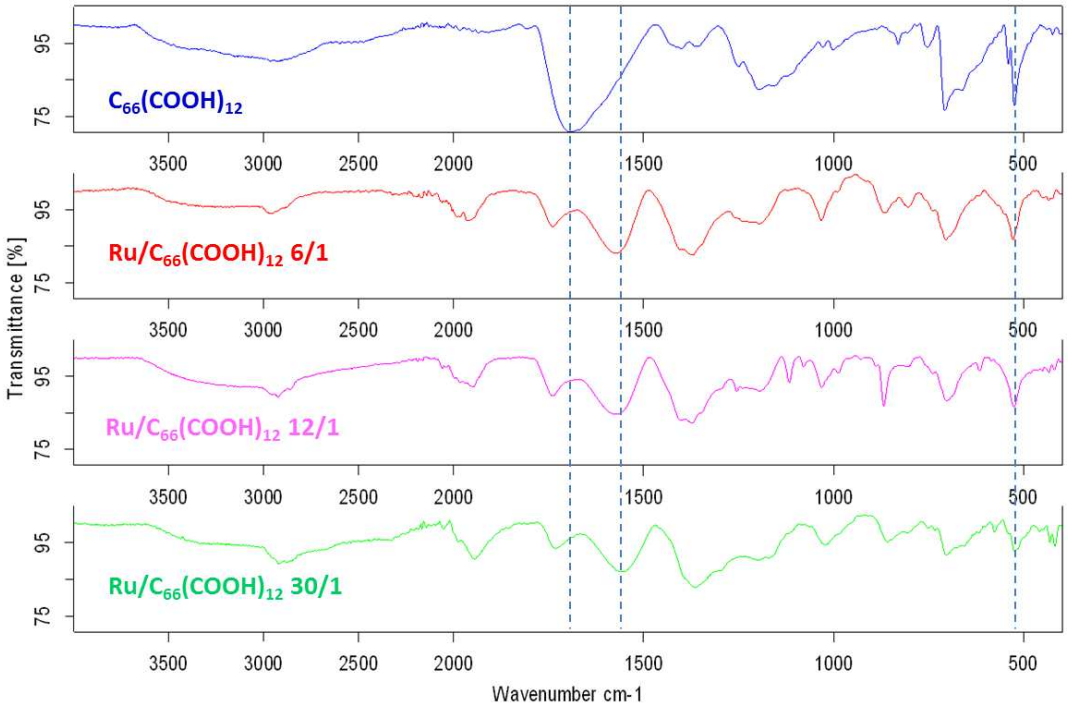

Figure 3.19. ATR-IR spectra of $C_{66}(COOH)_{12}$ (top) and Ru@$C_{66}(COOH)_{12}$ 6/1, 12/1 and 30/1 (bottom).

Peaks at 540 and 524 cm^{-1} are attributed to the fullerene cage that remaines unchanged, while the C=O vibration of the COOH group observed at 1700 cm^{-1} vanished in the Ru nanostructures when compared to the free ligand. Two new peaks at 1555 and 1367 cm^{-1} were attributed to the C=O vibrations of a new COO-Ru species, confirming again the coordination of the fullerene through carboxylate species. These data are in accordance with published values for Ru-carboxylate complexes.[37] The peak at around 1900 cm^{-1} could be caused by the bond vibration of Ru-H.[38,39]

3.2.2.8 DFT calculations

In order to get better insights of the molecular structure of the Ru@C_{60} hybrids, Density Functional Theory (DFT) calculations have been performed, using the computational details presented in Chapter 2. To investigate the coordination modes of the functionalized C_{60} with Ru NPs, we have modelled the system using two

functionalized C_{60} in interaction with a Ru_{13} cluster. As shown in Figure 3.20, the coordination mode implies 3 oxygens with a facet of the cluster consisting of 3 surface Ru atoms.

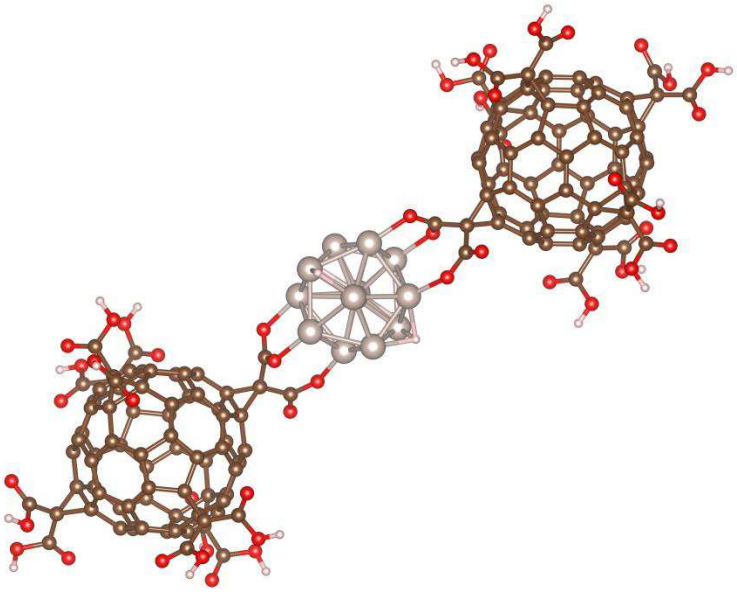

Figure 3.20. Optimized structure of the $C_{66}(COOH)_{12}$-Ru_{13}-$C_{66}(COOH)_{12}$ species.

The Ru-O distances are typical of such systems with values ranging from 1.97 to 2.05 Å, in good agreement with a previous study on the interaction of Ru NPs with oxidized nanotubes sidewalls.[28] Interestingly, as in a former study,[28] the migration of hydrides on the Ru cluster is spontaneous, resulting in the formation of carboxylates groups, with an energy gain of around 15 kcal/mol per H adsorbed. Globally, the formation of this complex is highly favourable: -149 kcal/mol.

3.3 Conclusions

Several functionalized fullerenes have been successfully synthesized using reported procedures. In particular, hexasubstituted fullerene $C_{66}(COOH)_{12}$ is able to stabilize small Ru NPs (1.23-2.37nm) synthesised under mild reaction conditions from [Ru(COD)(COT)]. The SAXS analyses show that Ru NPs are organised displaying a Ru NPs-Ru NPs distance of 2.85 nm in the case of $Ru@C_{66}(COOH)_{12}$ 12/1 synthesized in THF. TEM analyses together with WAXS measurements corroborate

that the Ru NPs are well crystallized and displayed a *hcp* structure. Furthermore, IR, SSNMR and XPS point out that the substituted fullerene coordinates to the Ru NPs *via* carboxylate groups, which is corroborate by DFT calculations.

3.4 Experimental section

General methods

All operations were carried out under argon atmosphere using standard Schlenk techniques or in an MBraun glovebox. Solvents were purified by standard methods or by an MBraun SPS-800 solvent purification system. [Ru(COD)(COT)] was purchased from Nanomeps Toulouse, fullerene C_{60} (99.5%), diethyl malonate(99%), Malonyl dichloride (97.0%), *tert*-Butyl 3-hydroxypropionate(98.0%), carbon tetrabromide (CBr_4 99%), 1,8-diazabicyclo[5.4.0]undec-7-ene (DBU 98%), caesium carbonate (Cs_2CO_3 99.0%), sodium hydride (60 % dispersion in mineral oil), triethylamine (Et_3N 99.0%), 4-(dimethylamino)pyridine (DMAP, 99.0%), 5-aminoisophthalic acid(94.0%), di-tert-butyl dicarbonate ($(Boc)_2O$ 99%), 4-toluenesulfonyl chloride (98.0%), copper(I) bromide dimethyl sulfide complex ($CuBr{\bullet}SMe_2$ 99%), anhydrous Na_2SO_4(99.0%) from Sigma-Aldrich, CO and H_2 from Air Liquid. All these reactants were used as received. The ruthenium content was measured by inductively coupled plasma optical emission spectroscopy (ICP-OES) performed at the LCC with a Thermo Scientific ICAP 6300 instrument. Solid state NMR (MAS-NMR) with and without ^{1}H-^{13}C cross polarization (CP) were performed at the LCC on a Bruker Avance 400WB instrument equipped with a 4 mm probe with the sample rotation frequency being set at 12 kHz, unless otherwise indicated. Measurements were carried out in a 4 mm ZrO_2 rotor. Liquid NMR spectra were obtained on Bruker Fourier 300 systems using $CDCl_3$ as solvent, TMS as internal standard substance, with proton and carbon resonances at 300 and 75 MHz, respectively. ATR-IR spectra were recorded on a Perkin-Elmer GX2000 spectrometer available in a glovebox, in the range 4000-400 cm^{-1}. The Raman spectra have been recorded with an Explora (Horiba)

spectrometer in backscattering geometry using an optical objective x100 (NA 0.9). The wavelength of the incident laser has been 532 nm and the laser power was set to 1 mW.

TEM analyses. TEM and HREM analyses were performed at the "Centre de microcaracterisation Raimond Castaing, UMS 3623, Toulouse" by using a JEOL JEM 1011 CX-T electron microscope operating at 100 kV with a point resolution of 4.5 Å and a JEOL JEM 1400 electron microscope operating at 120 kv. The high resolution analyses were conduct using a JEOL JEM 2100F equipped with a Field Emission Gun (FEG) operating at 200 kV with a point resolution of 2.3 Å and a JEOL JEM-ARM200F Cold FEG operating at 200 kV with a point resolution of >1.9 Å. The approximation of the particles mean size was made through a manual analysis of enlarged micrographs by measuring at least 200 particles on a given grid. Other TEM micrographs were acquired with a JEOL 2100F S/TEM microscope equipped with a FEG operating at 200 kV, a spherical aberration probe corrector and a GATAN Tridiem energy filter.

WAXS and XPS analyses. Wide Angle X-ray Scattering measurements were performed at CEMES on a diffractometer dedicated to Pair Distribution Function (PDF) analysis: graphite-monochromatized Molybdenum radiation (0.07169nm), solid state detection and low background setup. Samples were sealed in Lindemann glass capillaries (diameter 1.5mm) to avoid any oxidation after filling in a glove box. For all samples data were collected on an extended angular range (129 degrees in 2theta) with counting times of typically 150s for each of the 457 data points, thus allowing for PDF analysis. Classic corrections (polarization and absorption in cylindrical geometry) were applied before reduction and Fourier transform. The samples were also analyzed by X-ray photoelectron spectroscopy (XPS) using a VG Escalab MKII spectrophotometer, which operated with a non monochromatized Mg K source (1253.6 eV).

Synthesis of fullerene derivatives

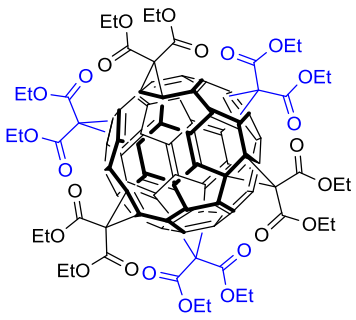

1a

Compound 1a. CBr_4 (22.8g, 69.5 mmol), diethyl malonate (1.104 g, 6.9 mmol) and 1,8-diazabicyclo[5.4.0]undec--ene (DBU, (2.1 g, 13.8 mmol) were successively added to a fullerene C_{60} solution (500 mg, 0.7 mmol) in dry toluene (500 ml). The resulting reaction mixture was stirred under argon for 72h at room temperature. Finally, toluene was evaporated under reduced pressure and the crude was purified by flash column chromatography using a toluene/ethyl acetate mixture as eluting solvent. The product was isolated as a yellow solid (580 mg, 49% yield). ^{1}H NMR ($CDCl_3$, 300 MHz) δ (ppm) 4.33 (q, J = 7.14 Hz, 24H), 1.33(t, J = 7.11 Hz, 36H); ^{13}C NMR ($CDCl_3$, 75 MHz) δ (ppm) 164 (C=O), 146 (sp^2-C C_{60}), 141 (sp^2-C C_{60}), 69.2 (sp^3-C C_{60}), 62.9 (-CH_2-), 45.5 (tert-C), 14.2 (-CH_3).

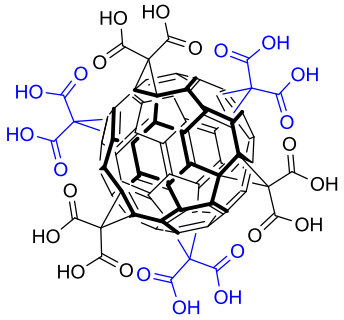

1

Compound 1. 1a (200 mg, 0.119 mmol) was dissolved in 50 mL toluene, and NaH (57.2 mg, 2.38 mmol) was slowly added to the solution. The resulting mixture was stirred 3h at 75 °C. The reaction mixture was centrifuged, the precipitate was washed with toluene three times (10 ml). Afterwards the crude was dissolved in distilled water

and the solution passed through a resin (Amberlite IR-120 hydrogen form). The water was evaporated to afford a yellow-brown solid (127 mg, 80% yield) ^{13}C NMR ($(CD_3)_2CO$, 75 MHz) δ (ppm) 164.7(C=O), 146.3 (sp^2-C C_{60}), 142.5 (sp^2-C C_{60}), 70.4 (sp^3-C C_{60}), 47.7 (tert-C). IR(ATR): *v* 2900(COOH), 1700(C=O), 1192(C-O), 830, 708, 540 (-C_{60}), 524(-C_{60}). Anal. Calcd for $C_{78}O_{24}H_{12}$ (1332 g mol^{-1}): C, 70.3; H, 0.01. Found: C, 60; H, 1.8.

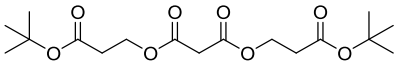

2a

Compound 2a. Et_3N 4 mL, DMAP (4-Dimethylaminopyridine) (15 mg, 0,12 mmol) were dissolved in 20 ml CH_2Cl_2. The mixture was cooled at 0°C and a malonyl chloride (0.3 mL, 2 mmol) solution in 2 mL CH_2Cl_2, was slowly added under argon atmosphere. The reaction was stirred during 30 min at 0°C. The reaction mixture was washed twice with 15 ml of HCl 1M, then with a saturated $NaHCO_3$ solution, and finally twice with 15 ml of brine. The organic layer was dried with Na_2SO_4 and the solvent was evaporated under reduced pressure. The obtained crude was purified by flash chromatography (hexane/ CH_2Cl_2 3/7) to afford a colorless liquid (140 mg, 20% yield). ^1H NMR ($CDCl_3$, 300MHz) δ (ppm) 4.36 (t, *J* = 8.8 Hz, 4H), 3.35 (s, 2H), 2.57 (t, *J* = 8.8 Hz, 4H), 1.44 (s, 18H).

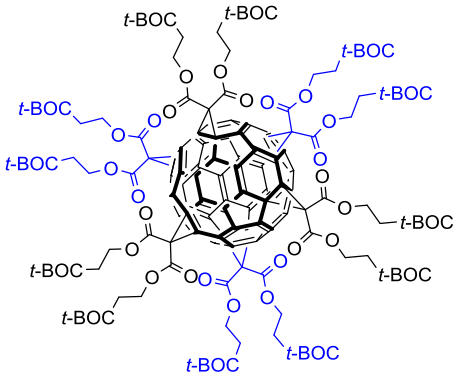

2b

Compound 2b. This compound was prepared from the CBr_4 (0.884 g, 2.7 mmol), diethyl malonate **2a** (100 mg, 0.27 mmol) in toluene and DBU (82 mg, 0.54 mmol) in toluene, which were successively added to a fullerene C_{60} solution (20 mg, 0.027 mmol). After column chromatography (toluene/EtOAc 200/10 to 75/25), traces of a brown solid was obtained. NMR (mixture).

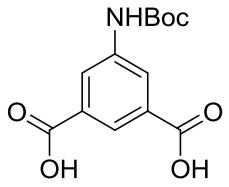

3a

Compound 3a. A solution of 5-Aminoisophthalic acid (5.02 g, 36 mmol) and Et_3N (11.5 ml) in 60 ml of DMF was added dropwise to a $(Boc)_2O$ (9 g, 54 mmol) solution in 20 ml DMF at room temperature. The resulting mixture was stirred 10 min at room temperature and then heated to 50 °C overnight. The reaction mixture was poured into water and extracted with EtOAc (2 x 50ml), the aqueous phase was acidified to pH = 4~5 with HCl 1M and finally extracted with CH_2Cl_2. The combined organic layers were dried with $MgSO_4$, and the obtained crude was purified by flash chromatography using a $CHCl_3/CH_3OH$ 13/1 mixture as eluting solvent). Compound 3a was obtained as a yellow solid (4.0 g, 40% yield). ^1H NMR ($CDCl_3$, 300 MHz) δ (ppm) 8.30 (s, 2H), 8.27 (s, 1H), 1.54 (s, 9H).

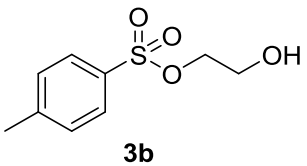

3b

Compound 3b. Toluenesulfonyl chloride (1.54 g, 8 mmol) was slowly added to a solution of DMAP (5.08 g, 14.2 mmol) in 6 ml of ethylene glycol at -5 °C. The reaction mixture was monitored using thin-layer chromatography. After 20 h of

reaction 20 ml of water were added to the reaction mixture, and extracted with EtOAc (3 x 20 ml). All the organic layer were combined and dried with anhydrous $MgSO_4$. After filtration the solvent was evaporated under reduced pressure and the crude was purified by flash chromatography using EtOAc/Pentane as the eluting solvent. Compound 3b was obtained as a colourless solid (1.01g, 58% yield). ^{1}H NMR ($CDCl_3$, 300 MHz) δ (ppm) 7.8 (d, *J* = 11.2 Hz, 2H), 7.87 (d, *J* = 10.8 Hz 1H), 4.1(t, *J* = 6.4 Hz 9H), 3.78 (m, 2H), 2.42 (s, 3H).

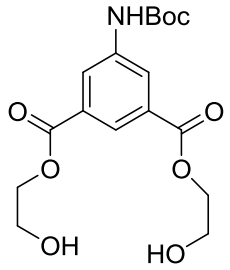

3c

Compound 3c. 3a (100 mg, 0.356 mmol) and Cs_2CO_3 (68.8 mg, 0.211 mmol) were dissolved in deionized water (1 ml). The light yellow solid obtained after the water evaporation was added to a **3b** (153 mg, 14.2 mmol) solution in 20 ml of DMF.. The resulting mixture was allowed to stir 48h at 60°C. Water was added to the reaction mixture and then extracted with ethyl acetate, and finally washed with brine. The organic layers were dried with anhydrous $MgSO_4$, concentrated and the crude was purified by flash chromatography using a ethyl acetate/CH_2Cl_2 1/1 mixture as eluting solvent. 64.8 mg of a light yellow solvent were obtained (49% yield). ^{1}H NMR ($CDCl_3$, 300 MHz) δ (ppm) 8.25 (s, 1H, Ph-), 8.17 (s, 2H, Ph-), 7.1 (s, 1H, -NH-), 4.2 (t, *J*= 6.5 Hz, 4H, -OCH_2-), 3.5 (t, *J*= 6.5 Hz, 4H, -CH_2OH), 1.51 (s, 9H, -CH_3).

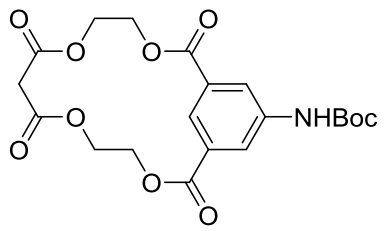

3d

Compound 3d Compound **3c** (60 mg, 0.162 mmol) and malonyl chlororide (28 mg, 0.324 mmol) were dissolved in 5 ml of CH_2Cl_2, respectively, and filled in two syringes. Then the two solutions were added to a three-neck flask cointaining a solution of $NaHCO_3$ (24 mg, 0.178 mmol) in 20 ml of CH_2Cl_2 using a syringe pump with a fixed speed of 0.04ml/min with vigorously stirring. The resulting mixture was allowed to react overnight. 20 ml of water were added to make an extraction, and finally washed with brine. Then the organic layer was dried in Na_2SO_4 and concentrated. The obtained crude was purified by thin layer chromatography plate to afford **3d** as a yellow solid (13.8mg 19.4 % yield). ^1H NMR ($CDCl_3$, 300 MHz) δ (ppm) 8.28 (s, 1H), 8.2 (s, 2H), 6.6 (s, 1H), 4.5 (s, 8H), 3.56 (s, 2H), 1.53 (s, 9H).

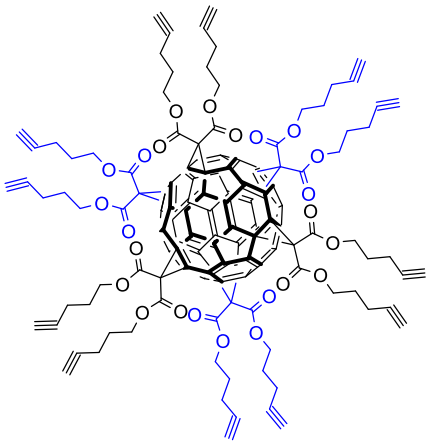

4a

Compound 4a CBr_4 (4.56 g, 13.90 mmol), dipent-4-ynyl malonate (326 mg, 1.38 mmol), and DBU (420 mg, 2.76 mmol) were successively added to a solution of C_{60} (100 mg, 0.14 mmol) in dry toluene (150 mL). The mixture was stirred for 72 h and evaporated. Then, aqueous Na_2CO_3 solution (sat.) was added, and the resulting

mixture was extracted with $NaHCO_3$ (3×150 mL). The combined organic layer was washed with HCl (1 M, 2x150 mL) water (2×150 mL) and brine (100 mL), dried over MgSO4, and concentrated under vacuum. The crude was purified by column chromatography (SiO_2, CH_2Cl_2, CH_2Cl_2: AcOEt; 95:5) giving 1 (184 mg, 62%) as an orange glassy product. ^{1}H NMR ($CDCl_3$, 300 MHz) δ (ppm) 4.55-4.11 (m, 24H, -OCH_2-), 2.41-2.12 (m, 24H,-$CH_2C{\equiv}C$), 2.06-1.76 (m, 36H, -CH_2- and -C≡CH). ^{13}C NMR ($CDCl_3$, 75 MHz) δ (ppm) 162.4 (-C=O), 144.7 (sp^2-C -C_{60}), 139.8 (sp^2-C C_{60}), 81.3 (-C≡CH), 68.7 (sp^3-C C_{60}), 64.4 (-C≡CH), 62.1(-OCH_2-), 15.6(-CH_2-), 14.1(-$CH_2C{\equiv}CH$).

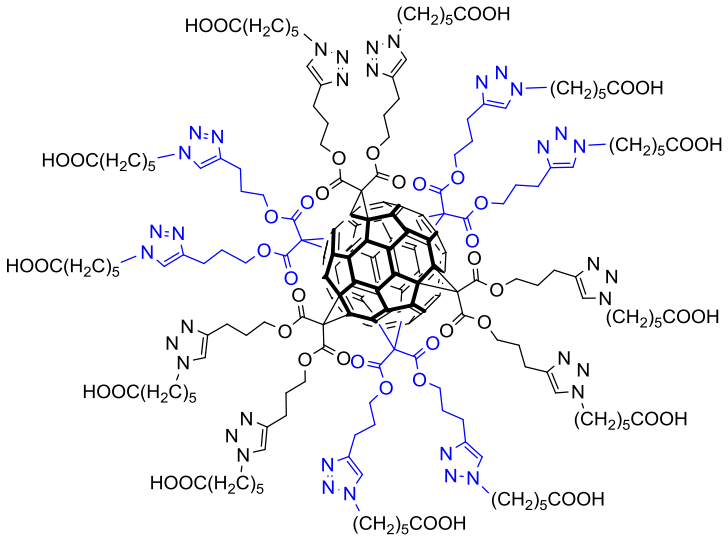

4

Compound 4 To a mixture of **4a** (42 mg, 0.0197 mmol), CuBr•SMe_2 (22.0 mg, 0.107 mmol) in DMSO (1 mL) the 6-azidohexanoic acid (92.7 mg, 0.591 mmol) was added under atmospheric pressure of Ar, and the solution was stirred at ambient temperature for 24 h. AcOEt was added to the reaction mixture and the desired compound was precipitated by centrifugation (3500 rpm, 20 min), suspended in AcOEt (2x3mL) and Et_2O and centrifuged again (3500 rpm, 20 min, each time). The title compound 4 thus obtained was as an orange-brown solid (48 mg, 61 %). **4b** ^{1}H NMR ($CDCl_3$, 300 MHz) δ (ppm) 77.6 (s, 12H, -triazole), 4.37-4.35 (m, 48H, -CH_2-triazole and -CH_2CO), 2.69-2.67 (m, 24H, -CH_2-triazole), 2.28-2.23 (m, 24H, -CH_2COOH), 1.90-1.86 (m,

24H, -CH_2-), 1.62-1.57 (m, 24H, -CH_2-), 1.31-1.29 (m, 24H, -CH_2-); ^{13}C NMR ($CDCl_3$, 75 MHz) δ (ppm) 175.5 (-COOH), 163.1 (-C=O), 146.1 (-triazole), 145 (sp^2-C C_{60}), 141 (sp^2-C C_{60}), 120 (-triazole), 69.1 (sp^3-C C_{60}), 66.2 (-OCH_2-), 49.5 (tert-C), 38.9 (N-CH_2-triazole), 33.1 (-CH_2COOH), 29.5 (-CH_2-triazole), 27.5 (-CH_2-), 26.3 (-CH_2-), 23.4 (-CH_2-), 21.5 (-CH_2-).

Synthesis of Ru@C_{66}(COOH)$_{12}$ nanostructures

In a typical experiment [Ru(COD)(COT)] complex was introduced in a Fisher-Porter bottle, and a solution of $C_{66}(COOH)_{12}$ in the desired solvent was then introduced in the reactor. The resulting solution was stirred for 30 min at room temperature, after which the bottle was pressurized with 3 bar of H_2. The solution, which turned black after few min of reaction, was kept under stirring overnight at room temperature. After this period of time, excess of H_2 was eliminated and the volume of solvent was reduced under vacuum. Pentane was then added to the colloidal suspension to precipitate the Ru@$C_{66}(COOH)_{12}$ nanostructures. After filtration under argon with a cannula, the black solid powder was washed twice with pentane and filtrated again before drying under vacuum. For each ratio studied, the quantities of reactants are detailed hereafter:

Ru@$C_{66}(COOH)_{12}$ 6/1: 100 mg (0.317 mmol) of [Ru(COD)(COT)]; 70.4 mg (0.0529 mmol) of $C_{66}(COOH)_{12}$ and 150 mL of THF. Yield: 82 mg. Ru: 22.6 %.

Ru@$C_{66}(COOH)_{12}$ 12/1: 113.5 mg (0.36 mmol) of [Ru(COD)(COT)]; 45 mg (0.035 mmol) of $C_{66}(COOH)_{12}$ and 100 mL of THF. Yield: 69mg. Ru: 40.7 %.

Ru@$C_{66}(COOH)_{12}$ 30/1: 282 mg (0.895 mmol) of [Ru(COD)(COT)]; 40 mg (0.0298 mmol) of $C_{66}(COOH)_{12}$ and 90 mL of THF. Yield: 116 mg. Ru: 52.4 %.

3.5 References

1. Rao, C. R.; Kulkarni, G. U.; Thomas, P. J.; Edwards, P. P., Metal nanoparticles and their assemblies. *Chem. Soc. Rev.* **2000,** *29* (1), 27-35.

2. Daniel, M.-C.; Astruc, D., Gold nanoparticles: Assembly, supramolecular chemistry, quantum-size-related properties, and applications toward biology, catalysis, and nanotechnology. *Chem. Rev.* **2004,** *104* (1), 293-346.

3. Liao, J.; Blok, S.; van der Molen, S. J.; Diefenbach, S.; Holleitner, A. W.; Schönenberger, C.; Vladyka, A.; Calame, M., Ordered nanoparticle arrays interconnected by molecular linkers: Electronic and optoelectronic properties. *Chem. Soc. Rev.* **2015,** *44* (4), 999-1014.

4. Volokitin, Y.; Sinzig, J.; Dejongh, L.; Schmid, G.; Vargaftik, M.; Moiseev, I., Quantum-size effects in the thermodynamic properties of metallic nanoparticles. *Nature* **1996,** *384* (6610), 621-623.

5. Respaud, M.; Broto, J.; Rakoto, H.; Fert, A.; Thomas, L.; Barbara, B.; Verelst, M.; Snoeck, E.; Lecante, P.; Mosset, A., Surface effects on the magnetic properties of ultrafine cobalt particles. *Phys. Rev. B* **1998,** *57* (5), 2925-2935.

6. Zhang, Y.; Liu, Q.; Mundoor, H.; Yuan, Y.; Smalyukh, I. I., Metal nanoparticle dispersion, alignment, and assembly in nematic liquid crystals for applications in switchable plasmonic color filters and e-polarizers. *ACS Nano* **2015,** *9* (3), 3097-3108.

7. (a) Edel, J. B.; Kornyshev, A. A.; Urbakh, M., Self-assembly of nanoparticle arrays for use as mirrors, sensors, and antennas. *ACS Nano* **2013,** *7* (11), 9526-9532; (b) Nie, Z.; Petukhova, A.; Kumacheva, E., Properties and emerging applications of self-assembled structures made from inorganic nanoparticles. *Nat. Nano* **2010,** *5* (1), 15-25.

8. Lee, G.; Shim, J. H.; Kang, H.; Nam, K. M.; Song, H.; Park, J. T., Monodisperse Pt and PtRu/C_{60} hybrid nanoparticles for fuel cell anode catalysts. *Chem. Commun.* **2009,** (33), 5036-5038.

9. (a) Munnik, P.; de Jongh, P. E.; de Jong, K. P., Control and impact of the nanoscale distribution of supported cobalt particles used in Fischer-Tropsch catalysis. *J. Am. Chem. Soc.* **2014,** *136* (20), 7333-7340; (b) Prieto, G.; Meeldijk, J. D.; de Jong, K. P.; de Jongh, P. E., Interplay between pore size and nanoparticle spatial distribution: Consequences for the stability of CuZn/SiO_2 methanol synthesis catalysts. *J. Catal.* **2013,** *303*, 31-40; (c) Prieto, G.; Shakeri, M.; de Jong, K. P.; de Jongh, P. E., Quantitative relationship between support porosity and the stability of pore-confined metal nanoparticles studied on CuZn/SiO_2 methanol synthesis catalysts. *ACS Nano* **2014,** *8* (3), 2522-2531; (d) Prieto, G.; Zečević, J.; Friedrich, H.; de Jong, K. P.; de Jongh, P. E., Towards stable catalysts by controlling collective properties of supported metal nanoparticles. *Nat. Mater.* **2013,** *12* (1), 34-39.

10. Fujihara, H.; Nakai, H., Fullerenethiolate-functionalized gold nanoparticles: A new class of surface-confined metal-C_{60} nanocomposites. *Langmuir* **2001,** *17* (21), 6393-6395.

11. Sudeep, P.; Ipe, B. I.; Thomas, K. G.; George, M.; Barazzouk, S.; Hotchandani, S.; Kamat, P. V., Fullerene-functionalized gold nanoparticles. A self-assembled photoactive antenna-metal nanocore assembly. *Nano Lett.* **2002,** *2* (1), 29-35.

12. Shon, Y.-S.; Choo, H., [60] fullerene-linked gold nanoparticles: Synthesis and layer-by-layer growth on a solid surface. *Chem. Commun.* **2002,** (21), 2560-2561.

13. Lu, F.; Xiao, S.; Li, Y.; Song, Y.; Liu, H.; Li, H.; Zhuang, J.; Liu, Y.; Gan, L.; Zhu, D., Fullerene-functionalized gold core-shell nanoparticles: Preparation and optical limiting properties. *Inorg. Chem. Commun.* **2004,** *7* (8), 960-962.

14. Geng, M.; Zhang, Y.; Huang, Q.; Zhang, B.; Li, Q.; Li, W.; Li, J., Functionalization of C_{60} with gold nanoparticles. *Carbon* **2010,** *48* (12), 3570-3574.

15. Zhang, P.; Li, J.; Liu, D.; Qin, Y.; Guo, Z.-X.; Zhu, D., Self-assembly of gold nanoparticles on fullerene nanospheres. *Langmuir* **2004,** *20* (4), 1466-1472.

16. Lim, I. I. S.; Ouyang, J.; Luo, J.; Wang, L.; Zhou, S.; Zhong, C.-J., Multifunctional fullerene-mediated assembly of gold nanoparticles. *Chem. Mater.* **2005,** *17* (26), 6528-6531.

17. Lim, I.-I. S.; Pan, Y.; Mott, D.; Ouyang, J.; Njoki, P. N.; Luo, J.; Zhou, S.; Zhong, C.-J., Assembly of gold nanoparticles mediated by multifunctional fullerenes. *Langmuir* **2007,** *23* (21), 10715-10724.

18. Hirsch, A.; Vostrowsky, O., C_{60} hexakisadducts with an octahedral addition pattern a new structure motif in organic chemistry. *Eur. J. Org. Chem.* **2001,** *2001* (5), 829-848.

19. Pierrat, P.; Vanderheiden, S.; Muller, T.; Brase, S., Functionalization of hexakis methanofullerene malonate crown-ethers: Promising octahedral building blocks for molecular networks. *Chem Commun* **2009,** (13), 1748-50.

20. Rousseau, G.; Lavenn, C.; Cardenas, L.; Loridant, S.; Wang, Y.; Hahn, U.; Nierengarten, J.-F.; Demessence, A., One-pot synthesis of sub-3 nm gold nanoparticle networks connected by thio-based multidentate fullerene adducts. *Chem. Commun.* **2015,** *51* (31), 6730-6733.

21. Guldi, D. M.; Zerbetto, F.; Georgakilas, V.; Prato, M., Ordering fullerene materials at nanometer dimensions. *Acc. Chem. Res.* **2005,** *38* (1), 38-43.

22. Bingel, C., Cyclopropanierung von fullerenen. *Chem. Ber.* **1993,** *126* (8), 1957-1959.

23. Hirsch, A.; Lamparth, I.; Karfunkel, H. R., Fullerene chemistry in three dimensions: Isolation of seven regioisomeric bisadducts and chiral trisadducts of C_{60} and di (ethoxycarbonyl) methylene. *Angew. Chem. Int. Ed. Engl.* **1994,** *33* (4), 437-438.

24. Hirsch, A., Principles of fullerene reactivity. In *Fullerenes and related structures*, Springer: 1999; pp 1-65.

25. Camps, X.; Hirsch, A., Efficient cyclopropanation of C_{60} starting from malonates. *J. Chem. Soc., Perkin Trans. 1* **1997,** (11), 1595-1596.

26. Nakamura, Y.; Suzuki, M.; Imai, Y.; Nishimura, J., Synthesis of [60] fullerene adducts bearing carbazole moieties by bingel reaction and their properties. *Org. Lett.* **2004,** *6* (16), 2797-2799.

27. Knight, B.; Martín, N.; Ohno, T.; Ortí, E.; Rovira, C.; Veciana, J.; Vidal-Gancedo, J.; Viruela, P.; Viruela, R.; Wudl, F., Synthesis and electrochemistry of electronegative spiroannelated

methanofullerenes: Theoretical underpinning of the electronic effect of addends and a reductive cyclopropane ring-opening reaction. *J. Am. Chem. Soc.* **1997,** *119* (41), 9871-9882.

28. Machado, B. F.; Oubenali, M.; Axet, M. R.; Nguyen, T. T.; Tunckol, M.; Girleanu, M.; Ersen, O.; Gerber, I. C.; Serp, P., Understanding the surface chemistry of carbon nanotubes: Toward a rational design of Ru nanocatalysts. *J. Catal.* **2014,** *309*, 185-198.

29. Pan, C.; Pelzer, K.; Philippot, K.; Chaudret, B.; Dassenoy, F.; Lecante, P.; Casanove, M.-J., Ligand-stabilized ruthenium nanoparticles: Synthesis, organization, and dynamics. *J. Am. Chem. Soc.* **2001,** *123* (31), 7584-7593.

30. Kraft, A.; Gsänger, M.; Beuerle, F., Arranging fullerenes through hydrogen bonding. *Eur. J. Org. Chem.* **2014,** *2014* (3), 523-528.

31. Sánchez‐Navarro, M.; Muñoz, A.; Illescas, B. M.; Rojo, J.; Martín, N., [60] fullerene as multivalent scaffold: Efficient molecular recognition of globular glycofullerenes by concanavalin a. *Chem. Eur. J.* **2011,** *17* (3), 766-769.

32. Amiens, C.; Chaudret, B.; Ciuculescu-Pradines, D.; Collière, V.; Fajerwerg, K.; Fau, P.; Kahn, M.; Maisonnat, A.; Soulantica, K.; Philippot, K., Organometallic approach for the synthesis of nanostructures. *New J. Chem.* **2013,** *37* (11), 3374-3401.

33. Haynes, W. M., *Crc handbook of chemistry and physics*. CRC press: 2014.

34. Gambill, W., How to estimate mixtures viscosities. *Chem. Eng.* **1959,** *66*, 151-152.

35. Jouyban, A.; Soltanpour, S.; Chan, H.-K., A simple relationship between dielectric constant of mixed solvents with solvent composition and temperature. *Int. J. Pharm.* **2004,** *269* (2), 353-360.

36. Chen, M.-Y.; Huang, Y.-B.; Pang, H.; Liu, X.-X.; Fu, Y., Hydrodeoxygenation of lignin-derived phenols into alkanes over carbon nanotube supported ru catalysts in biphasic systems. *Green Chem.* **2015,** *17* (3), 1710-1717.

37. Stephenson, T.; Wilkinson, G., New ruthenium carboxylate complexes. *J. Inorg. Nucl. Chem.* **1966,** *28* (10), 2285-2291.

38. Jasim, N. A.; Perutz, R. N.; Foxon, S. P.; Walton, P. H., Synthesis, characterisation and reactivity of ruthenium bis-bifluoride, ruthenium hydride bifluoride and ruthenium hydride fluoride complexes. *J. Chem. Soc., Dalton Trans.* **2001,** (11), 1676-1685.

39. Wang, X.; Andrews, L., Infrared spectra and theoretical calculations for Fe, Ru, and Os metal hydrides and dihydrogen complexes. *J. Phys. Chem. A* **2008,** *113* (3), 551-563.

40. Iehl, J.; Nierengarten, J. F., A click-click approach for the preparation of functionalized [5:1]−hexaadducts of C_{60}. *Chem. Eur. J.* **2009,** *15* (30), 7306-7309.

Chapter 4 Catalytic applications of ruthenium@fullerene nanostructures

Part of the work descrided in chapter 4 has been published in: F. Leng, I. C. Gerber, P. Lecante, S. Moldovan, M. Girleanu, M. R. Axet and P. Serp, Controlled and chemoselective hydrogenation of nitrobenzene over Ru@C_{60} catalysts, *ACS Catal.,* **2016**, *6(9),* 6018-6024.

4.1 Introduction

Fullerene and fullerene-based materials have shown superior catalytic activity and selectivity in heterogeneous catalysis[1,2,3,4,5,6] because of their specific properties, such as thermal stability,[7] high capacity for hydrogen adsorption[8,9,10,11] and the ability of various coordination modes.[12,13,14] Fullerene-based materials, typically transition metal fullerene compounds, have been developed for several catalytic reactions.[3] For instance, these kind of compounds have been successfully used in the hydrogenation reaction of several functional groups including nitro,[15,16,16b,17] alkyne,[18] C=C,[5] and C=O bonds.[19] Although progresses have been achieved in the past, there is still little information on the catalytic properties of metallic nanoparticles anchored on fullerene C_{60}. For instance, no data are available concerning the influence of the size and shape of the metallic NPs as well as the morphology of the nanostructures, parameters which have been proved to be crucial for catalytic performances.

In this chapter, the catalytic properties of several Ru@fullerene C_{60} nanostructures have been studied. Ruthenium-fullerene nanostructures synthesized in CH_2Cl_2 ($Ru@C_{60}$) and in toluene (T-$Ru@C_{60}$), as well as $Ru@C_{66}(COOH)_{12}$ nanostructures have been used as catalysts in the hydrogenation reactions of nitrobenzene and *trans*-cinnamaldehyde. The best performances were obtained with $Ru@C_{60}$ nanocatalysts in both hydrogenation reactions. Interestingly, electron deficient ruthenium NPs supported on Ru fulleride nanospheres, $Ru@C_{60}$, allow the successive and chemoselective hydrogenation of nitrobenzene to aniline and then to cyclohexylamine. The same behavior, *i.e.* a two-step successive hydrogenation, has been observed for several substituted nitroarenes. DFT calculations suggest that the observed chemoselectivity is mainly governed by the presence of surface hydrides on the electron-deficient Ru nanoparticles.

4.2 Results and discussion

4.2.1 Hydrogenation of nitrobenzene

Selective hydrogenation lay at the heart of many industrial processes, and is one of the widest areas of research in catalysis. The catalytic hydrogenation of nitrobenzene (NB) is an industrially important reaction, which may lead as major products to aniline (AN) or cyclohexyl amine (CA). Additionally, condensation side reaction may produce dicylohexylamine (DCA) as the major by-product (Scheme 4.1).

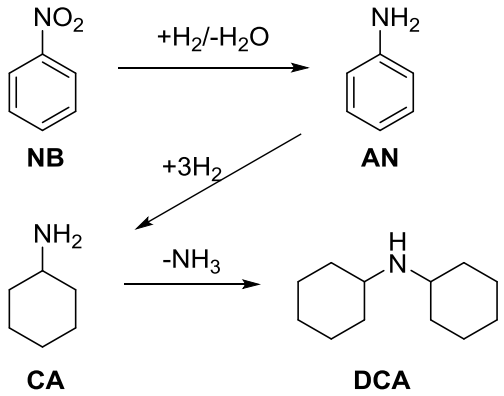

Scheme 4.1. Main products and by-products formed during NB hydrogenation.

It is generally admitted that in NB, the aromatic ring is electron deficient and coordinates only weakly to metals typically used in hydrogenation reactions. In contrast, the nitro group is strongly coordinating and is usually hydrogenated first. AN, which is an important intermediate for polyurethanes, dyes, pharmaceuticals, explosives, and agricultural products,[20] is industrially produced *via* NB selective hydrogenation. Reactions performed in the liquid phase used a variety of metal catalysts (Ni, Pt, and Pd) associated to modifiers, and organic solvents. DuPont hydrogenates nitrobenzene in liquid phase using a Pt-Pd catalyst on a carbon support with iron as modifier. The modifier provides good catalyst life time, high activity, and protection against hydrogenation of the aromatic ring.[20] CA can be used in the synthesis of artificial sweeteners, metal corrosion inhibitors, rubber vulcanizing additives, dyestuff, plasticizers and extracting agents for natural products.[21]

Commercially, it may be produced *via* reductive amination of cyclohexanol or phenol, or hydrogenation of AN. A variety of metals such as Ni, Co, Rh, Ru, Pd and Pt can be used for the hydrogenation of AN either in the vapor or in the liquid phase.

The design of a single metal and non-promoted catalyst, which could hydrogenated in a controlled manner NB to selectively produce either AN, or CA in a single step is therefore of paramount interest. In that context, recent advances in the design of nanostructured catalysts for selective hydrogenation have been reviewed.[22] Supported ruthenium catalysts could be interesting candidates since the literature indicates that Ru is the best of the platinum metal catalysts for the hydrogenation of aromatic amines to alicyclic anilines,[23] and in addition high selectivity towards AN can also be obtained by careful choice of the support.[24] Electron deficient Ru nanoparticles (NPs) have been reported to be highly active since AN desorption is facilitated,[24a] furthermore in the case of a controlled reaction they could be more selective to AN, thanks to a preferential coordination of the nitro group. Concerning the choice of the support, high NB conversions have been reported when using carbon supports rather than silica or alumina.[25] Carbon is a chemically quite inert support that allows to skirt condensation reactions known for more acidic oxide supports. The direct reduction of NB to AN by carbon materials (carbocatalysis) such as fullerenes (C_{60}) or carbon nanotubes (CNTs) has also been discussed.[1, 26] Ruthenium supported on CNTs allow for hydrogenation of both the aromatic ring and the nitro group,[23b] and CA was produced with 90% selectivity. In that case, the AN selectivity reached a maximum of 64%. The use of mixtures of CNT-supported Pt and Ru catalysts has also been proposed.[27] Indeed, mixtures of Pt/CNT, having a high activity in NB hydrogenation, and of Ru/CNT, highly selective for the hydrogenation of AN to CA, provided high activity at constant high selectivity. A Ru/C-$NaNO_2$ catalyst was found to catalyze NB hydrogenation to produce AN (100% selectivity at 80°C) or CA (100% selectivity at 90°C) in high yield, depending on the reaction temperature.[28] Considering the fact that C_{60} is a well-known electron acceptor, a Ru@C_{60} catalyst should provide electron

deficient Ru NPs, which could be of interest for this reaction. In this context, Ru@C_{60}, T-Ru@C_{60}, and Ru@$C_{66}(COOH)_{12}$ nanostructures appear as excellent candidates as catalysts for the NB hydrogenation reaction. Nitrobenzene hydrogenation was studied at 30 bar of H_2 and 80 °C in ethanol. All catalysts were found to be active for NB hydrogenation. We independently checked that, under these experimental conditions, C_{60} has no activity for this reaction. The main reaction products were AN and CA; DCA and N-ethylaniline (AN-Et), which is formed from N-alkylation of aniline due to reaction with the solvent,[29,30] were the only detected byproducts. First, Ru@C_{60} nanocatalysts were tested in the NB hydrogenation reaction and the reaction followed over time. Table 4.1 shows the results obtained with the Ru@C_{60} nanocatalysts and Figure 4.1 the evolution of the conversion over time.

All catalysts were active in NB hydrogenation (Figure 4.2). The low loading catalysts (Ru/C_{60} ratio < 5) were found inactive for the hydrogenation of the aromatic ring, and AN was produced with selectivity > 80%. This might be due to the extreme small size of the Ru NPs present in these samples, which might be poorly active for aromatic ring hydrogenation.[31,14] At Ru/C_{60} ratio ≥ 5, all catalysts were active for AN hydrogenation to CA. The remarkable feature of all these catalysts is that AN hydrogenation to CA starts only when complete NB hydrogenation to AN finished (see Figure 4.1 for the Ru@C_{60} 10/1 catalyst). To the best of our knowledge such behavior has never been reported before. Controlled and chemoselective hydrogenation of nitrobenzene over these Ru@C_{60} catalysts is thus possible. Selectivity towards AN higher than 90% and selectivity towards CA higher than 80% have been obtained whatever the Ru/C_{60} ratio. If we consider the activity of these catalysts, the TOF were systematically higher for the hydrogenation of the aromatic ring compared to the nitro group.

Table 4.1. Results of hydrogenation of nitrobenzene in ethanol over different Ru@C_{60} catalysts.[a]

Ru@C_{60}	Nitro- group		Selectivity (%)[b]		Aromatic ring		Selectivity(%)[b]		
	TOF (h^{-1})[c]	Time h	AN	AN-Et	TOF (h^{-1})[d]	Time h	CA	DCA	CA-Et
1/1	18.7	48	80	20	--	---	---	--	---
2/1	33.6	48	84	16	---	---	trace	--	---
5/1	44.3	24	96	4	132.2	6	91	4	5
10/1	55.7	4	90	10	100.4	3.5	86	7	7
20/1	60.8	3.5	91	9	182.1	2	84.5	8.5	7
30/1	59.8	3	91	9	123.1	1.5	82.5	9	8.5
50/1	42.6	3	92	8	134.5	1.5	89	5	6

[a]Reaction conditions: 5 mg of Ru@C_{60} catalyst, 500 mg (4.06 mmol) of nitrobenzene, 200 mg (1.1 mmol) of dodecane (internal standard), 30 bar of H_2, 80 °C, 30 mL of EtOH. [b]Determined by GC-MS using internal standard techniques. [c]TOFs calculated at 1 h of reaction (~30% of conversion) except for ratios 1/1 and 2/1 (3 h). [d]TOFs calculated at 0.5 h of reaction (~50% of conversion) except for ratios 5/1 and 10/1 (1 h).

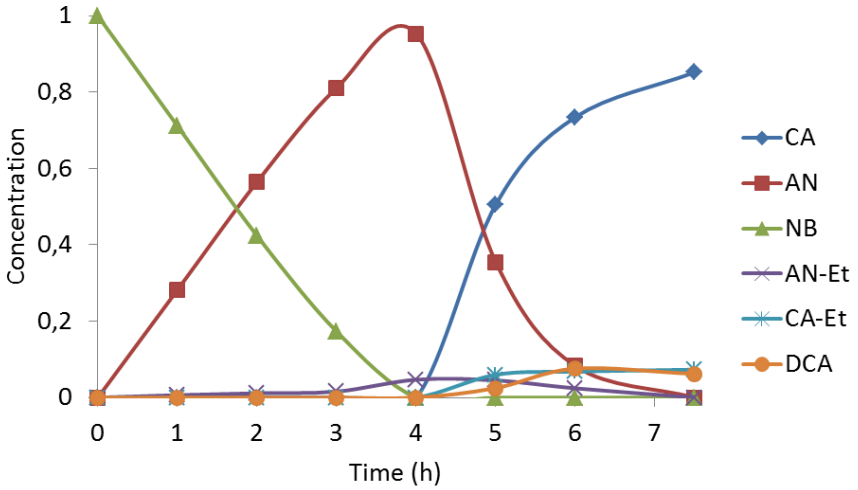

Figure 4.1. Time-concentration curve for NB hydrogenation with Ru@C_{60} (Ru/C_{60} = 10/1).

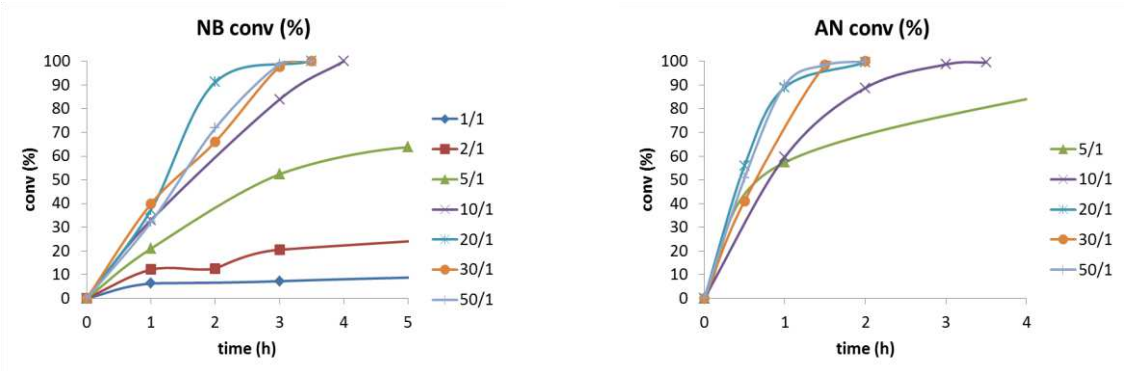

Figure 4.2. Evolution of conversion of nitrobenzene (left) and aniline (right) with time with different Ru@C_{60} catalysts.

Apparent activation energies for nitrobenzene and aniline hydrogenation for the Ru@C_{60} 10/1 catalyst were calculated using the kinetics measured at 60, 80 and 90°C (5 mg of Ru@C_{60} 10/1 catalyst, NB or AN 0.2M, 30 bar H_2, 20 mL EtOH see Table 4.2 and Table 4.3 for further details). According to the nitrobenzene and aniline hydrogenation conversion rates in the temperature range of 60-90°C, the calculated activation energies are 63.4 and 34.6 kJ/mol, respectively.

Table 4.2. Kinetics and activation energy of nitrobenzene hydrogenation.

T (°C)	Time(h)	Conv (%)[a]	*k* (M/h)[b]	E_a (kJ/mol)[c]
60	2	14	0.016	63.4
	4	34		
	6	49		
80	1	29	0.054	
	2	54		
	3	81		
90	0.2	9	0.109	
	0.5	33		
	1	56		
	1.5	80		

Reaction conditions: 5 mg Ru@C_{60} 10/1 catalyst, 500 mg (4.06mmol) nitrobenzene, 200 mg (1.1 mmol) dodecane (internal standard), 30 bar H_2, 20 mL solvent. [a]Determined by GC-MS using internal standard technique.[b]Conversion rate of NB [c] Calculated using the Arrhenius equation $k=AE^{-(Ea/RT)}$: ploting ln*k* *vs* 1/T(K) yields a straight line with a slope of $-E_a/R$ (R=8.314 J/mol.K; A: Arrhenius factor; *k*: conversion rate).

Table 4.3. Kinetics and activation energy of aniline hydrogenation.

T (°C)	Time(h)	Conv (%)[a]	*k* (M/h) [b]	E_a (kJ/mol) [c]
60	2	22	0.0231	34.6
	4	47		
	8	93		
80	1	22	0.0414	
	2	41		
	3	61		
	4	85		
90	1	34	0.0671	
	2	68		
	2.5	84		

Reaction conditions: 5 mg Ru@C_{60} 10/1 catalyst, 500 mg (4.06mmol) aniline, 200mg (1.1 mmol) dodecane (internal standard), 30 bar H_2, 20 mL solvent. [a]Determined by GC-MS using internal standard technique.[b]Conversion rate of AN [c] Calculated using the Arrhenius equation $k=AE^{-(Ea/RT)}$: ploting ln*k* *vs* 1/T(K) yields a straight line with a slope of $-E_a/R$ (R=8.314 J/mol.K; A: Arrhenius factor; *k*: conversion rate).

Competitive hydrogenation in the presence of both nitrobenzene and aniline was performed using the Ru@C_{60} 10/1 catalyst (see Table 4.4). The reaction proceed similarly: nitrobenzene was selectively hydrogenated first with no presence of CA in the reaction mixture. The direct hydrogenation of AN also produced selectively CA, nevertheless the activity of the catalyst was lower.

After reaction, the size of the Ru NPs as well as the size of the Ru@C_{60} nanospheres did not significantly change (Table 4.5 and Table 4.6). Recyclability tests were performed employing Ru@C_{60} 10/1 catalyst in order to confirm the stability of the catalytic species (Table 4.7). A slight decrease of the final conversion was detected in the successive catalytic runs.

Table 4.4. Nitrobenzene hydrogenation in the presence of aniline.

	NB hydrogenation[a]			NB hydrogenation in the presence of AN[b]		
Time (h)	**Conv (%)[c]**	**TOF (h^{-1})**	**AN Selec. (%)[c]**	**Conv. (%)[c]**	**TOF (h^{-1})**	**AN Selec. (%)[c]**
1	33	55.7	86	24	39.8	100
2	-	-	-	44	36.8	100
3	84	47.2	90	69	38.8	99
4	100	42.1	92	81	35.5	99

[a]Reaction conditions: 5 mg Ru@C_{60} catalyst, 4.06 mmol nitrobenzene, 1.1 mmol dodecane (internal standard), 30 bar H_2, 80°C, 30 mL EtOH. [b]Reaction conditions: 5 mg Ru@C_{60} catalyst, 4.06mmol nitrobenzene, 4.06mmol aniline,1.1 mmol dodecane (internal standard), 30 bar H_2, 80°C, 30 mL EtOH. [c]Determined by GC-MS using internal standard technique.

Table 4.5. Ru NPs mean size before and after nitrobenzene hydrogenation.

Ru@C_{60}	**Before reaction[a]**	**After reaction[a]**
2/1	1.16 ± 0.02 nm	1.01 ± 0.01 nm
5/1	1.31 ± 0.03 nm	1.50 ± 0.006 nm
10/1	1.26 ± 0.03 nm	1.50 ± 0.01 nm
20/1	1.10 ± 0.01 nm	1.56 ± 0.023 nm
30/1	1.35 ± 0.02 nm	1.76 ± 0.01 nm
50/1	1.31 ± 0.03 nm	1.87 ± 0.02 nm

[a]Manual measurement from enlarged TEM micrographs of at least 200 objects.

Table 4.6. Ru@C_{60} nanospheres size before and after the hydrogenation of nitrobenzene.

Ru/C_{60}	Before reaction[a]	After reaction[a]
1/1	36.2 ± 1.2 nm	43.6 ± 0.1 nm
2/1	31.6 ± 0.6 nm	40 ± 0.9 nm
5/1	42.6 ± 1.0 nm	51 ± 0.8 nm
10/1	32.4 ± 0.3 nm	44 ± 0.4 nm
20/1	39.8 ± 1.1 nm | 85.2 ± 2.9 nm	49 ±0.2nm | 95±1.1nm
30/1	56.4 ± 4.7 nm | 103.2 ± 1.0 nm	112.5 ±1.8nm
50/1	63.3 ± 0.8 nm	81.5± 1.4 nm

[a]Manual measurement from enlarged micrographs of at least 200 objects.

Table 4.7. Catalytic recycling tests for NB hydrogenation with the Ru@C_{60} catalyst.

Ru@C_{60} 10/1	Nitrobenzene conv. (%)[a]	Aniline conv. (%)[a]	Cyclohexylamine selectivity (%)[a]
Fresh catalyst	100	97	90
1st recycling	100	93	86
2nd recycling	100	88	87

Reaction conditions: 20 mg Ru@C_{60} 10/1 catalyst, 16.14 mmol nitrobenzene, 4 mmol dodecane (internal standard), 30 bar H_2, 80°C, 120 mL EtOH, 8h. [a]Determined by GC-MS using internal standard technique.

Nevertheless, Ru was not detected in the final product by ICP analyses, indicating that there is no leaching of soluble Ru species. Taking into account these results, the decrease of the conversion in the recycling test is more likely due to the slight increase of the Ru NPs mean size after catalysis.

4.2.2.1 Solvent effect

Highly exothermic reactions, such as the NB hydrogenation reaction often employ a solvent to help dissipate the excess heat generated during reaction and to prevent possible explosion. It has been shown that the nature of the solvent employed has a significant effect on the rate and selectivity of the catalytic hydrogenation reaction.[32] Solvents have different roles, in addition to the usual one (heat management, solubilisation): i) they can change the solubility of hydrogen, ii) compete with the reactants for adsorption at the metal surface, iii) catalyze side reactions, iv) provoke catalyst agglomeration, and v) interact with the reactant. Concerning the latter effect, favorable thermodynamic interaction between the solvent and the reactant is expected to reduce the adsorption of the reactant on the catalyst while unfavorable interaction should favor the adsorption. The Ru@C_{60} 10/1 catalyst was used to evaluate the influence of the solvent (Table 4.8). Methanol, ethanol and isopropanol were compared. Hydrogen solubility in these solvent is expected to follow the order: iPrOH > EtOH > MeOH, as H_2 solubility in alcohols increases with the number of carbon atoms.[33] The relative permittivity (εr) follow the order MeOH (εr = 32.7) > EtOH (εr = 24.5) > iPrOH (εr = 17.9). A significant solvent effect was noticed both on catalyst activity and selectivity. As far as the activity is concerned, methanol is by far the best solvent. Results obtained on Pd/C catalysts have shown that NB[34] or nitrotoluene[32] hydrogenations proceed much more rapidly in methanol than in isopropanol or ethanol. It has been proposed that the interaction between the solvent and the reactant is probably the dominant factor that decides the overall effect of the solvent on the rate of hydrogenation. The interactions seem to affect the energetics of the reaction, as reflected in the value of the activation energy, which was observed to change with the reaction medium.[32] However, over palladium catalysts supported on nanodiamonds the higher rates of NB hydrogenation were obtained in butanol, followed by ethanol and then methanol.[35]

Table 4.8. Results of hydrogenation of nitrobenzene with the Ru@C_{60} (Ru/C_{60} = 10/1) catalyst in different solvents.

Solvent	Nitro- group		Selectivity (%)[a]		Aromatic ring		Selectivity (%)[a]		
	TOF (h^{-1}) [b]	Time h	AN	N-alkylation	TOF (h^{-1})[c]	Time h	CA	DCA	N-alkylation
MeOH	42.6	3	98	2	134.5	3	88	5	7
EtOH	55.7	4	90	10	100.4	3.5	86	7	7
iPrOH	37.0	6	100	0	45	4	94.5	2	3.5

Reaction conditions: 5 mg Ru@C_{60} 10/1 catalyst, 500 mg (4.06mmol) nitrobenzene, 200mg (1.1 mmol) dodecane (internal standard), 30 bar H_2, 80°C, 30 mL solvent. [a]Determined by GC-MS using internal standard technique. [b]TOFs calculated at 1h of reaction (≈30% of conversion). [c] TOFs calculated at 1h of reaction.

4.2.2.3 Scope of the NB hydrogenation

Finally, we also broadened the spectrum of substrates to substituted nitrobenzene (Table 4.9), varying the electron donating/withdrawing character of the substituent.

In all substrates tested the stepwise hydrogenation to produce the fully hydrogenated alkylanime was observed. As expected from the electronic effect, *p*-chloronitrobenzene and *p*-fluoronitrobenzene react faster than *p*-nitrotoluene to produce the respective aniline.[36]

The further hydrogenation of toluidine provides particular challenges with respect to chemo- and diastereoselectivity. Indeed: i) the aromatic ring can be fully or partially hydrogenated; ii) the amino group can be cleaved off or may be susceptible to parallel or consecutive reactions; and iii) the methyl group adds *cis/trans* diastereomerism to the hydrogenated product. Para-toluidine was fully converted only after 4.5h. In parallel with the consumption of *p*-toluidine, *cis*- and *trans*-4-MCyNH$_2$ and small amounts of the three secondary amine (4-MCy)$_2$NH diastereomers were formed as

Table 4.9. Results of hydrogenation of substituted nitroarenes with the Ru@C_{60} (Ru/C_{60} = 10/1) catalyst in ethanol.

Substrate	Nitro- group		Selectivity (%)[a]		Aromatic ring		Selectivity(%)[a]		
	TOF (h^{-1})[b]	Time h	s-AN	N-alkylation	TOF (h^{-1})[b]	Time h	s-CA	s-DCA	N-alkylation
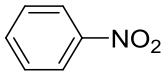	55.7	4	90	10	100.4	3.5	86	7	7
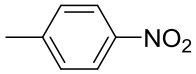	94.8	2.5	94	6	36.0	4.5	89	3.1	7.8
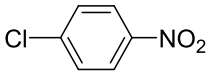	109.3	2	92	8	38.6	5	96.7[c]	1.5	1.8
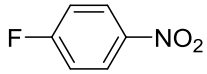	236.0	1	92.5	7.5	114.3	3	85.2[c]	9.1	5.7
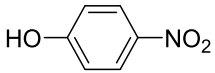	168.4	1	98	2	24.3	7	87	n.d.	12

Reaction conditions: 5 mg Ru@C_{60} 10/1 catalyst, (4.06mmol) nitroarene, 200 mg dodecane (internal standard), 30 bar H_2, 80°C, 30 mL solvent. [a]Determined by GC-MS using internal standard technique at 100% conversion, [b]TOFs calculated at 1h of reaction, [c]Selectivity towards the dehalogenated substrate.

well as N-alkylation product. *Cis*- and *trans*-4-MCyNH$_2$ were formed in a ratio of 4, which is unusually high for Ru/C catalysts.[37,38]

For chloro nitrobenzene hydrogenation, ruthenium is known as a good catalyst for minimizing dehalogenation, combined with a fast rate of reduction of the nitro group.[39,40,41] Chloroaniline is usually obtained with high selectivity on carbon supports.[42,43] The complete hydrogenation that should produce chlorocyclohexylamine has not been reported. However, it is known that on Pt/Al_2O_3 catalysts, after the hydrogenation of *p*-chloronitrobenzene to *p*-chloroaniline, the aromatic haloamine undergoes hydro-dechlorination to aniline, and further ring hydrogenation to cyclohexylamine.[44] After 2 hours of reaction the Ru@C_{60} catalyst allows the production of *p*-chloroaniline with 92% selectivity. In a second stage, the *p*-chloroaniline undergoes hydro-dechlorination to AN, and further ring hydrogenation to produce CA. *p*-fluoronitrobenzene presented the same behavior.

4.2.2.3 NB hydrogenation with Ru@C_{60}, T-Ru@C_{60}, and Ru@$C_{66}(COOH)_{12}$ nanocatalysts

Catalysts prepared with different solvent or fullerenes were also tested in the NB hydrogenation. Table 4.10 summarizes the results obtained with the Ru@C_{60}, T-Ru@C_{60}, and Ru@$C_{66}(COOH)_{12}$ catalysts.

All T-Ru@C_{60} compounds were active in the NB hydrogenation giving AN as major product with selectivity up to 93% at 6h of reaction. However, no conversion to CA was detected using these catalysts The reason is probably because of the Ru content and the Ru NP size. The T-Ru@C_{60} catalyst 1/1 (6.8% Ru), 10/1 (15.7% Ru) and 55/1 (47.5% Ru) have similar percentage of Ru than Ru@C_{60} 2/3 (6.4% Ru), 2/1 (16.7% Ru) and 10/1 (48.7% Ru), respectively. As previously shown the low loading catalysts (Ru@C_{60} ratio < 5) were found inactive for the hydrogenation of the aromatic ring and T-Ru@C_{60} 1/1 and 10/1 are comparable to these catalysts.

Table 4.10. Results of hydrogenation of nitrobenzene with Ru@C_{60}, T-Ru@C_{60}, and Ru@$C_{66}(COOH)_{12}$.[a]

Catalyst	Ratio	TOF[b]	Conversion (%)[c]	Selectivity (%)[c]				
				AN	AN-Et	CA	DCA	CA-Et
T-Ru@C_{60}	1/1	85	24	85	15	---	---	---
	10/1	119	51	92	8	---	---	---
	55/1	41	69	93	7	---	---	---
Ru@$C_{66}(COOH)_{12}$	6/1	120	53	92	8	---	---	---
	12/1	61	53	92	8	---	---	---
	30/1	51	100	2	---	86	traces	11
Ru@C_{60}	1/1	19	10	80	20	---	----	----
	10/1	49	100	90	10	86	7	7
	50/1	42	100	92	8	89	5	6

[a]Reaction conditions: 5 mg catalyst, 500 mg (4.06 mmol) nitrobenzene, 200mg (1.1 mmol) dodecane (internal standard), 30 bar H_2, 80°C, 30 mL EtOH. [b]TOFs calculated at 1h of reaction. [c]Determined by GC-MS using internal standard technique at 6h of reaction.

On the other hand, T-Ru@C_{60} 55/1 did not show activity for the aromatic ring hydrogenation, indicating that the Ru loading is not the only factor that plays a role but Ru particles size also have a remarkable effect. The Ru nanoparticles size are 1/1 (< 1 nm), 10/1 (< 1 nm) and 55/1 (1.15 ± 0.03 nm) in different T-Ru@C_{60} catalyst. It is comparable with the size of Ru@C_{60} 2/1 (1.16 ± 0.02 nm). The T-Ru@C_{60} catalysts and Ru@C_{60} 2/1 nanostructure have a similar NPs size, as consequence, they show similar catalytic behavior, i.e. they are active for the hydrogenation of NO_2 group and in active for the aromatic ring hydenation. Additionally, the BET measurement of Ru@C_{60} 10/1 and T-Ru@C_{60} 10/1 show a surface area of 13.9 and 4.8 m^2/g, respectively, indicating that in T-Ru@C_{60} nanocatalysts, the ruthenium active species are probably less accessible and explaining the different behavior than observed in Ru@C_{60} nanocatalysts.

The case of Ru@$C_{66}(COOH)_{12}$ samples seems to be similar. Low loading nanocatalysts were less active than Ru@C_{60} catalysts at similar Ru content. However,

$Ru@C_{66}(COOH)_{12}$ 30/1 was able to hydrogenate AN to CA in 6h, which is comparable to $Ru@C_{60}$ 20/1. Again, this results points out that the accessibility of the metal plays an important role for the activity and selectivity in this reaction.

4.2.2.4 DFT calculations

In order to understand the controlled and chemoselective hydrogenation of NB over the $Ru@C_{60}$ catalysts, a DFT study has been performed, to explore the coordination thermodynamics of a single NB molecule on a $2C_{60}$-Ru_{13} molecular model. Two coordination modes, denoted π-mode and nitro-mode in the following, appeared to be in competition. The first mode is when the π -system of the NB interacts with a facet of the Ru_{13}. The second one corresponds to the nitro group attached to an edge of the cluster (see Figure 4.3a and b).

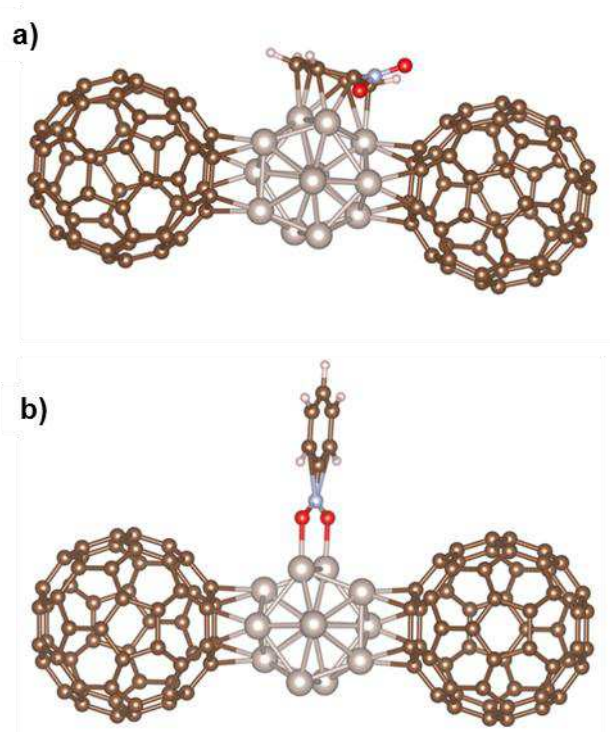

Figure 4.3. a) Side view of the π–mode coordination of a nitrobenzene molecule on a facet of a naked $2C_{60}$-Ru_{13} molecular complex; and b) Side view of the NO_2-mode coordination of a nitrobenzene molecule on the edge of a naked $2C_{60}$-Ru_{13} molecular complex.

It is then clear that in the π-mode, both hydrogenation of the aromatic ring and the nitro group are possible, when only the latter will be possible in the nitro-mode coordination. Without any hydrides on the metallic surface, the adsorption energy of both configurations are close together, -50 and -57 kcal/mol for nitro- and π-mode respectively. Mind that for an infinite Ru(0001) surface, which could be viewed as a good approximation of facets presented by large Ru NPs,[45] the adsorption energy is rised but remains in favor of the π-mode, -45 kcal/mol *vs*. -30 kcal/mol.

Here, we propose that the NO_2-mode is favored by the presence of numerous hydrides on the metallic surface, with an experimental ratio between 1.3 and 2 H per surface Ru atom.[46,47] Recently, a theoretical study has shown that on small Ru NPs, the maximum coverage value is 1.6 H per Ru surface atom.[48] As shown in Figure 4.4, for low coverage values the π-mode is thermodynamically favored, but as soon as enough hydrides are present on the surface, the NO_2-mode becomes more stable. Considering the experimental conditions (temperature and pression of H_2), it is possible to consider that the small metallic NPs are fully covered, and are preferential sites for the selective hydrogenation to aniline.

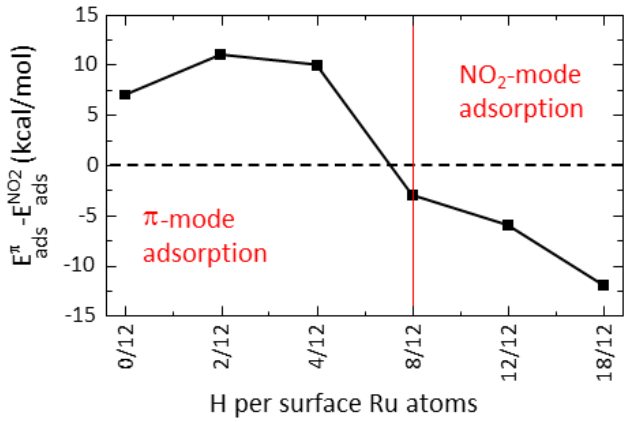

Figure 4.4. Evolution of the energy difference between the two adsorption modes with respect to the ratio of H per Ru surface atoms present on the metallic cluster.

To conclude, we have successfully prepared in a straightforward manner different Ru@C_{60} nano-objects. Among them, the Ru@C_{60} catalysts are the most interesting

These structures consist in a ruthenium fulleride core (kinetic product of the reaction), surrounded by a shell of Ru NPs (≈ 1.5 nm). These materials are characterized by a significant charge transfer between Ru and C_{60} providing electron deficient Ru centers (see Chapter 2). The remarkable feature of this study is the controlled and chemoselective hydrogenation of NB, which provide with high selectivity, first AN, and then CA. DFT calculations have shown that the coordination mode of NB on such nano-objects changes with the hydride coverage. At low coverage, π–mode coordination is favored, for which both hydrogenation of the aromatic ring and the nitro group are possible. Whereas at high hydride coverage, NO_2-mode coordination prevails, for which only NO_2 hydrogenation is possible. Thus the combination of electron poor ruthenium nanoparticles and high hydride coverage explain the peculiar observed selectivity of Ru@C_{60}. For comparison, a Ru/CNT catalyst give only a maximum selectivity towards AN of 64%.[23b]

4.2.2 Hydrogenation of *trans*-cinnamaldehyde

Selective hydrogenation of α,β-unsaturated aldehydes is of industrial importance.[49,50,51] The hydrogenation products are widely used for pharmaceuticals, perfumes, and flavors.[52] The hydrogenation of the double bond produces the saturated aldehyde, while carbonyl group hydrogenated lead to unsaturated alcohols (Scheme 4.2). In this reaction, the formation of the saturated aldehyde (HCAL) is favoured over the unsaturated alcohol (COL) because of thermodynamics. The definition of selective catalysts for the production of COL is thus very challenging.[53]

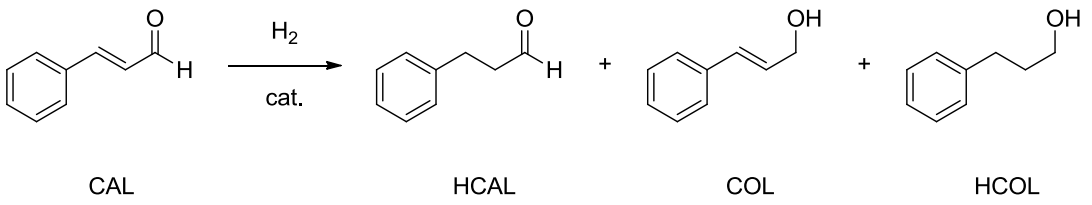

Scheme 4.2. *trans*-cinnamaldehyde hydrogenation reaction.

To obtain the unsaturated alcohol COL, the catalyst should allow controlling the reduction rate of the double bond and the carbonyl group, and changing the adsorption

constants of the components. It was found that the polarization of the C=O group and hindering the adsorption of the substrate though C=C group are very useful strategies to achieve the selective C=O hydrogenation. Thus many factors have been considered for the selective hydrogenation of α,β-unsaturated aldehydes, including the choice of the support materials,[54,55,56] the size of the metal nanoparticles,[57,51,58,59] the presence of a second metal,[60,61] and the use of some additives like bases or Lewis salts.[62,63,64] The selective synthesis of cinnamyl alcohol has been achieved by the use of metal oxides supports, following the order: MgO > SiO_2 > ZnO > SWCNTs > MWCNTs.[65,54] Even if carbon based supports usually provide less selective catalysts for the hydrogenation of cinnamaldehyde, there are few reports that use carbon based materials-C_{60}, which present a good selectivity towards cinnamyl alcohol.[19] In this context, the selective hydrogenation of CAL has been studied with Ru@fullerene catalysts. Solvent and additive effects have been investigated, showing a marked effect on the selectivity. In this chapter, a comparison of the different catalyst Ru@C_{60}, T-Ru@C_{60}, and Ru@$C_{66}(COOH)_{12}$ will be described. Ru@C_{60} 10/1 exhibits the best selectivity for cinnamyl alcohol. Besides, saturated aldehyde was also synthesized with a high selectivity by controlling the reaction conditions.

Cinnamaldehyde hydrogenation was studied at 20 bar of H_2 and 70 °C in several solvents and using different bases. Ru@C_{60} 10/1 nanocatalysts was used to optimize the reaction conditions, then other ratios as well as T-Ru@C_{60} and Ru@$C_{66}(COOH)_{12}$ catalysts were tested in this hydrogenation reaction. In general, the addition of a base in the reaction mixture prevents significantly the formation of acetals(a typically by-product) and improves the selectivity towards COL.[66,67,68] Two types of bases have been studied, including amines and alkali hydroxides. The mechanism of C=O activation with addition of amines is still uncertain. However, it was proposed that amines could be in interaction with the metal surface *via* lone electron pair, which disfavors the C=C bond hydrogenation.[69] For the alkali hydroxides, the improvement of the selectivity towards C=O bond hydrogenation was attributed to the polarization

of the C=O bond by an interaction between the metal cation that act a Lewis acidic site and the lone electron pair of oxygen atom in the C=O group.[70,71]

The different bases were tested as additive and the results of the catalysis are summarized in Table 4.11. In the absence of any base, the Ru@C_{60} catalyst formed very large amounts of acetals, from the condensation reaction between CAL and the solvent (iPrOH). This could be explained by the fact that the Ru NPs are electron deficient. We independently checked that the Ru@C_{60} catalyst was active for this condensation reaction under argon (78 % conversion after 20 h at 70°C). At 20% of conversion, 61% of COL was obtained without any base, which is a high selectivity for a Ru catalyst (≈ 40% selectivity is usually reported for Ru/C catalysts)[19,72]. However, such high selectivity has already been reported in the case of a 5% Ru/C_{60} catalyst that shows a poor catalytic activity; and in that case also acetal formation was reported.[19]

Table 4.11. Effect of the base on cinnamaldehyde hydrogenation using Ru@C_{60} 10/1.[a]

Ru@C_{60} 10/1	**TOF (h^{-1})**[b]	**Selectivity (%)**[c]		
		HCAL	**HCOL**	**COL**
No base[d]	16.7	14	25	61
KOH	11.6	56	1	43
Et_3N	54.7	45	13	42
Pyridine	17.7	20	3	77
Pyridine (3 mL)	23.8	27	2	71

[a]Reaction conditions: 4.0 mmol cinnamaldehyde 528 mg, nonane 200 mg, isopropanol 30 mL, 70 °C, 1.5 eq. base, 2.0 MPa H_2, 1000 rpm/min. [b]TOF was calculated at 2h of reaction.[c] At 20 % conversion of CAL. [d]Acetals are the main products of the reaction, and the given selectivity do not take into account the acetals.

The addition of 1.5 eq. of pyridine was beneficial, increasing the selectivity towards COL up to 77% and suppressing completely the formation of acetals. However, the addition of an excess of pyridine did not improve further the selectivity. In contrast,

the addition of strong bases such as KOH or Et_3N significantly decreased the selectivity.

It has been shown that the nature of the solvent employed has a significant effect on the rate and selectivity of the catalytic hydrogenation reaction.[32] In this case (Table 4.12) we observed that the use of protic solvents such as MeOH and isopropanol give the best selectivity towards COL, while a polar aprotic solvent, dioxane, gives high selectivity towards the C=C bond hydrogenation (Scheme 4.2).

Table 4.12. Effect of the solvent on cinnamaldehyde hydrogenation using Ru@C_{60} 10/1[a]

Ru@C_{60} 10/1	TOF (h^{-1})[b]	Selectivity(%)[c]		
		HCAL	HCOL	COL
1,4-Dioxane	14.7	73	6	21
Acetone	21.1	22	11	67
Isopropanol	17.8	20	3	77
MeOH	128.4	17.2	6.9	76[d]
MeOH/water (1/1)	35.9	55	2	43

[a]Reaction conditions: 4.0 mmol cinnamaldehyde 528 mg, nonane 200mg, solvent 30 mL, pyridine (0.5 mL), 70 °C, 1.5 eq. base, 2.0 MPa H_2, 1000 rpm/min. [b]TOF was calculated at 2h of reaction. [c]At 20 % conversion of CAL. [d] At 77 % conversion of cinnamaldehyde.

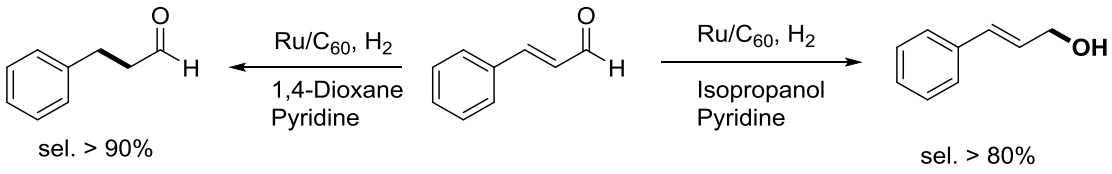

Scheme 4.2 Selective hydrogenation of CAL over Ru@C_{60} catalyst.

Like for NB hydrogenation, the highest TOF were obtained in methanol. Presumably because of a specific interaction between CAL or intermediates with this solvent.

4.2.3.2 Effect of different nano-catalysts Ru@C_{60}, T-Ru@C_{60} and Ru@$C_{66}(COOH)_{12}$

Under these optimized conditions, Ru@C_{60}, T-Ru@C_{60} and Ru@$C_{66}(COOH)_{12}$ catalysts were tested, and the results are listed in Table 4.13.

Table 4.13. The effect of Ru@C_{60} ratio and of catalysts on cinnamaldehyde hydrogenation.[a]

Catalyst	Ratio	TOF (h^{-1})[b]	Selectivity (%)[c]		
			HCAL	HCOL	COL
Ru@C_{60}	1/1	12.6	23	12	65
	10/1	17.7	20	3	77
	30/1	32	33	2	65
T-Ru@C_{60}	55/1	6.9	16	9	74
Ru@$C_{66}(COOH)_{12}$	6/1	7.2	39	7	54
	12/1	11.3	28	9	63

[a]Reaction conditions: 4.0 mmol cinnamaldehyde 528 mg, nonane 200 mg, solvent 30 mL, pyridine (0.5 mL), 70 °C, 1.5 eq. base, 2.0 MPa H_2, 1000 rpm/min. [b]TOF was calculated at 2h of reaction. [c] at 20 % conversion of CAL.

All Ru@fullerene catalysts gave relatively similar selectivity to COL ranging from 54 to 77 %. The best performances in the sense of activity and selectivity were obtained with the Ru@C_{60} 10/1 nanocatalysts, pointing out that the approachability of the active centers is fundamental in catalysis.

4.3 Conclusions

In conclusion, Ru@C_{60}, T-Ru@C_{60} and Ru@$C_{66}(COOH)_{12}$ catalysts were tested in the hydrogenation of nitrobenzene. The results revealed that the Ru@C_{60} catalyst not only can produce aniline but also cyclohexylamine by selective and consecutive hydrogenation. For T-Ru@C_{60}, only aniline was formed. This catalyst is not effective for the hydrogenation of aniline, presumably because of the small Ru NP size.

Similarly, $Ru@C_{66}(COOH)_{12}$ with ratio 6/1 and 12/1 only hydrogenate nitrobenzene to aniline. However, the behavior of $Ru@C_{66}(COOH)_{12}$ 30/1 is different, and in this case cyclohexylamine is produced such as in the case of $Ru@C_{60}$ 10/1. The controlled selective hydrogenation of nitrobenzene over $Ru@C_{60}$ was studied by DFT calculations. The results suggest that indeed, the nitro group will be hydrogenated first, and then the aromatic ring provided a high concentration of hydride is present on the Ru surface.

Then, the hydrogenation of cinnamaldehyde was investigated over the same catalysts. The results show that the nature of the solvent has a pronounced effect on the selectivity. The HCAL is the predominant product if 1,4-dioxane is used, while COL is produce with high selectivity in isopropanol. In alcoholic solvents, the addition of a base completly suppressed the formation of acetals, by preventing alcohols to react with the aldehyde. Compared to T-$Ru@C_{60}$ and $Ru@C_{66}(COOH)_{12}$ catalysts, $Ru@C_{60}$ 10/1 allows reaching the best selectivity (81% to COL).

4.4 Experimental section

Materials and methods

All operations were carried out under argon atmosphere using standard Schlenk techniques or in an MBraun glovebox. Solvents were purified by standard methods or by an MBraun SPS-800 solvent purification system. Nitroarenes (>99.0%), dodecane (>99%), and *trans*-cinnamaldehyde (99.0%) were purchased from Sigma-Aldrich, and CO and H_2 from Air Liquid. All these reactants were used as received. Ru-fullerene nanocatalysts were prepared as described in chapters 2 and 3. The ruthenium content was established by inductively coupled plasma optical emission spectroscopy (ICP-OES) performed at the LCC in a Thermo Scientific ICAP 6300 instrument. GC-MS analyses were performed in a PerkinElmer Autosystem GC equipped with an Elite-5MS Capillary Column (30 m × 0.25 mm × 0.25 μm) coupled to a Turbo Mass mass spectrometer.

General procedure for the hydrogenation of nitrobenzene. Hydrogenation reactions were performed in a Top Industrie high pressure and temperature stainless steel autoclave with a controlling system. In a typical experiment, the autoclave was purged by three vacuum/argon cycles. A mixture of Ru@C_{60} catalyst (5mg), dodecane (200 mg) and the corresponding nitroarene (4.06 mmol) in 30 mL of solvent was ultrasonicated for 5 min and transferred into a high-pressure autoclave under argon atmosphere. The autoclave was heated to 80°C and pressurized with 30 bar of H_2; the stirring rate was fixed at 1000 rpm. Samples of the reaction mixture were taken periodically and then analysed by GC-MS. Quantitative analysis of reaction mixtures was performed *via* GC-MS using calibration solutions of commercially available products.

Catalytic recycling tests. The autoclave was purged by three vacuum/argon cycles. The mixture of Ru@C_{60} 10/1 catalyst (20 mg), dodecane (as internal standard, 4 mmol) and nitrobenzene (16.14 mmol) in 120 mL of ethanol was prepared in a glovebox, ultrasonicated for 5 min and then transferred into a high-pressure autoclave under an argon atmosphere. The autoclave was heated to 80°C and pressurized with 30 bar of H_2 during 8h; the stirring rate was fixed at 1000 rpm. After 8h, the autoclave was cooled to room temperature and depressurized. The reaction mixture was cannulated to a Schlenck tube and the catalyst was allowed to precipitate. A sample of the reaction mixture was analysed by GC-MS. After filtration under argon with a cannula, the black solid powder was washed twice with EtOH and filtrated again before drying under vacuum. The catalyst was kept for reuse. All solutions were combined, the solvent was removed under reduced pressure, and the residue analysed by ICP. Two recycling tests were performed following this procedure.

Activation energy and kinetic. A series of experiments of hydrogenation of NB and AN were performed in order to evaluate the apparent activation energies. The hydrogenation of 4.06 mmol of nitrobenzene was carried out with 5mg of Ru@C_{60}

10/1 catalyst in 20 mL of ethanol (0.2 M) at 30 bar of hydrogen pressure with the stirring rate fixed at 1000 rpm at 60, 80 and 90°C. The same conditions were used in the hydrogenation of AN. The reaction was followed by sampling the mixture, and the products were analysed by GC-MS.

General procedure for the hydrogenation of cinnamaldehyde. Hydrogenation reactions were performed in a Top Industrie high pressure and temperature stainless steel autoclave with a controlling system. In a typical experiment, 5 mg of catalyst, nonane (200mg) and *trans*-cinnamaldehyde (4.0mmol, 528mg) and 30 mL of isopropanol were added into the autoclave. Then, four vacuum/argon cycles were performed and the autoclave was sealed with 20 bar of H_2. The hydrogenation experiment was carried out under 20 bar H_2 at 70°C temperature with magnetic stirring at 1000 rpm. The products were analysed on a PerkinElmer gas chromatograph equipped with Elite-5MS capillary column (30 m × 0.32 mm ×0.25 μm) with a flame ionization detector. The response factors of each component were determined with standard samples and were used to calculate the conversion and selectivity.

TEM analyses. TEM and HREM analyses were performed at the "Centre de microcaracterisation Raimond Castaing, UMS 3623, Toulouse" by using a JEOL JEM 1011 CX-T electron microscope operating at 100 kV with a point resolution of 4.5 Å and a JEOL JEM 1400 electron microscope operating at 120 kV. The high resolution analyses were conduct using a JEOL JEM 2100F equipped with a Field Emission Gun (FEG) operating at 200 kV with a point resolution of 2.3 Å and a JEOL JEM-ARM200F Cold FEG operating at 200 kV with a point resolution of >1.9 Å. The approximation of the particles mean size was made through a manual analysis of enlarged micrographs by measuring at least 200 particles on a given grid. Other TEM micrographs were acquired with a JEOL 2100F S/TEM microscope equipped with a FEG operating at 200 kV, a spherical aberration probe corrector and a GATAN

Tridiem energy filter. The resolutions attained are 2 Å and 1.1 Å under parallel TEM mode and scanning STEM modes, respectively.

DFT calculations were carried out using the Vienna *ab initio* simulation package VASP [73,74,75,76]. The code uses the full-potential projector augmented wave (PAW) framework[77,78]. Exchange-correlation effects have been approximated using the PBE functional [79] and applied in spin-polarized calculations. A kinetic-energy cutoff of 400 eV was found to be sufficient to achieve a total-energy convergence within several meV, considering a k-point sampling in Gamma-point only calculations for isolated molecules and complexes, in conjunction with a Gaussian smearing with a width of 0.05 eV. The (4×4) cell of the Ru (0001) was modeled by a slab of 6 layers separated to its periodic images in the z direction by a vacuum of 13.2 Å for a total cell height of 24 Å, as proposed in a previous work[80]. In these cases the k-point sampling was performed on a (3×3×1) Gamma-centered grid for the optimization procedure, when a (5×5×1) grid was used for analysis runs. During geometry optimization runs, all the atoms were fully relaxed until forces on individual atoms were smaller than 0.01 eV/Å. Calculation cells for isolated molecules and complexes were (25×26×27) $Å^3$, to avoid spurious interactions between periodic images. Figures of the different geometries were produced thanks to the 3D visualization program VESTA[81]. Bader charge analyses were performed using Henkelmann's group code [82]. The optimal geometries upon H_2 adsorption were constructed following the results of Ref [80], meaning that all available μ_3 sites were occupied and then the top sites and if necessary some Bridge sites were used to build the starting geometries.

4.5 References

1. Niemeyer, J.; Erker, G., Fullerene-mediated activation of dihydrogen: a new method of metal-free catalytic hydrogenation. *ChemCatChem* **2010,** *2* (5), 499-500.

2. Coq, B.; Planeix, J. M.; Brotons, V., Fullerene-based materials as new support media in heterogeneous catalysis by metals. *Appl. Catal., A.***1998,** *173* (2), 175-183.

3. Goldshleger, N. F., Fullerenes and fullerene-based materials in catalysis. *Fullerene Sci. Technol.* **2001,** *9* (3), 255-280.

4. Serp, P.; Figueiredo, J. L., *Carbon materials for catalysis*. John Wiley & Sons: 2009.

5. Ivanova, V., Fullerene compounds with transition metals M_nC_{60}: Preparation, structure, and properties. *J. Struct. Chem.* **2000,** *41* (1), 135-148.

6. Malhotra, R.; Hirschon, A.; McMillen, D.; Bell, W. In *Catalytic properties of fullerene materials*, MRS Proceedings, Cambridge Univ Press: 1997; p 137.

7. Stetzer, M.; Heiney, P.; Fischer, J.; McGhie, A., Thermal stability of solid C_{60}. *Ph. Rv. B* **1997,** *55* (1), 127-131.

8. Pupysheva, O. V.; Farajian, A. A.; Yakobson, B. I., Fullerene nanocage capacity for hydrogen storage. *Nano Lett.* **2007,** *8* (3), 767-774.

9. Schur, D. V.; Zaginaichenko, S. Y.; Savenko, A. F.; Bogolepov, V. A.; Anikina, N. S.; Zolotarenko, A.; Matysina, Z. A.; Veziroglu, T. N.; Skryabina, N. E., Experimental evaluation of total hydrogen capacity for fullerite C_{60}. *Int. J. Hydrogen Energy* **2011,** *36* (1), 1143-1151.

10. Zhao, Y.; Kim, Y.-H.; Dillon, A.; Heben, M.; Zhang, S., Hydrogen storage in novel organometallic buckyballs. *Phys. Rev. Lett.* **2005,** *94* (15), 155504.

11. Chandrakumar, K.; Ghosh, S. K., Alkali-metal-induced enhancement of hydrogen adsorption in C_{60} fullerene: an ab initio study. *Nano Lett.* **2008,** *8* (1), 13-19.

12. Soto, D.; Salcedo, R., Coordination modes and different hapticities for fullerene organometallic complexes. *Molecules* **2012,** *17* (6), 7151-7168.

13. Lebedeva, M. A.; Chamberlain, T. W.; Khlobystov, A. N., Harnessing the synergistic and complementary properties of fullerene and transition-metal compounds for nanomaterial applications. *Chem. Rev.* **2015,** *115* (20), 11301-11351.

14. Axet, M.; Dechy-Cabaret, O.; Durand, J.; Gouygou, M.; Serp, P., Coordination chemistry on carbon surfaces. *Coord. Chem. Rev.* **2016,** *308*, 236-345.

15. Pacosová, L.; Kartusch, C.; Kukula, P.; van Bokhoven, J. A., Is fullerene a nonmetal catalyst in the hydrogenation of nitrobenzene? *ChemCatChem* **2011,** *3* (1), 154-156.

16. (a) Li, B.; Li, H.; Xu, Z., Experimental Evidence for the Interface interaction in ag/c_{60} nanocomposite catalyst and its crucial influence on catalytic performance. *J. Phys. Chem. C* **2009,** *113* (52), 21526-21530; (b) Niemeyer, J.; Erker, G., Fullerene-mediated activation of dihydrogen: a new method of metal-free catalytic hydrogenation. *ChemCatChem* **2010,** *2* (5), 499-500.

17. Keypour, H.; Noroozi, M.; Rashidi, A.; Shariati Rad, M., Application of response surface methodology for catalytic hydrogenation of nitrobenzene to aniline using ruthenium supported fullerene nanocatalyst. *Iranian Journal of Chemistry and Chemical Engineering (IJCCE)* **2015,** *34* (1), 21-32.

18. Yu, R.; Liu, Q.; Tan, K.-L.; Xu, G.-Q.; Ng, S. C.; Chan, H. S.; Hor, T. A., Preparation, characterisation and catalytic hydrogenation properties of palladium supported on C_{60}. *J. Chem. Soc., Faraday Trans.* **1997,** *93* (12), 2207-2210.

19. Lashdaf, M.; Hase, A.; Kauppinen, E.; Krause, A., Fullerene-based ruthenium catalysts in cinnamaldehyde hydrogenation. *Catal. Lett.* **1998,** *52* (3-4), 199-204.

20. Kahl, T.; Schröder, K.-W.; Lawrence, F. R.; Marshall, W. J.; Höke, H.; Jäckh, R., Aniline. In *Ullmann's Encyclopedia of Industrial Chemistry*, Wiley-VCH Verlag GmbH & Co. KGaA: 2000.

21. Roose, P.; Eller, K.; Henkes, E.; Rossbacher, R.; Höke, H., Amines, Aliphatic. In *Ullmann's Encyclopedia of Industrial Chemistry*, Wiley-VCH Verlag GmbH & Co. KGaA: 2000.

22. Vilé, G.; Albani, D.; Almora-Barrios, N.; López, N.; Pérez-Ramírez, J., Advances in the design of nanostructured catalysts for selective hydrogenation. *ChemCatChem* **2016,** *8* (1), 21-33.

23. (a) Greenfield, H., Hydrogenation of aniline to cyclohexylamine with platinum metal catalysts. *J. Org. Chem.* **1964,** *29* (10), 3082-3084; (b) Tomkins, P.; Gebauer-Henke, E.; Leitner, W.; Müller, T. E., Concurrent hydrogenation of aromatic and nitro groups over carbon-supported ruthenium catalysts. *ACS Catal.* **2015,** *5* (1), 203-209.

24. (a) Komandur V. R. Chary , C. S. S., Selective hydrogenation of nitrobenzene to aniline over Ru/SBA-15 catalysts. *Catal. Lett.* **2009,** *128* (1), 164-170; (b) Srikanth, C. S.; Kumar, V. P.; Viswanadham, B.; Srikanth, A.; Chary, K. V. R., Vapor phase hydrogenation of nitrobenzene to aniline over carbon supported ruthenium catalysts. *J. Nanosci. Nanotech.* **2015,** *15* (7), 5403-5409.

25. Zhao, F.; Zhang, R.; Chatterjee, M.; Ikushima, Y.; Arai, M., Hydrogenation of nitrobenzene with supported transition metal catalysts in supercritical carbon dioxide. *Adv. Syn. Catal.* **2004,** *346* (6), 661-668.

26. (a) Li, B.; Xu, Z., A Nonmetal catalyst for molecular hydrogen activation with comparable catalytic hydrogenation capability to noble metal catalyst. *J. Am. Chem. Soc.* **2009,** *131* (45), 16380-16382; (b) Wu, S.; Wen, G.; Wang, J.; Rong, J.; Zong, B.; Schlogl, R.; Su, D. S., Nitrobenzene reduction catalyzed by carbon: does the reaction really belong to carbocatalysis? *Catal. Sci. Tech.* **2014,** *4* (12), 4183-4187.

27. Tomkins, P.; Gebauer-Henke, E.; Müller, T. E., Molecular assembly line: stepwise hydrogenation of multifunctional substrates over catalyst mixtures. *ChemCatChem* **2016,** *8* (3), 546-550.

28. Oh, S. G.; Mishra, V.; Cho, J. K.; Kim, B.-J.; Kim, H. S.; Suh, Y.-W.; Lee, H.; Park, H. S.; Kim, Y. J., One pot catalytic NO_2 reduction, ring hydrogenation, and N-alkylation from nitroarenes to generate alicyclic amines using Ru/C-$NaNO_2$. *Catal. Commun.* **2014,** *43*, 79-83.

29. Watanabe, Y.; Tsuji, Y.; Ohsugi, Y., The ruthenium catalyzed N-alkylation and N-heterocyclization of aniline using alcohols and aldehydes. *Tetrahedron Lett.* **1981,** *22* (28), 2667-2670.

30. Guillena, G.; J. Ramón, D.; Yus, M., Hydrogen autotransfer in the N-alkylation of amines and related compounds using alcohols and amines as electrophiles. *Chem. Rev.* **2009,** *110* (3), 1611-1641.

31. Pushkarev, V. V.; An, K.; Alayoglu, S.; Beaumont, S. K.; Somorjai, G. A., Hydrogenation of benzene and toluene over size controlled Pt/SBA-15 catalysts: Elucidation of the Pt particle size effect on reaction kinetics. *J. Catal.* **2012,** *292*, 64-72.

32. Rajadhyaksha, R.; Karwa, S., Solvent effects in catalytic hydrogenation. *Chem. Eng. Sci.* **1986,** *41* (7), 1765-1770.

33. d'Angelo, J. V. H.; Francesconi, A. Z., Gas-liquid solubility of hydrogen in n-alcohols ($1 \leqslant n \leqslant 4$) at pressures from 3.6 MPa to 10 MPa and temperatures from 298.15 K to 525.15 K. *J. Chem. Eng. Data.* **2001,** *46* (3), 671-674.

34. Gelder, E. A.; Jackson, S. D.; Lok, C. M., A study of nitrobenzene hydrogenation over palladium/carbon catalysts. *Catal. Lett.* **2002,** *84* (3-4), 205-208.

35. Obraztsova, I.; Eremenko, N.; Velyakina, Y. N., Reaction kinetics of nitrobenzene hydrogenation on a palladium catalyst supported on nanodiamonds. *Kinet. Catal.* **2008,** *49* (3), 401-406.

36. Sun, J.; Fu, Y.; He, G.; Sun, X.; Wang, X., Catalytic hydrogenation of nitrophenols and nitrotoluenes over a palladium/graphene nanocomposite. *Catal. Sci. Tech.* **2014,** *4* (6), 1742-1748.

37. Gebauer-Henke, E.; Blumenthal, L.; Prokofieva, A.; Vogt, H.; Voss, G.; Müller, T., Diastereomer control in the hydrogenation of o-and p-toluidine over ruthenium catalysts. *International Scientific Journal for Alternative Energy and Ecology* **2010,** *4(84)*, 29-36.

38. Gebauer-Henke, E.; Tomkins, P.; Leitner, W.; Müller, T. E., Nitro promoters for selectivity control in the core hydrogenation of toluidines: controlling adsorption on catalyst surfaces. *ChemCatChem* **2014,** *6* (10), 2910-2917.

39. Tijani, A.; Coq, B.; Figueras, F., Hydrogenation of para-chloronitrobenzene over supported ruthenium-based catalysts. *Appl. Catal.* **1991,** *76* (2), 255-266.

40. Zuo, B.; Wang, Y.; Wang, Q.; Zhang, J.; Wu, N.; Peng, L.; Gui, L.; Wang, X.; Wang, R.; Yu, D., An efficient ruthenium catalyst for selective hydrogenation of ortho-chloronitrobenzene prepared via assembling ruthenium and tin oxide nanoparticles. *J. Catal.* **2004,** *222* (2), 493-498.

41. Pietrowski, M.; Wojciechowska, M., An efficient ruthenium-vanadium catalyst for selective hydrogenation of ortho-chloronitrobenzene. *Catal. Today* **2009,** *142* (3), 211-214.

42. Oubenali, M.; Vanucci, G.; Machado, B.; Kacimi, M.; Ziyad, M.; Faria, J.; Raspolli-Galetti, A.; Serp, P., Hydrogenation of p-chloronitrobenzene over nanostructured-carbon-supported ruthenium catalysts. *ChemSusChem* **2011,** *4* (7), 950-956.

43. Antonetti, C.; Oubenali, M.; Galletti, A. M. R.; Serp, P.; Vannucci, G., Novel microwave synthesis of ruthenium nanoparticles supported on carbon nanotubes active in the selective hydrogenation of p-chloronitrobenzene to p-chloroaniline. *Appl. Catal., A.* **2012,** *421*, 99-107.

44. Vitulli, G.; Verrazzani, A.; Pitzalis, E.; Salvadori, P.; Capannelli, G.; Martra, G., Pt/γ-Al_2O_3 catalytic membranes vs. Pt on γ-Al_2O_3 powders in the selective hydrogenation of p-chloronitrobenzene. *Catal. Lett.* **1997,** *44* (3-4), 205-210.

45. Pan, C.; Pelzer, K.; Philippot, K.; Chaudret, B.; Dassenoy, F.; Lecante, P.; Casanove, M.-J., Ligand-stabilized ruthenium nanoparticles: synthesis, organization, and dynamics. *J. Am. Chem. Soc.* **2001,** *123* (31), 7584-7593.

46. García-Antón, J.; Axet, M. R.; Jansat, S.; Philippot, K.; Chaudret, B.; Pery, T.; Buntkowsky, G.; Limbach, H. H., Reactions of olefins with ruthenium hydride nanoparticles: NMR characterization, hydride titration, and room-temperature C-C bond activation. *Angew. Chem. Int. Ed.* **2008,** *47* (11), 2074-2078.

47. Berthoud, R.; Délichère, P.; Gajan, D.; Lukens, W.; Pelzer, K.; Basset, J.-M.; Candy, J.-P.; Copéret, C., Hydrogen and oxygen adsorption stoichiometries on silica supported ruthenium nanoparticles. *J. Catal.* **2008,** *260* (2), 387-391.

48. Cusinato, L.; Martínez-Prieto, L. M.; Chaudret, B.; del Rosal, I.; Poteau, R., Theoretical characterization of the surface composition of ruthenium nanoparticles in equilibrium with syngas. *Nanoscale* **2016,** *8* (21), 10974-10992.

49. Claus, P., Selective hydrogenation of ά, β-unsaturated aldehydes and other C=O and C=C bonds containing compounds. *Top. Catal.* **1998,** *5* (1-4), 51-62.

50. Singh, U. K.; Vannice, M. A., Kinetics of liquid-phase hydrogenation reactions over supported metal catalysts-a review. *Appl. Catal., A.***2001,** *213* (1), 1-24.

51. Gallezot, P.; Richard, D., Selective hydrogenation of α, β-unsaturated aldehydes. *Catal. Rev.* **1998,** *40* (1-2), 81-126.

52. Consonni, M.; Touroude, R.; Murzin, D. Y., Deactivation and selectivity pattern in crotonaldehyde hydrogenation. *Chem. Eng. Technol.* **1998,** *21* (7), 605-609.

53. Mäki-Arvela, P.; Hajek, J.; Salmi, T.; Murzin, D. Y., Chemoselective hydrogenation of carbonyl compounds over heterogeneous catalysts. *Appl. Catal., A.***2005,** *292*, 1-49.

54. Blackmond, D. G.; Oukaci, R.; Blanc, B.; Gallezot, P., Geometric and electronic effects in the selective hydrogenation of α,β-unsaturated aldehydes over zeolite-supported metals. *J. Catal.* **1991,** *131* (2), 401-411.

55. Toebes, M. L.; Zhang, Y.; Hájek, J.; Nijhuis, T. A.; Bitter, J. H.; Van Dillen, A. J.; Murzin, D. Y.; Koningsberger, D. C.; de Jong, K. P., Support effects in the hydrogenation of cinnamaldehyde over carbon nanofiber-supported platinum catalysts: characterization and catalysis. *J. Catal.* **2004,** *226* (1), 215-225.

56. Cano, I.; Huertos, M. A.; Chapman, A. M.; Buntkowsky, G.; Gutmann, T.; Groszewicz, P. B.; van Leeuwen, P. W., Air-stable gold nanoparticles ligated by secondary phosphine oxides as catalyst for

the chemoselective hydrogenation of substituted aldehydes: a remarkable ligand effect. *J. Am. Chem. Soc.* **2015,** *137* (24), 7718-7727.

57. Giroir-Fendler, A.; Richard, D.; Gallezot, P., Chemioselectivity in the catalytic hydrogenation of cinnamaldehyde. Effect of metal particle morphology. *Catal. Lett.* **1990,** *5* (2), 175-181.

58. Minot, C.; Gallezot, P., Competitive hydrogenation of benzene and toluene: Theoretical study of their adsorption on ruthenium, rhodium, and palladium. *J. Catal.* **1990,** *123* (2), 341-348.

59. Plomp, A. J.; Vuori, H.; Krause, A. O. I.; de Jong, K. P.; Bitter, J. H., Particle size effects for carbon nanofiber supported platinum and ruthenium catalysts for the selective hydrogenation of cinnamaldehyde. *Appl. Catal., A.* **2008,** *351* (1), 9-15.

60. Vu, H.; Gonçalves, F.; Philippe, R.; Lamouroux, E.; Corrias, M.; Kihn, Y.; Plee, D.; Kalck, P.; Serp, P., Bimetallic catalysis on carbon nanotubes for the selective hydrogenation of cinnamaldehyde. *J. Catal.* **2006,** *240* (1), 18-22.

61. Coq, B.; Kumbhar, P. S.; Moreau, C.; Moreau, P.; Figueras, F., Zirconia-supported monometallic Ru and bimetallic Ru-Sn, Ru-Fe catalysts: Role of metal support interaction in the hydrogenation of cinnamaldehyde. *J. Phys. Chem.* **1994,** *98* (40), 10180-10188.

62. Koo-amornpattana, W.; Winterbottom, J. M., Pt and Pt-alloy catalysts and their properties for the liquid-phase hydrogenation of cinnamaldehyde. *Catal. Today* **2001,** *66* (2), 277-287.

63. Gao, F.; Chen, Q.-H.; Wang, F.-P., Platinum-triethylamine-catalyzed hydrogenation of aldehydes and cyclohexanones. *Tetrahedron Lett.* **2009,** *50* (37), 5270-5273.

64. Mertens, P. G.; Wahlen, J.; Ye, X.; Poelman, H.; De Vos, D. E., Chemoselective C=O hydrogenation of α,β-unsaturated carbonyl compounds over quasihomogeneous and heterogeneous nano-Au^0 catalysts promoted by lewis acidity. *Catal. Lett.* **2007,** *118* (1-2), 15-21.

65. Gallezot, P.; Giroir-Fendler, A.; Richard, D., Chemioselectivity in cinnamaldehyde hydrogenation induced by shape selectivity effects in Pt-Y zeolite catalysts. *Catal. Lett.* **1990,** *5* (2), 169-174.

66. Bhogeswararao, S.; Srinivas, D., Intramolecular selective hydrogenation of cinnamaldehyde over CeO_2-ZrO_2-supported Pt catalysts. *J. Catal.* **2012,** *285* (1), 31-40.

67. Guo, Z.; Xiao, C.; Maligal-Ganesh, R. V.; Zhou, L.; Goh, T. W.; Li, X.; Tesfagaber, D.; Thiel, A.; Huang, W., Pt nanoclusters confined within metal-organic framework cavities for chemoselective cinnamaldehyde hydrogenation. *ACS Catal.* **2014,** *4* (5), 1340-1348.

68. Li, G.; Abroshan, H.; Chen, Y.; Jin, R.; Kim, H. J., Experimental and mechanistic understanding of aldehyde hydrogenation using Au_{25} nanoclusters with lewis acids: unique sites for catalytic reactions. *J. Am. Chem. Soc.* **2015,** *137* (45), 14295-304.

69. Mizoroki, T.; Seki, K.; Meguro, S.-i.; Ozaki, A., Rhodium complex catalyzed hydrogenation of. α, β-unsaturated aldehydes to unsaturated alcohols. *Bull. Chem. Soc. Jpn.* **1977,** *50* (8), 2148-2152.

70. Satagopan, V.; Chandalia, S. B., Selectivity aspects in the multi-phase hydrogenation of α,β-unsaturated aldehydes over supported noble metal catalysts: Part I. *J. Chem. Technol. Biotechnol.* **1994,** *59* (3), 257-263.

71. Satagopan, V.; Chandalia, S. B., Selectivity aspects in the multi-phase hydrogenation of α, β-unsaturated aldehydes over supported noble metal catalysts: Part II. *J. Chem. Technol. Biotechnol.* **1994,** *60* (1), 17-21.

72. Wang, Y.; Rong, Z.; Wang, Y.; Zhang, P.; Wang, Y.; Qu, J., Ruthenium nanoparticles loaded on multiwalled carbon nanotubes for liquid-phase hydrogenation of fine chemicals: An exploration of confinement effect. *J. Catal.* **2015,** *329*, 95-106.

73. Kresse, G.; Furthmüller, J., Efficiency of ab-initio total energy calculations for metals and semiconductors using a plane-wave basis set. *Comput. Mater. Sci.* **1996,** *6* (1), 15-50.

74. Kresse, G.; Hafner, J., Ab initio molecular dynamics for liquid metals. *Phys. Rev. B* **1993,** *47* (1), 558-561.

75. Kresse, G.; Furthmüller, J., Efficient iterative schemes for ab initio total-energy calculations using a plane-wave basis set. *Phys. Rev. B* **1996,** *54* (16), 11169-1186.

76. Kresse, G.; Hafner, J., Ab initio molecular-dynamics simulation of the liquid-metal–amorphous-semiconductor transition in germanium. *Phys. Rev. B* **1994,** *49* (20), 14251-14269.

77. Blöchl, P. E., Projector augmented-wave method. *Phys. Rev. B* **1994,** *50* (24), 17953-17979.

78. Kresse, G.; Joubert, D., From ultrasoft pseudopotentials to the projector augmented-wave method. *Phys. Rev. B* **1999,** *59* (3), 1758-1775.

79. Perdew, J. P.; Burke, K.; Ernzerhof, M., Generalized gradient approximation made simple. *Phys. Rev. Lett.* **1996,** *77* (18), 3865-3868.

80. del Rosal, I.; Truflandier, L.; Poteau, R.; Gerber, I. C., A density functional theory study of spectroscopic and thermodynamic properties of surfacic hydrides on Ru (0001) model surface: the influence of the coordination modes and the coverage. *J. Phys. Chem. C* **2010,** *115* (5), 2169-2178.

81. Momma, K.; Izumi, F., Vesta 3 for three-dimensional visualization of crystal, volumetric and morphology data. *J. Appl. Crystallogr.* **2011,** *44* (6), 1272-1276.

82. Tang, W.; Sanville, E.; Henkelman, G., A grid-based Bader analysis algorithm without lattice bias. *J. Phys.: Condens. Matter* **2009,** *21* (8), 084204-1/6.

General conclusions and perspectives

General conclusions and perspectives

In this thesis novel Ru nanostructures based on fullerene or functionalized fullerene and Ru NPs have been developed and employed in catalytic hydrogenation reactions.

First, Ru@C_{60} nano-architectures were synthesized by decomposition of [Ru(COD)(COT)] in the presence of C_{60} using an organometallic approach. For the synthesis of Ru@C_{60}, the effect of solvent and Ru/C_{60} ratio were investigated. These two parameters play a key role in the formation of the Ru@C_{60} nanostructure. The effect of different solvents (toluene, chlorobenzene, *o*-dichlorobenzene, dichloromethane, and decalin) was studied first with a Ru/C_{60} ratio of 2. It was found that the use of high permittivity and low viscosity solvents allow the production of spherical Ru@C_{60} polymeric particles with mean size of: 285 ± 3 nm for chlorobenzene, 200 ± 3 nm for o-dichlorobenzene and 39.6 ± 0.7 nm for dichloromethane. On the other hand, the permittivity and high viscosity solvent as decalin and toluene do not produce polymer spheres.

Using dichloromethane as solvent, which allow obtaining well-defined polymeric nanospheres, we examined the effect of the Ru/C_{60} ratio. Ru@C_{60} 1/1 displays polymeric nanospheres (37.8 ± 1.0 nm) with no Ru NPs. Polymeric nanospheres decorated with Ru NPs were obtained with the increase of the Ru content. The size of the nanospheres is constant (around 40 nm) and the Ru nanoparticle size shows a narrow distribution (1-1.5 nm). The characterization of the Ru@C_{60} 1/1 spherical particles has been performed. EXAFS, WAXS, and DFT calculations point to a polymeric structure, in which each Ru atoms is coordinated to two C_{60}, with a $\eta^{2(6)}$-η^{6} coordination mode. Solvent molecules contribute to stabilize this fulleride. This polymeric phase is the kinetic product of the reaction. An increase of the Ru/C_{60} ratio induces the formation of well-dispersed Ru NPs on the spheres (thermodynamic product of the reaction). Significant charge transfer from ruthenium to fullerene has been evidenced by Raman spectrometry and XPS for all the prepared materials, which

is an important factor to take into account, particularly if we consider the possible reactivity of this fulleride.

Using similar reaction conditions, several T-Ru@C_{60} were synthesized in toluene by decomposition of [Ru(COD)(COT)] in the presence of C_{60} under 3 bar hydrogen. The results indicate that sub-nanometer Ru NPs are produced for ratio 1/1 and 10/1, while Ru NPs around 1.1~1.5 nm were produced at higher ratios (20/1 and 55/1).

Next, in oder to introduce directionality to the C_{60} fullerene we have synthesized several functionalized fullerene. The functionalized hexa-adduct fullerene $C_{66}(COOH)_{12}$ was used as stabilizing agent or support to build three dimensional nanostructures. The Ru@$C_{66}(COOH)_{12}$ samples were synthesized with the same procedure as Ru@C_{60}. The use of fullerenehexamalonic acid $C_{66}(COOH)_{12}$ should insure directionality in the assembly. We investigated the solvent and Ru@$C_{66}(COOH)_{12}$ ratio effect for this reaction. For the solvent, the results were obtained in THF, methanol, and a THF/methanol mixture. Among these solvents, regular shapes and narrow size distributions of Ru nanoparticles (around 1.5 nm) occurred spontaneously in THF. Specifically, very small particles (< 1 nm) are formed in methanol, while a few big Ru NPs are obtained in the mixture of solvents THF/H_2O and THF/methanol. Furthermore, the effect of ratio of Ru/$C_{66}(COOH)_{12}$ was studied. TEM characterizations of Ru@$C_{66}(COOH)_{12}$ 6/1, 12/1 and 30/1 revealed that Ru NPs with a good distribution are obtained even at high ratio. The decomposition of the Ru precursor in the presence of this modified fullerene (Ru@$C_{66}(COOH)_{12}$ = 20/1) leads in the appropriate solvent to very small an monodispersed Ru NPs (1.5 ± 0.2 nm). SAXS analyses have been performed showing the presence of a peak at 0.22$Å^{-1}$ corresponding to a Ru NPs - Ru NPs distance 2.85 nm, perfectly consistent with Ru NPs organization in this material.

The Ru@C_{60}, T-Ru@C_{60} and Ru@$C_{66}(COOH)_{12}$ catalysts were tested in the hydrogenation of nitrobenzene and cinnamaldehyde. In the hydrogenation

nitrobenzene, the result revealed that $Ru@C_{60}$ can not only produce selectively aniline but also cyclohexylaime by the consecutively hydrogenation. T-$Ru@C_{60}$, only reduced aniline at a same reaction time, and further studies revealed that the T-$Ru@C_{60}$ catalysts are not effective for the hydrogenation of aniline. Similarly, $Ru@C_{66}(COOH)_{12}$ 6/1and 12/1 only provide hydrogenation of nitrobenzene to aniline. These result suggest that small Ru NPs (1.5 nm) are not active for aromatic ring hydrogenation. However, the behavior of $Ru@C_{66}(COOH)_{12}$ 30/1 is different, with results which are comparable with $Ru@C_{60}$ 10/1. The controlled selective hydrogenation of nitrobenzene over $Ru@C_{60}$ was studied by DFT calculation, which suggest that the nitro group will be hydrogenated first if high hydride coverage is reached on Ru NPs surface.

In the hydrogenation of cinnamaldehyde, our studies suggest that the nature of the solvent has a remarkable effect on the selectivity towards HCAL or COL. The HCAL is the predominant product if 1,4-dioxane is used, while COL is produced with a high selectivity in isopropanol, if we except the acetal formation. The addition of a base sharply suppressed the formation of acetals, by preventing the alcohol react with the aldehyde on the electron deficient Ru NPs. Comparing $Ru@C_{60}$, T-$Ru@C_{60}$ and $Ru@C_{66}(COOH)_{12}$ catalyst, it is shown that the $Ru@C_{60}$ 10/1 system allows reaching the best selectivity towards COL (81%).

This PhD work open a number of exciting perspectives.

- ✓ The preliminary results obtained with the $Ru@C_{66}(COOH)_{12}$ system are extremely encouraging. They show that it seems possible to produce 3D organizations with covalent bonding that associate Ru NPs and carbon NPs (fullerene). Other type of functionalized fullerenes as well as other metals (such as Co for its magnetic properties) should be investigated in order to: i) expand to 1D and/or 2D organizations, and ii) expand to other applications such as in physics.

- ✓ The results obtained in the case of T-Ru@C_{60} systems are also extremely exciting, since Ru NPs with size < 1 nm have been produced for a Ru/C_{60} ratio of 10 (size of a Ru_{13} cluster = 0.5 nm). Isolated atoms in a C_{60} matrix are produced for a Ru/C_{60} ratio of 1. It will be very interesting to produce samples with ratio between 1 and 10 to see if it is possible to produce a Ru NP almost atom per atom, and also to study the NP size effect in catalysis at the sub-nanometer scale.
- ✓ The Ru NPs associate to C_{60} are highly electron deficient. This has an effect on catalytic performances. The study of the electronic effects in catalysis is of course of paramount importance. The model systems synthesized offered enormous possibility to study these effects. Indeed, if we suppose that the electron transfer could be modulate *via* UV/visible light irradiation, it will be possible to study metal support electronic interaction for a given system showing the same support, the same metal loading and the same metal NP size.
- ✓ Finally, the application of the Ru@fullerene catalytic systems in other catalytic reactions, such as condensation reaction, and ammonia synthesis, could be interesting due to the presence of electron deficient Ru centers.

Chapitre 5 Résumé

5.1 Introduction

La catalyse est essentielle pour transformer de façon spécifique la structure chimique de la matière à grande échelle, et de fait les catalyseurs jouent un rôle central dans 90% des procédés de fabrication des produits chimiques. L'un des principaux défis pour la catalyse au 21eme siècle est de mieux comprendre et concevoir des catalyseurs afin de mieux contrôler l'activité catalytique, la sélectivité et la stabilité. Dans ce contexte, la recherche sur des matériaux poreux avec des structures de pores sur mesure, et sur la composition et le nano-environnement des sites catalytiques est d'une importance stratégique; et il est évident que toutes nouvelles branches de la catalyse, comme la nanocatalyse, devraient être considérées comme un levier potentiel pour atteindre ces objectifs. Parmi les différents nanocatalyseurs, les matériaux carbonés nanostructurés gagnent de plus en plus de visibilité. Le développement de nouvelles nanostructures de carbone au cours des dernières décennies permet un contrôle à des échelles de longueur multiples. La polyvalence de ces matériaux et la complexité de la chimie physique du carbone rend la conception de catalyseurs structurellement contrôlés une tâche difficile. Concevoir des nano-architectures catalytiques offre donc la promesse d'une plus grande activité, sélectivité et stabilité, à condition que les spécifications suivantes soient respectées: *a*) un contrôle de la taille et/ou de la forme des nanoparticules, *b*) un contrôle de l'environnement proche de la nanoparticule, et *c*) une interaction contrôlée et robuste (covalente) du métal avec le support.

La fonctionnalisation des composées nanostructurées de carbone avec des particules métalliques est un domaine de recherche en pleine effervescence. Les nanoparticules (NPs) métalliques ont été associés à des nanotubes de carbone, du graphène, des fullerènes, et même à des nano-diamants. Alors que le contrôle de la taille des NPs a parfois été atteint, la principale limitation de ces matériaux est, comme pour le charbon actif, l'absence presque complète d'un contrôle de leur organisation : à savoir les NPs métalliques sont réparties de manière aléatoire sur la surface du carbone, et les interactions de ces NPs avec le site d'ancrage du carbone n'est pas homogène en raison de la présence de différents types de groupes fonctionnels en surface du support. Compte tenu de l'importance fondamentale de l'interaction métal-support sur l'activité, la sélectivité et la stabilité des catalyseurs hétérogènes, ceci est clairement préjudiciable à leurs performances. En outre, la distance entre les NPs étant non contrôlée, leurs propriétés sont loin d'être optimales. En effet, il a été récemment mis en évidence que la proximité des NPs peut fortement affecter leurs performances catalytiques, y compris leur stabilité. Enfin, il est souvent extrêmement difficile

d'obtenir un chargement élevé en métal avec une petite taille de NPs métalliques, et ceci est désavantageux à de nombreuses applications catalytiques. Inspirés par les Metal-Organic Frameworks (MOF) et les Covalent Organic Frameworks (COF), nous proposons dans cette thèse de développer une famille originale de matériaux hybrides, associant d'une façon contrôlée et par des liaisons covalentes, des matériaux sp^2-C nanostructurés avec des NPs métalliques. Les matériaux nanostructurés sélectionnés comprennent le fullerène C_{60} et des fullerènes C_{60} fonctionnalisés. Plus précisément pour la catalyse, ce matériau devrait combiner: *a*) une taille de NP contrôlée, *b*) un environnement atomique défini pour les NPs, *c*) une interaction covalente avec le support, et *d*) une porosité élevée et une disponibilité de surface très dense des centres catalytiques. Pour atteindre ces objectifs une approche interdisciplinaire est nécessaire : *a*) fonctionnalisation du C_{60}, *b*) la synthèse et la caractérisation des NPs de métal (dans notre cas du ruthénium), *c*) l'assemblage contrôlé des structures hybrides, et *d*) une approche théorique visant à la modélisation et à la compréhension de la formation des édifices hybrides.

L'objectif de cette thèse est donc de produire des nanostructures Ru@carbone avec de telles spécifications qui ouvriront de nouvelles possibilités pour la catalyse du futur. Ainsi, une nouvelle chimie du carbone (chimie de surface) sera développée pour synthétiser un nouveau type d'architectures Ru@carbone constitué par des réseaux organisés de fullerènes et des nanoparticules de ruthénium. Ces nanocatalyseurs seront appliqués à un domaine stratégique de la catalyse dans les pays industrialisés : la chimie fine. Deux réactions d'intérêt industriel ont été sélectionnées pour lesquelles l'activité catalytique, la sélectivité et la stabilité sont de véritables défis : *a*) l'hydrogénation du nitrobenzene en aniline et/ou en cyclohexylamine, et *b*) l'hydrogénation du *trans*-cinnamaldéhyde.

5.2 Synthèse et caractérisation des nanostructures Ru@C_{60} et T-Ru@C_{60}.

Dans cette partie, nous décrivons la synthèse de matériaux bien définis, qui ont été caractérisés par une grande variété de techniques de caractérisation complémentaires.

5.2.1 Synthèse des nanostructures Ru@C_{60}

Les nano-architectures Ru@C_{60} ont été synthétisées par la décomposition du précurseur organométallique [Ru(COD)(COT)] (COD = 1,5 cyclooctadiène, COT = 1,3,5-cyclooctatriène) en présence du C_{60} sous 3 bars de H_2 à température ambiante (Schéma 5.1). Le contrôle des

conditions de réaction permet de synthétiser des polymères C_{60}-Ru-C_{60}-, des particules polymériques sphériques Ru-C_{60}, ou des particules polymériques sphériques Ru-C_{60} décorées avec des NPs de Ru.

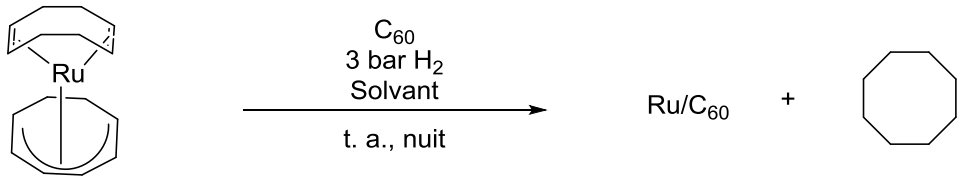

Schéma 5.1. Synthèse des nanoarchitectures Ru@C_{60}.

5.2.1.1 Effet du solvant et du rapport Ru/C_{60}

Dans un premier temps, nous avons étudié l'effet du solvant sur les architectures synthétisées, fixant le rapport Ru/C_{60} à 2/1. Plusieurs solvants ont été étudiés, y compris le toluène, le chlorobenzène, le 1,2-dichlorobenzène, le dichlorométhane et le chloroforme (Figure 5.1). Dans la décaline (bicyclo[4.4.0]décane), des structures avec des formes irrégulières décorées avec des petites NPs de Ru (1.23 ± 0,22 nm) ont été obtenues. Le toluène conduit à des structures plus petites avec des diamètres moyens d'environ 175 nm ne présentant pas de NPs de Ru. Des particules sphériques ont été obtenues en utilisant des solvants chlorés : chlorobenzène (285 ± 3 nm), 1,2-dichlorobenzène (200 ± 3 nm), $CHCl_3$ (229 ± 1.5 nm) et CH_2CI_2 (40 ± 0.7 nm). Les nanosphères synthétisées dans le CH_2Cl_2 ont un diamètre moyen nettement plus petit et une distribution plus étroite des tailles. En outre, dans le CH_2Cl_2, ces nanosphères sont décorées avec des NPS de Ru de taille très petite (1.15 ± 0.02 nm). Au cours de la synthèse réalisée dans la décaline, qui a la plus forte viscosité et la permittivité la plus faible (voir Figure 5.1), aucun ajustement de la forme n'est réalisé, tandis que dans le CH_2Cl_2 (viscosité plus faible et haute permittivité), des petites particules sphériques sont produites. Les autres solvants, montrant une viscosité intermédiaire, permettent aussi d'obtenir des sphères, cependant, avec des diamètres moyens plus importants. La seule exception est le nanomatériau synthétisé dans le toluène, qui a, comme la décaline, une permittivité faible.

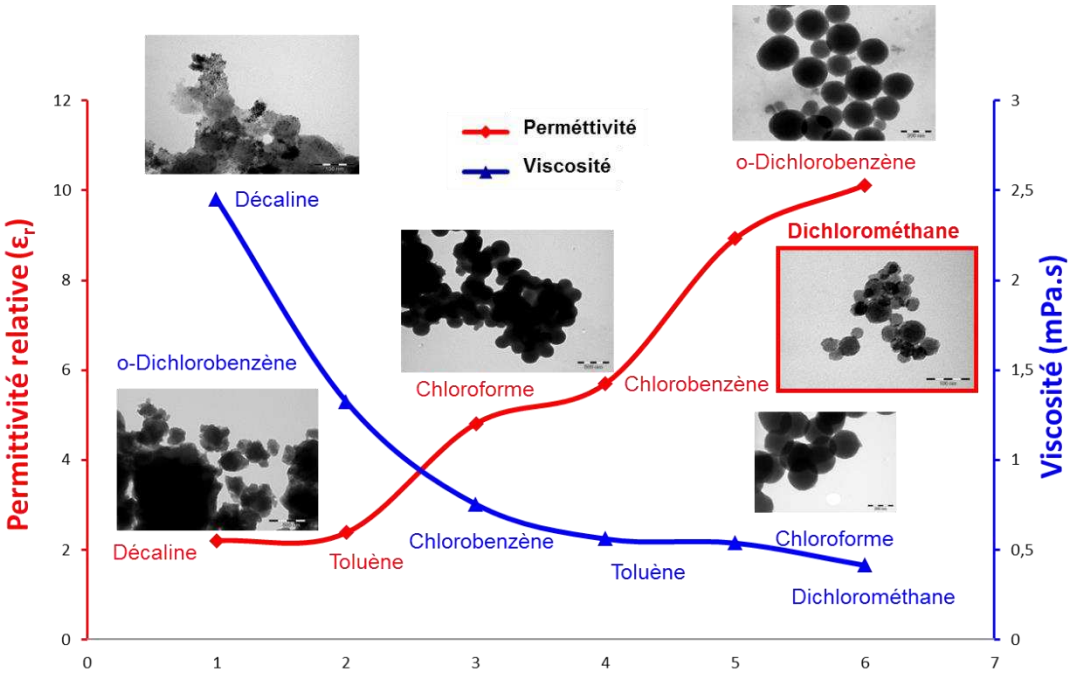

Figure 5.1. Effet de la viscosité et de la permittivité du solvant sur les assemblages Ru@C_{60} (Ru/C_{60} = 2/1). Conditions de réaction: [Ru(COD)(COT)] 2.0 éq, C_{60} 1.0 éq, solvant, 3 bar H_2, température ambiante, pendant une nuit.

Afin de mieux comprendre la structure des nanosphères produites, plusieurs nanostructures ont été synthétisées en utilisant le CH_2Cl_2 comme solvant et en changeant le rapport Ru/C_{60} avec une concentration de C_{60} fixe. Les rapports Ru/C_{60} étudiés sont les suivants : 2/3, 1, 2, 5, 10, 20, 30 et 50. Les analyses MET montrent que Ru@C_{60} 2/3 et 1/1 ne contiennent pas de NPs de Ru, en accord avec la HRMET. En augmentant la teneur en Ru, des NPs de Ru sont observées. Les NPs de Ru présentent dans tous les cas un diamètre moyen très petit, même à des rapports Ru/C_{60} élevés, allant de 1.10 à 1.35 nm.

5.2.1.1 Synthèse des nanostructures T-Ru@C_{60}

L'effet du rapport Ru/C_{60} a également été étudiée pour les nanostructures synthétises dans le toluène. Plusieurs rapports Ru/C_{60} (1/1, 10/1, 20/1 et 55/1) ont été étudiés en utilisant le toluène comme solvant de réaction (T-Ru@C_{60}). De même que pour le CH_2Cl_2, les faibles ratios Ru/C_{60} ne conduisent pas à la formation de NPs de Ru, qui ne sont observés que dans les échantillons T-Ru@C_{60} 20/1 et 55/1 en MET conventionnelle (Figure 5.2). Des structures sans forme régulière ont été observées pour tous les rapports, ce qui indique que la teneur en ruthénium de l'échantillon n'a aucun effet sur la forme de la structure.

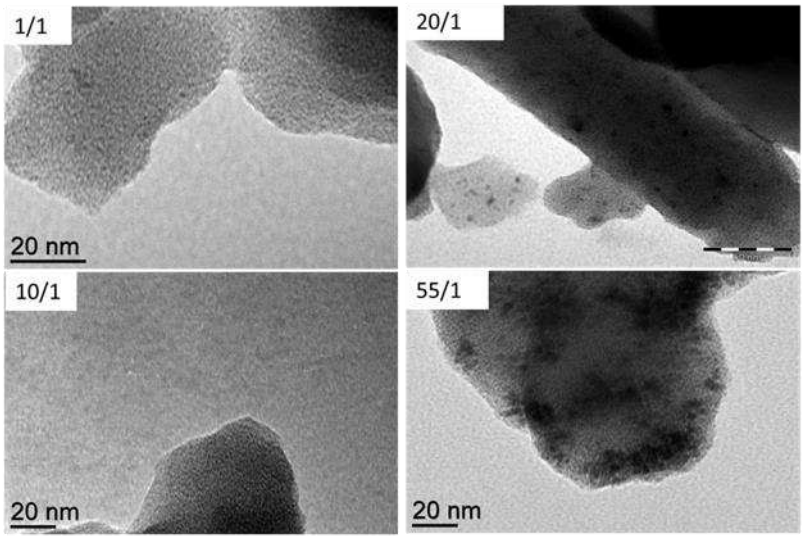

Figure 5.2. Structures T-Ru@C_{60} synthétisés dans le toluène avec des rapports Ru/C_{60} 1/1 (barre d'échelle de 20 nm), 10/1 (barre d'échelle de 20 nm), 20/1 (échelle de bar 50 nm) et 55/1 (barre d'échelle 20 nm).

5.2.2 Caractérisation des nanostructures Ru@C_{60}

Une grande variété de techniques complémentaires de caractérisation, y compris la MET en mode conventionnel, haute résolution et la tomographie, les spectroscopies Raman, XPS, WAXS et EXAFS, ainsi que des calculs DFT ont été utilisés.

Les analyses MET ou STEM sur les projections 2D de l'objet (Ru/C_{60} = 30), ne fournissent pas d'informations claires sur la présence éventuelle d'espèces de Ru (clusters ou petites NPs) à l'intérieur des sphères. A partir des tranches de vues 3D reconstruites (Figure 5.3) la présence de petites NPs de Ru est évidente sur la surface de la sphère, ce qui crée une coquille de NPs de Ru ayant une épaisseur d'environ 7 nm, ce qui correspond à une structure à plusieurs couches de NPs. Il est donc clair qu'aucune NP de Ru n'est présente à l'intérieur des sphères, mais cette analyse n'exclut pas la présence d'atomes de Ru dans la matrice polymère. L'analyse a également été réalisée pour l'échantillon Ru@C_{60} avec un rapport 1/1, mais la très petite taille des amas empêche leur localisation, la taille des agglomérats étant inférieure à la limite de résolution pour l'analyse par tomographie.

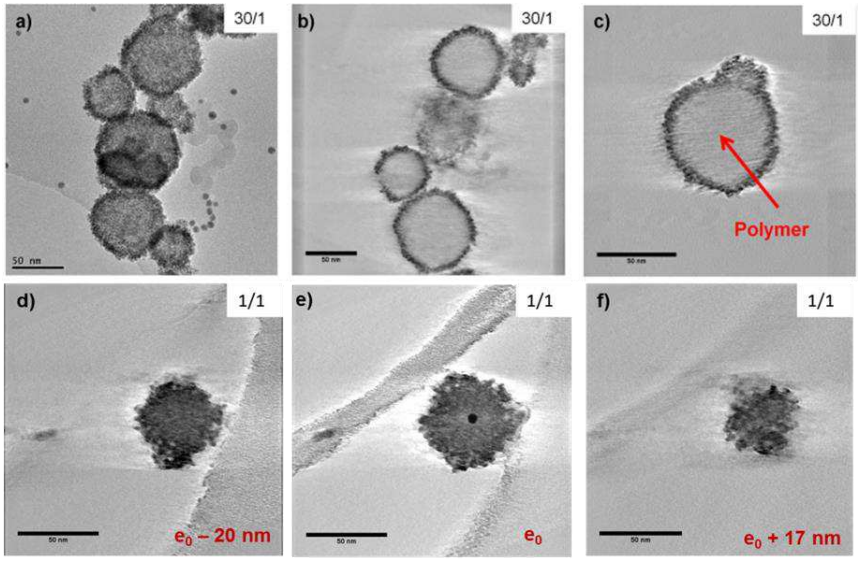

Figure 5.3. a) Analyse par tomographie de Ru@C_{60} 30/1 : a) à 0 ° d'inclinaison de la série d'inclinaison, b) et c) tranches en coupe transversale ; et d), e) et f) Ru@C_{60} 1/1 (barres d'échelle de 50 nm).

L'analyse WAXS montre que pour les échantillons avec un rapport Ru/C_{60} élevé, les diffractogrammes obtenus sont très proches et pleinement compatible avec du Ru métallique dans le système *hcp* sans contribution significative du fullerène C_{60}. Après corrections et transformées de Fourier, les fonctions PDF connexes sont comme prévu également très proches, et compatible avec des NPS métalliques de Ru. Pour le rapport 1/1, des NPs de Ru n'ont pas été identifiés.

Un transfert de charge du ruthénium au fullerène significatif a été mis en évidence par spectrométrie Raman et XPS pour tous les matériaux préparés, ce qui est un facteur important à prendre en compte, en particulier si l'on considère la réactivité possible de ces matériaux. La Figure 5.4a montre les spectres Raman excités à 532 nm du C_{60} et des structures Ru@C_{60} 1/1 et 20/1, dans le domaine spectral du mode Ag(2). Il a été montré que l'énergie du mode Ag(2) (1469.3 cm^{-1} pour le C_{60} pur) est sensible au transfert de charge dans les fullerures métalliques. On observe ici un décalage spectral de -8.7 cm^{-1} pour l'échantillon Ru@C_{60} 1/1 et de -11.6 cm^{-1} pour l'échantillon Ru@C_{60} 20/1, ainsi qu'un élargissement de la bande significatif avec une quantité croissante de C_{60}, causée par une forte interaction électron-phonon. Le transfert de charge a également été mis en évidence par XPS (Figure 5.4b), en comparant l'énergie de liaison de Ru 3p3/2 dans des échantillons Ru@C_{60} 1/1 et 20/1 avec celle du ruthénium métallique (462.2 eV). Les énergies de liaison mesurées étaient de 462.2 et 461.5 eV pour les échantillons Ru@C60 1/1 et 20/1, respectivement.

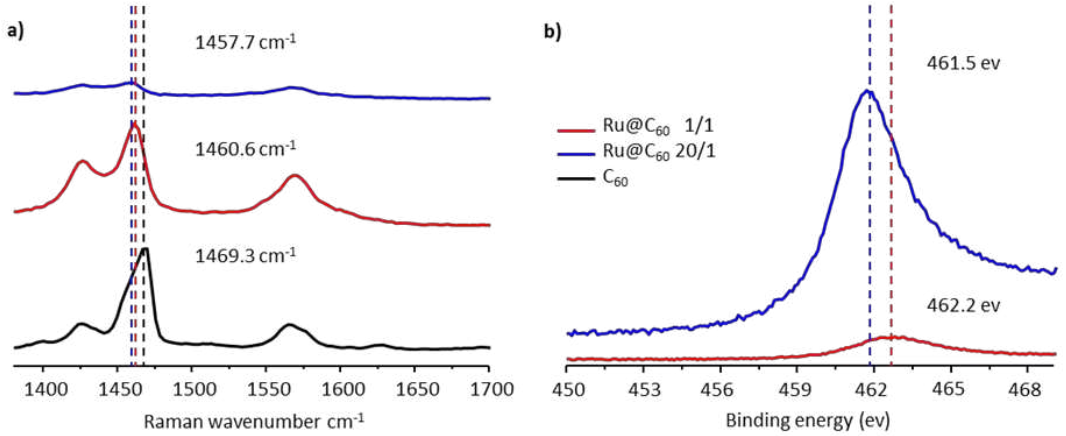

Figure 5.4. a) Spectres Raman excités à 532 nm du C_{60} et de Ru@C_{60} 1/1 et 20/1 dans la gamme spectrale du mode Ag(2); et b) spectres XPS Ru 3p3/2 du Ru@C_{60} 1/1 et 20/1.

Pour l'EXAFS, les spectres d'absorption au seuil K des échantillons Ru@C_{60} 1/1 et 2/1 ont été obtenus sous azote et après chauffage sous 4% de H_2/He pendant 1 h à 150 °C. L'énergie XANES mesurée est de 22.1244 keV pour les deux spectres. L'énergie XANES de Ru@C_{60} 2/1 est la même que celle du Ru@C_{60} 1/1; cependant, la forme de l'enveloppe XANES est légèrement différente, ce qui indique une petite différence de structure. Le nanocatalyseur Ru@C_{60} 1/1 a 8 liaisons Ru-C, qui sont stables à la réduction sous l'H_2 à 150 °C; tandis que dans l'échantillon Ru@C_{60} 2/1, environ un tiers du Ru est présent sous forme de NPs de Ru métallique de 1.5 nm de diamètre. Dans ce dernier cas, les deux tiers restants des Ru-C sont identiques à celles de l'échantillon Ru@C_{60} 1/1. Les résultats de l'EXAFS sont donc en bon accord avec les calculs DFT réalisés qui ont par ailleurs confirmé que le Ru est lié à 8 atomes de carbone en forme des liaisons η^2-η^6 (voir ci-dessous).

Pour comprendre la structure des nanostructures Ru@C_{60}, des calculs DFT ont été réalisés. Plusieurs modèles optimisés ont été obtenus dans des conditions spécifiques. Pour un seul atome de Ru qui interagit avec une molécule de C_{60}, la configuration la plus stable est $\eta^{2(6)}$, avec une énergie d'adsorption de -48 kcal/mole. En interaction avec deux fullerènes, un seul atome de Ru sera de préférence coordonné dans une position pontante η^2-η^2 utilisant deux liaisons $\eta^{2(6)}$. Une autre structure stable qui présente une coordination $\eta^{2(6)}$-η^6 est représentée sur la Figure 5.5. Un changement significatif de la coordination du Ru est observé lors de l'adsorption d'H_2 et la structure la plus stable possède des liaisons $\eta^{2(6)}$-η^4. Pour des chaînes 1D hypothétiques de polymère -C_{60}-Ru-C_{60}- avec un rapport Ru/C_{60} 1/1, on constate que les deux modes de coordination $\eta^{2(6)}$-η^4 et $\eta^{2(6)}$-η^6 pourraient être stabilisés.

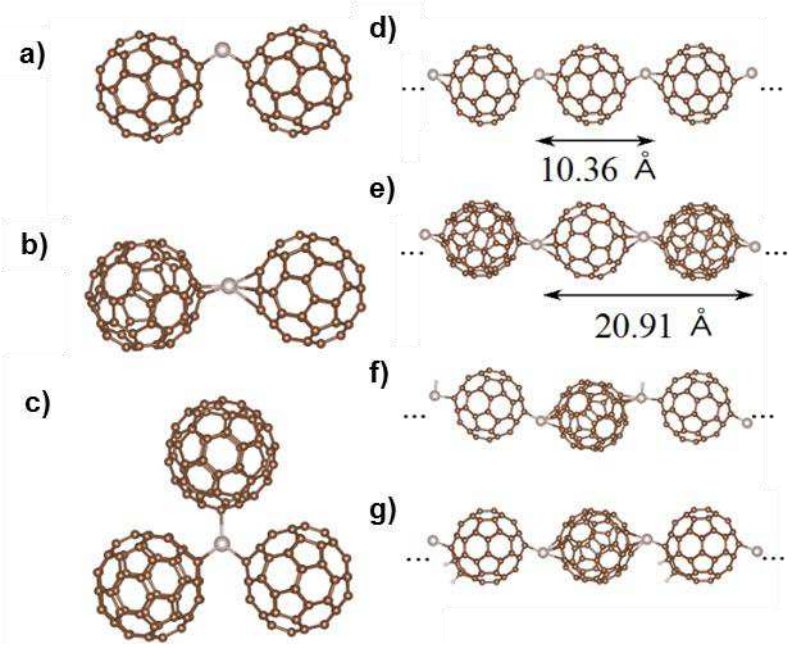

Figure 5.5. Vues : a) d'un complexe C_{60}-Ru-C_{60}; b) en mode de coordination $\eta^{2(6)}$-η^6; et c) du complexe le plus stable Ru-$(C_{60})_3$. Les chaînes 1D idéales et leurs paramètres de maille correspondants pour le rapport Ru/C_{60} 1/1 sont également donnés : en d) pour l'état $\eta^{2(6)}$-η^4 et e) pour l'état $\eta^{2(6)}$-η^6. Dans les deux derniers panneaux sont donnés les chaînes polymères idéales partiellement hydrogénées : en f) un atome de Ru est hydrogéné ou g) un C_{60} . Les atomes de Ru sont en gris, les atomes de carbone en brun et l'hydrogène en blanc.

5.3 Synthèse et caractérisation des nanostructures à base de ruthénium et de fullerène fonctionnalisé

Dans le but de construire des matériaux hybrides contenant des NPs de Ru avec des espaceurs organiques de taille nanométrique, un composé de fullerène hexa-substitué, qui contient douze acides carboxyliques comme groupes fonctionnels ($C_{66}(COOH)_{12}$) a été préparé (Schéma 5.2).

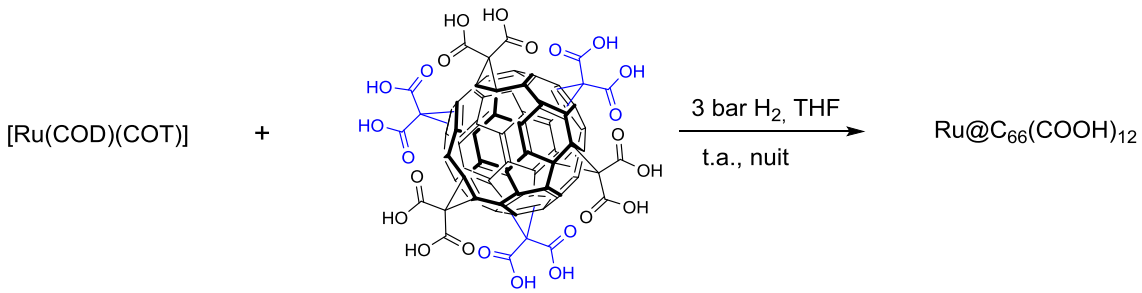

Schéma 5.2. Synthèse des nanostuctures Ru@$C_{66}(COOH)_{12}$

5.3.1 Effet du solvant et du rapport Ru/$C_{66}(COOH)_{12}$

L'effet du solvant sur la nanostructure synthétisée a été étudié en utilisant un rapport Ru/$C_{66}(COOH)_{12}$ de 6/1. Les solvants ont été choisis en fonction de la solubilité du fullerène $C_{66}(COOH)_{12}$, il s'agit du THF (tétrahydrofuranne), du MeOH, du DMF (diméthylformamide), et des mélanges de solvants THF/H_2O (10/1) et THF/MeOH (1/1). Dans tous les cas, des matrices de formes irrégulières décorées avec des NPs de Ru ont été produits (Figure 5.6), à l'exception du composé synthétisé dans un mélange THF/MeOH (1/1), où nous avons obtenu des nanosphères. Les diamètres moyens des NPs métalliques sont dans la gamme de 1.03 à 2.37 nm. Les nanostructures Ru/$C_{66}(COOH)_{12}$ synthétisées dans du THF et du MeOH contiennent des NPs de très petite taille, 1.23 ± 0.02 et 1.03 ± 0.06 nm, respectivement. Les NPs sont très proches indiquant un certain degré d'ordre. En revanche, la synthèse réalisée dans du DMF a donné des NPs de Ru supportées sur une matrice qui est similaire à celle observée dans les images MET du polymère Ru@C_{60}.

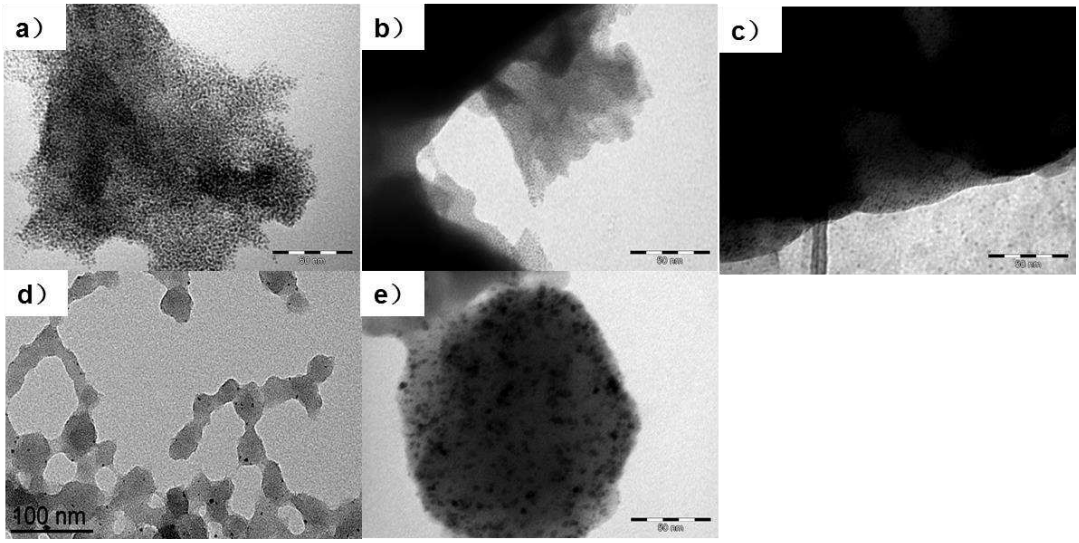

Figure 5.6. Images MET des structures Ru@$C_{66}(COOH)_{12}$ 6/1 synthétisées dans différents solvants : a) THF (barre d'échelle de 50 nm), b) MeOH (barre d'échelle de 50 nm), c) DMF (barre d'échelle de 50 nm), d) THF/H_2O (10/1) (barre d'échelle de 100 nm), et e) THF/MeOH (1/1) (barre d'échelle de 50 nm).

Une série d'expériences en utilisant différents rapports Ru/$C_{66}(COOH)_{12}$ (de 6/1 jusqu'à 100/1) ont également été effectuées (en utilisant le THF comme solvant de réaction) afin de mieux comprendre les structures Ru@$C_{66}(COOH)_{12}$. Les analyses MET montrent que, dans tous les cas des NPs de Ru ont été obtenu, et dans tous les cas, les NPs étaient près les unes des autres formant de plus grandes superstructures. Fait intéressant, la distribution moyenne de taille des NPs de Ru augmente avec l'augmentation de la teneur en Ru tandis, que la nanostructure est

restée pratiquement inchangée, sauf pour l'échantillon $Ru@C_{66}(COOH)_{12}$ 100/1, probablement dû à forte teneur en Ru de la nanostructure.

5.3.2 Caractérisation des nanostructures $Ru@C_{66}(COOH)_{12}$

Les nanostructures $Ru@C_{66}(COOH)_{12}$ ont été étudiées en détail en utilisant plusieurs techniques de caractérisation : WAXS, SAXS, RMN du solide, XPS et ATR-IR.

Les analyses WAXS des nanostructures $Ru@C_{66}(COOH)_{12}$ 6/1, 12/1 et 30/1 montrent trois diffractogrammes très similaires (Figure 5.7) ; ils sont parfaitement compatibles avec du Ru métallique dans le système *hcp* (2theta = 20°). Le signal aux petits angles pourrait être attribué au ligand $C_{66}(COOH)_{12}$, car il est très proche de celui du $C_{66}(COOH)_{12}$ pur. Après corrections et transformées de Fourier, les fonctions PDF connexes sont également et comme prévu très proches, et la taille (longueur de cohérence) peut atteindre 1.5 nm. Dans le cas présent, nous n'observons pas une diminution ou une augmentation de la PDF du Ru métallique comme dans le cas des structures $Ru@C_{60}$. Les PDF indiquent également que les NPs de Ru ont une distribution de taille unique et un diamètre moyen proche de 1.5 nm, en accord avec les mesures MET.

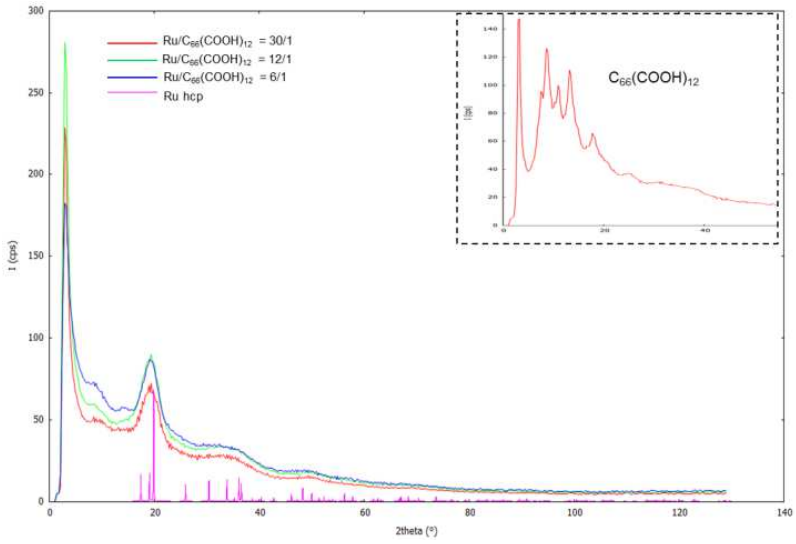

Figure 5.7. Diffractogrammes des nanostructures $Ru@C_{66}(COOH)_{12}$ 6/1, 12/1 et 30/1 ainsi que des données de référence du Ru *hcp*; encart diffractogramme de $C_{66}(COOH)_{12}$.

Pour mesurer la distance inter-particulaire des NPs de Ru, l'échantillon $Ru@C_{66}(COOH)_{12}$ 12/1 a été caractérisé par SAXS (Figure 5.8). Les spectres SAXS sont généralement représentés comme une intensité diffusée en fonction de l'amplitude du vecteur de diffusion q = $4\pi\sin\theta/\lambda$. Le spectre montre un petit pic à 0.22 $Å^{-1}$ qui correspond à une distance inter-particulaire de 2.85 nm.

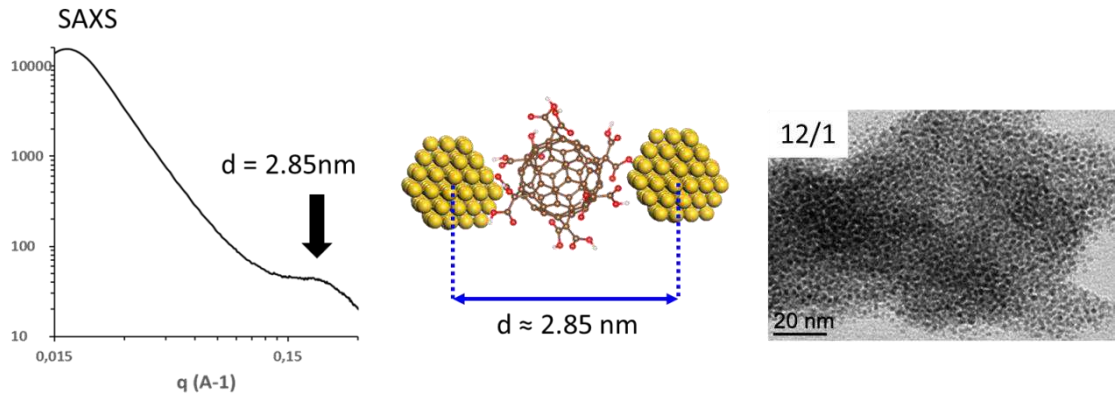

Figure 5.8. Gauche : spectre SAXS du Ru@$C_{66}(COOH)_{12}$ 12/1 ; centre : représentation schématique de la distance NP de Ru - NP de Ru ; et droite : image MET du Ru@$C_{66}(COOH)_{12}$ 12/1.

Les spectres de ^{13}C-RMN et CP-MAS à l'état solide ont été réalisés pour plusieurs nanostructures Ru@$C_{66}(COOH)_{12}$ (Figure 5.9). Les pics à 69 ppm et 141-150 ppm sont attribués à la structure du fullerène; ils restent inchangés par rapport au $C_{66}(COOH)_{12}$ libre. En revanche, le pic visible à 45 ppm, attribué à l'atome de carbone quaternaire, est décalé de 25 ppm et le pic attribué au groupes carboxyliques est décalée à 185 ppm, indiquant que le $C_{66}(COOH)_{12}$ se coordonne aux NPs de Ru par les groupes carboxyliques, probablement sous forme de carboxylate, fait qui a été confirmé par des analyses IR et des calculs DFT.

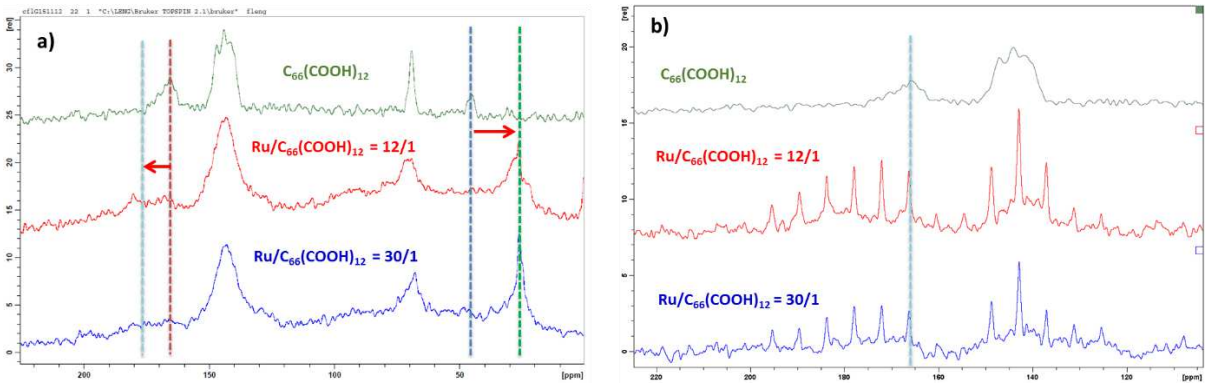

Figure 5.9. Spectre RMN ^{13}C : a) SSNMR; et b) CP-MAS SSNMR du $C_{66}(COOH)_{12}$, Ru@$C_{66}(COOH)_{12}$ 12/1 et 30/1.

Les analyses XPS ont été réalisées pour plusieurs nanostructures Ru@$C_{66}(COOH)_{12}$. L'analyse XPS du Ru@$C_{66}(COOH)_{12}$ 12/1 est détaillée sur la Figure 5.10. Les éléments Ru, C et O ont été identifiés. Le pic Ru 3d et C1s peuvent être déconvolués en plusieurs composantes : le pic attribué au O-C=O, au C_{60}, sp^2-C, sp^3-C, et les bandes du Ru $3d^{3/2}$ et du $3d^{5/2}$. L'énergie de liaison du pic O1s est attribuée au O=C-O et au RuO_2. L'énergie de liaison du Ru $3p^{3/2}$ à 462.5 eV est légèrement plus élevée que celle du Ru(0), qui apparaît normalement à 462.2 ev.

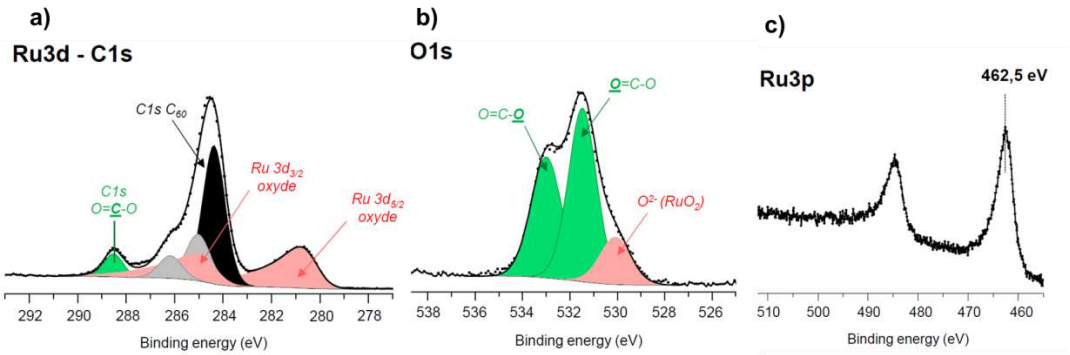

Figure 5.10. Spectre XPS du Ru@$C_{66}(COOH)_{12}$ 12/1 : a) Ru 3d, b) O1s, et c) énergie de liaison du Ru 3p.

Le spectre ATR-IR du $C_{66}(COOH)_{12}$ montrent des pics à 2900, 1700, 1192, 830, 708, 540 et 524 cm^{-1} (Figure 5.11). Les vibrations intenses à 2900 cm^{-1} (COOH), 1700 cm^{-1} (C=O), 1192 cm^{-1} (C-O) sont attribués au groupe -COOH, tandis que les autres pics sont attribués à des vibrations de la cage du fullerène. Les échantillons Ru@$C_{66}(COOH)_{12}$ 6/1, 12/1 et 30/1 ont donnés des spectres ATR-IR similaires. Les pics à 540 et 524 cm^{-1} sont attribués à la cage du fullerène qui reste inchangée ; tandis que les vibrations C=O du groupe COOH qui apparaissent à 1700 cm^{-1} ont disparues dans les nanostructures de Ru par rapport au ligand libre. Deux nouveaux pics à 1555 et 1367 cm^{-1} sont apparus qui ont été attribués aux vibrations C=O d'une nouvelle espèce COO-Ru, confirmant à nouveau la coordination du fullerène sous forme de ligand carboxylate. Ces données sont en accord avec les valeurs publiées pour des complexes Ru-carboxylate. Le pic à environ 1900 cm^{-1} pourrait être causé par la vibration de la liaison de Ru-H.

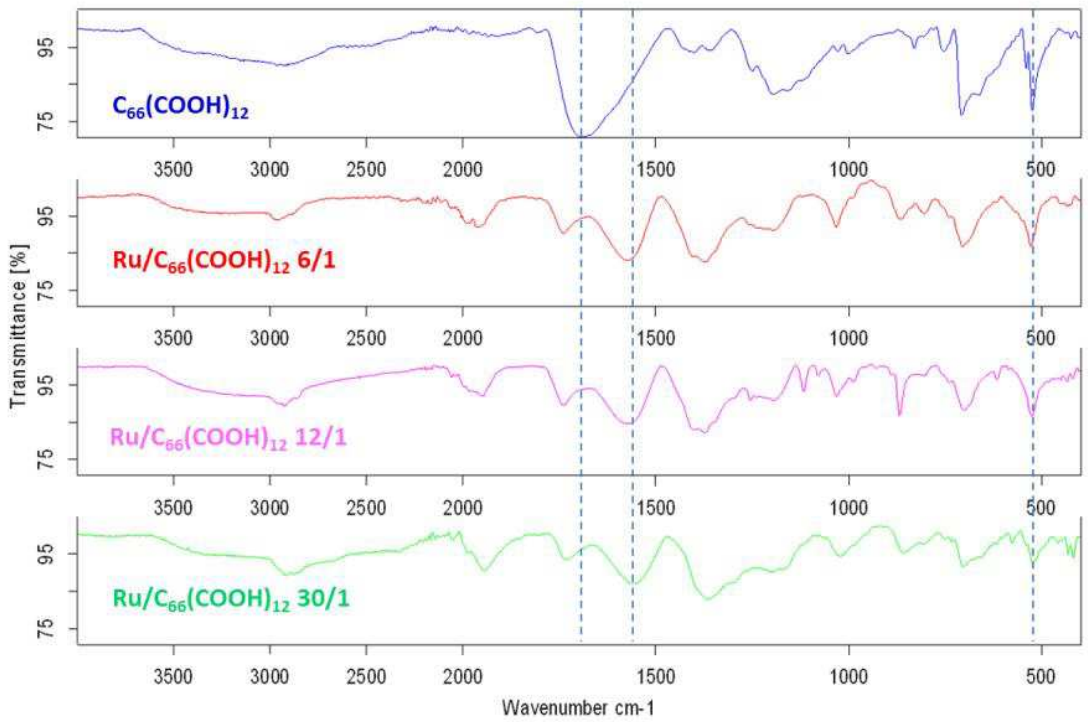

Figure 5.11. Spectres ATR-IR du $C_{66}(COOH)_{12}$ (en haut) et Ru@ $C_{66}(COOH)_{12}$ 6/1, 12/1 et 30/1 (en bas).

Pour étudier les modes de coordination du $C_{66}(COOH)_{12}$ avec les NPs de Ru, nous avons modélisé le système en utilisant deux espèces $C_{66}(COOH)_{12}$ en interaction avec un cluster Ru_{13}. Comme le montre la Figure 5.12, le mode de coordination implique 3 atomes d'oxygène avec une facette constituée de 3 atomes de Ru en surface de la NP. Les distances Ru-O sont typiques de ces systèmes avec des valeurs allant de 1.97 à 2.05 Å, en bon accord avec une étude précédente sur l'interaction de NPs de Ru avec les parois latérales de nanotubes de carbone oxydés (présence de groupe carboxylique en surface des nanotubes). Il est intéressant de noter que, comme dans l'étude précédente, la migration des hydrures sur le cluster de Ru est spontanée, ce qui entraîne la formation de groupes carboxylates, avec un gain énergétique de l'ordre de 15 kcal/mol par H adsorbé. Globalement, la formation de ce complexe est très favorable: -149 kcal/mol.

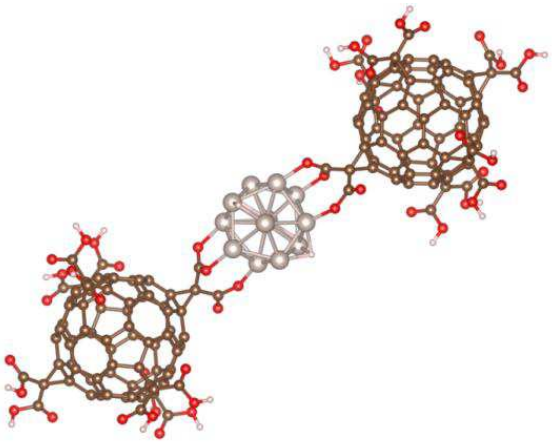

Figure 5.12. Structure optimisée de l'espèce $C_{66}(COOH)_{12}$-Ru_{13}-$C_{66}(COOH)_{12}$.

5.4 Applications catalytiques des nanostructures ruthénium@fullerène

Dans cette partie les propriétés catalytiques de plusieurs nanostructures Ru@fullerène ont été étudiées. Les nanostructures de ruthénium synthétisées dans le CH_2Cl_2 ($Ru@C_{60}$) et dans le toluène (T-$Ru@C_{60}$), ainsi que les nanostructures $Ru@C_{66}(COOH)_{12}$ ont été utilisées comme catalyseurs dans les réactions d'hydrogénation du nitrobenzène (NB) et du *trans*-cinnamaldéhyde (CAL).

5.4.1 Hydrogénation du nitrobenzène

5.4.1.1 Hydrogénation de nitrobenzène avec des catalyseurs $Ru@C_{60}$

L'hydrogénation du nitrobenzène (NB) a été étudiée sous 30 bars de H_2 à 80 °C dans l'éthanol (Schéma 5.3). Tous les catalyseurs se sont révélés actifs pour l'hydrogénation du NB (Tableau 5.1). Dans les conditions expérimentales testées, le fullerène C_{60} n'est pas d'actif pour cette réaction. Pour les catalyseurs avec les rapports Ru/C_{60} les plus faibles ($Ru/C_{60} < 5$) l'aniline (AN) a été produite avec une sélectivité > 80%, néanmoins la cyclohéxylamine (CA) n'a pas été détectée dans le milieu réactionnel. Cela peut être dû à la très petite taille des NPs de Ru présentes dans ces échantillons, ce qui pourrait les rendre inactives pour l'hydrogénation du cycle aromatique. Aux rapports $Ru/C_{60} \geq 5$, tous les catalyseurs sont actifs pour l'hydrogénation complète du NB pour produire la CA. La caractéristique remarquable de tous ces catalyseurs est que l'hydrogénation de l'AN pour produire la CA ne démarre que lorsque l'hydrogénation du NB en AN est terminée. Un tel comportement n'a jamais été rapporté

auparavant. Une hydrogénation chimiosélective et contrôlée du NB sur les catalyseurs $Ru@C_{60}$ est donc possible.

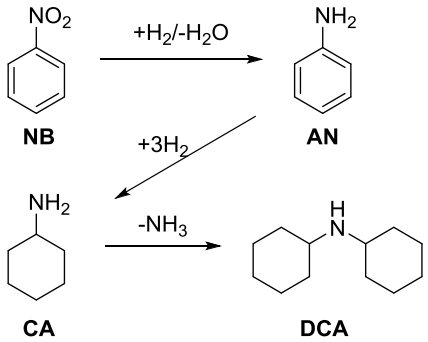

Schéma 5.3. Principaux produits et sous-produits formés au cours de l'hydrogénation du NB.

Tableau 5.1. Hydrogénation du nitrobenzène dans l'éthanol utilisant plusieurs catalyseurs $Ru@C_{60}$.[a]

$Ru@C_{60}$	Group nitro		Sélectivité (%)[b]		Cycle aromatique		Sélectivité (%)[b]		
	TOF (h^{-1})[c]	Temps h	AN	AN-Et	TOF (h^{-1})[d]	Temps h	CA	DCA	CA-Et
1/1	18.7	48	80	20	--	---	---	--	---
2/1	33.6	48	84	16	---	---	trace	--	---
5/1	44.3	24	96	4	132.2	6	91	4	5
10/1	55.7	4	90	10	100.4	3.5	86	7	7
20/1	60.8	3.5	91	9	182.1	2	84.5	8.5	7
30/1	59.8	3	91	9	123.1	1.5	82.5	9	8.5
50/1	42.6	3	92	8	134.5	1.5	89	5	6

[a]Conditions de réaction: 5 mg de catalyseur $Ru@C_{60}$, 500 mg (4.06 mmol) de NB, 200 mg (1.1 mmol) de dodécane (étalon interne), 30 bar d'H_2, 80 °C, 30 mL d'EtOH. [b]Déterminé par GC-MS en utilisant la technique de l'étalon interne. [c]TOFs calculés à 1 h de réaction (~30% de conversion) sauf pour les rapports 1/1 et 2/1 (3 h). [d]TOFs calculés à 0.5 h de réaction (~50% de conversion) sauf pour les rapports 5/1 and 10/1 (1 h).

Dans tous les cas, la sélectivité obtenue envers l'AN est supérieure à 90% et la sélectivité envers la CA est supérieure à 80%. Si l'on considère l'activité de ces catalyseurs, les TOF sont systématiquement plus élevés pour l'hydrogénation du cycle aromatique que pour l'hydrogénation du groupe nitro.

Plusieurs substrats ont également été testés, en variant le caractère donneur/attracteur d'électrons du substituant sur le cycle aromatique. Dans tous les substrats testés, l'hydrogénation par étapes a été observée pour produire l'amine entièrement hydrogénée. Comme prévu par l'effet électronique, le *p*-chloronitrobenzène et le *p*-fluoronitrobenzène réagissent plus vite que le *p*-nitrotoluène pour produire l'aniline respective. Le catalyseur Ru@C_{60} permet la production de la *p*-chloraniline avec 92% de sélectivité. Dans une deuxième étape, la *p*-chloroaniline subit une hydro-déchloration pour produire l'AN, qui est ensuite hydrogénée pour produire la CA. Le *p*-fluoronitrobenzène a présenté le même comportement. La *p*-toluidine a été entièrement convertie après seulement 4.5h de réaction. Les *cis*- et *trans*-4-MCyNH$_2$ ont été formées avec un rapport de 4, ce qui est exceptionnellement élevé pour des catalyseurs Ru/C.

5.4.1.2 DFT

Afin de comprendre l'hydrogénation chimiosélective et contrôlée du NB sur les catalyseurs Ru@C_{60}, une étude DFT a été réalisée, pour explorer la thermodynamique de la coordination d'une seule molécule de NB sur un modèle moléculaire 2C_{60}-Ru_{13}.

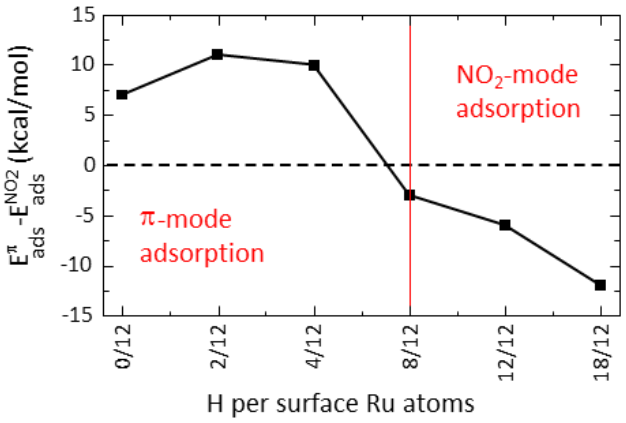

Figure 5.13. Evolution de la différence d'énergie entre les deux modes d'adsorption en fonction du rapport de H par atome de Ru de surface.

Deux modes de coordination, notés comme π-mode et nitro-mode dans ce qui suit, sont en compétition. Ici, nous proposons que le mode de nitro est favorisé par la présence de nombreux hydrures sur la surface métallique, avec un rapport expérimental entre 1.3 et 2 H par atome de Ru en surface. Comme le montre la Figure 5.13, pour des valeurs faibles du taux de recouvrement en H, la coordination π-mode est thermodynamiquement favorisée, mais dès que suffisamment d'hydrures sont présents en surface du Ru, le mode nitro devient plus stable. Compte tenu des conditions expérimentales (température et pression d'H_2), il est possible de

considérer que les petites NPs métalliques sont entièrement couvertes d'hydrures, et sont des sites préférentiels pour l'hydrogénation sélective en aniline.

5.4.1.3 Hydrogénation du nitrobenzène utilisant les nanocatalyseurs Ru@C_{60}, T- Ru@C_{60}, et Ru@$C_{66}(COOH)_{12}$

Tous les nanocatalyseurs T-Ru@C_{60} sont actifs dans l'hydrogénation du NB pour produire de l'AN en tant que produit majoritaire avec une sélectivité allant jusqu'à 93% à 6h de réaction (voir le Tableau 5.2). Cependant, aucune conversion en CA n'a pas été détectée en utilisant ces catalyseurs. La raison est probablement la teneur en Ru et la taille des NPs. Les catalyseurs T-Ru@C_{60} 1/1 (6.8% Ru), 10/1 (15.7% Ru) et 55/1 (47.5% Ru) ont un pourcentage similaire de Ru que les nanocatalyseurs Ru@C_{60} 2/3 (6.4% Ru), 2/1 (16.7% de Ru) et 10/1 (48.7% de Ru), respectivement. Ces catalyseurs Ru@C_{60} avec des rapports Ru/C_{60} faibles (Ru/C_{60} <5) se sont avérés inactifs pour l'hydrogénation du cycle aromatique et les catalyseurs T-Ru/C_{60} 1/1 et 10/1 sont donc comparables.

Tableau 5.2. Hydrogénation du nitrobenzène en utilisant les catalyseurs Ru@C_{60}, T-Ru@ $_{60}$, et Ru@$C_{66}(COOH)_{12}$.[a]

Catalyseur	Rapport	TOF[b]	Conversion (%)[c]	Sélectivité (%)[c]				
				AN	AN-Et	CA	DCA	CA-Et
T-Ru@C_{60}	1/1	85	24	85	15	---	---	---
	10/1	119	51	92	8	---	---	---
	55/1	41	69	93	7	---	---	---
Ru@$C_{66}(COOH)_{12}$	6/1	120	53	92	8	---	---	---
	12/1	61	53	92	8	---	---	---
	30/1	51	100	2	---	86	traces	11
Ru@C_{60}	1/1	19	10	80	20	---	----	----
	10/1	49	100	90	10	86	7	7
	50/1	42	100	92	8	89	5	6

[a]Conditions de réaction: 5 mg de catalyseur, 500 mg (4.06 mmol) de NB, 200 mg (1.1 mmol) de dodécane (étalon interne), 30 bar d'H_2, 80 °C, 30 mL d'EtOH. [b]TOFs calculés à 1 h de réaction. [c]Déterminé par GC-MS utilisant la technique d'étalon interne a 6h de réaction.

D'autre part, le système T-Ru@C_{60} 55/1 n'a pas montré d'activité pour l'hydrogénation du cycle aromatique, ce qui indique que la charge en Ru n'est pas le seul facteur qui joue un rôle, et la taille des NPS de Ru a aussi un effet remarquable. Les tailles des NPs dans les

catalyseurs T-Ru@C_{60} sont : 1/1 (<1 nm), 10/1 (<1 nm) et 55/1 (1.15 ± 0.03 nm). Ces tailles sont comparables à la taille des NPs de Ru dans le catalyseur Ru@C_{60} 2/1 (1.16 ± 0.02 nm). Les catalyseurs T-Ru@C_{60} et Ru@C_{60} 2/1 ont une taille similaire de NPs, par conséquent, ils présentent un comportement catalytique similaire, à savoir qu'ils sont actifs pour l'hydrogénation du groupe NO_2 et inactifs pour l'hydrogénation du cycle aromatique. Le cas des catalyseurs Ru@$C_{66}(COOH)_{12}$ semble être similaire. Les nanocatalyseurs à bas chargement sont moins actifs que les catalyseurs Ru@C_{60} à teneur de Ru similaire. Cependant, Ru@$C_{66}(COOH)_{12}$ 30/1 a été capable d'hydrogéner l'AN en CA en 6 h de réaction, ce qui est comparable au nanocatalyseur Ru@C_{60} 20/1. Là encore, ce résultat souligne que l'accessibilité du métal joue un rôle très important pour l'activité et la sélectivité de cette réaction.

5.4.2 Hydrogénation du *trans*-cinnamaldéhyde

L'hydrogénation sélective du *trans*-cinnamaldéhyde (CAL) (Schéma 5.4) a été étudiée en utilisant les catalyseurs Ru@fullerène. L'effet du solvant ainsi que de l'ajout d'additifs ont été étudiés. Un effet marqué sur la sélectivité a été observé. Enfin, une comparaison des différents catalyseurs Ru@C_{60}, T-Ru@C_{60}, et Ru@$C_{66}(COOH)_{12}$ sera décrite. Le nanocatalyseur Ru@C_{60} 10/1 présente la meilleure sélectivité pour l'alcool cinnamylique (COL). En outre, l'aldéhyde saturé (HCAL) a également été synthétisée avec une sélectivité élevée en contrôlant les conditions de la réaction.

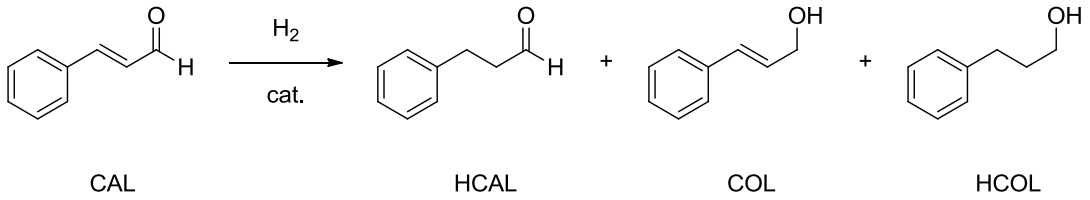

Schéma 5.4. Réaction d'hydrogénation du *trans*-cinnamaldéhyde.

5.4.2.1 Effet du solvant et de la base

L'hydrogénation du *trans*-cinnamaldéhyde a été étudiée à 20 bars de H_2 et 70 °C dans plusieurs solvants et en utilisant plusieurs bases. Le nanocatalyseur Ru@C_{60} 10/1s a été utilisé pour optimiser les conditions de réaction, puis, à partir des conditions optimisées les autres catalyseurs Ru@C_{60}, T-Ru@C_{60} et Ru@$C_{66}(COOH)_{12}$ ont été évalués. En général, l'addition d'une base dans le mélange réactionnel empêche de manière significative la formation d'acétals et améliore la sélectivité envers le COL. Deux types de bases ont été étudiés, des amines et des hydroxydes alcalins. Les résultats de la catalyse sont résumés dans le Tableau 5.3. En l'absence de toute base, le catalyseur Ru@C_{60} forme de très grandes quantités d'acétals,

dû à la réaction de condensation entre le CAL et le solvant (iPrOH). Ceci pourrait être expliqué par le fait que les NPs de Ru sont déficientes en électrons (catalyseur acide). Nous avons indépendamment vérifié que le catalyseur Ru@C_{60} est actif pour cette réaction de condensation sous atmosphère d'argon (conversion de 78% des CAL/iPrOH en acétal en 20 h à 70°C). À 20% de conversion et en présence d'hydrogène, 61% de COL a été obtenus sans aucune base (en faisant abstraction de la formation d'acétals) en utilisant le nanocatalyseur Ru@C_{60} 10/1, ce qui est déjà une haute sélectivité pour un catalyseur de Ru (≈40% de sélectivité en COL sont généralement rapportés sur des catalyseurs Ru/C).

Tableau 5.3. Effet de la base sur l'hydrogénation du *trans*-cinnamaldéhyde utilisant Ru@C_{60} 10/1.[a]

Ru@C_{60} 10/1	TOF (h^{-1})[b]	Sélectivité (%)[c]		
		HCAL	HCOL	COL
Sans base[d]	16.7	14	25	61
KOH	11.6	56	1	43
Et_3N	54.7	45	13	42
Pyridine	17.7	20	3	77
Pyridine (3 mL)	23.8	27	2	71

[a]Conditions de réaction : 528 mg (4.0 mmol) de *trans*-cinnamaldéhyde, 200 mg de nonane, 30 mL d'isopropanol, 70 °C, 1.5 eq. base, 20 bar H_2, 1000 rpm/min [b]TOFs calculés à 2 h de réaction.[c]A 20 % de conversion de CAL. [d]Les acétals sont les produits majoritaires de la réaction, la sélectivité reportée ne tient pas en compte ces acétals.

L'addition de 1,5 équivalents de pyridine augmente la sélectivité envers le COL jusqu'à 77% et supprime totalement la formation d'acétals. L'addition d'un excès supplémentaire de pyridine, n'a pas amélioré davantage la sélectivité. En revanche, l'ajout de bases plus fortes telles que KOH ou la triéthylamine diminue de manière significative la sélectivité.

5.4.2.2 Effet des différents nanocatalyseurs Ru@C_{60}, T-Ru@C_{60} et Ru@$C_{66}(COOH)_{12}$

En utilisant les conditions optimisées, les nanocatalyseurs Ru@C_{60}, T-Ru@C_{60} et Ru@$C_{66}(COOH)_{12}$ ont été testés, et les résultats sont résumés dans le Tableau 5.4. Tous les catalyseurs Ru@fullerène présentent des sélectivités relativement similaires envers le COL allant de 54 à 77%. Les meilleures performances dans le sens de l'activité et de la sélectivité

ont été obtenues avec les nanocatalyseurs Ru@C_{60}, soulignant que l'accessibilité des centres actifs est fondamentale dans la catalyse.

Tableau 5.4. Effet des catalyseurs sur l'hydrogénation du *trans*-cinnamaldéhyde

Catalyseur	Rapport Ru/fullerène	TOF (h^{-1})[b]	Sélectivité (%)[c]		
			HCAL	HCOL	COL
Ru@C_{60}	1/1	12.6	23	12	65
	10/1	17.7	20	3	77
	30/1	32	33	2	65
T-Ru@C_{60}	55/1	6.9	16	9	74
Ru@$C_{66}(COOH)_{12}$	6/1	7.2	39	7	54
	12/1	11.3	28	9	63

[a]Conditions de réaction : 528 mg (4.0 mmol) de *trans*-cinnamaldéhyde, 200 mg de nonane, 30 mL d'isopropanol, 70 °C, 1.5 eq. base, 20 bar H_2, 1000 rpm/min [b]TOFs calculés à 2 h de réaction.[c]A 20 % de conversion de CAL.

5.5 Conclusions

Dans cette thèse des nanostructures à base de fullerène C_{60} ou de fullerène fonctionnalisés et de NPs de Ru ont été synthétisées et utilisées pour des réactions catalytiques d'hydrogénation. Tout d'abord, les nano-architectures Ru@C_{60} ont été synthétisées par décomposition du [Ru(COD)(COT)], en présence du C_{60}. Pour la synthèse des échantillons Ru@C_{60}, l'effet du solvant et du rapport Ru/C_{60} ont été étudiés. Ces deux paramètres jouent un rôle clé dans la formation des nanostructures Ru@C_{60}. L'effet de différents solvants (toluène, chlorobenzène, *o*-dichlorobenzène, chloroformr, dichlorométhane, et décaline) a d'abord été étudié avec un rapport Ru/C_{60} de 2. On a constaté que les solvants de permittivité élevée et de faible viscosité permettent la production de particules sphériques de polymère Ru-C_{60}, ces particules ont une taille moyenne de 285 ± 3 nm pour le chlorobenzène, de 200 ± 3 nm pour le *o*-dichlorobenzène et de 39.6 ± 0.7 nm, pour le dichlorométhane. D'autre part, la faible permittivité et la viscosité élevée de la décaline et du toluène ne permettent pas l'obtention des sphères polymèriques.

En utilisant du dichlorométhane comme solvant, ce qui permet l'obtention de nanosphères polymériques bien définies, nous avons examiné l'effet du rapport Ru/C_{60}. En utilisant un rapport Ru/C_{60} 1/1 des nanosphères polymériques (37.8 ± 1,0 nm) sans NPs de Ru ont été

obtenues. En augmentant le teneur en Ru des nanosphères polymériques décorées avec des NPs de Ru ont été synthétisées. La taille des nanosphères est constante (environ 40 nm) et la taille des nanoparticules de Ru montre une distribution étroite (1-1.5 nm) dans tous les échantillons synthétisés ($Ru/C_{60} > 1$). La caractérisation des particules sphériques $Ru@C_{60}$ 1/1 a été réalisée. L'EXAFS, le WAXS et les calculs DFT pointent vers une structure polymérique, dans laquelle chacun des atomes de Ru est coordonné à deux C_{60}, avec un mode de coordination original du type $\eta^{2(6)}$-η^6. Les molécules de solvant contribuent à stabiliser ce fullerure. Cette phase polymérique est le produit cinétique de la réaction. Une augmentation du rapport Ru/C_{60} induit la formation de NPs de Ru bien dispersées sur la surface des sphères (produit thermodynamique de la réaction). Un transfert de charge significatif du ruthénium vers les fullerènes a été mis en évidence par spectrométrie Raman et XPS pour tous les matériaux préparés, ce qui est un facteur important à prendre en compte, en particulier si l'on considère la réactivité possible de ce fullerure.

En utilisant des conditions de réaction similaires, plusieurs nano-architectures T- $Ru@C_{60}$ ont été synthétisés dans le toluène par décomposition de [Ru(COD)(COT)] en présence du C_{60} sous 3 bars d'hydrogène. Les résultats indiquent que des NPs de Ru sous-nanométriques sont produites pour les rapport 1/1 et 10/1, alors que des NPs de Ru d'environ 1.1 ~ 1.5 nm ont été produites à des rapports Ru/C_{60} plus élevés (20/1 et 55/1).

Afin d'introduire de la directionnalité sur le fullerène C_{60}, nous avons synthétisé plusieurs fullerènes fonctionnalisés. Le fullerène hexa-substitué avec douze groupes carboxyliques, $C_{66}(COOH)_{12}$ a été utilisé comme agent de stabilisation pour construire des nanostructures tridimensionnelles. Les nanostructures $Ru@C_{66}(COOH)_{12}$ ont été synthétisées par le même mode opératoire que celui décrit pour le $Ru@C_{60}$. L'utilisation de l'acide fullerènehexamalonique $C_{66}(COOH)_{12}$ (fonctionnalisation octaédrique) devrait assurer la directionnalité dans l'assemblage. Nous avons étudié l'effet du solvant et du rapport $Ru/C_{66}(COOH)_{12}$ pour cette réaction. Plusieurs solvants dont, le THF, le MeOH et des mélanges de solvant THF/MeOH et THF/H_2O ont été utilisés. Parmi ces solvants, des formes régulières et des distributions de taille étroite des NPs de Ru (environ 1.5 nm) sont produites spontanément dans le THF. En particulier, de très petites particules (<1 nm) sont formées dans le MeOH, tandis que des NPs de Ru de taille plus importante sont obtenues dans les mélanges de solvants THF/MeOH et THF/H_2O. L'effet du rapport de $Ru/C_{66}(COOH)_{12}$ a également été étudié. La caractérisation par microscopie électronique des échantillons $Ru@C_{66}(COOH)_{12}$ 6/1, 12/1 et 30/1 a révélé que des NPs de Ru avec une distribution étroite

en taille ont été obtenues même a des rapports Ru/$C_{66}(COOH)_{12}$ élevés. Les analyses SAXS effectuées montrent la présence d'un pic à 0.22$Å^{-1}$ correspondant à une distance NP de Ru-NP de Ru de 2.85 nm, parfaitement cohérente avec l'organisation des NPs de Ru dans ce matériau.

Les nanocatalyseurs Ru@C_{60}, T-Ru@C_{60} et Ru@$C_{66}(COOH)_{12}$ ont été testés dans l'hydrogénation du nitrobenzène et du *trans*-cinnamaldéhyde. Dans l'hydrogénation du NB, les résultats ont révélés que les nanostructures Ru@C_{60} peuvent non seulement produire l'aniline, mais aussi la cyclohexylamine par hydrogénations consécutives. Le nanocatalyseur T-Ru@C_{60}, réduit seulement le NB en AN et est inactif pour l'hydrogénation du cycle aromatique. De même, les nanocatalyseurs Ru@$C_{66}(COOH)_{12}$ 6/1 et 12/1 n'hydrogènent pas le NB en CA. Toutefois, le Ru@$C_{66}(COOH)_{12}$ 30/1 avec une teneur en Ru plus élevée est capable d'hydrogéner complètement le NB pour produire la CA, avec des résultats qui sont comparables au nanocatalyseur Ru@C_{60} 10/1. L'hydrogénation sélective et contrôlée du NB sur Ru@C_{60} a été étudiée par DFT, les résultats obtenus suggèrent que le groupe NO_2 est hydrogéné d'abord si une couverture élevée en hydrures est atteinte en surface des NPs de Ru.

Dans l'hydrogénation du *trans*-cinnamaldéhyde, les études suggèrent que la nature du solvant a un effet remarquable sur la sélectivité envers le HCAL ou le COL. Le HCAL est le produit majoritaire si le 1,4-dioxane est utilisé comme solvant, tandis que le COL est produit avec une sélectivité élevée dans l'isopropanol, si la formation d'acétal n'est pas comptabilisée. L'addition d'une base supprime la formation d'acétals, en empêchant l'alcool (solvant) de réagir avec l'aldéhyde. En comparant les catalyseurs Ru@C_{60}, T-Ru@C_{60} et Ru@$C_{66}(COOH)_{12}$, il est démontré que le système Ru@C_{60} permet d'atteindre la meilleure sélectivité envers le COL (81%).